Simulation of Coupled Processes of Flow, Transport, and Storage of CO_2 in Saline Aquifers

Final Scientific Report

Reporting Period: 1 October 2009 – 30 September 2014

PI: Professor Yu-Shu Wu (Colorado School of Mines)

Co-PI:

Professor Zizhong Chen (University of California, Riverside)

Professors Hossein Kazemi and Xiaolong Yin (Colorado School of Mines)

Drs. Karsten Pruess and Curt Oldenburg (Lawrence Berkeley National Laboratory)

Research Personnel:

Drs. Philip Winterfeld and Ronglei Zhang (Colorado School of Mines)

December 2014

Submitting Organizations:

Colorado School of Mines
1500 Illinois St., Golden, CO 80401

Lawrence Berkeley National Laboratory
1 Cyclotron Road, Berkeley, CA 94720

Disclaimer

This report was prepared as an account of work sponsored by an agency of the United States Government. Neither the United States Government nor any agency thereof, nor any of their employees, makes any warranty, express or implied, or assumes any legal liability or responsibility for the accuracy, completeness, or usefulness of any information, apparatus, product, or process disclosed, or represents that its use would not infringe privately owned rights. Reference herein to any specific commercial product, process, or service by trade name, trademark, manufacturer, or otherwise does not necessarily constitute or imply its endorsement, recommendation, or favoring by the United States Government or any agency thereof. The views and opinions of authors expressed herein do not necessarily state or reflect those of the United States Government or any agency thereof.

Abstract

This report is the final scientific one for the award DE- FE0000988 entitled "Simulation of Coupled Processes of Flow, Transport, and Storage of CO_2 in Saline Aquifers." The work has been divided into six tasks. In task, "Development of a Three-Phase Non-Isothermal CO_2 Flow Module," we developed a fluid property module for brine-CO_2 mixtures designed to handle all possible phase combinations of aqueous phase, sub-critical liquid and gaseous CO_2, supercritical CO_2, and solid salt. The thermodynamic and thermophysical properties of brine-CO_2 mixtures (density, viscosity, and specific enthalpy of fluid phases; partitioning of mass components among the different phases) use the same correlations as an earlier fluid property module that does not distinguish between gaseous and liquid CO_2-rich phases. We verified the fluid property module using two leakage scenarios, one that involves CO_2 migration up a blind fault and subsequent accumulation in a secondary "parasitic" reservoir at shallower depth, and another investigating leakage of CO_2 from a deep storage reservoir along a vertical fault zone.

In task, "Development of a Rock Mechanical Module," we developed a massively parallel reservoir simulator for modeling THM processes in porous media brine aquifers. We derived, from the fundamental equations describing deformation of porous elastic media, a momentum conservation equation relating mean stress, pressure, and temperature, and incorporated it alongside the mass and energy conservation equations from the TOUGH2 formulation, the starting point for the simulator. In addition, rock properties, namely permeability and porosity, are functions of effective stress and other variables that are obtained from the literature. We verified the simulator formulation and numerical implementation using analytical solutions and example problems from the literature. For the former, we matched a one-dimensional consolidation problem and a two-dimensional simulation of the Mandel-Cryer effect. For the latter, we obtained a good match of temperature and gas saturation profiles, and surface uplift, after injection of hot fluid into a model of a caldera structure.

In task, "Incorporation of Geochemical Reactions of Selected Important Species," we developed a novel mathematical model of THMC processes in porous and fractured saline aquifers, simulating geo-chemical reactions associated with CO_2 sequestration in saline aquifers. Two computational frameworks, sequentially coupled and fully coupled, were used to simulate the reactions and transport. We verified capabilities of the THMC model to treat complex THMC processes during CO_2 sequestration by analytical solutions and we constructed reactive transport models to analyze the THMC process quantitatively. Three of these are 1D reactive transport under chemical equilibrium, a batch reaction model with equilibrium chemical reactions, and a THMC model with CO_2 dissolution.

In task "Study of Instability in CO_2 Dissolution-Diffusion-Convection Processes," We reviewed literature related to the study of density driven convective flows and on the instability of CO_2 dissolution-diffusion-convection processes. We ran simulations that model the density-driven flow instability that would occur during CO_2 sequestration. CO_2 diffused through the top of the system and dissolved in the aqueous phase there, increasing its density. Density fingers formed along the top boundary, and coalesced into a few prominent ones, causing convective flow that forced the fluid to the system bottom. These simulations were in two and three dimensions. We ran additional simulations of convective mixing with density contrast caused by variable

dissolved CO_2 concentration in saline water, modeled after laboratory experiments in which supercritical CO_2 was circulated in the headspace above a brine saturated packed sand in a pressure vessel. As CO_2 dissolved into the upper part of the saturated sand, liquid phase density increases causing instability and setting off convective mixing. We obtained good agreement with the laboratory experiments, which were characterized by finger development and associated mixing of dissolved CO_2 into the system. We then varied a wide range of parameters and conceptual models in order to analyze the possibility of convective mixing under different conditions, such as various boundary conditions, and chemical reaction conditions. The CO_2 fingers from different simulations showed great differences as time progressed, caused by permeability heterogeneity. The early time diffusive phenomenon was captured by fine grid resolution, and the permeability heterogeneity affected the pattern of the CO_2 fingers. In addition, the fingers from three-dimensional simulations tended to be larger and flatter than the two-dimensional ones.

In task "Implementation of Efficient Parallel Computing Technologies," we made enhancements and modifications to our code in order to substantially increase the grid size that could be run. We installed and ran it on various platforms, including a multi-core PC and a cluster, and verified the numerical implementation and parallel code using an example problem from the literature. This problem, with a grid size of sixty million, utilized the cluster's entire memory and all of its processors.

In task "Implementation of General Fracture Conceptual Models," we used the MINC approach, a generalization of the double-porosity concept, to model flow through porous and fractured media. In this approach, flow within the matrix is described by subdividing the matrix into nested volumes, with flow occurring between adjacent nested matrix volumes as well as between the fractures and the outer matrix volume. We generalized Hooke's law to a thermo-multi-poroelastic medium, and derived from the fundamental equations describing deformation of porous and fractured elastic media a momentum conservation equation for thermo-multi-poroelastic media. This equation is a generalization to multi-poroelastic media of the one derived in Task 3.0 for single porosity media. We describe two simulations to provide model verification and application examples. The first, one-dimensional consolidation of a double-porosity medium, is compared to an analytical solution. The second is a match of published results from the literature, a simulation of CO_2 injection into hypothetical aquifer-caprock systems.

3

Table of Contents

List of Figures

List of Tables

Executive Summary

This report is the final scientific one for the award DE- FE0000988 entitled "Simulation of Coupled Processes of Flow, Transport, and Storage of CO_2 in Saline Aquifers." The work has been divided into six tasks and the progress in each is outlined below.

Task 2.0: Development of a Three-Phase Non-Isothermal CO_2 Flow Module

Numerical simulation of CO_2 sequestration remains in the developmental stage, with relatively few studies. Chemical reactions are absent from many of these simulations, and much of the work in the area of reaction modeling is proprietary or in the developmental stage. We present a brief overview of published work in CO_2 sequestration modeling.

For mixtures of CO_2 and brine there are seven possible phase combinations, and fourteen when solid salt is included. The fluid property module for brine-CO_2 mixtures, called ECO2M, is designed to handle all possible phase combinations of aqueous phase, sub-critical liquid and gaseous CO_2, supercritical CO_2, and solid salt. The thermodynamic and thermophysical properties of brine-CO_2 mixtures (density, viscosity, and specific enthalpy of fluid phases; partitioning of mass components among the different phases) use the same correlations as in the ECO2N fluid property module, an earlier TOUGH2 one, that does not distinguish between gaseous and liquid CO_2-rich phases.

We verified the fluid property module using a previously investigated leakage scenario that involves CO_2 migration up a blind fault and subsequent accumulation in a secondary "parasitic" reservoir at shallower depth, and an investigation of leakage CO_2 from a deep storage reservoir along a vertical fault zone.

Task 3.0: Development of a Rock Mechanical Module

We developed a massively parallel reservoir simulator, called TOUGH2-CSM, for modeling THM processes in porous media brine aquifers. We derived, from the fundamental equations describing deformation of porous elastic media, a momentum conservation equation relating mean stress, pressure, and temperature, and incorporated it alongside the mass and energy conservation equations from the TOUGH2 formulation. In addition, rock properties, namely permeability and porosity, are functions of effective stress and other variables that are obtained from the literature. The starting point for our simulator is the massively parallel TOUGH2-MP code.

We verified the simulator formulation and numerical implementation using analytical solutions and example problems from the literature. For the former, we matched a one-dimensional consolidation problem and a two-dimensional simulation of the Mandel-Cryer effect. For the latter, we compared our results to those from two coupled computer codes, one that simulates fluid flow and heat transport, and the other that simulates rock deformation. We obtained a good

match of temperature and gas saturation profiles and surface uplift after injection of a hot fluid into a model of a caldera structure.

Task 4.0: Incorporation of Geochemical Reactions of Selected Important Species

We developed a novel mathematical model for simulation of THMC processes in porous and fractured saline aquifers. The novel frameworks were designed to keep a generalized computational structure, which can be easily applied for the numerical simulation of other THMC processes. In this case, we are simulating geo-chemical reactions associated with CO_2 sequestration in saline aquifers. Two computational frameworks, sequentially coupled and fully coupled, were used to simulate the reactions and transport.

We verified capabilities of the THMC model to treat complex THMC processes during CO_2 sequestration by analytical solutions and we constructed reactive transport models to analyze the THMC process quantitatively. We present here one of these analytical solutions, 1D reactive transport under chemical equilibrium. We also present here two of the reactive transport models, a batch reaction model with equilibrium chemical reactions and a THMC model with CO_2 dissolution.

Task 5.0: Study of Instability in CO_2 Dissolution-Diffusion-Convection Processes

We reviewed literature related to the study of density driven convective flows and on the instability of CO_2 dissolution-diffusion-convection processes. We used our modified TOUGH2-MP to run simulations that model the density-driven flow instability that would occur during CO_2 sequestration. CO_2 diffused through the top of the system and dissolved in the aqueous phase there, increasing its density. Density fingers formed along the top boundary, and coalesced into a few prominent ones, causing convective flow that forced the fluid to the system bottom. These simulations were in two and three dimensions.

We ran additional simulations of convective mixing with density contrast caused by variable dissolved CO_2 concentration in saline water, modeled after laboratory experiments in which supercritical CO_2 was circulated in the headspace above a brine saturated packed sand in a pressure vessel. As CO_2 dissolves into the upper part of the saturated sand, liquid phase density increases causing instability and setting off convective mixing. We obtained good agreement with the laboratory experiments, which were characterized by finger development and associated mixing of dissolved CO_2 into the system. We then varied a wide range of parameters and conceptual models in order to analyze the possibility of convective mixing under different conditions, such as various boundary conditions, and chemical reaction conditions. The CO_2 fingers from different simulations showed great differences as time progressed, caused by permeability heterogeneity. The early time diffusive phenomenon was captured by fine grid resolution, and the permeability heterogeneity affected the pattern of the CO_2 fingers. In addition, the fingers from three-dimensional simulations tended to be larger and flatter than the two-dimensional ones.

Task 6.0: Implementation of Efficient Parallel Computing Technologies

We developed a massively parallel reservoir simulator, called TOUGH2-CSM, for modeling THM processes in fractured and porous media brine aquifers. The starting point for our simulator is the massively parallel TOUGH2-MP code. We made enhancements and modifications to the original code in order to substantially increase the grid size that could be run. We installed and ran TOUGH2-CSM on various platforms, including a multi-core PC and a cluster.

We verified the numerical implementation and parallel code using an example problem from the literature. This problem, with a grid size of sixty million, utilized the cluster's entire memory and all of its processors. We obtained a good match of surface uplift after three years of CO_2 injection into the water leg of a depleting gas field.

Task 7.0: Implementation of General Fracture Conceptual Models

We use the MINC approach, a generalization of the double-porosity concept, to enable TOUGH2-CSM to model flow through porous and fractured media. In this approach, flow within the matrix is described by subdividing the matrix into nested volumes, with flow occurring between adjacent nested matrix volumes as well as between the fractures and the outer matrix volume. Flow within the matrix is one-dimensional and transient and the MINC approach reduces to the double-porosity one if there is only one matrix subdivision.

We generalize Hooke's law to a thermo-multi-poroelastic medium, and derive from the fundamental equations describing deformation of porous and fractured elastic media a momentum conservation equation for thermo-multi-poroelastic media that is incorporated into TOUGH2-CSM. This equation is a generalization to multi-poroelastic media of the one derived in Task 3.0 for single porosity media.

We describe two simulations to provide model verification and application examples. The first, one-dimensional consolidation of a double-porosity medium, is compared to an analytical solution. The second is a match of published results from the literature, a simulation of CO_2 injection into hypothetical aquifer-caprock systems.

14

Introduction

This report is the final scientific one for the award DE- FE0000988 entitled "Simulation of Coupled Processes of Flow, Transport, and Storage of CO_2 in Saline Aquifers." The work has been divided into tasks and these tasks are:

> Task 2.0: Development of a Three-Phase Non-Isothermal CO_2 Flow Module
> Task 3.0: Development of a Rock Mechanical Module
> Task 4.0: Incorporation of Geochemical Reactions of Selected Important Species
> Task 5.0: Study of Instability in CO_2 Dissolution-Diffusion-Convection Processes
> Task 6.0: Implementation of Efficient Parallel Computing Technologies
> Task 7.0: Implementation of General Fracture Conceptual Models

The progress for each of the above tasks is described in the following sections.

Task 2.0: Development of a Three-Phase Non-Isothermal CO_2 Flow Module

Literature Survey

Numerical simulation of CO_2 sequestration remains in the developmental stage, with relatively few studies. Chemical reactions are absent from many of these simulations, and much of the work in the area of reaction modeling is proprietary or in the developmental stage. A brief overview of published work in CO_2 sequestration modeling is provided in this section.

An early example of a non-reactive transport simulation (van der Meer, 1993) is CO_2 sequestration in a circular anticlinal stratigraphic trap. In a subsequent study (Holt et al., 1993), ECLIPSE 100, a black oil reservoir simulator, was modified to include the solubility of CO_2 in water and empirical relative permeability relations between liquid and gas phases. Their findings indicated that injection rate and absolute permeability were the dominant factors influencing injected CO_2 migration. van der Meer (1995) addressed CO_2 injection into a two-dimensional, quasi-infinite aquifer and concluded it was possible to sequester significant amounts of CO_2 in the subsurface, but capturing the combined effects of viscous fingering and gravity segregation would require three dimensional modeling.

Lindeberg (1995) described simulations of CO_2 injection at 8,000 meters depth in a horizontally finite aquifer. He concluded that CO_2 storage was feasible beneath horizontal seals, provided that injection locations were sufficiently deep.

A general approach to evaluating sedimentary basins for CO_2 disposal was presented by Bachu et al. (1994). It was exemplified by the Alberta Basin in western Canada, where a wealth of geological and hydrogeological data from more than 150,000 wells was available to allow for a good estimate of the potential for long-term CO_2 storage there. Besides stratigraphic trapping, CO_2 interactions with aquifer water and rocks and CO_2 transport in miscible and immiscible phases were two additional mechanisms cited for the capture and long-term retention of CO_2 in the subsurface. Law and Bachu (1996) used the reservoir simulator STARS to simulate CO_2 injection into a sedimentary basin for 30 years. This multidimensional, multi-component model allowed CO_2 to partition between a liquid and a gaseous phase. They concluded that permeability and injection pressure are important factors effecting CO_2 storage potential. Bachu (2003) developed a method for estimating an upper limit to the CO_2 sequestration capacity in solution for an aquifer and applied it to the Viking aquifer in the Alberta Basin in western Canada. Formation water analyses performed at laboratory conditions are brought to in situ conditions using a geochemical speciation model to account for dissolved gasses that are lost from the water sample. To account for the decrease in CO_2 solubility with increasing water salinity, the maximum CO_2 content in formation water is calculated by applying an empirical correction to the CO_2 content at saturation in pure water. The CO_2 sequestration capacity is then calculated with consideration of the effect of dissolved CO_2 on formation water density, aquifer thickness, and aquifer porosity.

Weir et al. (1996) used the multiphase, multi-component TOUGH2 reservoir model to simulate CO_2 injection in geologic media. They concluded that the most significant factor affecting

volumetric CO_2 storage potential is permeability. Pruess *et al.* (2001) incorporated a realistic description of brine-CO_2 mixture properties for supercritical conditions and a reaction model of representative aquifer minerals into a multi-purpose reservoir simulator. They used it to evaluate dynamic effects of CO_2 injection into aquifers, and found that under favorable conditions, the amount of CO_2 sequestered by precipitation of secondary carbonates is comparable to that dissolved in aquifer water.

Ozah *et al.* (2005) used a compositional reservoir simulator to understand factors effecting the long-term storage potential of pure CO_2 and CO_2-H_2S mixtures in deep saline aquifers. Aquifer characteristics such as heterogeneity, dip angle, and vertical to horizontal permeability ratio were shown to effect storage potential and injectivity of CO_2-H_2S gas mixtures. Gas injection into aquifers was greatly aided by the use of horizontal wells to promote trapping and dissolution and to avoid contact with the top seal, which can potentially cause escape of the gas.

Zhang *et al.* (2007) developed an efficient parallel simulator for CO_2 sequestration in saline aquifers. The three-dimensional fully implicit simulator includes a comprehensive description of thermodynamics and thermophysical properties of H_2O-$NaCl$-CO_2 mixtures, and can handle non-isothermal flow as well. This simulator can solve larger and more complex problems than a single CPU one could.

Delshad *et al.* (2009) used an iterative IMPEC method with a volume balance convergence criterion to solve for non-isothermal compositional flow coupled with chemical reactions. Field scale CO_2 sequestration, as an EOR process or for containment in deep saline aquifers where chemical reactions and temperature variations may have an impact on the flow and transport of CO_2, can be simulated using this method.

Wellman *et al.* (2003) used the results of CO_2-brine flow experiments in rock cores to calibrate a reactive transport simulator, and then used the simulator to model several of CO_2 sequestration options in depleted oil and gas reservoirs.

Spycher *et al.* (2003) presented a relatively simple non-iterative procedure to calculate the composition of the compressed CO_2 and liquid H_2O phases at equilibrium. The procedure is based on equating chemical potentials and uses the Redlich-Kwong equation of state to express departure from ideal behavior. Spycher and Pruess (2005) extended these correlations by including activity coefficients for aqueous CO_2 derived from several literature sources, primarily for NaCl solutions. Best results were obtained by combining the previous solubility correlations with the activity coefficient formulation of Rumpf *et al.* (1994) and Duan and Sun (2003).

Development of a Three-Phase Non-Isothermal CO_2 Flow Module

For mixtures of CO_2 and brine there are seven possible phase combinations (Figure 2.1). The fluid property module for brine-CO_2 mixtures will be designed to handle all possible phase combinations of aqueous phase, sub-critical liquid and gaseous CO_2, and supercritical CO_2.
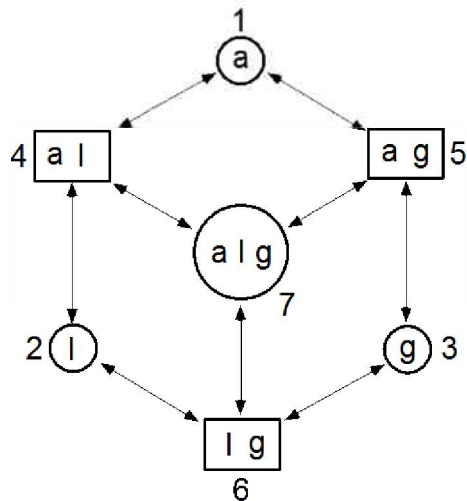
Figure 2.1. Possible phase combinations in the system water-CO_2. The phase designations are (a) - aqueous, (l) - liquid CO_2, (g) - gaseous CO_2. Separate liquid and gas phases exist only at subcritical conditions.

Our work starts from a fluid property module dubbed "EOSMS" that we had developed for TOUGH2 (Pruess *et al.*, 1999) some years ago to represent all possible phase combinations of brine-CO_2 mixtures. The main drawback of EOSMS is that it uses the concept of a partial pressure for CO_2 to perform phase diagnostics and calculate thermophysical properties. We eliminated any use of the partial pressure concept, and instead used only total pressure, to enable implementation of the accurate phase-partitioning model of Spycher *et al.* (2003), that is used in the ECO2N fluid property module (Pruess and Spycher, 2007). This new module is called "ECO2M."

For ECO2M we adopt the same correlations for thermodynamic and thermophysical properties of brine-CO_2 mixtures as in ECO2N. This includes density, viscosity, and specific enthalpy of fluid phases as function of temperature, pressure, and composition; and partitioning of mass components H_2O, NaCl and CO_2 among the different phases. We consider all seven possible phase combinations in the brine-CO_2 system (Figure 2.1; the number of phase combinations doubles to fourteen when allowing for the possibility of solid salt appearing and disappearing). In ECO2M we identify phase conditions by means of a separate numerical index (Table 2.1). Depending upon the phase combination present, not all thermodynamic parameters are independent, and different sets of primary thermodynamic variables must be used for different phase combinations (see Table 2.1). The meaning of variables not yet explained is X - mass fraction of CO_2, S_a - saturation of aqueous phase, S_g - saturation of gas phase, and Y - mass fraction of water. The second primary variable X_{sm} refers to NaCl and denotes salt mass fraction X_s in the two-component water-salt system when there is no solid salt, or "solid saturation" S_s+10 when halite precipitate is present. Here, "solid saturation" denotes the fraction of pore volume with solid salt.

Table 2.1. Primary thermodynamic variables used for multiphase mixtures of brine and CO_2.

Phase Conditions	Phase Index	Primary Variables			
		1	2	3	4
aqueous only	1	P	X_{sm}	X	T
liquid only	2	P	X_{sm}	X	T
gas only	3	P	X_{sm}	X	T
aqueous and liquid	4	P	X_{sm}	S_a	T
aqueous and gas	5	P	X_{sm}	S_a	T
liquid and gas	6	P	X_{sm}	S_g	Y
three phase	7	P	X_{sm}	S_a	S_g

When thermodynamic conditions change in the course of a simulation, the primary thermodynamic variables are monitored to determine whether phase conditions change. For example, for a grid block that is in two-phase a-l conditions (index = 4), we monitor the third primary variable, aqueous phase saturation S_a. Liquid phase saturation is $S_l = 1 - S_s - S_a$, so that, as long as $0 < S_a < 1-S_s$, we have $S_l > 0$ and two-phase a-l conditions are maintained. If $S_a \geq 1-S_s$, the liquid CO_2 phase disappears, and we make a transition from a-l to single-phase aqueous conditions. If $S_a \leq 0$, the aqueous phase disappears, and we transition to single-phase liquid conditions. For sub-critical temperatures, we also need to check whether a gaseous CO_2 phase evolves. This is done by comparing fluid pressure with the CO_2 saturation pressure at prevailing temperature, $P_{sat,CO2}(T)$. Ignoring the effects of water on fluid pressures, which are small at the modest temperatures considered here, we require that $P \geq P_{sat,CO2}(T)$ in order that no gas phase evolves. If this inequality is violated, we make a transition to three-phase a-l-g conditions, and initialize the new gas phase with a small saturation of order 10^{-6}. Figure 2.1 indicates that there are 18 possible phase changes between the 7 possible phase combinations, and similar checks are employed for all of them.

Experience has shown that phase change criteria as outlined above may be prone to generating unstable behavior with severe limitations for attainable time steps, especially when dealing with transitions between a-l <==> a-l-g <==> a-g. We achieve a more robust behavior by introducing a finite "window" for phase change, as follows. In the above example, instead of performing a transition from a-l to a-l-g whenever $P < P_{sat,CO2}(T)$, we evolve a gas phase only when P drops below $P_{sat,CO2}(T)$ by a finite amount, $P < (1-\epsilon) * P_{sat,CO2}(T)$, where ϵ is a small parameter of order 10^{-3} - 10^{-5}. As a further refinement, we may optionally apply a "hair trigger" criterion $P < P_{sat,CO2}(T)$ for phase change only for the first few Newtonian iterations during a time step, and switch to a finite window for the subsequent Newtonian iterations. The added robustness in simulator behavior achievable from dynamic finite-size windows for phase change is essential for efficient simulation of highly non-linear flow processes that involve boiling and condensation of liquid and gaseous CO_2 phases, with strong associated latent heat effects.

From a thermodynamic standpoint, it is possible for liquid CO_2 to change into gas, or vice versa, without a phase change, as long as the path from initial to final state avoids crossing the CO_2 saturation line. In order to achieve a consistent description of CO_2 phase conditions throughout the entire T,P-plane (Figure 2.2), we adopt the convention that for supercritical temperatures, a

change between liquid and gaseous CO_2 conditions is made whenever fluid pressure moves past the critical value. Note that this change of phase designation is merely an accounting device, and fluid properties for $T > T_{crit}$ are continuous when P changes past P_{crit}.

ECO2M includes a capability for modeling conductive heat exchange with semi-infinite half spaces, using a semi-analytical method developed by Vinsome and Westerveld (1980). This technique allows to accurately represent heat transfer between fluids in a permeable fault zone and the adjacent wall rocks of low permeability, without any need for including the wall rocks in the simulation domain.
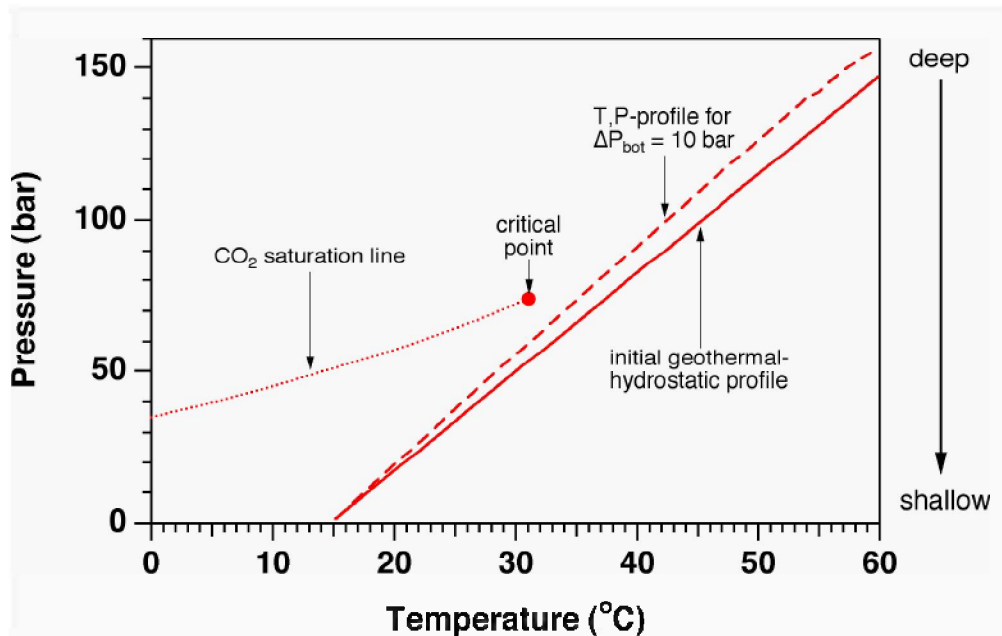
Figure 2.2. T,P-diagram of a typical geothermal-hydrostatic profile. The CO_2 saturation line is also shown, as is a profile that corresponds to a pressure increase of $\Delta P = 10$ bar at 1500 m depth.

Verification of Three-Phase Non-Isothermal CO_2 Flow Module

1) CO_2 Leakage from a Secondary Accumulation at Shallow Depth

We revisit a previously investigated leakage scenario that had been purposefully designed to enable positive feedback for CO_2 discharge, and thereby gain insight into the potential strength of self-enhancing processes (Pruess, 2008). The scenario involves CO_2 migration up a blind fault and subsequent accumulation in a secondary "parasitic" reservoir at shallower depth (Figure 2.3). CO_2 discharge to the land surface is initiated after a sufficient quantity of CO_2 has accumulated to reach a spill point. A potential for a self-enhancing discharge exists when the water column in the upper fault is replaced by CO_2 of much lower density and viscosity, and accumulated CO_2 expands in response to reduced fluid pressures.

Our earlier analysis of this problem had used a preliminary version of a three-phase fluid property module for brine-CO_2 mixtures (Pruess, 2004), and had indeed shown transient enhancements of CO_2 outflow relative to the inflow by factors up to 3.5, depending on the assumed hydrogeologic parameters (Pruess, 2008). While this confirmed the expected self-enhancement, the simulations also revealed significant self-limiting features, including boiling of upflowing liquid CO_2 accompanied by strong declines in temperature, and evolution of three-phase conditions with small mobility for all fluid phases. Our earlier fluid property formulation had treated the mutual dissolution of H_2O and CO_2 by means of an extended Henry's law for CO_2 and an evaporation model for H_2O. This approach overestimated CO_2 dissolution and underestimated H_2O dissolution, with inaccuracy becoming greater at increasing pressures. In contrast, the new ECO2M module includes much improved correlations that describe the compositions of the various fluid phases generally within the uncertainty of the experimental data (Spycher *et al.*, 2003).

Figure 2.4 shows simulated CO_2 land surface discharge per unit fault length for a case with an upper fault zone permeability of 80×10^{-15} m^2. At early time the TOUGH2/ECO2M simulation shows close agreement with our previous results, but starting at about 55×10^6 s we now see stronger cyclic excursions of CO_2 flow. Peak CO_2 discharge is reached a bit sooner, although the magnitude is very little changed. These minor differences are consistent with lower solubility for CO_2 and increased solubility for water in our current model, as both effects will amplify the evolution and mobility of CO_2-rich phases.
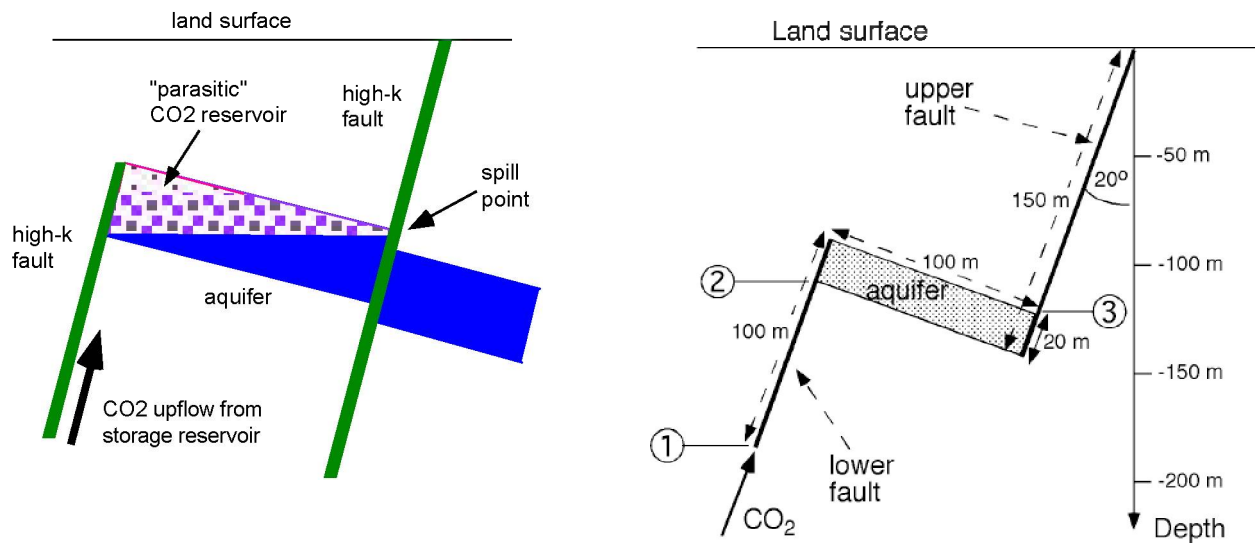
Figure 2.3. Conceptual sketch of a leakage scenario (left) and actual dimensions of the flow system (right).
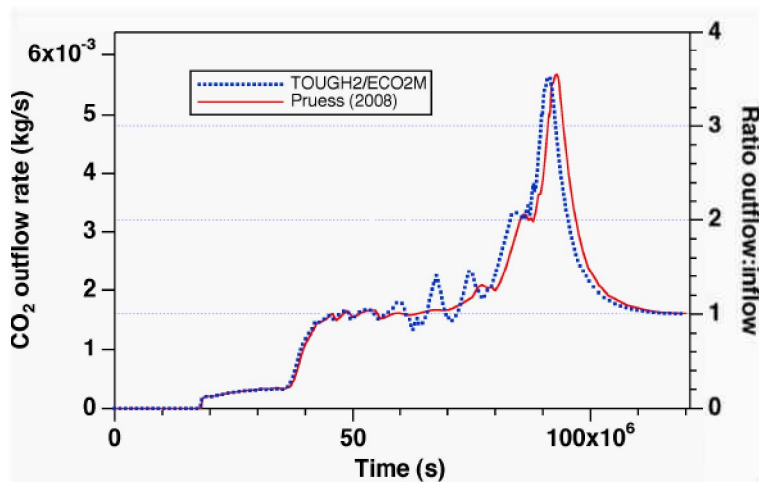
Figure 2.4. CO$_2$ outflow at the land surface per unit length of the fault zone, comparing our new TOUGH2/ECO2M model with earlier results.

2) CO$_2$ Discharge from a Deep Fault Zone

We consider leakage of CO$_2$ from a deep storage reservoir along a vertical fault zone of 5 m thickness. The fault is assumed to intersect the CO$_2$ reservoir at a depth of $Z = -1500$ m. Fault zone permeability is assumed as $k = 100 \times 10^{-15}$ m^2, porosity $\phi = 15$ %, with wall rocks assumed completely impermeable. Initial conditions in the fault correspond to hydrostatic equilibrium in a typical geothermal gradient, as shown in Figures 2.5 and 2.6. Initial conditions at $Z = -1500$ m depth are found to be $(T, P) = (60\ °\text{C}, 147.475\ \text{bar})$.
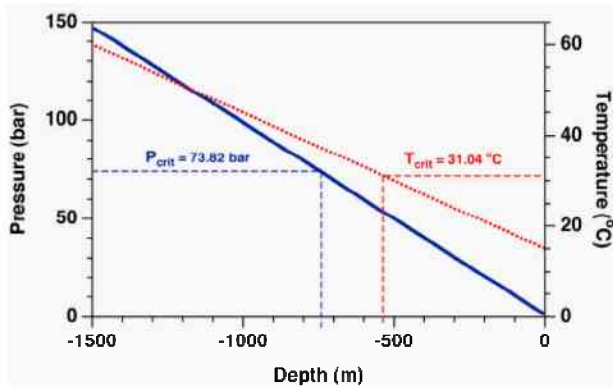
Figure 2.5. Typical temperature and pressure profiles in terrestrial crust.
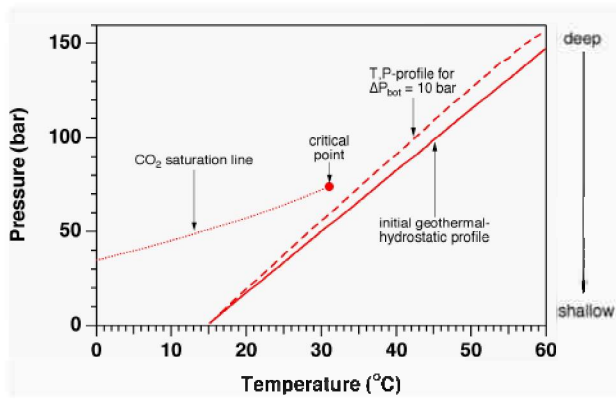
Figure 2.6. T,P-diagram of a typical geothermal-hydrostatic profile. The CO_2 saturation line is also shown, as is a profile that corresponds to a pressure increase of $\Delta P = 10$ bar at 1500 m depth.

The scenario considered here does not model the CO_2 storage reservoir as such; instead, we assume that a CO_2 plume from a nearby storage reservoir reaches the bottom of the fault zone at some pressure in excess of hydrostatic. We model a finite-length section of the fault as a 1-D system, and initiate upflow of CO_2 by specifying boundary conditions of supercritical CO_2 at an overpressure of 10 bar relative to hydrostatic pressure at the bottom of the fault. Land surface conditions are kept unchanged. The pressurization from the step change in bottom boundary conditions rapidly migrates up the fault; the resulting T,P-profile is shown in Figure 2.6 In response to CO_2 injection water is being pushed upward, and a front of free-phase CO_2 is advancing towards the land surface. Our model accounts for non-isothermal effects that arise from (1) upflow of warmer (T = 60 °C) fluid into colder regions, (2) Joule-Thomson cooling as upflowing CO_2 expands (Katz and Lee, 1990), (3) boiling of liquid CO_2 into gas, and (4) mutual dissolution of H_2O and CO_2. An important aspect of system evolution is conductive heat exchange with the wall rocks, which we model by means of a semi-analytical method (Vinsome and Westerveld, 1980).

Our simulation stops after 36.3 years (1.145×10^9 s), when temperatures near 275 m depth approach the freezing point of water. Figure 2.7 shows profiles of temperature and CO_2 phase saturations at different times. The saturation profile at t = 6.42 yr gives a snapshot just prior to commencement of CO_2 discharge at the land surface at 6.425 yr.

25
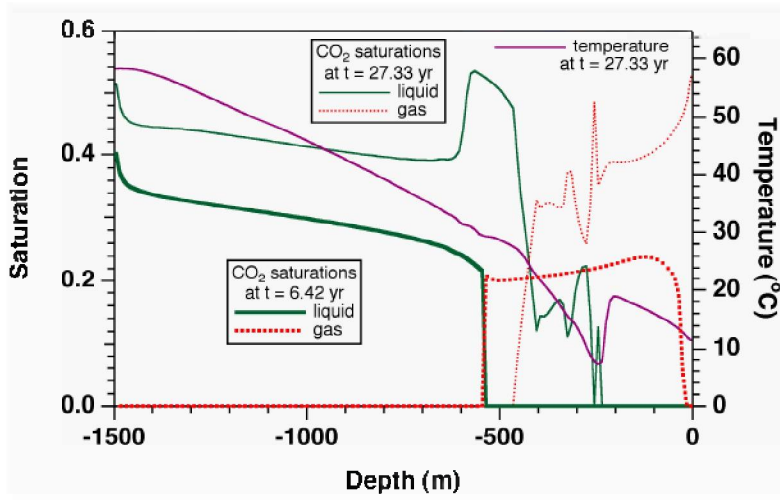
Figure 2.7. Saturation and temperature profiles at different times.

Note a sharp transition from liquid to gaseous CO_2 at 540 m depth. As will be seen below, this transition occurs almost exactly at the critical point of CO_2. Over time the system experiences predominant cooling effects, and evolves an extended region with 3-phase fluid conditions (aqueous - liquid CO_2 - gaseous CO_2). After t = 27.33 yr, three-phase conditions are seen to extend from - 240 m to -460 m depth (note that an aqueous phase is present throughout, which is not shown in Figure 2.7). There is a precipitous temperature decline in the three-phase zone, reflecting heat loss as liquid CO_2 boils into gas. Lowest temperatures are reached at the liquid CO_2 front, where rates of boiling and associated heat loss are largest. We note that saturations of liquid CO_2 increase to large values beneath the three-phase zone. This represents buoyant accumulation of less dense fluid (liquid CO_2) beneath a region of low effective permeability. The three-phase zone acts as a mobility block, because in three-phase conditions, relative permeabilities are small for all phases. Within the three-phase zone, liquid and gas saturations show strong fluctuations, which are due to the interplay between multiphase flow and conductive heat transfer in the fault walls with different time constants. The sum of liquid and gas saturations, $S_{liq}+S_{gas}$, shows much smaller fluctuations than either S_{liq} or S_{gas} (not shown).

At early times, outflow at the land surface is just aqueous phase. A large "burp" of water outflow occurs as free CO_2 approaches the land surface, reflecting the strong volume expansion there (Figure 2.8). CO_2 flux at the land surface shows non-monotonic behavior. Periods of large CO_2 outflow correlate with declining temperatures of the discharge (Figure 2.8). The largest CO_2 flux approaches 2×10^{-3} kg/s/m^2, which for the assumed fault zone thickness of 5 m translates into an outflow rate of somewhat less than 10^{-2} kg/s per meter fault length, or 1 kg/s per 100 m fault length. During periods when the CO_2 outflow rate is relatively small, three-phase conditions migrate upward, and the region with three-phase conditions thickens (Figure 2.9). As CO_2 outflow rates increase, the upward extension of three-phase conditions slows and eventually turns around when liquid CO_2 is boiled off the top of the three-phase zone at large rates.

Additional insight into the system dynamics can be gained by examining the evolution of profiles in T,P-space. Figure 2.10 shows that, as a consequence of the pressure increase and temperature decline during CO_2 migration, the T,P-profile is rapidly shifted towards the CO_2 saturation line. Thermodynamic conditions get drawn towards the critical point and then approximately follow the saturation line. Note that three-phase points must fall right on the saturation line, while in the vicinity of three-phase zones, thermodynamic conditions will plot near the saturation line. At time t = 27.33 yr we have a large extent of three-phase conditions (Figures 2.7, 2.9), and a correspondingly large region of T,P-conditions overlapping with the saturation line. Temperatures have a local minimum at the lowest pressure (shallowest depth) with three-phase conditions. Temperatures increase near the bottom of the overlying two-phase aqueous-gas zone, but resume enhanced decline due to Joule-Thomson cooling as the gas expands during upward flow.
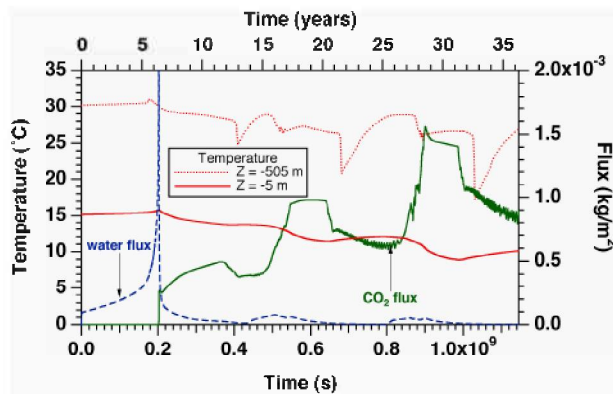
Figure 2.8. Time dependence of water and CO_2 outflow at the land surface, and temperatures at two different depths.
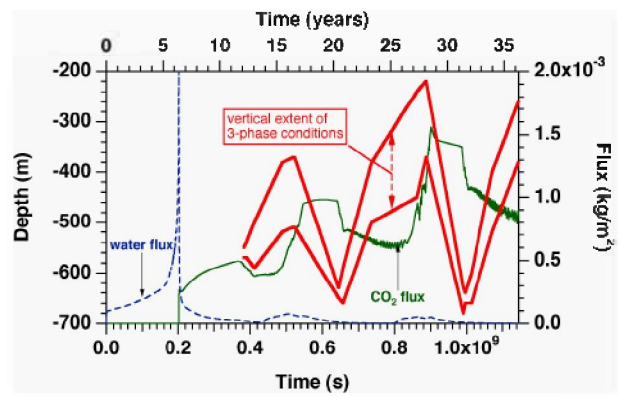
Figure 2.9. Water and CO_2 fluxes as shown in Figure 2.8, with the heavy superposed lines indicating the top and bottom of three-phase conditions, respectively.
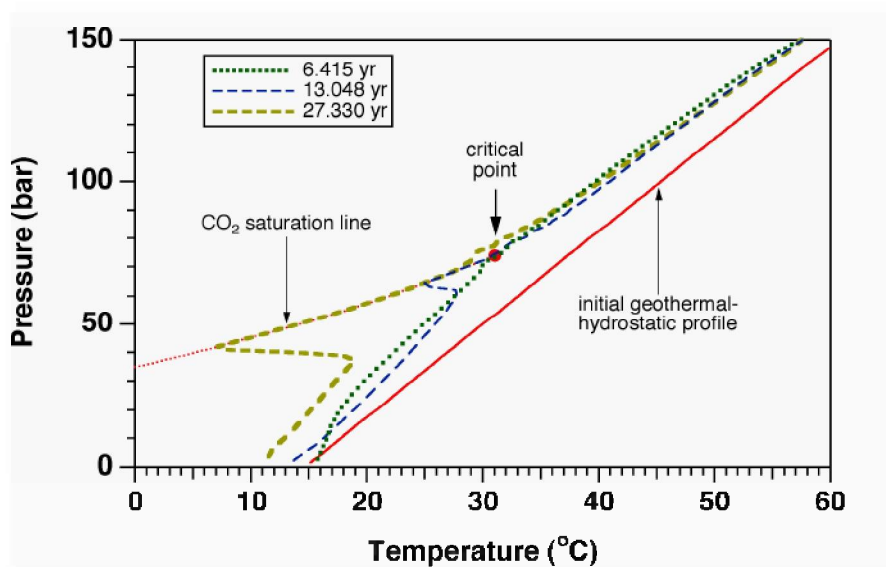
Figure 2.10. Temperature-pressure profiles at different times.

28

Integration of ECO2M into the iTOUGH2 Simulation-Optimization Framework

ECO2M, developed in this project, is a fluid property module for the TOUGH2 simulator designed for applications to geologic storage of CO_2 in saline aquifers. It includes a comprehensive description of the thermodynamics and thermophysical properties of H_2O - NaCl - CO_2 mixtures. ECO2M can describe all possible phase conditions for brine-CO_2 mixtures, including transitions between super- and sub-critical conditions, and phase change between liquid and gaseous CO_2. This allows for seamless modeling of CO_2 storage and leakage.

The application of ECO2M for the study of CO_2 storage and leakage scenarios requires specifying a large number of hydrological and thermal model parameters, initial and boundary conditions, and possibly geometrical features of the geologic system. Many of these parameters are unknown or uncertain. Site-specific values thus must be derived from available observations of the system state. Parameter estimation is supported by iTOUGH2, which provides automatic model calibration capabilities along with formal sensitivity, uncertainty propagation, and data-worth analyses.

As a follow-on to the development of ECO2M in this project, ECO2M has been fully integrated into the iTOUGH2 simulation-optimization framework to make parameter estimation and related uncertainty analyses available for the development of conceptual and numerical models and the analysis of CO_2 storage and leakage scenarios.

Summary and Conclusions

We extended a previously developed TOUGH2 fluid property module, ECO2N, to include all possible phase compositions of brine-CO_2 mixtures, including three-phase conditions of aqueous, liquid and gaseous CO_2 phases. The new fluid property module, ECO2M, retains the original ECO2N-formulation for the compositions and properties of the aqueous and CO_2-rich phases, and allows a seamless description of CO_2 storage and leakage systems for super- and sub-critical conditions in the temperature range 10 °C $\leq$ T $\leq$ 110 °C, pressures up to 600 bar, and dissolved NaCl with salinity up to full halite saturation.

We verified the new fluid property module using CO_2 leakage scenarios that demonstrate strong cooling effects from liquid CO_2 boiling into gas, and from Joule-Thomson cooling of upflowing and expanding gas. These scenarios show the emergence of three-phase conditions that lead to low mobilities for all phases and act to reduce CO_2 discharge rates. The original ECO2N module, with only one CO_2-rich phase, would predict higher phase mobilities and CO_2 discharge rates.

Task 3.0: Development of a rock mechanical module

Introduction

We describe here the development of a fully coupled, fully implicit thermal-hydrological-mechanical (THM) simulator called TOUGH2-CSM (Carbon Storage Model, Colorado School of Mines). The geomechanical equations relating stresses and displacements are combined to yield an equation for mean stress as a function of pore pressure and temperature, as well as an equation for volumetric strain. The multiphase flow formulation is based on the TOUGH2 (Pruess *et al.*, 1999) formulation, but with mean stress as an additional primary variable. Effective stress, the difference between mean stress and pore pressure, was first introduced by Terzaghi (1936) during his studies of the mechanics of saturated soils and its details were further refined by Biot (1941) and others. Theories of poroelasticity (Geertsma, 1957; Carroll and Katsube, 1983; Zimmerman, 1991) have correlated rock properties such as porosity to effective stress, and experimental studies (Nur and Byerlee, 1971) have supported these relations. The dependence of permeability on porosity has had numerous investigators (Bear, 1972) and an early example is the Carman-Kozeny hydraulic radius model. In addition, Gobran *et al.* (1987) concluded that permeability is dependent on the difference between confining pressure and pore pressure (effective stress) but not on their actual values. We incorporate these dependencies of porosity and permeability into our simulator, obtained from theories of poroelasticity and empirical correlations from the literature.

The starting point for the TOUGH2-CSM code is the TOUGH2-MP code (Zhang *et al.*, 2008), the massively parallel version of TOUGH2. The details of the parallel code will be covered in "Task 6.0: Implementation of Efficient Parallel Computing Technologies." In addition, TOUGH2-CSM, simulates multiphase CO_2 flow coupled with rock deformation in porous and fractured rock. The single-porosity TOUGH2-CSM formulation is described in this section and the multiple porosity one will be covered in "Task 7.0: Implementation of General Fracture Conceptual Models."

TOUGH2-CSM Single-Porosity Geomechanical Equations

The TOUGH2-CSM geomechanical equations are based on an extended version of the classical theory of elasticity. In this theory of elasticity, the stress-strain behavior of an isothermal elastic material is described by Hooke's law:

$$\tau = 2G\varepsilon + \lambda\left(tr\varepsilon\right)I \tag{3.1}$$

where G is shear modulus and λ is the Lamé parameter. For isothermal fluid-filled porous rocks, the stress-strain behavior is also dependent on pore pressure and the poroelastic version of Hooke's law is:

$$\tau - \alpha PI = 2G\varepsilon + \lambda\left(tr\varepsilon\right)I \tag{3.2}$$

where α is Biot's coefficient (Biot and Willis, 1957). For an elastic material subject to changes in both temperature and stress, the theory of thermoelasticity assumes the resulting strain is the sum of the thermal strain and the stress-caused strain. This theory is mathematically analogous to poroelastic theory (Norris, 1992) and Hooke's law for thermoelastic media has the form:

$$\tau - 3\beta K \left(T - T_{ref} \right) I = 2G\varepsilon + \lambda \left(tr\varepsilon \right) I \tag{3.3}$$

where T_{ref} is reference temperature for a thermally unstrained state, K is bulk modulus, and β is linear thermal expansion coefficient. For a thermo-poroelastic medium, a porous medium subject to changes in both temperature and stress (McTigue, 1986), the pore pressure and temperature terms both appear in Hooke's law as:

$$\tau - \alpha P I - 3\beta K \left(T - T_{ref} \right) I = 2G\varepsilon + \lambda \left(tr\varepsilon \right) I \tag{3.4}$$

Two other fundamental relations in the theory of linear elasticity are the relation between the strain tensor and the displacement vector $\boldsymbol{u}$:

$$\varepsilon = \frac{1}{2} \left(\nabla \boldsymbol{u} + \nabla \boldsymbol{u}^t \right) \tag{3.5}$$

and the static equilibrium equation:

$$\nabla \cdot \tau + \boldsymbol{F}_b = 0 \tag{3.6}$$

where $\boldsymbol{F}_b$ is the body force. We combine Equations 3.4-3.6 to obtain the thermo-poroelastic Navier equation:

$$\nabla \left(\alpha P + 3\beta KT \right) + \left(\lambda + G \right) \nabla \left(\nabla \cdot \boldsymbol{u} \right) + G \nabla^2 \boldsymbol{u} + \boldsymbol{F}_b = 0 \tag{3.7}$$

Taking the divergence of Equation 3.7 yields:

$$\nabla^2 \left(\alpha P + 3\beta KT \right) + \left(\lambda + 2G \right) \nabla^2 \left(\nabla \cdot \boldsymbol{u} \right) + \nabla \cdot \boldsymbol{F}_b = 0 \tag{3.8}$$

The divergence of the displacement vector is the sum of the normal strain components, the volumetric strain:

$$\nabla \cdot \boldsymbol{u} = \frac{\partial u_x}{\partial x} + \frac{\partial u_y}{\partial y} + \frac{\partial u_z}{\partial z} = \varepsilon_{xx} + \varepsilon_{yy} + \varepsilon_{zz} = \varepsilon_v \tag{3.9}$$

The trace of the stress tensor is an invariant, having the same value for any coordinate system. We obtain the following by taking the trace of Equation 3.4, Hooke's law for a thermo-poroelastic medium:

31

$$\tau_{xx} + \tau_{yy} + \tau_{zz} - 3\left(\alpha P + 3\beta K \left(T - T_{ref}\right)\right) = \left(3\lambda + 2G\right)\left(\varepsilon_{xx} + \varepsilon_{yy} + \varepsilon_{zz}\right) \tag{3.10}$$

Defining mean stress as the average of the normal stress components, and using the relationship between bulk modulus, shear modulus, and Lamé parameter:

$$K = \frac{\left(3\lambda + 2G\right)}{3} \tag{3.11}$$

yield the following equation relating volumetric strain, mean stress, pore pressure, and temperature:

$$K\varepsilon_v = \tau_m - \left(\alpha P + 3\beta K \left(T - T_{ref}\right)\right) \tag{3.12}$$

Finally, combining Equations 3.8, 3.9, and 3.12, and using the relationship between Poisson's ratio, υ, shear modulus, and Lamé parameter:

$$\frac{\lambda}{G} = \frac{2\upsilon}{\left(1 - 2\upsilon\right)} \tag{3.13}$$

yield an equation relating mean stress, pore pressure, temperature, and body force:

$$\nabla \cdot \left[\frac{3\left(1 - \upsilon\right)}{1 + \upsilon} \nabla \tau_m + F_b - \frac{2\left(1 - 2\upsilon\right)}{1 + \upsilon} \nabla \left(\alpha P + 3\beta KT\right)\right] = 0 \tag{3.14}$$

Equations 3.12 and 3.14 are the governing single-porosity geomechanical equations for TOUGH2-CSM, and mean stress and volumetric strain are the geomechanical variables associated with those equations. Equation 3.14 is a statement of momentum conservation in terms of mean stress and other variables and Equation 3.12 is a property relation, relating volumetric strain to mean stress and other variables.

TOUGH2-CSM Single-Porosity Conservation Equations

The TOUGH2-CSM conservation equations are based on the TOUGH2 formulation (Pruess *et al.*, 1999) of mass and energy balance equations that describe fluid and heat flow in general multiphase, multicomponent systems. Fluid advection is described with a multiphase extension of Darcy's law; in addition, there is diffusive mass transport in all phases. Heat flow occurs by conduction and convection, the latter including sensible as well as latent heat effects. The description of thermodynamic conditions is based on the assumption of local equilibrium of all phases. Fluid and formation parameters can be arbitrary nonlinear functions of the primary thermodynamic variables. We modify this formulation to include geomechanics. In addition to the mass and energy balance equations, we solve a momentum balance equation for mean stress that was derived in the previous section (Equation 3.14), we add mean stress to the primary

thermodynamic variables, and we add volumetric strain to the calculated properties. The conservation equations for mass, momentum, and energy can be written in differential form as:

$$\frac{\partial M^k}{\partial t} = \nabla \cdot \boldsymbol{F}^k + q^k \tag{3.15}$$

where k refers to conserved quantity, M is conserved quantity per unit volume, q is source or sink per unit volume, and $\boldsymbol{F}$ is flux.

Mass per unit volume is a sum over phases:

$$M^k = \phi \sum_l S_l \rho_l X_l^k \tag{3.16}$$

where ϕ is porosity, S is phase saturation, ρ is mass density, and X is mass fraction of component k. Energy per unit volume accounts for internal energy in rock and fluid and is the following:

$$M^{N+1} = (1-\phi) C_r \rho_r T + \phi \sum_l S_l \rho_l U_l \tag{3.17}$$

where ρ_r is rock density, C_r is rock specific heat, T is temperature, U is phase specific internal energy, and N is the number of mass components. Momentum per unit volume is small compared to momentum flux and has been neglected in our formulation.

Advective mass flux is a sum over phases:

$$\boldsymbol{F}_{adv}^k = \sum_l \boldsymbol{F}_l X_l^k \tag{3.18}$$

and phase flux $\boldsymbol{F}_l$ is given by Darcy's law:

$$\boldsymbol{F}_l = -k \frac{k_{rl} \rho_l}{\mu_l} \left(\nabla P + \nabla P_{c,l} - \rho_l \boldsymbol{g} \right) \tag{3.19}$$

where k is absolute permeability, k_r is phase relative permeability, μ is phase viscosity, P is pore pressure, P_c is phase capillary pressure, and $\boldsymbol{g}$ is gravitational acceleration. Capillary pressure is relative to a reference phase, which is the gaseous phase. Diffusive mass flux is given by:

$$\boldsymbol{F}_{dis}^k = \sum_l \rho_l \boldsymbol{D}_l^k X_l^k \tag{3.20}$$

where $\boldsymbol{D}_l^k$ is the dispersion tensor. Energy flux includes conductive and convective components:

$$\boldsymbol{F}^{N+1} = -\lambda \nabla T + \sum_l h_l \boldsymbol{F}_l \tag{3.21}$$

where λ is thermal conductivity and h_l is phase l specific enthalpy.

Discretization of Single-Porosity TOUGH2-CSM Conservation Equations

The TOUGH2-CSM mass, energy, and momentum balance equations are discretized in space using the integral finite difference method (Narasimhan and Witherspoon, 1976). In this method, the simulation domain is subdivided into grid blocks and the conservation equations (Equation 3.15) are integrated over grid block volume V_n with flux terms expressed as an integral over grid block surface Γ_n using the divergence theorem:

$$\frac{d}{dt}\int_{V_n}M^k dV = \int_{\Gamma_n}\boldsymbol{F}^k \cdot \boldsymbol{n}d\Gamma + \int_{V_n}q^k dV \tag{3.22}$$

Volume integrals are replaced with volume averages:

$$\int_{V_n}M^k dV = M_n^k V_n \tag{3.23}$$

and surface integrals with discrete sums over surface averaged segments:

$$\int_{\Gamma_n}\boldsymbol{F}^k \cdot \boldsymbol{n}d\Gamma = \sum_m A_{nm}F_{nm}^k \tag{3.24}$$

where subscript n denotes an averaged quantity over volume V_n, A_{nm} is the area of a surface segment common to volumes V_n and V_m, and double subscript nm denotes an averaged quantity over area A_{nm}. The definitions of the geometric parameters used in this discretization are illustrated in Figure 3.1.

34
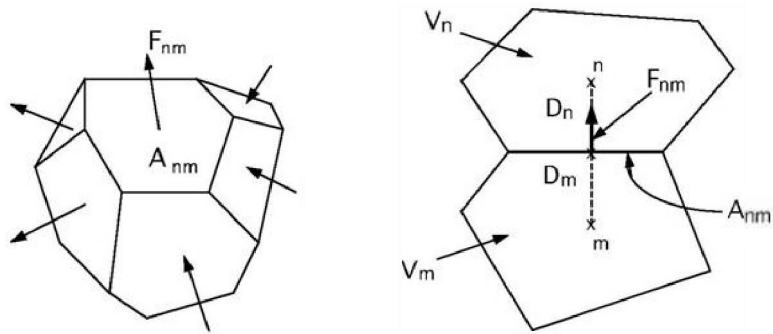
Figure 3.1. Parameter definitions for the integral finite difference method, adapted from Pruess *et al.* (1999).

Strictly speaking, the integrals in Equation 3.22 apply to fixed grid block geometry. Because volumetric strain is a variable in our geomechanical formulation, grid block volume as well as grid block distances and areas are no longer fixed. We introduce volumetric strain dependence into the volumes, areas, and distances that arise when the integrals in Equations 3.23 and 3.24 are evaluated. These dependencies are based on the definition of volumetric strain:

$$V_n\left(\varepsilon_{v,n}\right) = V_{n,0}\left(1 - \varepsilon_{v,n}\right) \tag{3.25}$$

where $V_{n,0}$ is grid block n volume at zero strain and $\varepsilon_{v,n}$ is grid block n average volumetric strain. Changes in volumetric strain also cause changes in grid block areas and distances. We account for these by first defining analogs of Equation 3.25 for areas and distances (A and D) in terms of average area and distance strain (ε_A and ε_D):

$$A_{nm}\left(\varepsilon_{A,nm}\right) = A_{nm,0}\left(1 - \varepsilon_{A,nm}\right) \tag{3.26}$$

and:

$$D_n\left(\varepsilon_{D,n}\right) = D_{n,0}\left(1 - \varepsilon_{D,n}\right) \tag{3.27}$$

where $\varepsilon_{A,nm}$ is the average of area strains $\varepsilon_{A,n}$ and $\varepsilon_{A,m}$. Substituting Equation 3.25 into the volume integral (Equation 3.23) yields:

$$\int_{V_n} M^k dV = M_n^k V_{n,0}\left(1 - \varepsilon_{v,n}\right) \tag{3.28}$$

and substituting Equation 3.26 into the surface integral (Equation 3.24) yields

$$\int_{\Gamma_n} \boldsymbol{F}^k \cdot \boldsymbol{n} d\Gamma = \sum_m A_{nm,0}\left(1 - \varepsilon_{A,nm}\right) F_{nm}^k \tag{3.29}$$

Next, we relate area and distance strains to volumetric strain. Because our geomechanical formulation is in terms of volumetric strain only, we must make an assumption to do this. We assume either isotropic or uniaxial volumetric strain. For isotropic volumetric strain, area strain and volumetric strain are related by:

$$\left(1 - \varepsilon_v\right) = \left(1 - \varepsilon_A\right)^{\frac{3}{2}} \tag{3.30}$$

and since strains are small:

$$\varepsilon_A \approx \frac{2\varepsilon_v}{3} \tag{3.31}$$

Distance strain and volumetric strain are related by:

36

$$\left(1 - \varepsilon_{\mathrm{v}}\right) = \left(1 - \varepsilon_D\right)^3 \tag{3.32}$$

and since strains are small:

$$\varepsilon_{\mathrm{D}} \approx \frac{\varepsilon_{\mathrm{v}}}{3} \tag{3.33}$$

For uniaxial volumetric strain, distance strain in the strain direction would be equal to volumetric strain and distance strain in other directions would be zero; area strain in the strain direction would be zero and area strain in the other directions would be equal to volumetric strain.

The integral finite difference approximation to the advective mass flux for component k (Equations 3.18 and 3.19) is the following:

$$A_{nm}F_{nm}^k = \sum_l -k_{nm} \left[\frac{k_{rl}\rho_l X_{lk}}{\mu_l}\right]_{nm} \left[\frac{P_n - P_m + P_{cl,n} - P_{cl,m}}{D_{n,0}\left(1 - \varepsilon_{D,n}\right) + D_{m,0}\left(1 - \varepsilon_{D,\mathrm{m}}\right)} - \rho_{l,nm}g_{l,nm}\right] A_{nm,0}\left(1 - \varepsilon_{A,nm}\right) \tag{3.34}$$

where g_{nm} is the component of gravitational acceleration pointing between grid block n and grid block m. The pressure and capillary pressure gradient terms in Equation 3.19 are approximated as their difference divided by grid block distances (D_n and D_m) that depend on distance strain. Analogous expressions can be obtained for energy and diffusive mass fluxes as well.

Applying the integral finite difference method to the geomechanical equations yields one equation for grid block volumetric strain in terms of grid block mean stress, pore pressure, and temperature:

$$K\varepsilon_{v,n} = \tau_{m,n} - \left(\alpha P_n + 3\beta K \left(T_n - T_{ref}\right)\right) \tag{3.35}$$

and another one that is a discrete sum of momentum fluxes over grid block surface segments:

$$\sum_m \left[\begin{array}{l} \left(\frac{3(1-\upsilon)}{(1+\upsilon)}\right)_{nm} \frac{\tau_n - \tau_m}{D_{n,0}\left(1-\varepsilon_{D,n}\right) + D_{m,0}\left(1-\varepsilon_{D,\mathrm{m}}\right)} + \left(F_b \cdot n\right)_{nm} - \\[4mm] \left(\frac{2(1-2\upsilon)}{(1+\upsilon)}\right)_{nm} \left(\alpha \frac{P_n - P_m}{D_{n,0}\left(1-\varepsilon_{D,n}\right) + D_{m,0}\left(1-\varepsilon_{D,\mathrm{m}}\right)} + \left(3\beta K\right)_{nm} \frac{T_n - T_m}{D_{n,0}\left(1-\varepsilon_{D,n}\right) + D_{m,0}\left(1-\varepsilon_{D,\mathrm{m}}\right)}\right) \end{array} \right]$$
$$A_{nm,0}\left(1 - \varepsilon_{A,nm}\right) = 0 \tag{3.36}$$

Solution of TOUGH2-CSM Conservation Equations

The TOUGH2-CSM conservation equations are assembled by using Equations 3.23 and 3.24 to approximate the volume and surface integrals in Equation 3.22, replacing the time derivative by the standard first order finite difference approximation, and evaluating the fluxes and source/sink terms fully implicitly. The resulting set of nonlinear of algebraic equations in residual form is:

$$\left[R_n^k \right]^{l+1} = \left[M_n^k \left(1 - \varepsilon_{v,n} \right) \right]^{l+1} - \left[M_n^k \left(1 - \varepsilon_{v,n} \right) \right]^{l} -$$
$$\frac{\Delta t}{V_{n,0}} \left[\sum_m A_{nm,0} \left(1 - \varepsilon_{A,nm} \right) F_{nm}^k + V_{n,0} \left(1 - \varepsilon_{v,n} \right) q_n^k \right]^{l+1} = 0 \tag{3.37}$$

where l is time level. These equations are expressed in vector form as:

$$R\left(x^{l+1} \right) = 0 \tag{3.38}$$

where x^{l+1} is the primary variable vector at time level $l+1$. The vector of equations, Equation 3.37, is solved by the Newton-Raphson method. The Newton-Raphson method is an iterative procedure used to solve systems of non-linear equations. Denoting iteration number by subscript p, the following system of equations result from applying the Newton-Raphson method to Equation 3.37:

$$J\left(x_p^{l+1} \right)\left(x_p^{l+1} - x_p^{l} \right) = -R\left(x_p^{l+1} \right) \tag{3.39}$$

where the Jacobian matrix $J(x)$ is defined as:

$$\left[J(x) \right]_{ij} = \frac{\partial R_i(x)}{\partial x_j} \tag{3.40}$$

The Jacobian matrix is evaluated by numerical differentiation:

$$\frac{\partial R_i(x)}{\partial x_j} \approx \frac{R_i\left(x(\forall i \neq j), x_j + \varepsilon_j \right) - R_i(x)}{\varepsilon_j} \tag{3.41}$$

where ε_j is the increment for primary variable x_j. The iteration is converged when all residuals R_i are less than a prescribed tolerance, ε_{tol}:

$$\frac{R_i\left(x_{p+1}^{l+1} \right)}{M_i\left(x_{p+1}^{l+1} \right)} \leq \varepsilon_{tol} \tag{3.42}$$

Geomechanical Boundary Conditions

The momentum conservation equation (Equation 3.14) is the divergence of a momentum flux and applying the integral finite difference method to it yields an integral of momentum flux over the grid block surface that is approximated as a discrete sum over surface averaged segments. Grid block surface segments are common to another grid block or border the surroundings. The Equation 3.36 summation term as is applies to surface segments that are common to another grid block. For grid block surface segments that border the surroundings, we modify that term by applying the geomechanical boundary conditions.

There are four terms that comprise the momentum flux: the body force, and the mean stress, pressure, and temperature difference terms. The body force term contains the dot product of the body force, which points in the direction of the gravitational vector, with the vector pointing between grid blocks n and m, as shown in Figure 3.1. We neglect this term for surface segments bordering the surroundings. For such a segment, the vector pointing between grid blocks n and m is arbitrary so we assume it is orthogonal to the gravitational vector. Surface segments bordering the surroundings generally have no fluid flowing through them (fluid loss to the surroundings is generally represented as a constant pressure sink), so there would be no pore pressure communication between a grid block and the surroundings. Consequently, we neglect the pressure difference term as well. Finally, we assume the temperature and mean stress of the surroundings are the grid block's initial values.

We apply the above boundary conditions to the Equation 3.36 summation term and obtain the form for a surface segment bordering the surroundings:

$$
\left[\begin{array}{l} \left(\dfrac{3(1-\upsilon)}{(1+\upsilon)} \right)_n \dfrac{\tau_n - \tau_n^0}{2D_{n,0}\left(1-\varepsilon_{D,n}\right)} - \\[4mm] \left(\dfrac{2(1-2\upsilon)}{(1+\upsilon)} \right)_n \sum_j \left(\left(3\beta K\omega_j\right)_n \dfrac{T_{j,n}-T_{j,n}^0}{2D_{n,0}\left(1-\varepsilon_{D,n}\right)} \right) \end{array} \right] A_{nm,0}\left(1-\varepsilon_{A,n}\right)
\tag{3.43}
$$

where superscript 0 refers to grid block initial value and D_m is replaced by D_n.

Rock Property Correlations

We describe the dependence of permeability and porosity on effective stress and other quantities in this section. Effective stress was initially defined as the difference between average stress and pore pressure by Terzhagi (1936) and was generalized by Biot and Willis (1957) as:

$$
\tau' = \tau_m - \alpha P
\tag{3.44}
$$

where α is the Biot's or effective stress coefficient. Correlations have been developed for porosity as a function of effective stress and other quantities and permeability as a function of either porosity or effective stress. There are numerous examples of the above correlations, with

39

each developed for a specific set of conditions. We describe those that have been incorporated into TOUGH2-CSM below.

We developed an expression for porosity starting with its definition. Porosity is the ratio of fluid volume to bulk volume, and since fluid volume plus solid volume equals bulk volume, porosity can be written as:

$$\phi = 1 - \frac{V_s}{V} \tag{3.45}$$

where V is bulk volume and V_s solid volume. Gutierrez and Lewis (2001) presented expressions for solid volume change with pressure and effective stress. These expressions can be integrated to yield an expression for solid volume:

$$V_s\left(P,\tau^{'}\right) = V_{s,r}\left(1 + \frac{1-\phi_r}{K_s}\left(P - P_r\right) - \frac{1}{K_s}\left(\tau^{'} - \tau_r^{'}\right)\right) \tag{3.46}$$

where subscript r refers to reference conditions. Equation 3.25 relates bulk volume to volumetric strain, and when combined with Equations 3.45 and 3.46, yield porosity as a function of pressure, temperature, and effective stress:

$$\phi = 1 - \left(1 - \phi_r\right)\frac{\left(1 + \frac{1-\phi_r}{K_s}\left(P - P_r\right) - \frac{1}{K_s}\left(\tau^{'} - \tau_r^{'}\right)\right)}{\frac{\left(1 - \varepsilon_v\right)}{\left(1 - \varepsilon_{v,r}\right)}} \tag{3.47}$$

An example of reference conditions for Equation 3.47 is the initial conditions for a simulation, where volumetric strain, porosity, mean stress, and pressure are specified.

Rutqvist *et al.* (2002) presented the following function for porosity, obtained from laboratory experiments on sedimentary rock (Davies and Davies, 2001):

$$\phi = \phi_1 + \left(\phi_0 - \phi_1\right)e^{-\alpha\tau^{'}} \tag{3.48}$$

where ϕ_0 is zero effective stress porosity, ϕ_1 is high effective stress porosity, and the exponent a is a parameter. They also presented an associated function for permeability in terms of porosity:

$$k = k_0 e^{c\left(\frac{\phi}{\phi_0} - 1\right)} \tag{3.49}$$

McKee *et al.* (1988) derived a relationship between porosity and effective stress from hydrostatic poroelasticity theory by assuming incompressible rock grains:

$$\phi = \phi_0 \frac{e^{-c_p(\tau'-\tau_0')}}{1-\phi_0\left(1-e^{-c_p(\tau'-\tau_0')}\right)}$$

(3.50)

where c_p is average pore compressibility. They also related permeability and porosity using the Carman-Kozeny equation:

$$k \sim \frac{\phi^3}{(1-\phi)^2}$$

(3.51)

These relationships fit laboratory and field data for granite, sandstone, clay, and coal.

Ostensen (1986) studied the relationship between effective stress and permeability for tight gas sands and approximated permeability as:

$$k^n = D\ln\frac{\tau'^*}{\tau'}$$

(3.52)

where exponential n is 0.5, D is a parameter, and τ'^* is effective stress for zero permeability, obtained by extrapolating measured square root permeability versus effective stress on a semi-log plot.

Verma and Pruess (1988) presented a power law expression relating permeability to porosity:

$$\frac{k-k_c}{k_0-k_c} = \left(\frac{\phi-\phi_c}{\phi_0-\phi_c}\right)^n$$

(3.53)

where k_c and ϕ_c are asymptotic values of permeability and porosity, respectively, and exponent n is a parameter.

A theory of hydrostatic poroelasticity (Jaeger *et al.*, 2007) that accounts for the coupling of rock deformation with fluid flow yields the following expression for porosity changes as a function of effective stress:

$$d\phi = -\left[\frac{1-\phi}{K} - C_r\right]d\tau_m$$

(3.54)

where C_r is rock grain compressibility.

Permeability and porosity are used to scale capillary pressure according to the relation by Leverett (1941):

$$P_c = P_{c0} \sqrt{\left(\frac{\phi}{k}\right)\left(\frac{k}{\phi}\right)_0}$$

(3.55)

Verification and Application Examples for Single-Porosity TOUGH2-CSM

We describe three simulations to provide model verification and application examples. The first two, one-dimensional consolidation of a porous medium and a simulation of the Mandel-Cryer effect, are compared to analytical solutions. The third is a match of published results from the literature, a simulation of deformation and fluid circulation in a caldera structure. In this problem, the authors modeled geomechanical processes by coupling two simulators, TOUGH2, which simulates fluid flow and heat transport, and FLAC, which simulates rock mechanics with thermomechanical and hydromechanical interactions.

1) One-Dimensional Consolidation

In the one-dimensional consolidation problem (Jaeger *et al.*, 2007), a z-direction stress is applied to the top of a fluid-filled porous rock column, instantaneously inducing a uniaxial deformation and a pore pressure increase. Afterwards, fluid is allowed to drain out of the column top and the induced pore pressure dissipates. An analytical solution to this problem is presented.

We adapt this problem to our flow and stress formulations. Starting from an initial unstressed state of the system where pore pressure and mean stress both equal P_i, the pore pressure P induced by an applied mean stress is given by

$$P = B\left(\tau_m - P_i\right) + P_i$$

(3.56)

where B is the Skempton coefficient. For uniaxial strain, mean stress, z-direction stress, and pore pressure are related by:

$$\tau_m = \frac{1}{3}\frac{(1+v)}{(1-v)}\left(\tau_{zz} - \alpha P\right) + \alpha P$$

(3.57)

For a constant z-direction stress, the induced pore pressure and mean stress are obtained by solving Equations 3.56 and 3.57. Our simulation is initialized with those results. Fluid leaves the top grid block via a constant pressure fluid sink that is set to the unstressed pore pressure P_i. The top grid block mean stress is obtained from Equation 3.57 using P_i and the constant z-direction stress. Finally, porosity varies according to Equation 3.54. Our input parameters are listed in Table 3.1.

Table 3.1. Input parameters for one-dimensional consolidation problem.

Initial porosity	0.09
Permeability, m^2	$1.0 \cdot 10^{-13}$
Bulk Modulus, GPa	3.33
Poisson's ratio	0.25
Applied load, MPa	3.0
Relaxation pressure, MPa	0.1
Fluid compressibility, 1/Pa	$4.0 \cdot 10^{-10}$
Fluid viscosity, Pa-s	$4.7 \cdot 10^{-04}$
Length, m	1000
Number of grid blocks	1000

We ran the simulation for 10^6 seconds with 10^2 second time steps. Comparisons of pore pressure from simulation and analytical solution are shown in Figure 3.2, with excellent agreement.
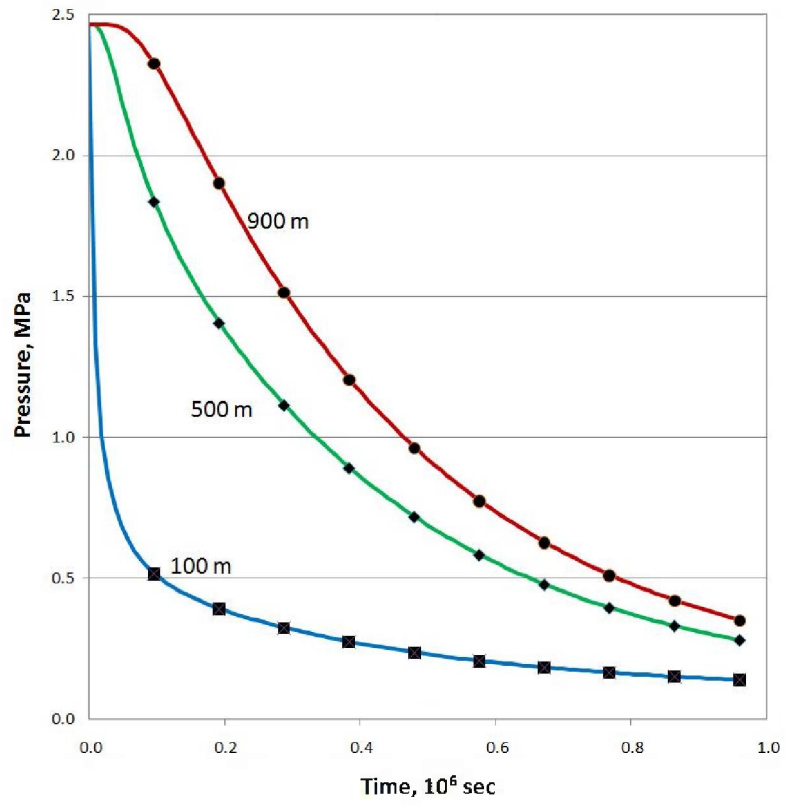
Figure 3.2. Simulated pressure (markers) and analytical (solid lines) versus time at 100 m, 500 m, and 900 m for one-dimensional consolidation problem.

2) Mandel-Cryer Effect

A constant compressive force is applied to the top and bottom of a fluid-filled poroelastic material, inducing an instantaneous uniform pore pressure increase and compression. Afterwards, the material is allowed to drain laterally. Because the pore pressure near the edges must decrease due to drainage, the material there becomes less stiff and there is a load transfer to the center, resulting in a further increase in center pore pressure that reaches a maximum and then declines. This pore pressure behavior is called the Mandel-Cryer effect (Mandel, 1953) and Abousleiman *et al.* (1996) present an analytical solution that we compare our simulated results to.

We simulate this problem in two steps. The first step is the application of force that induces the pore pressure increase. We start from an unstrained state where pore pressure and mean stress are both equal ($\tau_{m,0} = P_0$) and impose a greater mean stress ($\tau_{m,1}$) at the top and bottom. These greater stresses compress the system and produce a pore pressure increase from pressure P_0 to pressure P_1. In the analytical solution, uniaxial stress is assumed, so mean stress and z-direction stress are related by:

$$\tau_m = \frac{\tau_{zz}}{3} \tag{3.58}$$

We next simulate fluid drainage. The system is initially at the above equilibrated state, mean stress $\tau_{m,1}$ and pore pressure P_1, and we impose the initial pore pressure on the lateral boundaries to allow the system to drain.

We simulated the Mandel-Cryer effect for a 1000 m square domain that was subdivided into a uniform 200x200 grid. The initial pore pressure and mean stress were 0.1 MPa, the applied mean stress was 5 MPa, the equilibrium pore pressure was 2.18 MPa, and rock properties are shown in Table 3.2. The system drained for 50,000 seconds.

Table 3.2. Rock properties for Mandel-Cryer effect simulation.

Porosity	0.094
Permeability, m^2	$1.0 \cdot 10^{-13}$
Young's modulus, GPa	5.0
Poisson's ratio	0.25
Biot's coefficient	1.0

We compare pressure at the middle of the system with the analytical solution, shown in Figure 3.3. The simulated results exhibit the pore pressure maximum characteristic of the Mandel-Cryer effect and lie extremely close to the analytical solution. The analytical solution and simulator formulation do differ in that the simulator allows pore pressure to vary in two dimensions whereas in the analytical solution, pressure varies only laterally.
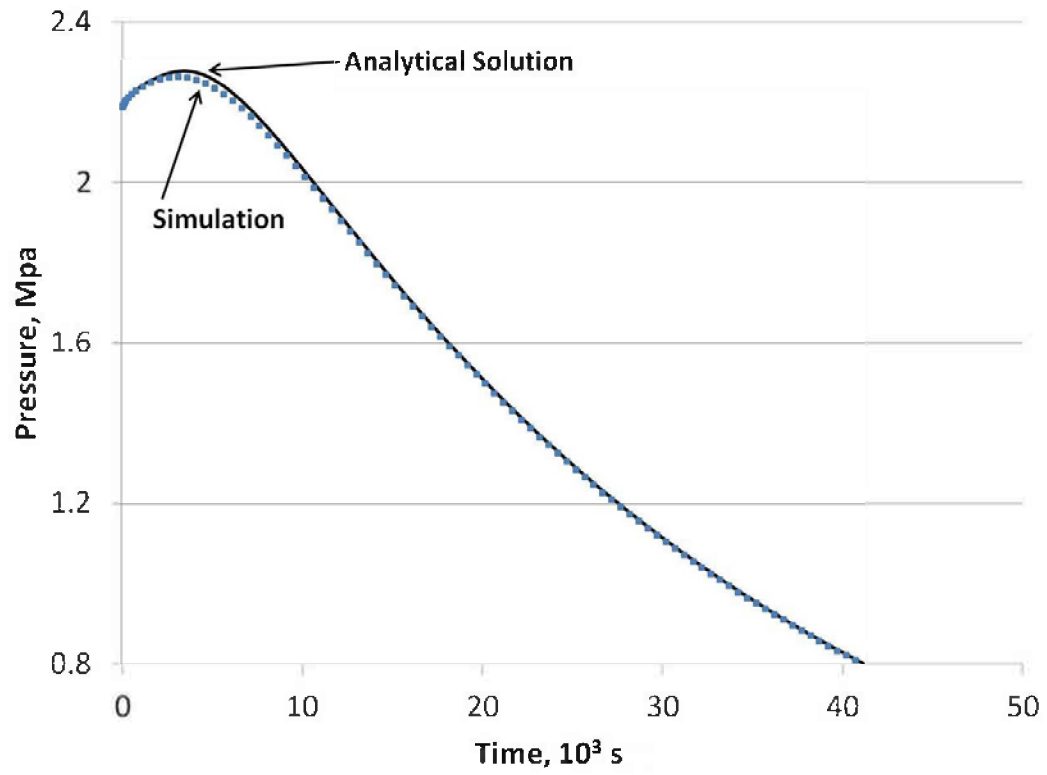
Figure 3.3. Comparison Mandel-Cryer effect analytical solution to simulation for pore pressure located at system center.

3) Ground Deformation and Heat Flow in a Caldera Structure

The Phlegrean Fields caldera, located near Naples, Italy, undergoes periodic episodes of volcanic unrest that includes seismic activity and slow ground movement. This unrest is believed to be caused by pressurization of the magma chamber and hot fluid migration. The caldera has been slowly subsiding with periodic short-lived minor uplifts after two major episodes of unrest during 1969-1972 and 1982-1984. Todesco *et al.* (2003) hypothesized that the recent activity was associated with periods of more intense magmatic degassing that would cause larger amounts of fluid to enter the caldera, accompanied by ground deformation, increased pore pressure, and higher temperatures. To verify this, they modeled hydrothermal fluid flow and porous medium deformation using the coupled TOUGH2-FLAC simulator (Rutqvist *et al.*, 2002), with fluid components water and carbon dioxide and the system heated by an influx of hot fluids from the bottom. Heat and fluid transport simulations were first done to match current conditions that were deduced from geochemical data. These results served as initial conditions for the periods of enhanced degassing, simulated by increasing the fluid influx for a given amount of time.

We reran one of their simulations on TOUGH2-CSM using the EOS2 module (Pruess *et al.*, 1999) for water-CO_2 property calculations due to the high injected fluid temperature. The cylindrical simulation domain was 2500 m in diameter and 1500 m in height. The r-z grid was 50x50, grid block height was constant, and grid block radial thickness varied logarithmically. Phlegrean Fields rock properties are shown in Table 3.3.

Table 3.3. Rock properties for Phlegrean Fields caldera.

Young's modulus, GPa	10.0
Poisson's ratio	0.286
Biot's coefficient	1.0
Porosity	0.2
Permeability, m^2	$1.0 \cdot 10^{-14}$
Density, $kg\text{-}m^{-3}$	2000.0
Thermal conductivity, W m^{-1} $°C^{-1}$	2.8
Specific heat, J kg^{-1} $°C^{-1}$	1000.0

We injected 3000 t d^{-1} of water and 1500 t d^{-1} of CO_2 at 350 °C for 4000 years uniformly through a 156 m radius area at the bottom. The top was at atmospheric pressure and ambient temperature (20 °C); the outer radial boundary and the rest of the bottom were impermeable and adiabatic. Figure 3.4 shows the TOUGH2-CSM temperature profile at 4000 years; it is similar to the reference one shown in Figure 3.5. The gas saturation profiles, shown in Figures 3.6 and 3.7, are also similar. Fluid injection rates were increased by a factor of ten for the next two years to simulate a period of enhanced degassing and surface uplift was calculated over this time. Figure 3.8 shows TOUGH2-CSM surface uplift and Figure 3.9 the reference surface uplift. TOUGH2-CSM surface uplift was calculated assuming isotropic strain. The maximum value and the rate of decline of the profiles agree with each other.

47
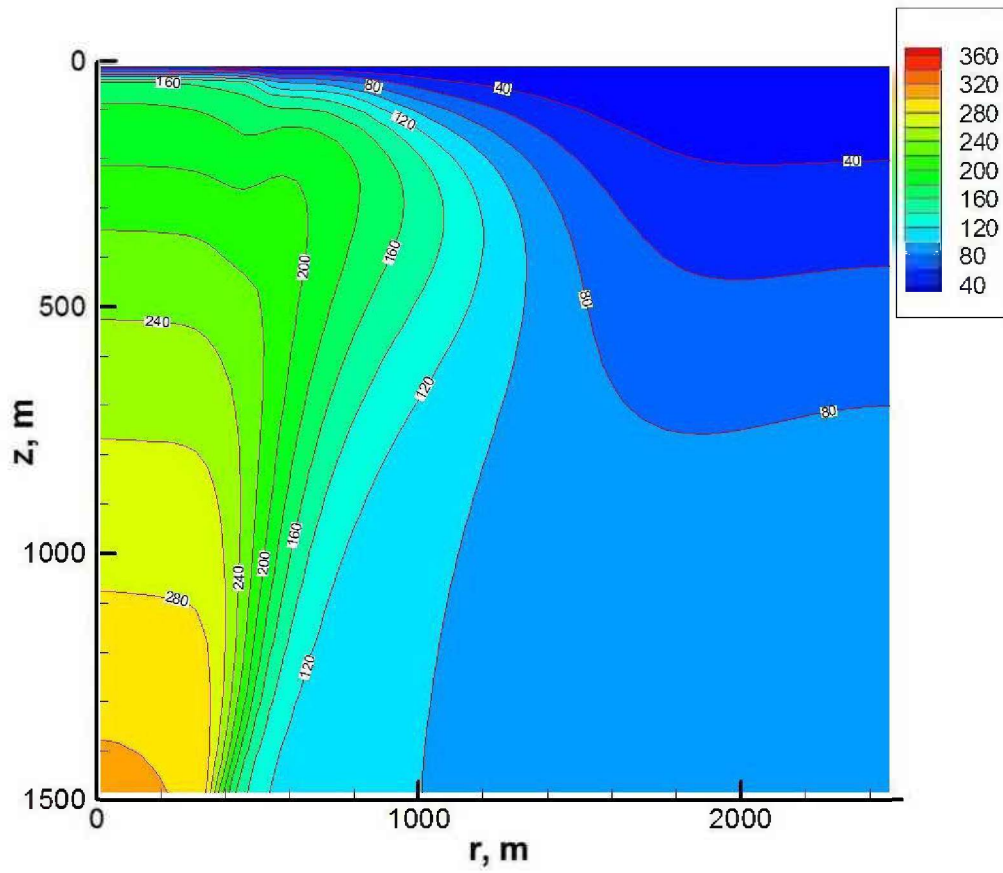
Figure 3.4. Temperature profile after 4000 years injection from TOUGH2-CSM.
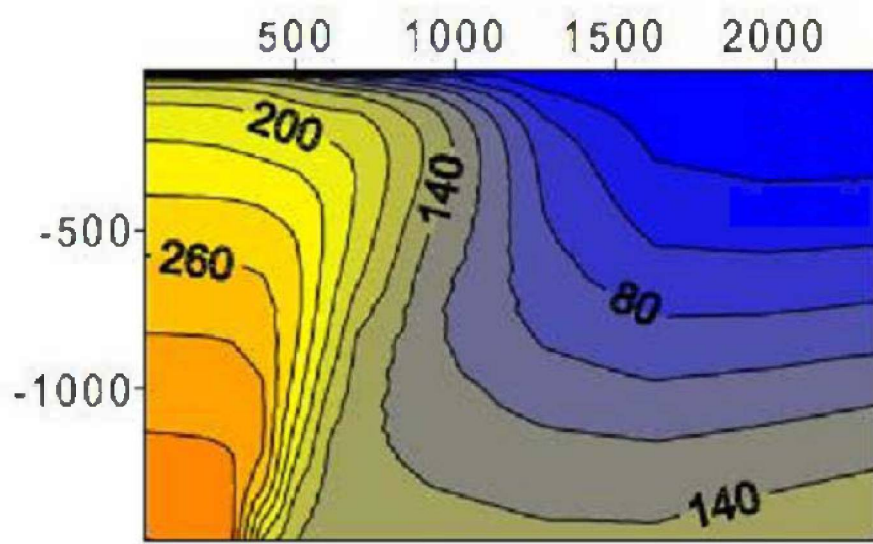
Figure 3.5. Temperature profile after 4000 years injection, adapted from Todesco *et al.* (2003).
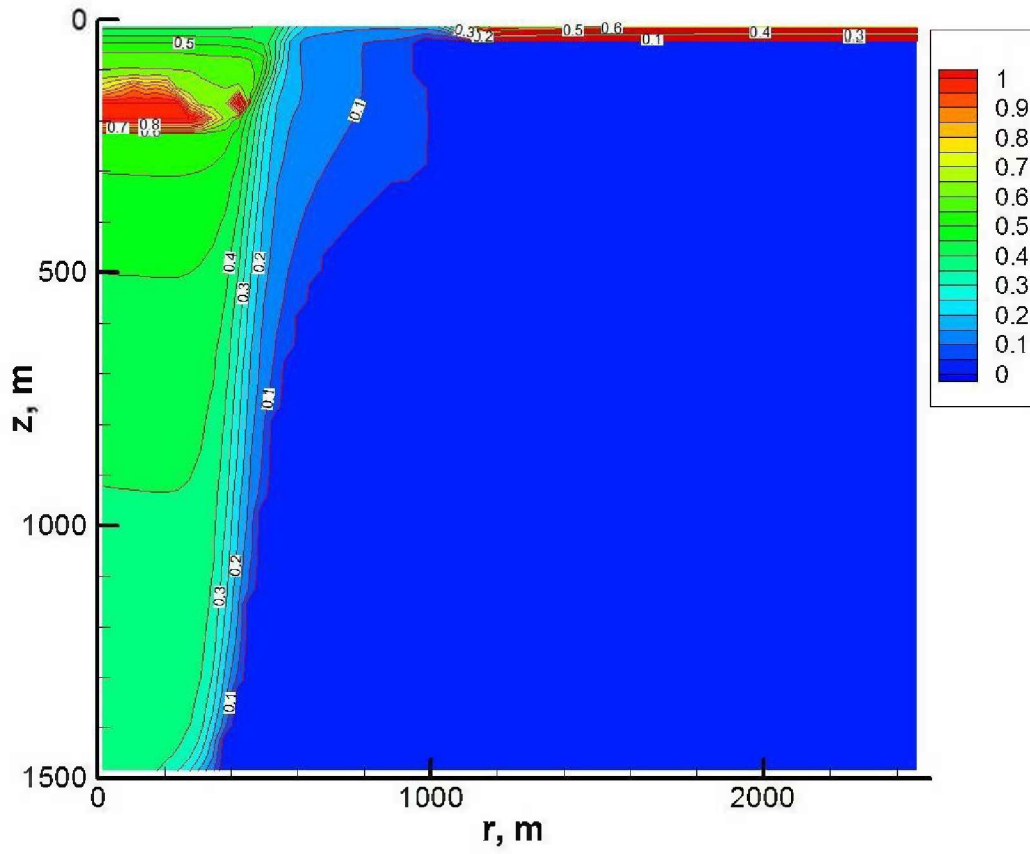
Figure 3.6. CO$_2$ saturation profile after 4000 years injection from TOUGH2-CSM.
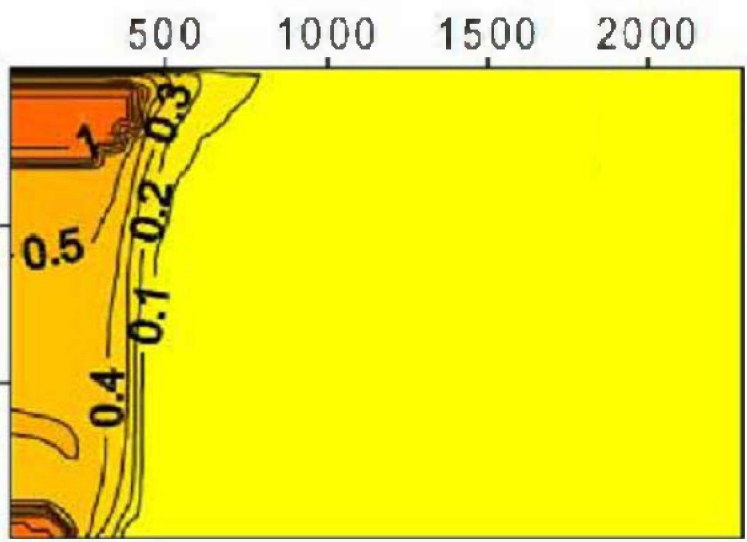
Figure 3.7. CO_2 saturation profile after 4000 years injection, adapted from Todesco *et al.* (2003).
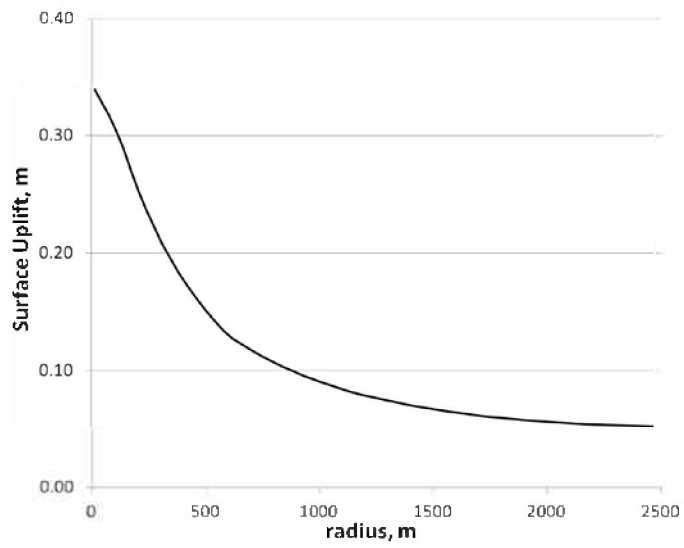
Figure 3.8. Surface uplift after two years of higher injection rates (10 times) from TOUGH2-CSM.
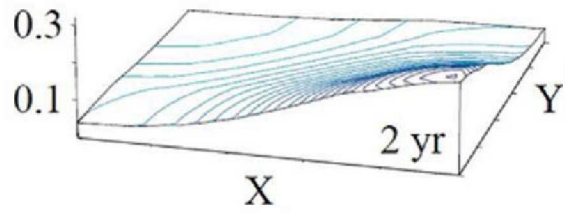
Figure 3.9. Surface uplift after two years of higher injection rates (10 times), adapted from Todesco *et al.* (2003).

Summary and Conclusions

We developed a massively parallel reservoir simulator, called TOUGH2-CSM, for modeling THM processes in porous media brine aquifers. We derived, from the fundamental equations describing deformation of porous and fractured elastic media, a momentum conservation equation relating mean stress, pressure, and temperature, and incorporated it alongside the mass and energy conservation equations from the TOUGH2 formulation. In addition, rock properties, namely permeability and porosity, are functions of effective stress and other variables that are obtained from the literature. The starting point for our simulator is the massively parallel TOUGH2-MP code.

We verified the simulator formulation and numerical implementation using analytical solutions and example problems from the literature. For the former, we matched a one-dimensional consolidation problem and a two-dimensional simulation of the Mandel-Cryer effect. For the latter, we compared our results to those from two coupled computer codes, one that simulates fluid flow and heat transport, and the other that simulates rock deformation. We obtained a good match of temperature and gas saturation profiles and surface uplift after injection of hot fluid into a model of a caldera structure. This agreement indicates that our formulation is able to capture THM effects modeled by a coupled simulation with a more detailed handling of rock mechanics.

Task 4.0: Incorporation of Geochemical Reactions of Selected Important Species

Literature Survey of Brine and Rock Composition, Reaction Equilibria, and Reaction Rates

We surveyed the compositions of brine and rock from current and completed CO_2 sequestration projects. Below is a table of current and future CO_2 sequestration projects, with many U. S. sequestration projects and some foreign ones. This table will be used to group the large body of existing literature on geochemical reaction modeling and experiments among injected CO_2, formation brine, and formation rock.

Table 4.1. Survey of CO_2 sequestration projects in the U. S. and worldwide.

CO_2 sequestration projects	Current or completed	Type	Selected References
Alberta Program, Canada	Completed	Enhanced coal-bed methane	Wong *et al.* (2001), Gunter *et al.* (2005), Mavor and Gunter (2006), Palmer *et al.* (2007)
Northern Netherland / Rotterdam	Current / Future	Depleted gas fields	
Otway Project, Australia	Current	Depleted gas fields	Spencer *et al.* (2006), Stalker *et al.* (2009)
CO2SINK, Ketzin, Germany	Current	Saline aquifer	Forster *et al.* (2009)
Zuid-Limburg, Netherland	Future	Enhanced coal-bed methane	
CO2STORE/Sleipner, Norway	Monitor	Saline aquifer	Gaus *et al.* (2005)
Deccan, India	Future	Flood basalt formation	
Fort Nelson, Canada (Coop with US DOE Regional CO_2 sequestration partner:	Current	Saline aquifer	

Plains)			
In Salah, Algeria	Current	Aquifer below gas reservoir	Ringrose *et al.* (2008)
Heartland Area Redwater Project, Canada	Future	Brine saturated carbonate	
Weyburn-Midale, Canada	Current	Enhanced oil recovery	Whittaker (2005)
Aquistore, Canada	Future	Saline aquifer	
Frio, United States	Completed	Saline aquifer	Doughty (2005)
Lacq, France	Future	Depleted gas field	
TX Energy, United States	Future	Enhanced oil recovery	
Zama, Canada (Coop with US DOE Regional CO2 sequestration partner: Plains)	Current	Acid gas enhanced oil recovery (CO_2 + SO_2)	Davison *et al.* (1996), Michael and Buschkuehle (2006)
ZEROGEN, Queensland, Australia	Future	Saline aquifer	
Arizona Utility and Northern California, United States (US DOE Regional CO_2 sequestration partner: Westcarb)	Current	Saline aquifer	
Permian Basin and Paradox Basin, United States (US DOE Regional CO_2 sequestration partner: Southwest)	Current	Enhanced oil recovery	
San Juan Basin, United States	Current	Enhanced coal-	

(US DOE Regional CO$_2$ sequestration partner: Southwest)		bed methane
Farnham Dome, United States (US DOE Regional CO$_2$ sequestration partner: Southwest)	Current	Saline aquifer
Basalt Pilot, United States (US DOE Regional CO$_2$ sequestration partner: BigSky)	Current	Basalt formation
Kelvin Dome and Nugget Sandstone, United States (US DOE Regional CO$_2$ sequestration partner: BigSky)	Future	Saline aquifer
Decatur Project, United States (US DOE Regional CO$_2$ sequestration partner: MGSC)	Current	Saline aquifer
Michigan Basin, Appalachian Basin, and East Bend, United States (US DOE Regional CO$_2$ sequestration partner: MRCSP)	Current	Saline aquifer
Tuscaloosa and Lowe Tuscaloosa formations, United States (US DOE Regional CO$_2$ sequestration partner: Southeast)	Current	Stacked: Enhanced oil recovery and saline aquifer
Central Appalachian and Black Warrior Basins, United States (US DOE Regional CO$_2$	Current	Coal seams

57

According to the Climate Change report of Intergovernmental Panel on Climate Change of Unites States (IPPC, 2007), the concentration of carbon dioxide in the atmosphere has increased by 31% since the start of the Industrial Revolution in the eighteenth century, from around 280 parts per million by volume (ppmv) in 1850 to around 380 ppmv to date, and is currently rising by about 1.7 ppmv per year. When CO_2 reacts with water content in atmosphere, soil and ocean, carbonic acid and hydrogen ions are formed, increasing the acidity of the whole environment. Around 30-40% of CO_2 emitted to the atmosphere dissolves into the oceans (Millero, 1995), where the reaction with sea water has increased ocean acidity by 0.1 pH units since pre-industrial times (IPCC, 2007). Ocean ecosystems are affected both through acidification and by associated reductions in carbonate ion concentrations (James et al., 2005). Around 20% of anthropogenic carbon dioxide emissions to the atmosphere are absorbed by the terrestrial biosphere (Feely et al., 2004). While how much of these changes is due to the emission of anthropogenic CO_2 is still under debate, many efforts to control CO_2 emission from fossil fuel consumption have already been proposed or practiced.

CO_2 geological sequestration is a viable solution that aims at storing CO_2 from burning of fossil fuels in geological formations. Saline aquifers have the largest capacity among the many options for long-term geological sequestration (IPCC, 2005). Saline aquifers are large underground formations saturated with brine, and are often rich in dissolved minerals. The primary flow and transport mechanisms that control the spread of CO_2 in saline aquifers include (IPCC, 2005):

1. Fluid flow (migration) in response to pressure gradients created by the injection process;
2. Fluid flow in response to natural hydraulic gradients;
3. Buoyancy caused by the density differences between CO_2 and the formation fluids;
4. Diffusion;
5. Dispersion and fingering caused by formation heterogeneities and mobility contrast between CO_2 and formation fluid;
6. Dissolution into the formation fluid;
7. Mineralization;
8. Pore space (relative permeability) trapping;
9. Adsorption of CO_2 onto organic material.

The effectiveness of geological storage depends on a combination of structural, physical and geochemical trapping mechanisms.

Stratigraphic and Structural Trapping: Initially, physical trapping of CO_2 below low-permeability seals (caprocks), such as very-low-permeability shale or salt beds, is the principal means to store CO_2 in geological formations.

Solubility Trapping: Solubility trapping occurs when CO_2 dissolves in formation brine in significant quantities.

Mineral Trapping: Dissolved CO_2 changes the pH of the formation brine and can trigger mineral reactions. These reactions involve not only dissolution of carbonates (a fast reaction), but also conversion of silicates (a slow reaction). The latter, after hundreds to thousands of years,

would eventually convert CO_2 into rock minerals. A good understanding of the geochemical reactions between CO_2 and dissolved minerals is important for the assessment of the effectiveness of long-term CO_2 storage in geological formations. Chemical reactions not only affect the material balance of CO_2 but also change the porosity and permeability of the rock through dissolution and precipitation processes.

A variety of software packages for numerical modeling have been developed for fluid flows coupled with geochemical reactions, including TOUGHREACT (Xu et al., 2006b), PHREEQC (Parkhurst et al., 1999) and GEOCHEMIST'S WORKBENCH (Bethke, 2002). In order to obtain a good understanding of the kinetics of the dissolution of CO_2 in water and the subsequent chemical reactions, we investigate the existing literature on geochemical reaction modeling associated with worldwide CO_2 geological sequestration projects. Our survey includes the main minerals in the brine and the rock at specific sequestrated sites and the modeling software employed.

Johnson et al. (2001) conducted and analyzed three distinct Sleipner simulations (XSH, CSH, and DSH models) within a single spatial domain representing the near-field sequestration environment at Sleipner, by means of an integrated toolbox: NUFT (integrated software package containing five modules facilitating numerical simulation of multiphase/multicomponent flow and reactive transport), GEMBOCHS (integrating thermodynamic/kinetic database and dedicated software library together to facilitate generation of application-specific data files for geochemical reaction software), and Xtool (GUI-driven graphics utility for extracting and visualizing a broad range of output data from NUFT simulations). Then they presented the adopted site-specific 2-D spatial domain and hydrologic/compositional data, and described the thermodynamic/kinetic data used to represent geochemical reaction between CO_2, water and lithologic minerals (quartz, K-feldspar, plagioclase, muscovite and phlogopite). Finally they concluded that calcite was expected to play a minor role in mineral trapping relative to siderite, magnesite, and their solid solutions in the Sleipner sequestrated site.

For the same CO_2 sequestration site, Sleipner field (North Sea), Gaus et al. (2003 and 2005) used PHREEQC (V2.6) to model the reactive transport of the CO_2-injection project where CO_2 is injected in the Utsira Sands underlying the Nordland Shale cap rock. The Davies approach was used for the aqueous speciation calculation, and the LLNL.dat database was adapted for thermodynamic calculation. They investigated kinetic batch modeling in short term and long term. In the short term, pH decreased after contact of the formation water with the CO_2 occurred. This resulted in the dissolution of calcite, which stabilized the pH at 4.5 after approximately 9 years. There were two cases for the long term geochemical reaction modeling: (1) All plagioclase was present as albite, and the dominant reaction in the system over the 15,000 year time period was the dissolution of albite with the subsequent formation of kaolinite. After approximately 10000 years, this reaction slows down due to the decreasing Ca^{2+} concentration in the formation water and the formation of dawsonite; (2) All plagioclase was present as albite and anorthite, the alteration of anorthite dominates the feldspar reactions leading to the formation of calcite and kaolinite, and this reaction was completed after approximately 5000 years when all anorthite has disappeared.

Nghiem et al. (2004) presented a study including 1D, 2D and 3D models of CO_2 injection in aquifers using the commercial GEM-GHG code. This code is capable of modeling convective and dispersive flows, calculating phase equilibrium for reactions between the oil, gas and aqueous phases, and chemical equilibrium or kinetic dissolution and precipitation reactions between minerals. A method for solving all equations simultaneously in a more robust way is described. A simpler set of reactions was chosen for the 3D models than for the 1D or 2D model.

Frangeul et al. (2004) presented a simulation of CO_2 injection at Sleipner using GEM-GHG. The simulation was for a time period of 5000 years and included 3D convective flows induced by density differences, but used homogeneous reservoir properties and a very simplified mineral assemblage containing only calcite and dolomite.

Audigane et al. (2006 and 2007) used a conceptual model based on the Sleipner dataset, with different and realistic mineralogy implemented for the sand and shale layers to establish a 2D vertical model with a radial mesh geometry containing 22 layers, including 4 semi-permeable shale layers. Batch reaction and reactive transport simulations were performed with TOUGHREACT software for a long storage period (10,000 years). The impact of CO_2 on the minerals (albite, calcite, chalcedony, chlorite, muscovite, kaolinite, K-feldspar, siderite) was simulated by batch geochemical modeling. For batch reaction modeling with CO_2 injection in the shale, the overall reactivity resulted in an absolute porosity reduction of approximately 0.01 (from 0.1025 initially down to 0.093 after 10,000 years). For batch reaction modeling with CO_2 injection in the sand, only 0.002 percent of the albite and 0.0002 percent of the chlorite reacted after 10,000 years. Four main types of interactions (calcite dissolution and precipitation, albite alteration, chlorite alteration, muscovite alteration) were identified for 10,000 years' simulation.

Secondly, there are a lot of literature focusing on geochemical reaction modeling in Alberta Basin and Weyburn oil field Canada. Gunter et al. (2000) used a geochemical computer model (PATHARC) to compute the interaction of industrial waste streams comprising CO_2, H_2SO_4 and H_2S with the minerals in typical carbonate and sandstone aquifers from the Alberta Basin. They modeled the geochemical reactions associated with CO_2, H_2SO_4 and H_2S disposal into the Nisku and Glauconitic Sandstone aquifers . Then they concluded that siliciclastic aquifers appeared to be a better host for mineral trapping than carbonate aquifers, especially with regard to CO_2. Carbonate aquifers might be more prone to leakage due to high CO_2 pressures generated by reaction with H_2SO_4 and H_2S.

Xu et al. (2004a) performed batch reaction modeling of the geochemical evolution of three different aquifer mineral compositions (glauconitic sandstone from the Alberta Sedimentary Basin, a proxy for a sediment from the United States Gulf Coast and a dunite, an essentially monomineralic rock consisting of olivine) in the presence of CO_2 at high pressure by TOUGHREACT. The modeling considered three important factors affecting CO_2 sequestration: (1) the kinetics of chemical interactions between the host rock minerals and the aqueous phase, (2) CO_2 solubility dependence on pressure, temperature and salinity of the system, and (3) redox processes that could be important in deep subsurface environments. Their main conclusions were as follows: for glauconitic sandstone, most CO_2 is trapped as ankerite and siderite, with a minor amount as dolomite and dawsonite. For the Gulf Coast case, the major trapping minerals are dawsonite and ankerite, with minor ones calcite and siderite, and for the olivine rock (dunite)

case, the trapping minerals are magnesite and siderite. The mineral-trapping capacity can be comparable with or be larger than that of solubility trapping.

Cantucci *et al.* (2009) used PRHEEQC (V2.14) Software Package with a modified thermodynamic database and a correction for supercritical CO_2 fugacity to perform kinetic modeling. This geochemical modeling procedure was based on the dataset provided by the Weyburn Project, which includes: a) bulk mineralogy of the Marly and Vuggy reservoirs; b) selected pre- and post-CO_2 injection water samples of Midale Beds and c) mean gas-cap composition at the wellheads. The main results can be summarized, as follows: 1) the calculated pre-injection chemical composition of the Midale Beds brine is consistent with the analytical data of the waters collected in 2000; 2) the main reservoir reactions (CO_2 and carbonate dissolution) take place within the first year of simulation, 3) the temporal evolution of the chemical features of the fluids in the Weyburn reservoir suggests that CO2 can be safely stored by solubility (as CO_2 (aq)) and mineral trapping (via dawsonite precipitation).

Raistrick *et al.* (2009) carried a geochemical modeling based on the samples of the fluid and gas of four wells in part of the reservoir volume targeted by CO_2 injection by means of Geochemical Reaction Pathway Modeling Software GWB (Geochemists Workbench React). The measured changes of chemical data in the selected monitoring well were simulated over 750 days following the arrival of injected CO_2. The modeling timescale was extended to investigate the fate of CO_2 over post injection timescales, which showed that alteration of K-feldspar and other silicate minerals present in the Weyburn reservoir will lead to further storage of injected CO_2 in the aqueous phase and as carbonate minerals.

Thirdly, a lot of CO_2 sequestration projects have been carried out in West Texas, Colorado Plateau, Williston Basin, Ohio and Gulf Coast in United States. Geochemical reaction modeling has been performed to investigate the fate of CO_2 injection in these sites. Wellman *et al.* (2003) compared simulator predictions to laboratory core flooding experiments to evaluate model efficacy. The modeling code used was a combination of TOUGH2 simulator (groundwater/brine and heat flow simulation) with the chemistry code TRANS (chemical reactive transport). Five types of rock (pure calcite, pure quartz, quartz and carbonates, quartz and evaporates, dolomite and anhydrite) from the Seminole field in west Texas were featured in TRANSTOUGH model simulations. Simulation results indicated that varying brine pH and alkalinity caused 0 to 5 percent differences on the resultant volumetric mineral fractions.

White *et al.* (2005) performed geochemical reaction modeling of CO_2 injection into the White Rim Sandstone by the reactive chemical simulator ChemTOUGH. Results indicated that 1000 years after the 30 year injection period began, approximately 21% of the injected CO_2 was permanently sequestered as a mineral, 52% was beneath the ground surface as a gas or dissolved in the groundwater and 17% had leaked to the surface and leakage to the surface was continuing.

Zerai *et al.* (2006) used Geochemist's Workbench to conduct equilibrium, path-of-reaction and kinetic modeling of CO_2-brine-mineral reactions in the Rose Run Sandstone, one of Ohio's deep saline aquifers, to investigate the factors that were likely to influence the capacity of this formation to trap injected CO_2 as solid carbonate mineral phases. Three types of mineral

assemblages were investigated for the geochemical reaction: a carbonate assemblage composed of calcite, dolomite and siderite; a sandstone assemblage composed of quartz, K-feldspar, kaolinite, albite, annite, and siderite; and a mixed assemblage (sandstone-carbonate), which represents the aquifer as a whole. Results indicated that the stability of carbonate rocks is controlled by the brine-to-rock ratio, the pH of the system, the fugacity of CO_2, and the kinetic rate of dissolution.

Bacona et al. (2009) conducted 2D reactive transport modeling based on the data from Rose Run formation and Copper Ridge formation by STOMP-WCS-R (water, CO_2, salt and reactions) and add-on module of ECKEChem (Equilibrium-Conservation-Kinetic Equation Chemistry). Fourteen carbonate, silicate and sulfate aqueous species, and four mineral species were considered (88% dolomite, 8% quartz, 2% calcite, and 2% anhydrite by volume for dolomite layers and 88% quartz, 8% dolomite, 2% calcite, and 2% anhydrite by volume for sandstone layers). It was shown that for a 330,000 metric ton injection of CO_2 with a 100-year recovery period, mineral dissolution/precipitation does not significantly affect the rate of carbon sequestration in, or the formation properties of, the Rose Run and Copper Ridge formations.

Sorensen et al. (2009) used the geochemical code PHREEQC, whose thermodynamic database was adjusted with SUPRCRT92 code, to perform numerical modeling. The modeling was based on selected rock samples from several different formations of the Williston Basin, including Bakken, Broom Creek, Madison, and Winnipeg. XRD analysis was performed on each sample after CO_2 exposure to determine the mineralogical components of the samples and to evaluate any physical or chemical changes. It was reported that anhydrite, calcite, dolomite, forsterite, and quartz are the dominant phases. The results suggested that laboratory experimental results could be reasonably correlated to some aspects of geochemical modeling.

Berger et al. (2009) used React 7.0.4 and PHREEQC 2.13.2 (for kinetic and equilibrium models), and TOUGHREACT (for reaction modeling with carbonate and silicate minerals) to conduct geochemical reaction modeling based on data from brine and freshwater samples associated with EOR in the Loudon oil field and Illinois Basin Decatur project. The reaction modeling of Loudon oil field indicated an increase in the reservoir permeability from reservoir property changes. Predictive models for the Illinois Basin Decatur project were helpful to understand potential reactions in the subsurface.
Xu et al. (2003) developed a reactive fluid flow and geochemical transport numerical model for evaluating long term CO_2 disposal in deep geologic formations, and they performed numerical simulations utilizing TOUGHREACT software for a commonly encountered Gulf Coast sediment under natural and $CO2$ injection conditions to analyze the impact of CO_2 immobilization through carbonate precipitation. They concluded from the simulations that the CO_2 mineral trapping capability after 10,000 years was comparable to CO_2 dissolution in pore waters. The addition of CO_2 mass as secondary carbonates to the solid matrix decreased porosity results in a significant decrease in permeability. The simulation was partially validated by field observations of the diagenesis of Gulf Coast sediments, and in particular, sandstones of the Frio formation of Texas.

Then, simulations using CMG's GEM module were carried out by Ozah et al. (2005) for 10,000 years to investigate the precipitation/dissolution reactions that have the potential for mineral

storage of CO2 and quantified the amount of CO_2 stored as minerals for a particular case. The simplification of mineral reactions was the same as discussed by Kumar *et al.* (2005). The results of both 2D and 3D simulations showed that in 10,000 years significant calcite precipitation took place simultaneously with anorthite dissolution. The pH of the brine in the aquifer decreased and the concentration of H^+ ions increased during this period. This caused anorthite to dissolve into brine and thus liberate Ca^{2+} ions over long periods of time even after the injection of CO_2 was stopped.

In 2004b and 2007, Xu *et al.* developed 1D and 2D numerical simulations for the injection of CO_2, H_2S and SO_2 mixtures in a sandstone-shale sequence using hydrogeologic properties and mineral compositions commonly encountered in Gulf Coast sediments. Simulations were performed with the reactive fluid flow and geochemical transport code TOUGHREACT to analyze mineral alteration, acid-gas immobilization through precipitation, and changes in porosity. Results indicated that for short time periods (10,000 years in present simulations) shale plays a limited role in mineral alteration and sequestration of gases within a sandstone horizon. The co-injection of SO_2 results in a different pH distribution, mineral alteration patterns, and CO_2 mineral sequestration than the co-injection of H_2S or injection of CO_2 alone.

Geochemical reaction modeling was performed by Kharaka *et al.* (2006) to evaluate gas-water-rock interactions in sedimentary basins of Frio formation during CO_2 sequestration. The results of geochemical modeling, using modified SOLMINEQ, indicated that buffering by dissolution of calcite and Fe oxyhydroxides limited the drop of brine pH. Then, a kinetic model of Fe release from the solid to aqueous phase was developed for the Frio-I Brine Pilot (Xu *et al.*, 2010), which could reproduce the observed increases in aqueous Fe concentration. The trend of Fe concentrations decreasing in brine samples due to carbonate precipitation could be captured by our modeling. Long-term simulations showed that all injected CO_2 could ultimately be sequestered as carbonate minerals for Frio-I Brine Pilot.

Finally, we investigated the study of geochemical reaction in the other parts of the word including Italy, France, Japan and Brazil. Cipolli *et al.* (2004) investigated the feasibility of CO_2 sequestration through injection into deep aquifers hosted by the ultramafic-serpentinitic rocks of the Gruppo di Voltri (Genova, Italy). A total of 25 samples were collected from the 15 springs of high pH identified in the Gruppo di Voltri area and chemical characteristics of waters interacting with ultramafic rocks and serpentinite were surveyed. The irreversible mass exchange that presumably takes place during high-pressure CO_2 injection into a deep aquifer hosted in serpentinitic rocks was modeled by means of the software package EQ3/6. The results indicated that serpentinitic rocks and ultramafites had a high CO_2 sequestration capacity, mainly through mineral fixation as magnesite and subordinately through solubility trapping.

Prior to the CO_2 greenhouse gas injection in the south-west of Nagaoka City, Niigata Prefecture, Japan, Zwingmann *et al.* (2005) conducted geochemical reaction modeling of CO_2 injection using the geochemical modeling code EQ3/6. The injection formation is the sedimentary marine Haizume Formation (Pleistocene) in the Uonuma Group, which is covered by a mudstone seal. The formation is mainly composed of quartz, plagioclase, feldspar, pyroxene, and clays (smectite, chlorite). The sandstone shows minor consolidation and grain size is medium to coarse sand. The modeling results showed a high reactivity of the minerals in the CO_2 rich environment

and high mineral conversion rate within the formation. At the final state, approximately 23 mol of CO_2 were taken into 1 kg of formation water and more than 90% of this was stored within carbonate minerals. In the simulation, some uncertainty was associated with the time scale and a more detailed investigation was planned and addressed accurate evaluation.

Andre' *et al.* (2007) conducted numerical simulation of fluid-rock chemical interactions at the supercritical CO_2-liquid interface during CO_2 injection into a carbonate reservoir of the Dogger aquifer (Paris Basin, France). Modified TOUGHREACT software and SCALE2000 software were employed for reactive transport simulation and batch geochemical modeling. They presented the numerical results of two CO_2 injection scenarios, first with CO_2-saturated water and second with pure supercritical CO_2. The simulation results confirmed that the high reactivity of CO_2-saturated water, which can dramatically damage the reservoir structure, and supercritical CO_2 injection appeared to be weakly reactive with a limited modification of well injectivity.

Thibeau *et al.* (2009) carried out the geochemical assessment of injection of CO_2 into the Rousse depleted gas reservoir of the Lacq-CO_2 pilot, the first French pilot. The geochemical modeling was performed in three steps: (1) combination of x-ray diffraction and fluorescence data in order to establish the initial mineralogy; (2) construction of a batch thermodynamic model to evaluate the effect of CO_2 injection by means of CHESS software; (3) using CMG's GEM to develop a 3D coupled reservoir and geochemical model to investigate the variation of reactive processes in space and time.

Experimental and numerical modeling studies performed (Ketzer *et al.* 2009) in sandstones of the saline aquifer of the Rio Bonito Formation, Parana Basin are presented. The geochemical reaction modeling software (PHREEQC Version 2.8) is employed for geochemical interaction modeling of the water-rock-CO_2 system through equilibrium and kinetic batch modeling. The simulation results showed that the studied sandstones of the Rio Bonito Formation consist of good reservoirs for CO_2 storage because of its stable mineralogy (quartzarenites and subarkoses) and mineral integrity of the reservoirs.

Table 4.2. Summary of geochemical reaction software for worldwide CO_2 sequestration sites.

Location	Software	Reference
Sleipner, North Sea	NUFT,SUPCRT92	Johnson *et al.* (2001)
Sleipner, North Sea	PHREEQC V2.6	Gaus *et al.* (2003, 2005)
Sleipner, North Sea	TOUGHREACT	Audigane *et al.* (2006)
Sleipner, North Sea	TOUGHREACT	Audigane, *et al.* (2007)
Sleipner, North Sea	Chess module	Lagneau, *et al.* (2005)
Sleipner, North Sea	PHREEQC	Wigand, *et al.* (2008)
Alberta Basin, Canada	PATHARC	Gunter, *et al.* (2000)
Alberta Basin, Canada	TOUGHREACT	Xu *et al.* (2004a)
Weyburn oilfield, Canada	Solmineq 88	Emberley *et al.* (2005)
Weyburn oilfield, Canada	PHREEQC	Cantucci *et al.* (2009)
Weyburn oilfield, Canada	Geochemists Workbench	Raistrick *et al.* (2009)
West Texas, US	TOUGH2	Wellman *et al.* (2003)
Colorado Plateau, US	ChemTOUGH	White, *et al.* (2005)

Rose Run Sandstone, Ohio	Geochemist's Workbench	Zerai *et al.* (2006)
Rose Run, Copper Ridge	STOMP, ECKEChem	Bacona *et al.* (2009)
Williston Basin	PHREEQC, SUPRCRT92	Sorensen *et al.* (2009)
Illinois Basin	PHREEQC, TOUGHREACT	Berger *et al.* (2009)
US Gulf Coast	TOUGHREACT	Xu *et al.* (2003, 2006b, 2007, 2010)
US Gulf Coast	GEM module of CMG	Ozah *et al.* (2005)
US Gulf Coast	SOLMINEQ	Kharaka, *et al.* (2006)
Niigata Basin,Japan	Software package EQ3/6;	Zwingmann *et al.* (2005)
Southern Brazil	PHREEQC	Ketzer, *et al.* (2009)
Genova, Italy	EQ3/6 Package	Cipoli *et al.* (2004)
Northern Italy	TOUGHREACT	Gherardi *et al.* (2007)
Paris Basin, France	TOUGHREACT	Andre *et al.* (2007)
Paris Basin, France	Crunch Code	Credoz *et al.* (2009)
Lacq CO2 pilot, French	Chess, GEM	Thibeau *et al.* (2009)

Below is a comparison of the geochemical reaction software used in out literature survey.

Table 4.3. Comparisons of geochemical reaction modeling software.

Software	Batch Modeling	Chemical Equilibrium	Fluid Flow
TOUGHREACT	Fully-coupled	Fully-coupled	Fully-coupled
GEM Module	Limited	Fully-coupled	Fully-coupled
PHREEQC	Fully-coupled	Fully-coupled	-----
EQ3/6 Package	-----	Fully-coupled	-----
Geochemist Workbench	Fully-coupled	Fully-coupled	-----
SUPRCRT92	-----	Fully-coupled	-----
Chess software	Fully-coupled	Fully-coupled	-----

According to Table 4.3, kinetic modeling and reactive transport flow are fully coupled in TOUGHREACT code; other software has limited capability in coupling reaction kinetics and equilibrium with fluid flow and transport. We will use TOUGHREACT to perform reactive transport modeling and we will categorize the formation rock and brine compositions into representative groups and develop a kinetic model for mineral dissolution and precipitation.

Availability of rock-forming chemical components for CO_2 sequestration

Mineral trapping of carbon dioxide in deep aquifers depends on the quantity and reactivity of metal oxide components that can react with carbon dioxide to form solid carbonates with low solubility. Xu *et al.* (2001) surveyed the oxide components and their abundance in the earth's crust. Only a limited number of rock forming metal oxides have the capability of trapping carbon dioxide via geochemical reactions. In the order of availability, these oxides are FeO, CaO, MgO, MnO, SrO and BaO. Theses minerals come from common igneous and metamorphic rocks in combination with silica and sometimes with alumina at high temperatures. At a specific

environment, these primary rock forming minerals decompose at various rates, and react with carbon dioxide to form secondary solid carbonates.

The properties of rock and the rock forming minerals determine the abundance and availability of sequestering oxide components. Xu *et al.* (2001) summarized and divided those minerals into classes with similar crystal structures in Table 4.4.

Table 4.4. Category of rock forming minerals with similar crystal structures.

Framework Silicates	Ortho and Ring Silicates	Chain Silicates	Sheet silicates
Plagioclase	Olivine Group	Pyroxene group	Mica Group
Barium feldspars	Garnet group	Amphibole group	Septechlorite group
Sodalite	Epidote group	Wollastonite	Chlorite group
Cancrinite	Melilite group	Pectolite	Clay Minerals
Scapolite	Calcium	Rhodonite	Talc
Zeolite Group	Borosilicates	Pyrox-manganite	Stilpnomelate
	Metamorphic minerals		Serpentine
			Apophyllite
			Prehnite

The abundance of a given mineral or mineral group depends both on the bulk composition of the rock and the nature of its formation. Xu *et al.* (2001) summarized the major mineral series within each group and calculated the maximum quantity of carbon dioxide that could be sequestered by each mineral, which is shown in Table 4.5. The potential values were calculated by assuming complete alteration of the primary minerals. The majority of the minerals mentioned in Table 4.5 are solid solutions whose compositions vary depending on the bulk composition and prior history of the host rock. Some of the mineral groups are represented only by typical examples rather than being comprehensive, such as the zeolites, which contain many different structures. The minerals containing an essential component with low crustal abundance and minor non-essential substitutive components in solid solutions were omitted in the survey.

Table 4.5. Carbon dioxide sequestration potential of major rock forming minerals.

Mineral Name	Mineral Formula	Potential CO_2 Fixed (kg/m3 mineral)
Plagioclase (anorthite)	$Ca[Al_2Si_2O_8]$	436.4
Ba-Feldspar-Celsian	$Ba[Al_2Si_2O_8]$	398.2
Sodalite Group Hauyne Cancrinite Scapolite(meionite)	$Ca_4[Al_6Si_6O_{24}](SO_4)$ $Ca_{1.5}[Al_6Si_6O_{24}](CO_3)_{1-5} \cdot 1.5H2O$ $Ca_4[Al_6Si_6O_{24}](CO_3)$	383.8 132.5 387.3
Zeolites Group Heulandite Laumontite Scolecite Chabazite Thomsonite	$Ca_4Na[Al_9Si_{27}O_{72}] \cdot 24H_2O$ $Ca[Al_2Si_4O_{12}] \cdot 6H_2O$ $Ca[Al_2Si_3O_{10}] \cdot 3H_2O$ $(Ca,Na_2)[Al_2Si_4O_{12}] \cdot 6H_2O$ $NaCa_2[Al_5Si_5O_{20}] \cdot 6H_2O$	138.4 208.1 254.9 176.5 258.7
Olivine (forsterite-fayalite)	$Mg_2SiO_4-Fe_2SiO_4$	2014.7-1896.3
Garnet Group Almandine Andradite Grossular	$Fe(II)_3Al_2Si_3O_{12}$ Ca3Fe(III)2Si3O12 Ca3Al2Si3O12	1144.7 1002.3 1053.1

Pyrope	$Mg_3Al_2Si_3O_{12}$	1164.9
Hydrogrossular	$Ca_3Al_2Si_2O_8(OH)_4$	974.8
Epidote Group		
Epidote	$Ca_2Fe(III)Al_2O\cdot OH[Si_2O_7][SiO_4]$	628.8
Melilite Group		
Gehlenite	$Ca_2[Al_2SiO_7]$	972.4
Akermanite	$Mg_2[AlSi_2O_7]$	1423.0
Ca Borosilicates-Datolite	$CaB[SiO_4](OH)$	825.6
Staurolite	$(Fe(II),Mg)_2(Al,Fe(III))_9O_6[SiO_4]_2(O,OH)_4$	394.7
Vesuvianite	$Ca_{10}(Fe(II),Mg)_2(Al,Fe(III))Al_3O_2[SiO_4]_2(OH)_4$	1167.0
Chloritoid	$(Mg,Fe)_2Al_4[Si_2O_7][SiO_4]_8(OH)_4$	629.8
Lawsonite	$CaAl_2(OH)_2[Si_2O_7]H_2O$	422.7
Pumpellyite	$Ca_4(Mg,Fe(II))(Al,Fe(III))_5(OH)_3[Si_2O_7]_2[SiO_4]_2\cdot 2H_2O$	735.6
Cordierite	$Al_3(Mg,Fe(II))_2[Si_5O_{18}]$	749.4
Pyroxene group		
Enstatite	$(Mg,Fe)_2Si_2O_6$	1404.2
Diopside	$CaMgSi_2O_6$	1334.3
Hedenbergite	$Ca(Mg,Fe(II))Si_2O_6$	1290.3
Augite	$(Ca,Mg,Fe(II),Al)_2(Si,Al)_2O_6$	1306.3
Pigeonite	$(Mg,Fe(II),Ca)(Mg,Fe(II)),Fe(III),Al)Si_2O_6$	1345.4
Amphibole Group		
Anthophyllite Cummingtonite	$(Mg,Fe(II),Fe(III))_{5-7}Al_{0-2}[Si_{6-8}Al_{2-0}O_{22}](OH)_2$	1169.5-1041.8
Common Hornblende	$Ca_2Na_{0-1}(Mg,Fe(II))_{3-5}(Al,Fe(III))_{2-0}[Si_{6-8}Al_{2-0}O_{22}](O,OH)_2$	1000.4
Calcium Amphiboles-tremolite	$Ca_2Na_{0-1}(Mg,Fe(II))_{3-5}(Al,Fe(III))_{2-0}[Si_{6-8}Al_{2-0}O_{22}](O,OH)_2$	1119.3
Alkali Amphiboles-glaucophane	$Na_{2-3}Ca_{0-1}(Mg,Fe(II))_{5-3}(Al,Fe(III))_{0-2}Si_{7-8}Al_{1-0}O_{22}](O,OH)_2$	496.3
Wollastonite	$CaSiO_3$	1097.1
Pectolite	$Ca_2NaH[SiO_3]_3$	761.1
Mica group		
Glauconite	$(K,Na,Ca)_{1.2-2.0}(Fe(III),Al,Fe(II),Mg)_{4.0}[Si_{7-7.6}Al_{1-0.4}O_{20}](OH)_4\cdot nH_2O$	61.97
Phlogopite	$K_2(Mg,Fe(II))_6[Si_6Al_2O_{20}](OH)_4$	881.8
Biotite	$K_2(Mg,Fe(II))_{6-4}(Fe(III),Al)_{0-2}[SiAl_{2-3}O_{20}](OH)_{4-2}$	671.0
Margarite	$Ca_2Al_4[Si_4Al_4O_{20}](OH)_4$	328.6
Septechlorite Group		
Serpentine	$Mg_6Si_4O_{10}(OH)_8$	1232.7
Greenalite	$Fe(II)_6Si_4O_{10}(OH)_8$	1140.1
Chlorite Group	$(Mg,Al,Fe(II))_{12}[(Si,Al)_8O_{20}](OH)_{16}$	923.4
Clay Minerals		
Illite	$K_{1-1.5}(Fe(III),Al,Fe(II),Mg)_{4.0}[Si_{7-6.5}Al_{1-1.5}O_{20}](OH)_4$	78.42
Smectite	$(1/2Ca,Na)_{0.7}(Al,Mg,Fe)_4(Si,Al)_8O_{20}(OH)_4\cdot nH_2O$	161.2
Talc	$Mg_6[Si_8O_{20}](OH)_4$	1061.2
Stilpnomelane	$(K,Na,Ca)_{0-1.4}(Fe(III),Fe(II),Mg,Al,Mn)_{5.9-8.2}[Si_8O_{20}](OH)_4(O,OH,H_2O)_{3.6-8.5}$	266.5
Prehnite	$Ca_2Al[AlSi_3O_{10}](OH)_2$	626.9

Formation Categories for CO_2 Sequestration and Relative Kinetic Parameters

The mineral alteration caused by geochemical reactions between carbon dioxide and rock forming minerals is very slow under aquifer conditions and is typically not amenable to experimental study. Numerical modeling is necessary to investigate the geochemical effects of long-term CO_2 storage in deep aquifers. The chemical composition of geologic formations varies greatly from one sequestration site to another. Thus, we surveyed the mineral composition and equilibrium data for different sequestration sites with 4 different formation types.

Sandstone Formations: Geochemical reaction modeling between carbon dioxide and sandstone formation has been carried out for sandstone aquifer from the Alberta Sedimentary Basin, US Gulf Coast sediments and Frio-I Brine Pilot in US Gulf Coast (Xu *et al.*, 2004a, 2010), Rose-Run sandstone reservoir in Ohio (Zerai *et al.*, 2006), sandstone bed of Pleistocene Haizume Formation at Minami-Nagaoka gas field of Japan (Mito *et al.*, 2008), Bunter Sandstone

Formation from Europe (Wigand *et al.*, 2008), sandstone reservoirs of the Rio Bonito Formation (Permian) at Paraná Basin of southern Brazil (Ketzer *et al.*, 2009).

Xu *et al.* (2004a) carried out a batch-type geochemical reaction modeling between CO_2 and glauconitic sandstone from the Alberta Sedimentary Basin as a potential host for CO_2 sequestration. The glauconitic sandstone is a medium- to fine-grained litharenite. The average mineral composition is 87% quartz, 2% K-feldspar, 1% plagioclase, 5% glauconite, 2% kaolinite, 1% calcite, 1% dolomite, and 1% siderite. The average porosity is 12%. In their study, the mineral composition was modified to more closely reflect that observed in the formation, and Fe (III) reduction in glauconite was incorporated in the model. They estimated a representative glauconite chemical composition and thermodynamic properties from descriptions of the mineralogical compositions of glauconite and its paragenesis. The oligoclase is also incorporated as a solid solution of plagioclase and the thermodynamic properties of oligoclase are calculated from calorimetric studies of plagioclase solid solutions. The initial mineral abundances used by them is given in Table 4.6 and the kinetic parameters used in the simulation are given later in Table 4.10.

Table 4.6. List of initial mineral volume fractions and potential secondary mineral for the glauconitic sandstone.

Mineral	Chemical composition	Volume (%)
Primary mineral		
quartz	SiO_2	71.28
K-feldspar	$KAlSi_3O_8$	1.76
kaolinite	$Al_2Si_2O_5(OH)_4$	1.76
calcite	$CaCO_3$	0.88
dolomite	$CaMg(CO_3)_2$	0.88
siderite	$FeCO_3$	0.88
illite	$K_{0.6}Mg_{0.25}Al_{1.8}(Al_{0.5}Si_{3.5}O_{10})(OH)_2$	2.64
glauconite	$K_{1.5}Mg_{0.5}Fe_{2.5}Fe_{0.5}AlSi_{7.5}O_{20}(OH)_2$	4.4
kerogen-O	$C_{52}H_{82}O_{40}$	2.64
oligoclase	$CaNa_4Al_6Si_{14}O_{40}$	0.88
porosity	-	12
total	-	100
Secondary Mineral		
albite-low	$NaAlSi_3O_8$	
Na-smectite	$Na_{0.290}Mg_{0.26}Al_{1.77}Si_{3.97}O_{10}(OH)_2$	
Ca-smectite	$Ca_{0.145}Mg_{0.26}Al_{1.77}Si_{3.97}O_{10}(OH)_2$	
goethite	$FeOOH$	
dawsonite	$NaAlCO_3(OH)_2$	

They also did a batch geochemical simulation study on Gulf Coast sediments. The mineralogy is similar to that commonly encountered in sedimentary basins. The principal reservoir-quality sandstones within Gulf Coast sediments are respectively, the Frio, the Vicksberg and the Wilcox formations, all of which are found within the Lower Tertiary. Of the three formations, the Frio was chosen as a representative candidate for the sequestration of supercritical CO_2. According to the study, the Frio shows the greatest variation in mineral composition ranging from poorly

sorted fine-grained feldspathic litharenites to lithic arkoses to fine-grained lithic arkoses and sub-arkoses. The approximate mean composition of the Frio in the Middle Texas region of the Gulf Coast was chosen in the study. The composition is representative of a quartzose lithic arkose with 56% quartz (by weight), 28% feldspar and 16% lithic fragments. The actual mineral composition of the sandstone is shown in Table 4.7 and the kinetic parameters used in the simulation are shown later in Table 4.10.

Table 4.7 List of initial mineral volume fractions and potential secondary mineral phases for Gulf Coast sediments.

Mineral	Chemical composition	Volume (%)
Primary mineral		
quartz	SiO_2	49.7466
kaolinite	$Al_2Si_2O_5(OH)_4$	1.8135
calcite	$CaCO_3$	1.7361
illite	$K_{0.6}Mg_{0.25}Al_{1.8}(Al_{0.5}Si_{3.5}O_{10})(OH)_2$	0.8586
kerogen-O	CH_2O	2.6136
oligoclase	$CaNa_4Al_6Si_{14}O_{40}$	17.8155
K-feldspar	$KAlSi_3O_8$	7.3611
Na-smectite	$Ca_{0.145}Mg_{0.26}Al_{1.77}Si_{3.97}O_{10}(OH)_2$	3.5073
clinochlore-14A	$Mg_5Al_2Si_3O_{10}(OH)_8$	2.6793
daphnite-14A	$Fe_5Al_2Si_3O_{10}(OH)_8$	1.4211
hematite	Fe_3O_3	0.4473
porosity	-	10
total	-	100
Secondary mineral		
albite-low	$NaAlSi_3O_8$	
dolomite	$CaMg_{0.3}Fe_{0.7}(CO_3)_2$	
siderite	$FeCO_3$	
Ca-smectite	$Na_{0.290}Mg_{0.26}Al_{1.77}Si_{3.97}O_{10}(OH)_2$	
pyrite	FeS_2	
ankerite	$CaMg(CO_3)_2$	
dawsonite	$NaAlCO_3(OH)_2$	

Xu *et al.* (2010) incorporated a simple kinetic model into the reactive transport modeling for geologic storage of CO_2 in saline aquifers, the Frio-I Brine Pilot. The Frio site is located on the flank of a salt dome within the South Liberty oil field, near Dayton, Texas, a region of the Gulf Coast where industrial sources of CO_2 are abundant. The Frio Formation is composed of several reworked fluvial sandstone and siltstone beds that are separated by transgressive marine shale. The Frio "C" zone is a subarkosic fine-grained, moderately sorted quartz and feldspar sandstone, with minor amounts of illite or smectite and calcite. The fluid at the "C" zone has a pressure of about 152 bar and a temperature of about 59 °C. The initial rock mineral composition used in the modeling is presented in Table 4.8, which may be broadly representative of US Gulf Coast sandstone formations.

Initial total dissolved component concentrations are in Table 4.9 and the kinetic parameters used in the simulation are shown later in Table 4.10. O_2 (aq) concentration is obtained by equilibrium with initial mineral composition. Iron is the sum of Fe^{2+} and Fe^{3+} and their related complexes

(mainly Fe^{2+}). Carbon is the sum of CO_2 (aq), CH_4 (aq), and their related species such as HCO_3^- and acetic acid (aq). Sulfur is the sum of sulfate and sulfide species.

Table 4.8. Primary and secondary rock mineral composition used in the modeling.

Mineral	Volume fraction (%)
Primary Minerals	
Quartz	49.75
Kaolinite	1.81
Calcite	1.74
Illite	0.86
Oligoclase	17.82
K-feldspar	7.36
Na-smectite	3.51
Chlorite	4.1
Hematite	0.45
Secondary Minerals	
Magnesite	
Dolomite	
Low-albite	
Siderite	
Ankerite	
Dawsonite	
Ca-smectite	
Pyrite	

Table 4.9 Initial total dissolved component concentrations derived from baseline fluid samples.

Parameter	Value	Elements	Concentration (mol/kg)
Temperature(°C)	59	Na^+	1.35
pH	6.7	K^+	4.53×10^{-3}
Permeability(m^2)	2.3×10^{-12}	Ca^{2+}	6.6×10^{-2}
		Mg^{2+}	2.2×10^{-2}
		Carbon	5.04×10^{-2}
		Cl^-	1.49
		Sulfur	4.20×10^{-5}
		SiO_2(aq)	2.50×10^{-4}
		Al^{3+}	1.56×10^{-8}
		Iron	4.63×10^{-4}
		O_2(aq)	4.88×10^{-68}

The kinetic rate constants used in the reactive transport modeling carried out by Xu *et al.* (2004b, 2010) are summarized in Table 4.10.

Table 4.10. Kinetic parameters for mineral dissolution and precipitation.

Mineral	A (cm2/g)	Parameters for kinetic rate law							
		Neutral mechanism		Acid mechanism			Base mechanism		
		K_{25} (mol/m^{2}s)	Ea(kJ/mol)	K_{25}	Ea	n(H$^+$)	K_{25}	Ea	n(H$^+$)
Quartz	9.8	1.023×10^{-14}	87.7	-	-	-	-	-	-
Kaolinite	151.6	6.918×10^{-14}	22.2	4.898×10^{-12}	65.9	0.777	8.913×10^{-18}	17.9	-0.472
Calcite	9.8	1.549×10^{-6}	23.5	5.012×10^{-1}	14.4	1	-	-	-
Illite	151.6	1.660×10^{-13}	35	1.047×10^{-11}	22.6	0.34	2.020×10^{-17}	58.9	-0.4
Oligoclase	9.8	1.445×10^{-12}	69.8	2.138×10^{-10}	65	0.457	-	-	-
K-feldspar	9.8	2.890×10^{-13}	38	8.710×10^{-11}	51.7	0.5	6.310×10^{-12}	94.1	-0.823
Na-smectite	151.6	1.660×10^{-13}	35	1.047×10^{-11}	22.6	0.34	2.020×10^{-17}	58.9	-0.4
Chlorite	9.8	2.020×10^{-13}	88	7.762×10^{-12}	88	0.5	-	-	-
Hematite	12.9	2.512×10^{-15}	66.2	4.074×10^{-10}	66.2	1	-	-	-
Magnesite	9.8	4.571×10^{-10}	22.5	4.169×10^{-7}	14.4	1	-	-	-
Dolomite	9.8	2.951×10^{-8}	52.2	6.457×10^{-4}	36.1	0.5	-	-	-
Low-albite	9.8	2.754×10^{-13}	69.8	6.918×10^{-11}	65	0.457	2.512×10^{-16}	71	-0.572
Siderite	9.8	1.260×10^{-9}	62.76	6.457×10^{-4}	36.1	0.5	-	-	-
Ankerite	9.8	1.260×10^{-9}	62.76	6.457×10^{-4}	36.1	0.5	-	-	-
Dawsonite	9.8	1.260×10^{-9}	62.76	6.457×10^{-4}	36.1	0.5	-	-	-
Ca-smectite	151.6	1.660×10^{-13}	35	1.047×10^{-11}	22.6	0.34	2.020×10^{-17}	58.9	-0.4
Glauconite	151.6	1.660×10^{-13}	35	1.047×10^{-11}	22.6	0.34	2.020×10^{-17}	58.9	-0.4
Kerogen-O	151.6	6.918×10^{-14}	22.2	4.898×10^{-12}	65.9	0.777	8.913×10^{-18}	17.9	-0.472
Forsterite	151.6	6.918×10^{-14}	22.2	4.898×10^{-12}	65.9	0.777	8.913×10^{-18}	17.9	-0.472
Fayalite	151.6	6.918×10^{-14}	22.2	4.898×10^{-12}	65.9	0.777	8.913×10^{-18}	17.9	-0.472
Goethite	151.6	1.660×10^{-13}	35	1.047×10^{-11}	22.6	0.34	2.020×10^{-17}	58.9	-0.4
Clinochlore-14A	151.6	1.660×10^{-13}	35	1.047×10^{-11}	22.6	0.34	2.020×10^{-17}	58.9	-0.4
Daphnite-14A	151.6	1.660×10^{-13}	35	1.047×10^{-11}	22.6	0.34	2.020×10^{-17}	58.9	-0.4
Pyrite	12.9	$K_{25}=2.818\times10^{-5}$ Ea=56.9 n(O2(aq))=0.5		$K_{25}=2.02\times10^{-5}$ Ea=56.9 n(H$^+$)=0.5, n(Fe^{3+})=0.5					

Zerai *et al.* (2006) conducted the kinetic modeling of the Rose Run Sandstone using The Geochemist's Workbench. The Cambrian Rose Run Sandstone is a deep saline aquifer and oil-gas producing unit that extends beneath eastern Ohio, Pennsylvania, New York, and Kentucky in the Appalachian Basin of Eastern United States. It is also the only one of the Cambrian sandstones that is known to retain its sandstone composition in the eastern part of the state rather than passing laterally into carbonate, and it lies at depths suitable for injection of supercritical CO_2 and sealed by impermeable cap rock of the Trenton Limestone and Cincinnati Shale. The Rose Run Sandstone consists of alternating layers of sandstone and carbonate. The sandstone commonly has dolomite cement and glauconite. The total thickness of these capping formations ranges from 100 to 500 m. Like many deep aquifers of the eastern United States and Canada the Rose Run Sandstone consists of locally glauconitic, feldspathic quartz sandstone interbedded with dolostone and is heterogeneous at multiple scales. The typical range of porosity and permeability of the silicate rock assemblage in the Rose Run Sandstone are 7-15% and 1-15 md,

respectively. The mineral composition of Rose Run Sandstone, initial concentration of aqueous species in formation water and kinetic parameters is given in Tables 4.11-4.13.

Table 4.11. The mineral assemblages of the Rose Run Formation.

Carbonate	Mass fraction (%)	Sandstone	Mass fraction (%)	Mixed	Mass fraction (%)
Primary mineral					
Dolomite	60	Quartz	83	Quartz	70
Calcite	39	K-feldspar	10	Dolomite	13.8
Siderite	1	Kaolinite	3	Calcite	8
		Albite	2	K-feldspar	5
		Annite	1	Annite	1
		Siderite	1	Albite	1
				Kaolinite	1
				Siderite	0.2
Secondary mineral					
Dawsonite					
Muscovite					
Strontianite					

Table 4.12. Rate constants for the minerals used in the reactive transport simulations.

Mineral	Rate constants logK (25°C)(mol/m^2 s)	Ea (kJ/mol)	Surface area(cm^2/g)
Albite	-11	68	10
Annite	-10.5	45	10
Calcite	-5.8	63	10
Dawsonite	-8.4	64	10
Dolomite	-6.7	55	10
Kaolinite	-11.4	64	10
K-feldspar	-10.9	58	10
Muscovite	-11.7	64	10
Siderite	-6.7	62.8	10
Strontianite	-7.35	41.9	10
Quartz	-12	87.5	10

Table 4.13. Initial Brine composition of Rose Run Sandstone.

Parameter	Value	Elements	Concentration (mg/kg)
Temperature(°C)	54	Na^+	60122
pH	6.4	K^+	3354
		Ca^{2+}	37600
		Mg^{2+}	5880.6
		HCO_3^-	122
		Cl^-	191203
		SO_4^{2-}	326.4
		$SiO_2(aq)$	3
		Al^{3+}	2.16
		Fe^{2+}	140
		Sr^{2+}	455.52

72

Ketzer *et al.* (2009) studied the mineralogical integrity of sandstone reservoirs of the Rio Bonito Formation, Paraná Basin, and southern Brazil. The Rio Bonito Formation consists of paralic fine- to coarse-grained sandstones, and mudstones and coal, deposited during the early Permian in Paraná Basin. The sandstones of the Rio Bonito Formation are subarkose to quartzarenites in composition. The main detrital constituents are monocrystalline quartz grains (average 52 vol. %), and K-feldspars (average 4.5 vol. %). Other detrital constituents that average <1 vol. % each include plagioclase grains, volcanic rock fragments, sedimentary rock fragments, metamorphic rock fragments (quartzite, schist and gneiss), biotite, muscovite, heavy minerals (tourmaline, epidote, zircon and garnet), opaque minerals, and glaucony. Three representative samples of the aquifers of the Rio Bonito formation were selected from cores available near the Candiota coal mining area for equilibrium modeling and kinetic modeling of batch reaction. Table 4.14 and Table 4.15 show the main mineralogical composition and porosity of the samples selected for the geochemical reaction modeling and kinetic parameters used in calculations and simulation.

Table 4.14. Mineral compositions of the three samples from sandstone reservoirs of the Rio Bonito Formation.

Sample 1	Volume (%)	Sample 2	Volume (%)	Sample 3	Volume (%)
Quartz	67.66	Quartz	66.66	Quartz	67
Kaolinite	6.66	Calcite	13.66	Kaolinite	6.66
Calcite	4.66	K-feldspars	5	Dolomite	5.33
K-feldspars	4	Pyrite	1.33	K-feldspars	4.66
Albite	1.33	Plagioclase	0.33	Albite	1.33
other	0.66	other	1.33	Pyrite	0.33
Porosity	15	Porosity	11.66	Porosity	14.66

Table 4.15. The kinetic parameters used in the modeling.

Mineral	logk (25°C)	logk (200°C)	Ea(kJ/mol)	n	Surface area(m^2/g)
Quartz	-13.4	-7.51	90.9	0	0.01133
K-feldspar	-10.06	-6.71	51.7	0.5	0.01173
Kaolinite	-12.71	-9.6	48	0.22	0.01156
Calcite	-0.3	0.63	14.4	1	0.01107
Dolomite	-3.19	-0.85	36.1	0.5	0.01056
Albite	-10.16	-5.95	65	0.457	0.01145
Anorthite	-3.5	-2.42	16.6	1.411	0.01099
Pyrite	-7.52	-3.83	56.9	-0.500(O2(aq))	0.00599

Clay Formation: Gaus *et al.* (2005) and Audigane *et al.* (2006, 2007) performed reactive transport modeling of dissolved CO_2 in the cap rock at Sleipner. The Sleipner area is located in the Norwegian part of the North Sea. CO_2 is injected into the Mio-Pliocene Utsira Sand, a highly elongated sand reservoir with an area of some 26100 km^2 and a depth between 700 and 1000 m. The Utsira Sand is overlain by the sediments of the Nordland Group, which are mainly shales and have a thickness of approximately 250 m. These sediments are presumed to provide a seal

for the Utsira Sands and to inhibit vertical CO_2 migration, with capillary leakage of CO_2 unlikely to occur.

The lower part of the Nordland Shale extends well beyond the area currently occupied by the CO_2 injected at Sleipner. Cutting samples are comprised dominantly by grey clay silts or silty clays. Most are massive although some show a weak sedimentary fabric. XRD analysis typically reveals quartz, undifferentiated mica, kaolinite, K-feldspar, calcite, smectite, albite, chlorite, pyrite and gypsum together with traces of drilling mud contamination. The clay particle-size fraction is generally dominated by illite with minor kaolinite and traces of chlorite and smectite. The mineralogy of the Nordland shale cap rock used for the modeling is based on the composition of a selection of cutting samples in Table 4.16. The composition of the formation water in the cap rock is in Table 4.17, the molar volumes, specific surface areas and kinetic rate parameters used in the three simulation cases by Gaus *et al.* (2005) is in Table 4.18.

Table 4.16. Mineralogical composition of the Nordland Shale and the amounts introduced in the model.

Original composition	Mass percent	Minerals in simulation
Plagioclase	12.3	Albite Anorthite Oligoclase
Calcite	1	Calcite
Quartz	21.5	Chalcedony
Chlorite	4.1	Clinochlore-7A
Mica/Illite	24.7	Illite
Kaolinite	18	Kaolinite
K-feldspar	2.1	K-feldspar
Pyrite	2.8	Pyrite
Siderite	1.6	Siderite
Smectite	8.8	Smectite
Mixed layer clay	1.4	Not used
Total	98.3	

Table 4.17. Initial composition of the formation water in the cap rock.

Parameter	Value	Elements	Concentration (M)
Temperature($^{\circ}$C)	37	Al	3.51×10^{-8}
Ionic strength	0.647	Ba	1.25×10^{-5}
pH	7.67	C	6.92×10^{-5}
pe	-4.07	Ca	1.77×10^{-1}
		Cl	4.79×10^{-1}
		Fe	2.48×10^{-7}
		K	1.42×10^{-4}
		Mg	1.11×10^{-2}
		Na	1.06×10^{-1}
		S	4.81×10^{-4}
		Si	2.52×10^{-4}

Table 4.18. Molar volumes, specific surface areas and kinetic rate parameters at 37 °C of the minerals.

Mineral	Mass percent	Amount present (mol per REV)	Molar volume (10^{-6} m^3/mol)	Specific surface area (m^2/g)	Rate constant (log k$_{37}$) (mol/m^2 s)
Primary mineral					
Albite	12.4[a]/6.2[b]	25.6[a]/12.8[b]	100.25	0.0695	-8.44
Anorthite	0[a]/6.2[b]	0[a]/12.8[a]	100.75	0.0659	-4.93
Oligoclase	12.4[c]	25.6c	100.35	0.0695	-7.94
Calcite	1	5.6	36.93	0.0671	-6.35
Quartz	21.5	196	22.69	0.0686	-11.73
Clinochlore-7A	4.1	4	20.98	0.113	-11.63
Illite	24.7	35.21	59.89	0.468	-13.08
Kaolinite	18	38.15	99.52	1.16	-12.54
K-feldspar	2.1	4.08	108.87	0.0711	-8.79
Pyrite	2.8	12.9	23.94	0.0363	-3.72
Siderite	1.6	8.6	29.37	0.0461	-7.38
Smectite-Chigh-Fe-Mg	8.8	11.93	140.71	1.04	-13.25
Secondary mineral					
Dawsonite	0	0	59.3	0.0849	-6.86
Dolomite-dis	0	0	64.39	0.0635	-7.38
Magnesite	0	0	28.02	0.0604	-7.38

a Plagioclase composition for Case 1
b Plagioclase composition for Case 2
c Plagioclase composition for Case 3

Carbonate Formation: André *et al.* (2007) investigated the reservoir behavior subjected to hydraulic and chemical perturbations by CO_2 injection in the Dogger aquifer. The mineralogical characteristics of Dogger oolitic limestone present some analogies with Lavoux limestone encountered in many quarries of Paris Basin. Oolitic and bioclastic limestone constitute the most permeable part of the Dogger aquifer, which dates from the Jurassic (Bajocian and Bathonian). The mean porosity is 0.12 and the permeability is assumed to be spatially homogeneous at 10^{-13} m^2. Initial temperature and pressure are 75 °C and 180 bars, respectively. Geochemical reaction modeling is carried out for a carbonate reservoir represented by a cylindrical geometry centered on a vertical injection well with two injection scenarios (CO_2 saturated water and pure supercritical CO_2 injection). The mineral composition of Dogger reservoir, initial concentration of aqueous species in formation water and kinetic parameters is given in Tables 4.19-4.21.

Table 4.19. Dogger aquifer mineralogy and list of potential secondary minerals present in the reservoir.

Mineral composition	Volume fraction (%)
Primary Mineral	
Calcite	70
Disordered dolomite	10
Siderite	5

Illite	5
Albite	5
K-Feldspar	5
Secondary Mineral	
Kaolinite	
Chalcedony	
Magnesite	
Dawsonite	
Anhydrite	
Halite	

Table 4.20. Chemical composition of water from the Dogger aquifer in the region of Fontainebleau.

Parameter	Value	Elements	Concentration (ppm)
Temperature(°C)	75	Na	1794
pH	6.7	K	35.2
Alkalinity	427	Ca	148
		Mg	55.9
		Al	0.002
		Fe	1
		Cl	2485
		SO_4	633.6
		SiO_2	41.4
		HS	11.9

Table 4.21. Kinetic parameters for mineral dissolution and precipitation.

Mineral	Acid mechanism			Neutral mechanism		Carbonation mechanism		
	Logk	Ea	n	Logk	Ea	Logk	Ea	m
Calcite	-0.3	14.4	1	-5.81	23.5	-3.48	35.4	1
Dawsonite	-	-	-	-7	62.8	-	-	-
Dolomite	-3.19	36.1	0.5	-7.53	52.2	-5.11	34.8	0.5
Magnesite	-6.38	14.4	1	-9.34	23.5	-5.22	562.8	1
Siderite	-3.19	36.1	0.5	-7.53	52.2	-5.11	34.8	0.5
						Alkaline mechanism		
						Logk	Ea	n
Illite	-10.98	23.6	0.34	-12.78	35	-16.52	58.9	-0.4
K-Feldspar	-10.06	51.7	0.5	-12.4	38	-21.2	94.1	-0.823
Albite	-10.16	65	0.457	-12.56	69.8	-15.6	71	-0.572
Kaolinite	-11.31	65.9	0.777	-13.18	22.2	-17.05	17.9	-0.472
Chalcedony	-	-	-	-13.99	87.7	-	-	-
Anhydrite	-	-	-	-3.19	14.3	-	-	-
Halite	-	-	-	-0.21	7.4	-	-	-

Cantucci *et al.* (2009) proposed a geochemical model for the hosting aquifers of the Weyburn Oil Field (Canada), where anthropogenic CO_2 is injected since 2000, to reconstruct reservoir chemical composition of the two reservoirs (Marly and Vuggy) where CO_2 is stored by using the existing geochemical data and assess the (kinetic) evolution of the system during the CO_2 injection. The Weyburn Oil Field is located in the Prairie Province of Saskatchewan (Western

Canada) in the Midale Beds of the Mississippian Charles Formation. The latter is at the depth of 1300-1500 m and is divided in the Frobisher Evaporite and the Midale Carbonate. Shallow marine carbonate-evaporitic rocks form the Midale Carbonate where two aquifers, the dolomitic "Marly" and the underlying calcitic "Vuggy", sealed by an anhydrite cap-rock, are hosted. Pressure and temperature of the reservoirs are 15 MPa and 62 °C, respectively.

The mineralogical composition of the Marly and Vuggy reservoirs used in the geochemical simulation is calculated according to that obtained from 18 core boxes collected from 4 wells located into the injection area. The Marly reservoir (from 1 to 11m thick) is a chalky, microcrystalline dolomite layer with dominantly intercrystalline porosity (26%). The Vuggy reservoir (10 to 22m thick) mainly consists of grainstone and packestone with moldic, intergranular and intercrystalline porosity (14%). The mineralogical compositions of these two reservoirs are given in Table 4.22 and the kinetic parameters used in the geochemical reaction modeling are given in Table 4.23.

Table 4.22. Mineralogical composition of the Marly and Vuggy reservoirs.

Marly reservoir	Volume fraction	Vuggy reservoir	Volume fraction
Dolomite	0.8	Calcite	0.935
Calcite	0.145	Dolomite	0.03
Gypsum	0.03	Anhydrite	0.02
K-Feldspar	0.005	Authigenic silica	0.005
Authigenic silica	0.005	Pyrite	0.005
Pyrite	0.005	K-feldspar	0.005
Clay	0.0025	Porosity	0.14
Porosity	0.26		

Table 4.23. Kinetic parameters for mineral dissolution and precipitation.

Mineral	Acid mechanism			Neutral mechanism		Base mechanism			Specific surface area	
	$Logk_{25}$	Ea	n	Logk25	Ea	Logk25	Ea	n	Marly	Vuggy
Primary mineral										
K-Feldspar	-12.5	-	0.5	-15.3	-	-14.2	94.1	0.823	0.175	0.175
Calcite	-0.3	14.4	1	-5.81	23.5	-3.48a	35.4a	1.000[a]	0.034	0.015
Dolomite	-3.19	36.1	0.5	-7.53	52.2	-5.11a	34.8a	0.500[a]	0.105	0.014
Kaolinite	-11.31	65.9	0.777	-13.18	22.2	-17.05	17.9	0.472	2.317	0.015
Chalcedony	-	-	-	-12.23	74.5	-	-	-	0.038	0.015
Pyrite	-7.52	56.9	-0.50[b]	-4.55	56.9	-	-	0.50[c]	0.012	0.008
Secondary mineral										
Gypsum	-	-	-	-2.79	14.3	-	-	-	0.003	0.003
Anhydrite	-	-	-	-3.19	14.3	-	-	-	0.1	0.1
Dawsonite	-	-	-	-7	62.8	-	-	-	0.14	0.14
Magnesite	-6.38	14.4	1	-9.34	23.5	-5.22	62.8	1.000[a]	0.1	0.1
Muscovite	-11.85	22	0.37	-13.55	22	-14.55	22	0.22	0.106	0.106
Albite	-9.87	65	0.457	-12.04	69.8	-16.98	71	0.572	0.115	0.115
Chlorite	-11.11	88	0.5	-12.52	88	-	-	-	0.113	0.113

a Reaction order with respect to $p(CO_2)$.
b Reaction order with respect to H^+ and Fe^{3+}.
c Reaction order with respect to O_2.

Dunite Formation: Xu *et al.* (2004a) also conducted the geochemical reaction simulation for dunite subjected to CO_2 injection. The dunite rock is a monomineralic rock consisting essentially of olivine. This rock is a mantle residue after depletion of basaltic magma, and occurs rarely at the earth's surface. However, it has a very large CO_2 sequestration capacity we can observe from Table 4.5, and was chosen to be illustrative of the extreme limits possible for CO_2 sequestration by mineral trapping. Olivine is a binary solid solution of the pure end-member minerals, forsterite (Mg_2SiO_4) and fayalite (Fe_2SiO_4). The volume ratio of these end member components in typical olivine is about 9:1. The initial mineral abundances used in the simulations are presented in Table 4.24. The porosity of dunite is commonly small, and an initial porosity of 0.05 was assumed. The possible secondary mineral phases under CO_2 injection are also listed in Table 4.24 and the kinetic parameters used in the simulation are given in Table 4.10.

Table 4.24. List of initial mineral volume fractions and possible secondary mineral phases.

Mineral	Chemical composition	Volume fraction (%)
Primary mineral		
forsterite	Mg_2SiO_4	85.5
fayalite	Fe_2SiO_4	9.5
porosity	-	5
total	-	100
Secondary mineral		
magnetite	Fe_3O_4	0
magnesite	$MgCO_3$	0
siderite	$FeCO_3$	0
talc	$Mg_3Si_4O_{10}(OH)_2$	0
amorphous silica	SiO_2	0
iron	Fe	0

Reactive Transport Modeling of Calcite Dissolution

The dissolution of CO_2 into groundwater increases the acidity of water and changes the chemical equilibriums between formation water and aquifer rock. Numerical modeling of multiphase flow and reactive transport provides a powerful tool for understanding and predicting the flow and chemical evolution of the subsurface environment. However, in real systems a large number of chemical reactions are present simultaneously, making the reactive transport model inherently complex and computationally intensive. It is desirable to have a numerical model that uses simplified sets of geochemical reactions yet is able to capture the essential physics (dissolution and precipitation) of the system.

The geochemical reactions between CO_2 and different kinds of minerals in the formation are modeled using the non-isothermal multiphase reactive transport program TOUGHREACT (Xu *et al.*, 2006), which is developed by introducing reactive transport into the existing multi-phase fluid and heat flow simulator TOUGH2.

A simple reactive transport model is first developed to simulate fluid flow, solute transport and chemical reaction of injected CO_2, brine and minerals. Among many mineral compositions in the

subsurface formation, calcite ($CaCO_3$) reacts with CO_2 very quickly after CO_2 injection into the formation. Thus, we began building the model using calcite as the only mineral reacting with CO_2. The complexity of the model will be gradually increased with more reactions and species included later.

After CO_2 injection into the subsurface formation, it is dissolved in the surrounding formation water, forming H_2CO_3, HCO_3^- and CO_3^{2-} and increasing the acidity:

$$CO_2(gas) \Leftrightarrow CO_2(aq) \tag{4.1}$$

$$CO_2(aq) + H_2O \Leftrightarrow H_2CO_3 \tag{4.2}$$

$$H_2CO_3 \Leftrightarrow H^+ + HCO_3^- \tag{4.3}$$

$$HCO_3^- \Leftrightarrow H^+ + CO_3^{2-} \tag{4.4}$$
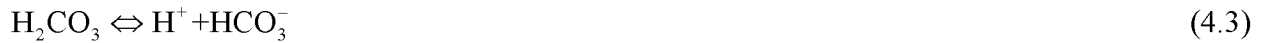
Then, the increased acidity results in the dissolution of many of the primary host rock minerals. The mineral dissolution increases concentrations of cations Ca^{2+}, which in turn causes complexing of dissolved cations with the bicarbonate ion to form $Ca(HCO_3)_2$:

$$CaCO_3 + CO_2(gas) + H_2O \Leftrightarrow Ca^{2+} + 2HCO_3^- \tag{4.5}$$

A simplified 1-D radial reactive transport model is shown in Figure 4.1. The geologic formation is assumed to be infinitely long and homogeneous with a thickness of 100 m, containing 1 M NaCl brine at a constant temperature of 75°C. The well field is modeled as a circular region of 10,000 m radius, at the center of which CO_2 is injected uniformly at a constant rate of 90 kg/s. A 1-D radial grid was used with a spacing gradually increasing away from the well. The CO_2 injection was assumed to continue for a period of 40 years. Prior to CO_2 injection, batch geochemical modeling for water-calcite interaction was performed to obtain a nearly equilibrated water chemistry using 1 M NaCl brine at a temperature of 75°C. The resulting water chemistry was used as the initial condition of reactive geochemical transport simulations. The hydraulic parameter and the initial concentration of aqueous species are given in Table 4.25.

Table 4.25. Hydrogeologic and geochemical parameters for the 1-D radial fluid flow problem.

Parameter	Value
Aquifer thickness	100 m
Permeability	10^{-13} m^2
Porosity	0.3
Compressibility	4.5×10^{-10} Pa^{-1}
Temperature	75 °C
Pressure	200 bar
CO_2 injection rate	90 kg/s
Volume fraction of calcite	0.12
Volume fraction of non-reactive mineral	0.88
Wellbore radius	0.3 m

Concentration of Ca^{2+}	0.01 mol/kg
Concentration of HCO_3^-	8.8×10^{-4} mol/kg
Concentration of Na^+	0.99 mol/kg
Concentration of Cl^-	1.0 mol/kg
pH	7.16
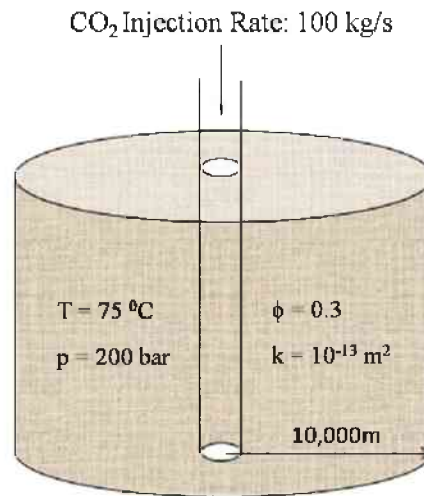
Figure 4.1 Simplified conceptual model for the CO_2 injection problem.

Results and discussion

The initial pH value is 7.16 in the assuming calcite formation. With the imposition of high-pressure CO_2, the pH of the system is lowered to 4.6 (Figure 4.2a). The abundance of hydrogen ion (H^+) in formation water results in the dissolution of calcite (Figure 4.2b). The porosity increases as a result of the dissolution of calcite, as shown in Figure 4.3.
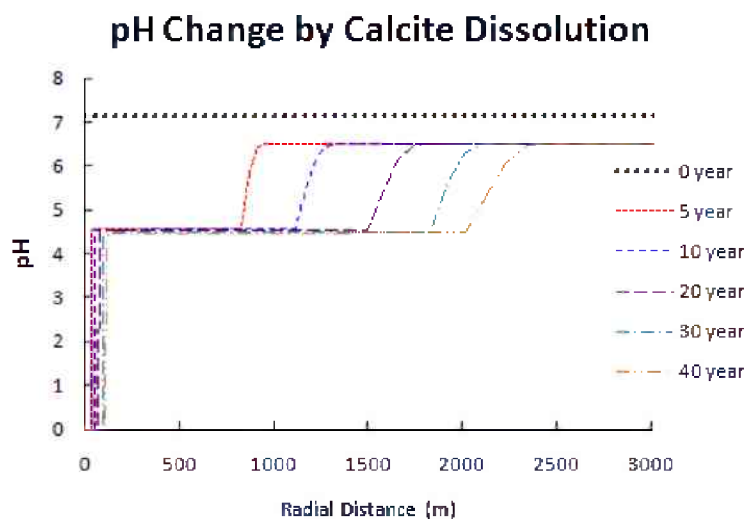
Figure 4.2a. pH values at different times for 1-D radial CO_2 injection problem.

Calcite Dissolution
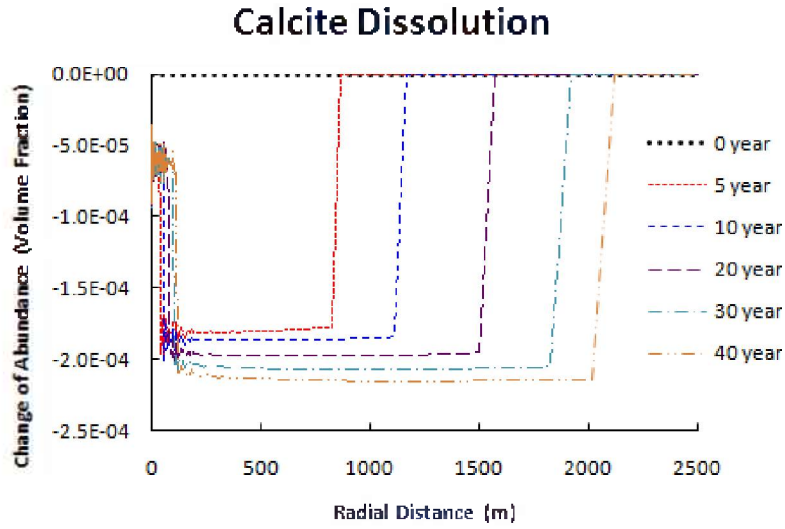
Figure 4.2b. Calcite change in abundance at different times for 1-D radial CO_2 injection problem (negative values indicate dissolution).

Porosity Change by Calcite Dissolution
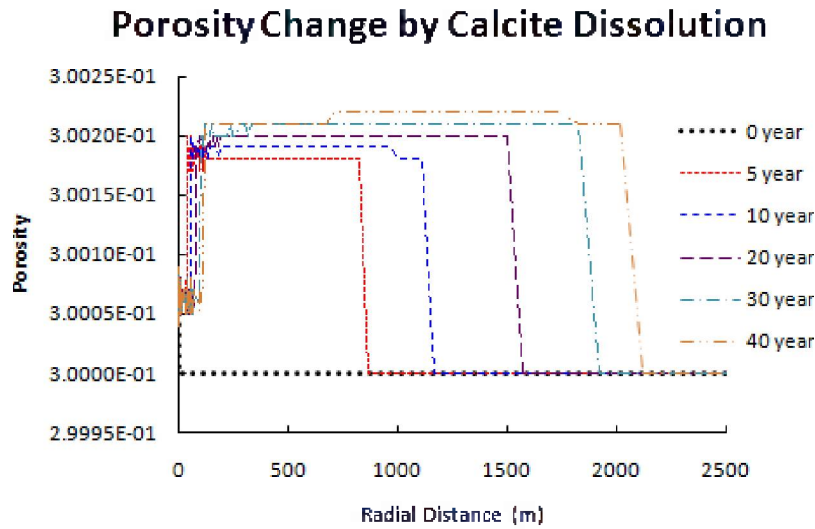
Figure 4.3: Porosity change at different times for 1-D radial CO_2 injection problem.

Significant dissolution of calcite occurs in the model system due to the lower pH induced by the dissolution of CO_2 at high pressure. Figures 4.4 and 4.5 show the concentrations of calcium ion and bicarbonate radical during a 40-year CO_2 injection period. The concentrations of calcium ion and bicarbonate radical increase with increasing gaseous CO_2 due to the continuous reaction between CO_2 and calcite mineral.

Figure 4.4: Calcium ion concentrations at different times for 1-D radial CO_2 injection problem.

Figure 4.5: Bicarbonate radical concentrations at different times for 1-D CO_2 injection problem.

Assessment of porosity and permeability changes associated with dissolution/precipitation

Background of Geochemical Reaction Modeling Study

There are many power plants located in the Colorado Plateau and southern Rocky Mountains region of the U.S. Over 100 million tonnes of CO_2 are released to the atmosphere each year from those power plants. This region contains broad anticlinal structures, not generally thought of as gas traps, that may be suitable for permanent sequestration of CO_2. Field studies of geochemical reaction modeling discussed in this section were conducted at the White Rim formation lying approximately Northwest-Southeast and in the vicinity of the Hunter power plant on the Colorado Plateau of Central Utah.

Geochemical Reaction Modeling Study for White Rim formation, Colorado Plateau, Central Utah

Geological Structure Beneath Hunter Power Plant: The geological characteristics beneath the power plant are given in Figure 4.6. The site is considered an important potential sequestration site in Colorado Plateau, as there are two power plants within 10 km with a combined capacity of 2000 MW producing 15 million tonnes of CO_2 emissions per year. The sedimentary sequence shown in Figure 4.6 contains potential reservoir and seal formations at over 1 km depth beneath the power plant.

Among the formations beneath Hunter Power Plant are four that have characteristics suitable for CO_2 sequestration (White *et al.*, 2005): (1) Jurassic Navajo Sandstone is a classic example of an eolian deposit with excellent porosity and permeability because it contains large-scale cross-beds, frosted quartz grains, and other sedimentary diagnostic eolian features. (2) Jurassic Wingate Sandstone is in the uplift and is relatively homogeneous. It was also deposited in an eolian environment and although little petrophysical work is available, it likely has good porosity and permeability. (3) Permian White Rim Sandstone with excellent porosity and permeability contains cross-beds in clean, fine-grained sandstone. The eolian White Rim i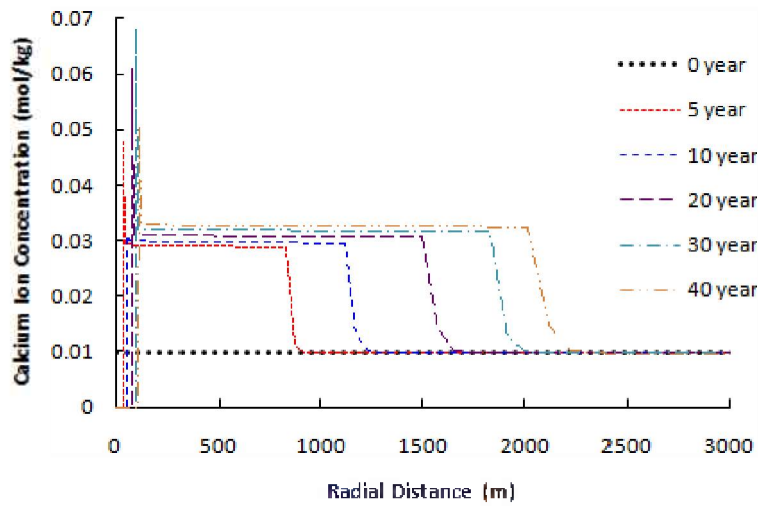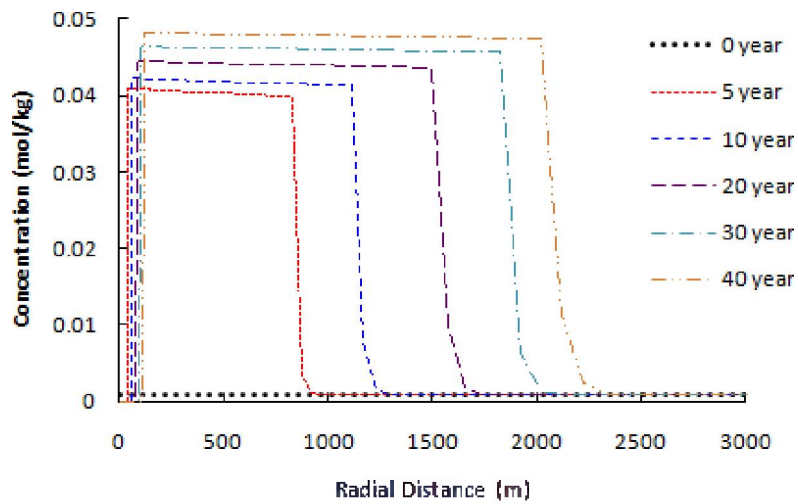s the best candidate for CO_2 injection. It is the main CO_2 reservoir at Gordon Creek field. (4) Mississippian Redwall Limestone, which was deposited in a shallow marine environment. The Redwall is the deepest candidate for CO_2 injection, has moderate porosity and permeability, and is a major producer of oil and gas in structural traps (faulted anticlines) to the southeast in the Paradox Basin. Also, there are some potential shale seals (Cretaceous Mancos Shale, Triassic Chinle Shale, Triassic Moenkopi Formation, Permian Black Box Dolomite, Devonian Elbert Formation and Cambrian Ophir Formation) and potential evaporite seals (Jurassic Carmel Formation and Pennsylvanian Honaker Trail/Paradox Formations) overlying or underlying the potential CO_2 sequestration formation.

White *et al.* (2005) simulated CO_2 injection into the entire potential sequestration site using two models. The first one was a hydrological model that simulated the injection of CO_2 into Navajo Sandstone, White Rim Sandstone, Wingate Sandstone, and Redwall Limestone aquifers, and tracked the location of the CO_2 over a period of 1000 years. Chemical reactions between the

reservoir brine and the host rock were ignored. Of the investigated potential sequestration reservoirs above mentioned, only the White Rim sandstone formation could provide containment of injected CO_2 for the hundreds to thousands of years required for mineral sequestration reactions. Therefore, in this quarter we studied the effects of water-rock interactions on CO_2 sequestration according to the mineral compositions of White Rim sandstone formation.
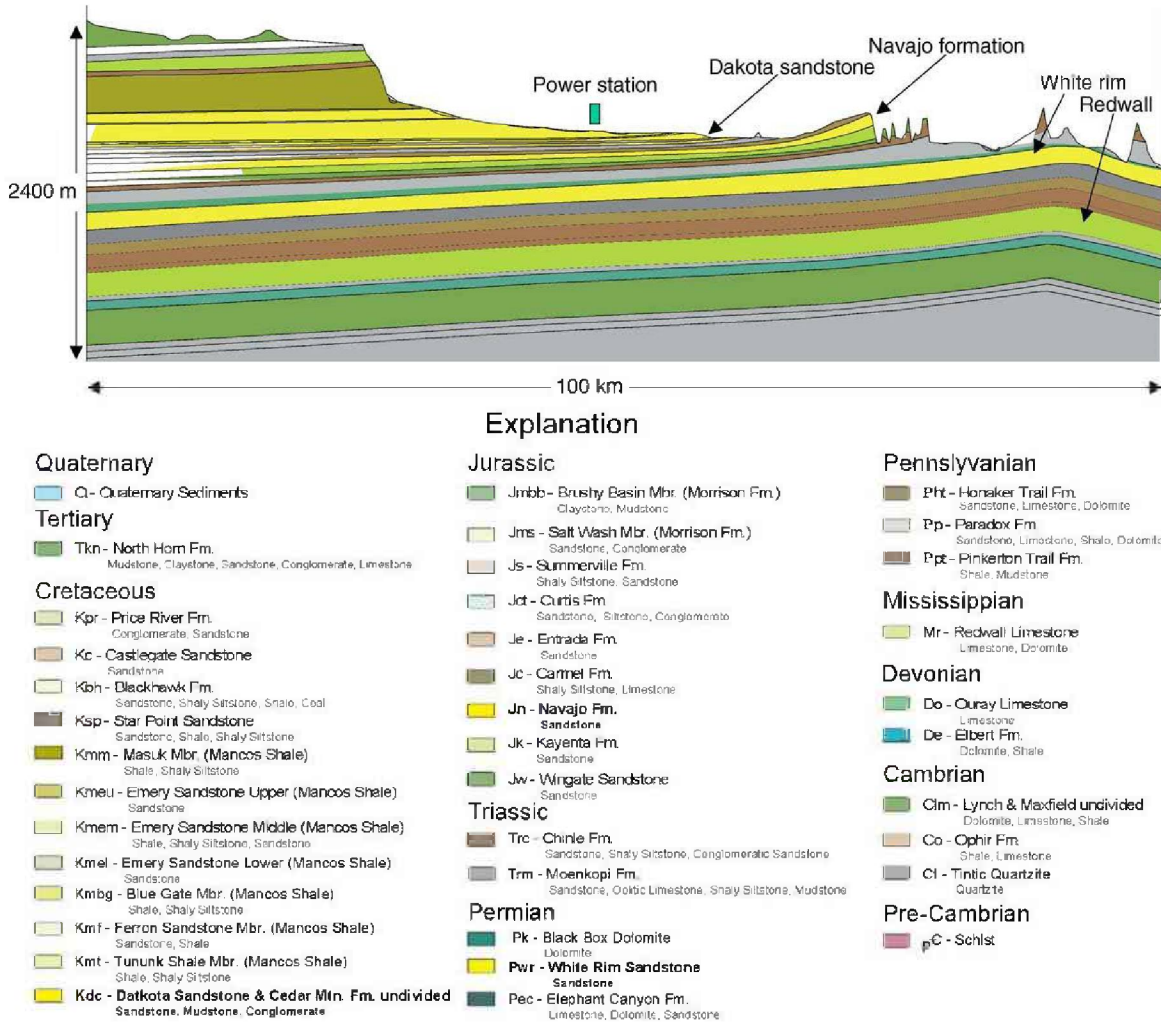
Figure 4.6. Geological condition on the cross-section beneath the Hunter Power Plant, Central Utah. (White *et al.*, 2005).

Reactive Transport Model Setup: In our study, we employ the original mineral compositions of the White Rim sandstone formation to establish a 2D reactive transport model to investigate the effect of mineral dissolution/precipitation on porosity and permeability of the formation. The mineral composition of White Rim sandstone formation was taken from the previous geochemical reaction model (White *et al.*, 2005). The initial mineral volume fractions of White Rim sandstone formation and potential secondary mineral phases are given in Table 4.26.

84

Table 4.26. Initial mineral volume fractions and potential secondary mineral phases.

Mineral	Chemical composition	Volume (%)
Primary minerals		
Quartz	SiO_2	77.0
Kaolinite	$Al_2Si_2O_5(OH)_4$	2.25
Calcite	$CaCO_3$	1.80
K-feldspar	$KAlSi_3O_8$	0.60
Na-smectite	$Ca_{0.145}Mg_{0.26}Al_{1.77}Si_{3.97}O_{10}(OH)_2$	2.15
Albite-low	$NaAlSi_3O_8$	0.60
Anorthite	$CaAl_2Si_2O_8$	0.66
Porosity	-	15
Secondary minerals		
Illite	$K_{0.6}Mg_{0.25}Al_{1.8}(Al_{0.5}Si_{3.5}O_{10})(OH)_2$	
Dolomite	$CaMg_{0.3}Fe_{0.7}(CO_3)_2$	
Dawsonite	$NaAlCO_3(OH)_2$	

In previous simulations of CO_2 injection into the Farnham Dome reservoir on the Colorado Plateau (Allis *et al.*, 2001; White *et al.*, 2001, 2002), 100 md permeability was used for the saline aquifers. White *et al.* (2005) found that estimates of hydraulic conductivities from several hydrologic studies conducted on the Colorado Plateau by the United States Geological Survey were consistent with the value used in the Farnham Dome modeling. Furthermore, for their 2005 simulation work, the permeability was initially set to that value, so in our reactive transport model, the White Rim sandstone formation permeability is assumed to be 100 md. The capillary pressure function we used in the reactive transport simulations is from White *et al.* (2005). They parameterized the measured curves using five parameters, shown in Figure 4.7.
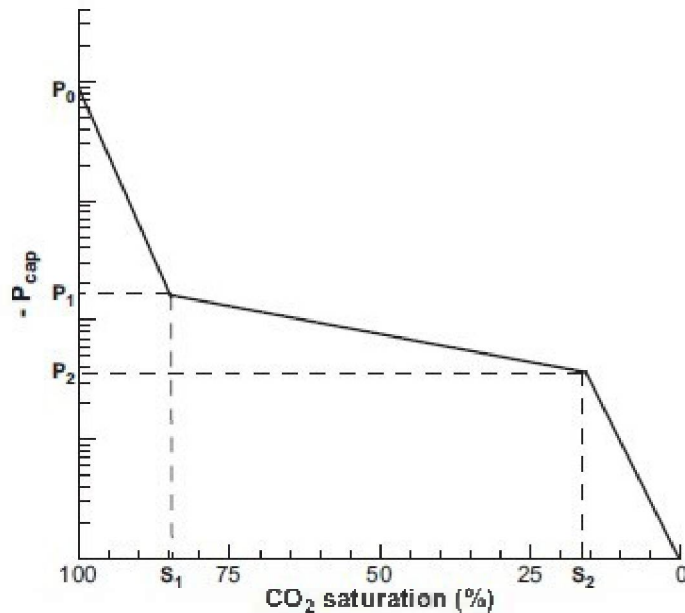
Figure 4.7. Definition of parameters used to define capillary pressure functions. $P_0=3.92\times10^7$, $P_1=1.10\times10^5$, $P_2=3.90\times10^3$, $S_1=0.05$ and $S_1=1.00$. (White *et al.*, 2005).

Initial equilibrium concentration of aquifer saline solution species is calculated using the mineralogy in Table 4.27, setting the reservoir fluid to a 0.03 M NaCl brine, and then allowing the brine to react with the reservoir for 1000 years. This equilibrium calculation model is a closed system comprised of a single element without any flow terms, a closed batch reaction system. Reservoir temperature is 54°C and initial pressure is 100 bars. Mineral dissolution and precipitation rates, and reactive surface area used in this work were taken from the geochemical reaction modeling conducted by Xu *et al.* (2010). The kinetic rate constants for mineral dissolution/precipitation used in the reactive transport modeling are summarized in Table 4.27. The initial brine composition in the White Rim sandstone obtained by the batch reaction modeling is given in Table 4.28.

Table 4.27. Kinetic parameters for mineral dissolution and precipitation.

Mineral	A (cm2/g)	Parameters for kinetic rate law								
		Neutral mechanism		Acid mechanism			Base mechanism			
		K_{25} (mol/m^2·s)	Ea(kJ/mol)	K_{25}	Ea	n(H$^+$)	K_{25}	Ea	n(H$^+$)	
Quartz	9.8	1.023×10^{-14}	87.7	-	-	-	-	-	-	
Kaolinite	151.6	6.918×10^{-14}	22.2	4.898×10^{-12}	65.9	0.777	8.913×10^{-18}	17.9	-0.472	
Calcite	9.8	1.549×10^{-6}	23.5	5.012×10^{-1}	14.4	1.000	-	-	-	
K-feldspar	9.8	2.890×10^{-13}	38.0	8.710×10^{-11}	51.7	0.500	6.310×10^{-12}	94.1	-0.823	
Na-smectite	151.6	1.660×10^{-13}	35.0	1.047×10^{-11}	22.6	0.340	2.020×10^{-17}	58.9	-0.400	
Albite-low	9.8	2.754×10^{-13}	69.8	6.918×10^{-11}	65.0	0.457	2.512×10^{-16}	71.0	-0.572	
Anorthite	9.8	2.754×10^{-13}	69.8	6.918×10^{-11}	65.0	0.457	2.512×10^{-16}	71.0	-0.572	

Illite	151.6	1.660×10^{-13}	35.0	1.047×10^{-11}	22.6	0.340	2.020×10^{-17}	58.9	-0.400
Dolomite	9.8	2.951×10^{-8}	52.2	6.457×10^{-4}	36.1	0.500	-	-	-
Dawsonite	9.8	1.260×10^{-9}	62.76	6.457×10^{-4}	36.1	0.500	-	-	-

Table 4.28. Initial equilibrium concentration of water species (in mol/kg).

Parameter	Value	Elements	Concentration (mol/kg)
Temperature(°C)	54	Na^+	0.2972
pH	8.517	K^+	0.4002×10^{-3}
		Ca^{2+}	0.2154×10^{-2}
		Mg^{2+}	0.1487×10^{-8}
		HCO_3^-	0.1898×10^{-2}
		Cl^-	0.3001
		$SiO_2(aq)$	0.4233×10^{-3}
		AlO_2^-	0.7058×10^{-8}

We used a two-dimensional radial model to assess the evolution of mineral composition, distribution of injected CO_2, and subsequent geochemical changes in the White Rim sandstone reservoir. This 2D reactive transport model is a homogeneous sandstone formation 1000 m thick with a cylindrical geometrical configuration. In the vertical direction (z-direction), 20 layers are used with a constant spacing of 50 m. In the horizontal direction (x-direction), a radius of 5 km is modeled with grid block radial spacing that increases gradually away from the injection well. A total of 50 radial grid elements are used. The cross-section of this 2D radial model is shown in Figure 4.8. The outer grid element is specified to be an infinitive lateral boundary representing a constant boundary of the 2D model, which is representative of the constant hydrostatic pressure on the vertical geological boundary in White Rim Sandstone formation (White *et al.*, 2005). CO_2 injection was applied at the bottom portion of (the thickness of the injection portion is 50m) the well using a constant rate of 100 kg/s for a period of 30 years. This rate corresponds to about 5 million tonnes/year, approximately equal to the emissions from a 600 MW coal fired power station. Then, a fluid flow and geochemical transport simulation is run for a period of 1000 years.
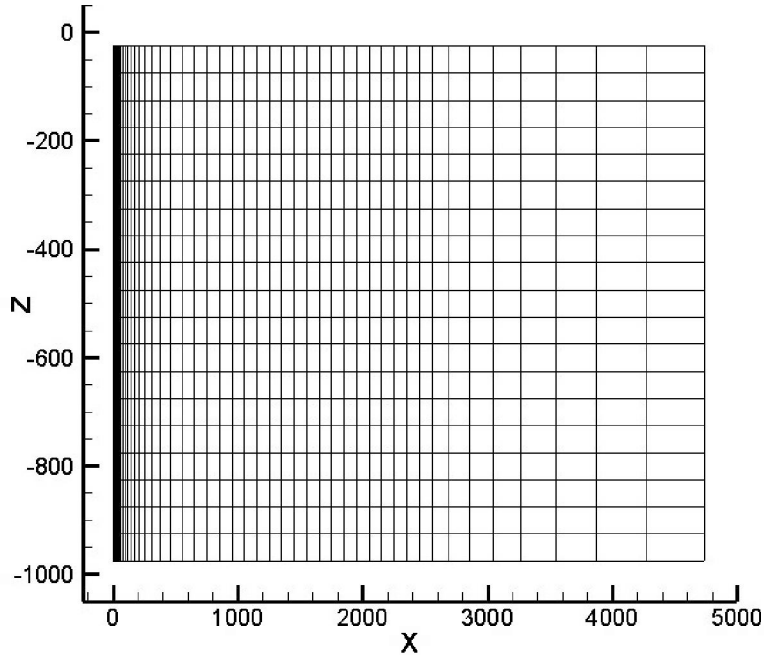
Figure 4.8. 2D Mesh structure used for reactive transport modeling.

Simulation Results and Discussion: Figure 4.9 shows the spatial distribution of CO_2 gas saturation in the saline formation after 30 years CO_2 injection and 1000 years storage period. The CO_2 gas saturation in the saline aquifer rock increases with the injection of CO_2, especially in the area around the injection well. A region 200 m in the vertical direction and 100 m radially are completely filled with CO_2 gas at 30 years of CO_2 injection. Due to its density, the injected supercritical CO_2 fluid at the bottom of the storage formation migrates upward rapidly, as shown in Figure 4.10. The CO_2 gas plume rose to the top layer of the saline aquifer after 1000 years storage. With the migration of CO_2 gas during the storage period, dissolved CO_2 rapidly increases the concentration of bicarbonate radical to over 2 mol/kg H_2O in the two-phase region (Figure 4.11). The injected CO_2 dissolves in the surrounding formation water, forming $H_2CO_3(aq)$, HCO_3^-, and CO_3^{2-}, and increasing acidity. The dissolution of CO_2 in the saline aquifer results in the change of pH, decreasing to 4.5 in the two phase area, which is shown in Figure 4.11. The dissolved CO_2 tends to migrate downward after 1000 years; that is not significant because precipitation of carbonate minerals partially consumes the dissolved CO_2. Therefore the spatial distribution of pH after 1000 years tends not to be homogeneous in the two phase area.
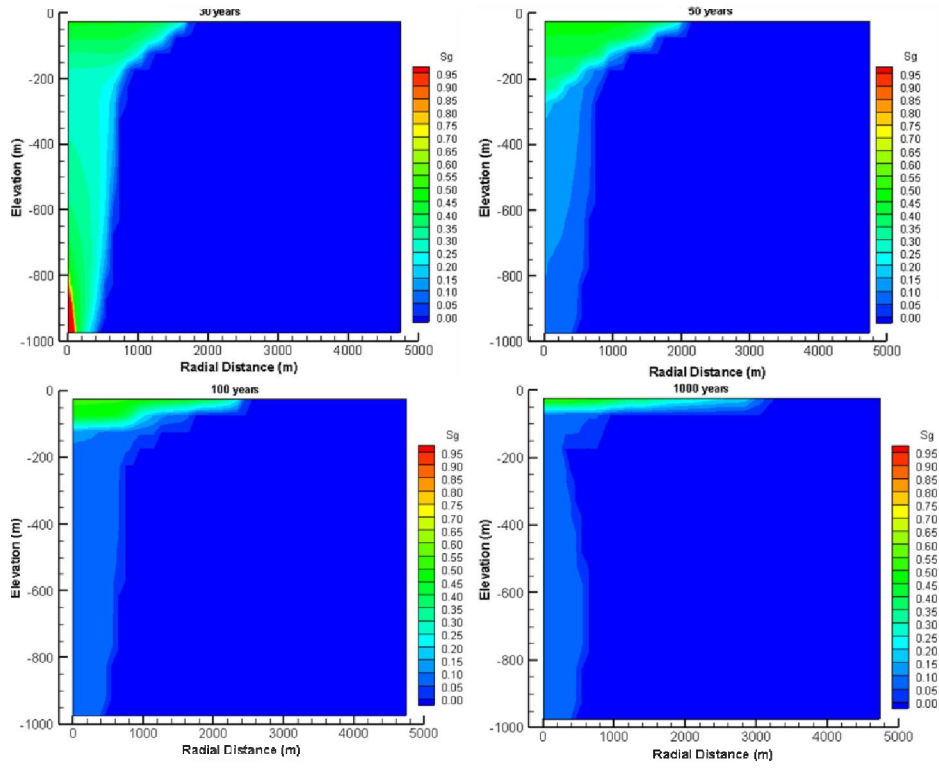
Figure 4.9. Spatial distribution of CO_2 gas saturation after 30, 50, 100 and 1000 years.
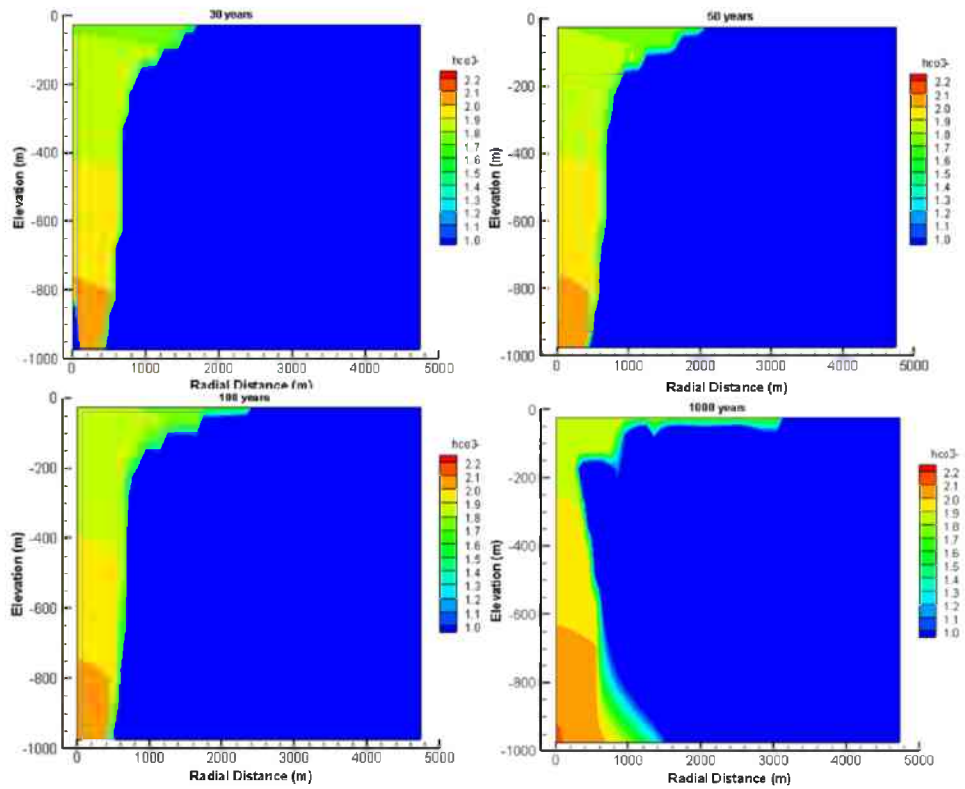
Figure 4.10. Spatial distribution of bicarbonate concentration (mol/kg formation water) due to the dissolution of CO_2 gas after 30, 50, 100 and 1000 years.
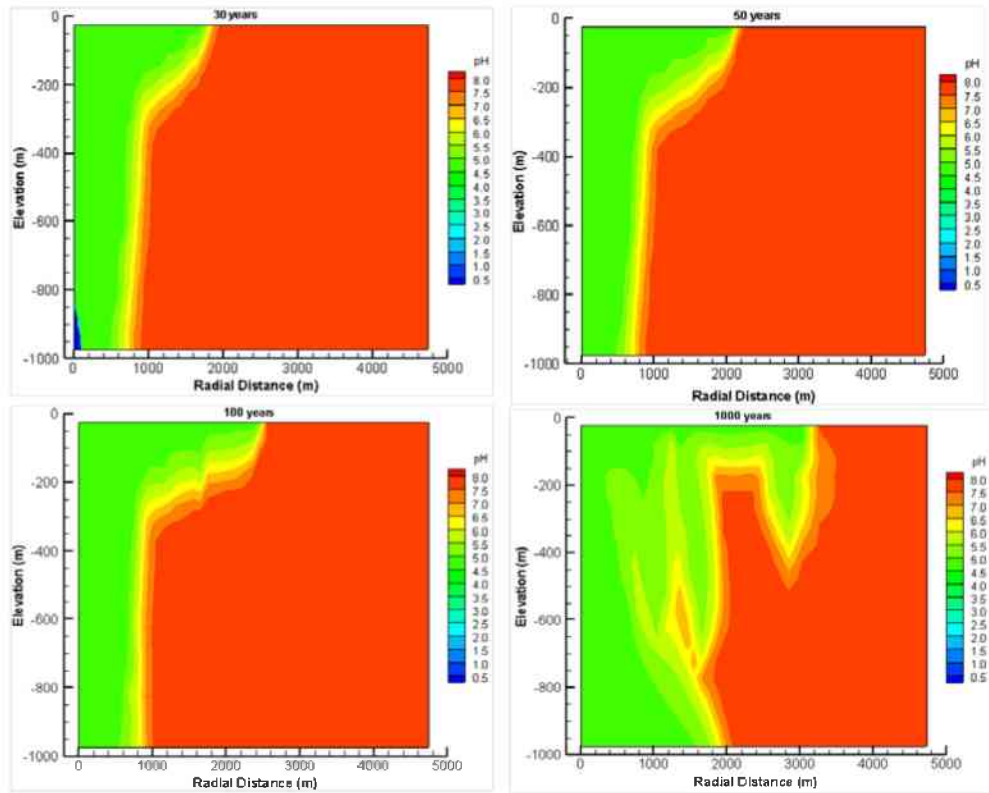
Figure 4.11. Spatial distribution of pH value due to the dissolution of CO_2 gas or mineral composition after 30, 50, 100 and 1000 years.

The dissolution/precipitation of minerals present in aquifer rock occurs from chemical reactions between the dissolved CO_2 and the minerals. The increased concentration of H^+ in the aqueous phase caused by CO_2 injection results in interactions with silicate minerals such as feldspars and clay minerals that release cations such as Ca^{2+} and Mg^{2+}. Figure 4.12 shows calcite volume fraction change due to the dissolution of calcite. The mineral dissolution increases concentrations of cations such as Na^+, Ca^{2+} and Mg^{2+}, which in turn causes complexing of dissolved cations with the bicarbonate ion to form $NaHCO_3$, $CaHCO_3^+$ and $MgHCO_3^+$. These tend to increase CO_2 solubility and enhance solubility trapping during the long storage time. Therefore, the concentration of these cations increases during the storage period. Figure 4.13 shows the Mg^{2+} concentration change during the 1000 years' storage period. It changes to 0.0018 mol/kg water in the two phase area.
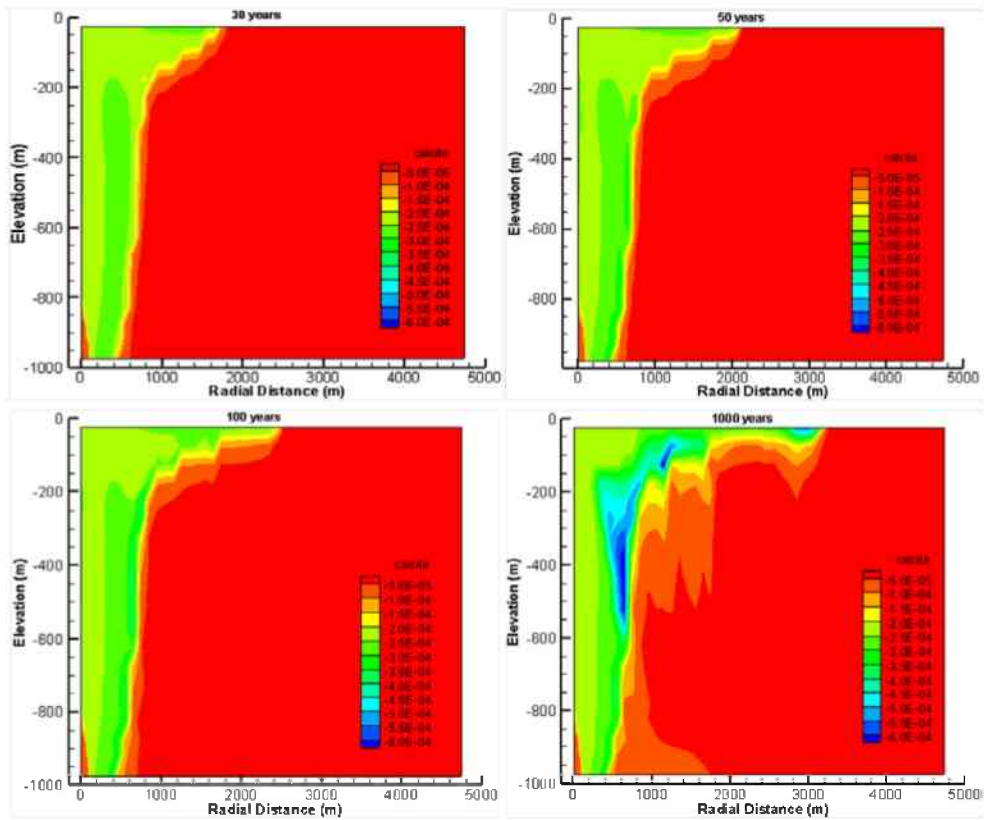
Figure 4.12. Spatial distribution of calcite volume fraction change due to increasing acidity after 30, 50, 100 and 1000 years (negative means dissolution).
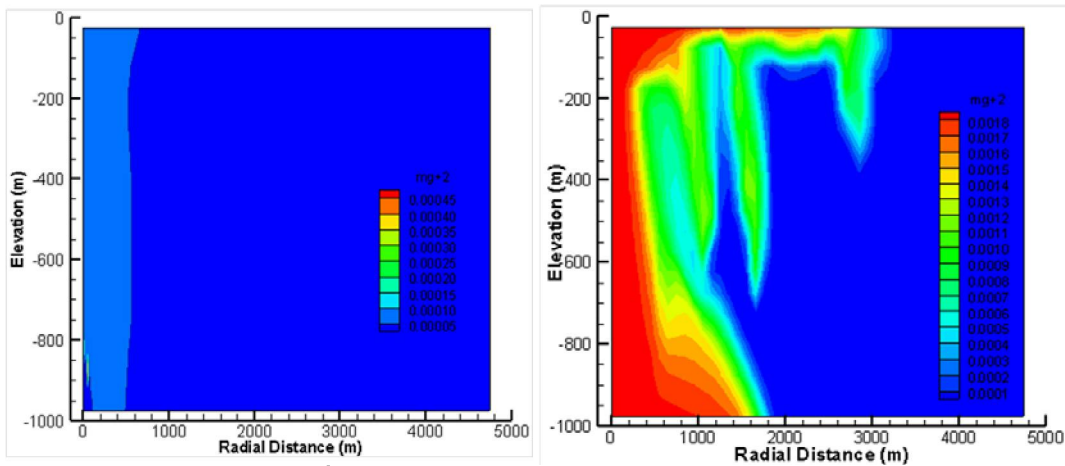
Figure 4.13. Spatial distribution of Mg^{2+} concentration (mol/kg water) due to the dissolution of Na-smectite after 30 and 1000 years.

Porosity and permeability changes are caused by mineral dissolution and precipitation in the saline aquifer. This affects CO_2 sequestration. Figures 4.14 and 4.15 show that porosity and permeability change after 1,000 years CO_2 storage. Porosity and permeability tend to increase, which means dissolution of rock mineral in the saline aquifer dominates geochemical reactions after 30 years of CO_2 injection. The simulation shows that after 100 years, only a small amount of illite and no dolomite and dawsonite have precipitated. In this case, we didn't observe

significant change of the host mineral volume fraction, porosity, and permeability. The reason might be that only 10% of the rock is reactive in the model. Moreover, the reactive rock mineral didn't react too much because of small reaction rate constants in the present geochemical reaction model. From the result of present modeling work, the main trapping mechanisms of CO_2 injection in White Rim sandstone reservoir is solubility trapping. Mineral dissolution increased the solubility of CO_2 - about 60% CO_2 gas injected into the reservoir dissolved or reacted with the species from the dissolution of the host rock minerals.
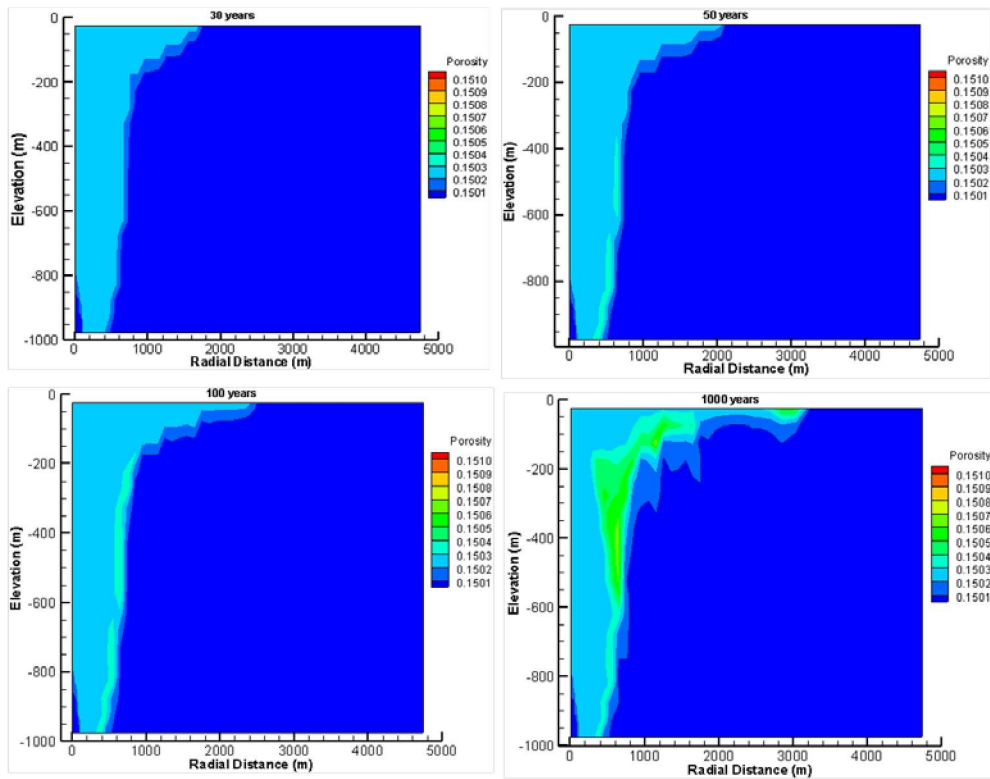
Figure 4.14. Spatial distribution of porosity due to the CO_2 injection after 30, 50, 100 and 1000 years.
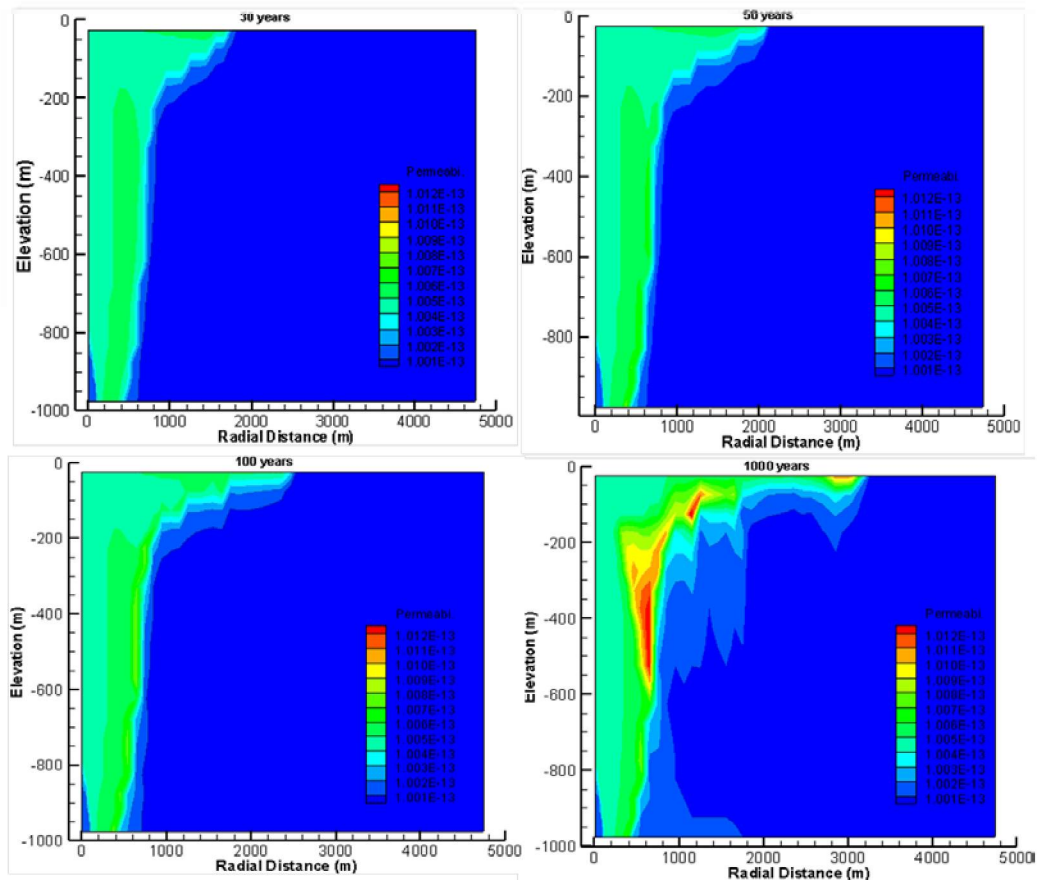
Figure 4.15. Spatial distribution of permeability due to the CO_2 injection after 30, 50, 100 and 1000 years.

Geochemical Reaction Modeling Study for Gulf Coast Sediments, U. S.

The geochemical reaction studies for Colorado Plateau and Southern Rocky Mountains indicate that the effect of CO_2 sequestration on a deep saline aquifer will vary with the volume fraction of the reactive mineral phase. In the geochemical reaction study for the White Rim formation, because only ten percent of the mineral is reactive, mineral trapping tends to be insignificant, and solubility trapping dominates the whole storage process. If more reactive minerals are present in the geochemical reaction system, there might be a significant change of the formation properties. Therefore, a great deal of specific and detailed information relative to the mineral trapping during CO_2 sequestration is required to assess the feasibility of disposing of CO_2 in a brine formation at any particular site. In Gulf Coast Sediments, 50 percent of the minerals are reactive, and reactive geochemical reaction modeling can be used to investigate the evolution of mineral compositions subjected to CO_2 sequestration. We used the same geochemical properties on our 2D geochemical reaction simulations as Xu *et al.* (2003, 2006b), who did modeling work on Gulf Coast Sediments.

Geological and Geochemical Structure of Gulf Coast Sediments: According to Xu *et al.* (2003), the majority of potential CO_2 sequestration studies on Tertiary Gulf Coast sediments are concentrated in the state of Texas. The principal reservoir-quality sandstones within that region are, respectively, the Frio, the Vicksberg, and the Wilcox formations, all of which are found within the lower Tertiary. Of the three formations, the Frio was chosen as a representative

candidate for the sequestration of supercritical carbon dioxide. It is the shallowest of the three formations, but is located at depths between 5000 and 20,000 ft over much of its areal extent, which is sufficient to ensure adequate CO_2 densities for effective storage. The initial mineral composition and kinetic parameters of a representative formation for CO_2 sequestration in Gulf Coast Sediments are shown in Table 4.29.

Table 4.29. Kinetic parameters for mineral dissolution and precipitation.

Mineral	Vol. % Of solid	A (cm²/ g)	Parameters for kinetic rate law								
			Neutral mechanism		Acid mechanism			Base mechanism			
			k_{25} (mol/m²/s)	E_a (KJ /mol	k_{25}	E_a	$n(H^+)$	k_{25}	E_a	$n(H^+)$	
Primary:											
Quartz	49.75	9.8	1.023×10^{-14}	87.7							
Kaolinite	1.81	151.6	6.918×10^{-14}	22.2	4.898×10^{-12}	65.9	0.777	8.913×10^{-18}	17.9	-0.472	
Calcite	1.74	Assumed at equilibrium									
Illite	0.86	151.6	1.660×10^{-13}	35	1.047×10^{-11}	22.6	0.34	2.020×10^{-17}	58.9	-0.4	
Oligoclase	17.82	9.8	1.445×10^{-13}	69.8	2.138×10^{-11}	65	0.457				
Kerogen-O	2.61	151.6	6.918×10^{-14}	22.2	4.898×10^{-12}	65.9	0.777	8.913×10^{-18}	17.9	-0.472	
K-feldspar	7.36	9.8	2.890×10^{-13}	38	8.710×10^{-11}	51.7	0.5	6.310×10^{-12}	94.1	-0.823	
Na-smectite	3.51	151.6	1.660×10^{-13}	35	1.047×10^{-11}	22.6	0.34	2.020×10^{-17}	58.9	-0.4	
Chlorite	4.10	9.8	2.02×10^{-13}	88	7.762×10^{-12}	88	0.5				
Hematite	0.45	12.9	2.512×10^{-15}	66.2	4.074×10^{-10}	66.2	1				
Secondary:											
Magnesite		9.8	4.571×10^{-10}	22.5	4.169×10^{-7}	14.4	1				
Dolomite		9.8	2.951×10^{-8}	52.2	6.457×10^{-4}	36.1	0.5				
Low-albite		9.8	2.754×10^{-13}	69.8	6.918×10^{-11}	65	0.457	2.512×10^{-16}	71	-0.572	
Siderite		9.8	1.260×10^{-9}	62.8	6.457×10^{-4}	36.1	0.5				
Ankerite		9.8	1.260×10^{-9}	62.8	6.457×10^{-4}	36.1	0.5				
Dawsonite		9.8	1.260×10^{-9}	62.8	6.457×10^{-4}	36.1	0.5				
Ca-smectite		151.6	1.660×10^{-13}	35	1.047×10^{-11}	22.6	0.34	2.020×10^{-17}	58.9	-0.4	
Pyrite		12.9	$k_{25}=2.818 \times 10^{-5}$ $E_a =56.9$		$k_{25}=2.02 \times 10^{-8}$ $E_a =56.9$						

Reactive Transport Model Setup: The sequestration formation is modeled as a circular region of 10,000 m radius with 100 m depth at the bottom center of which CO_2 is injected uniformly at a constant rate of 10 kg/s. A two-dimensional radial model is developed to achieve this purpose. This 2D reactive transport model is a homogeneous sandstone formation of 100 m thickness with a cylindrical geometrical configuration, which is shown in Figure 4.16. In the vertical direction (z direction), 10 layers are used with a constant spacing of 10 m. In the horizontal direction (x direction), a radial distance of 10,000 m is modeled with radial spacing that increases gradually away from the injection well. A total of 50 radial grid elements are used. The CO_2 injection was assumed to continue for a period of 40 years. The fluid flow and geochemical transport simulation was run for a period of 1000 years.

Initial equilibrium concentration of the species in the aquifer saline solution is calculated by using the mineralogy specified in Table 4.28, setting the reservoir fluid to a 0.3 M NaCl brine and then allowing the brine to react with the reservoir for 20 years. This equilibrium calculation model is a batch reaction system. Reservoir temperature is 75^0C and initial pressure is 200 bars. Kinetic parameters used in this work were taken from the geochemical reaction modeling conducted by Xu *et al.* (2010), which is listed in Table 4.28. Initial concentration of primary aqueous species and hydrogeologic parameters used in simulation are listed in Table 4.30.

Table 4.30. Initial equilibrium concentration of water species (in mol/kg).

Parameter	Value	Elements	Concentration (mol/kg)
Temperature(^oC)	75	Na^+	0.9905
pH	8.517	K^+	0.5980×10^{-2}
Permeability	10^{-13}	Ca^{2+}	0.4737×10^{-2}
Porosity	0.30	Mg^{2+}	0.2669×10^{-8}
Aquifer	100m	HCO_3^-	0.4562×10^{-1}
Compressibility	4.5×10^{-10}	Cl^-	0.1001
Initial pressure	200 bar	$SiO_2(aq)$	0.1034×10^{-2}
CO_2 injection rate	10 kg/s	AlO_2^-	0.1361×10^{-7}
		SO_4^{2-}	0.1342×10^{-8}
		Fe^{2+}	0.6457×10^{-3}

Relative permeability for liquid and gaseous phases, and capillary pressure, follows the geochemical reaction modeling work by Xu *et al.* (2003).

Relative permeability for liquid phase follows van Genuchten function (van Genuchten, 1980):

$$k_{rl} = \sqrt{S^*}\left\{1-\left(1-\left[S^*\right]^{\frac{1}{m}}\right)^m\right\}^2 \tag{4.6}$$

Where, $S^* = \dfrac{S_l - S_{lr}}{1 - S_{lr}}$, irreducible water saturation is S_{lr}=0.30 and exponent m=0.457.

Relative permeability for gas phase follows Corey function (Corey,1954):

$$k_{rg} = \left(1 - \overline{S}\right)^2 \left(1 - \overline{S}^2\right) \tag{4.7}$$

where, $\overline{S} = \dfrac{S_l - S_{lr}}{S_l - S_{lr} - S_{gr}}$ and irreducible gas saturation is S_{gr}=0.05.

Capillary pressure function follows van Genuchten function (van Genuchten, 1980):

$$P_{cap} = -P_0 \left(\left[S^*\right]^{-\frac{1}{m}} - 1\right)^{1-m} \tag{4.8}$$

where, $S^* = \dfrac{S_l - S_{lr}}{1 - S_{lr}}$, irreducible water saturation is S_{lr}=0.00, exponent m=0.457 and strength coefficient P_0=19.61kPa.
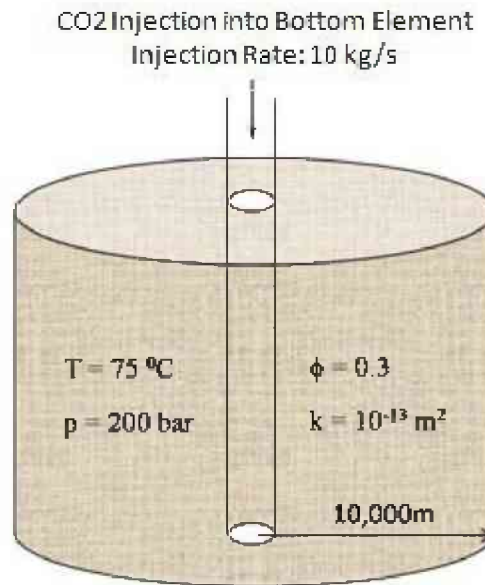
Figure 4.16. Conceptual model for the CO_2 injection into a sandstone formation.

Simulation Results and Discussion: Figure 4.17 shows the spatial distribution of CO_2 gas saturation in the saline formation after 40 years CO_2 injection and 1000 years storage period. The CO_2 gas saturation in the saline aquifer rock increases with the injection of CO_2, especially in the area around the injection well. A volume about 80 m in the vertical direction and 100 m in radial distance is completely filled by CO_2 gas at 40 years of CO_2 injection. Due to the density of supercritical CO_2 phase, the injected supercritical CO_2 fluid at the bottom of the storage formation migrates upward rapidly. Figure 4.17 shows the CO_2 gas plume at the top of the formation after 1000 years storage. With the migration of CO_2 gas during storage period, the

concentration of dissolved CO_2 rapidly increases, reflected by the concentration of bicarbonate radical in the saline water (close to 2.0 mol/kg H_2O in the two phase region, from Figure 4.18). The injected CO_2 is dissolved in the surrounding formation water, forming carbonic acid ($H_2CO_3(aq)$), which releases hydrogen ions and increases the acidity of the ground water. The dissolution of CO_2 in the saline aquifer directly results in the change of pH value, the pH value decrease to 5.2 in the two phase area, which is shown in Figure 4.19. In the location far from the injection point, the pH value tends to be 9.0 due to clay mineral dissolution that increases the alkalinity.
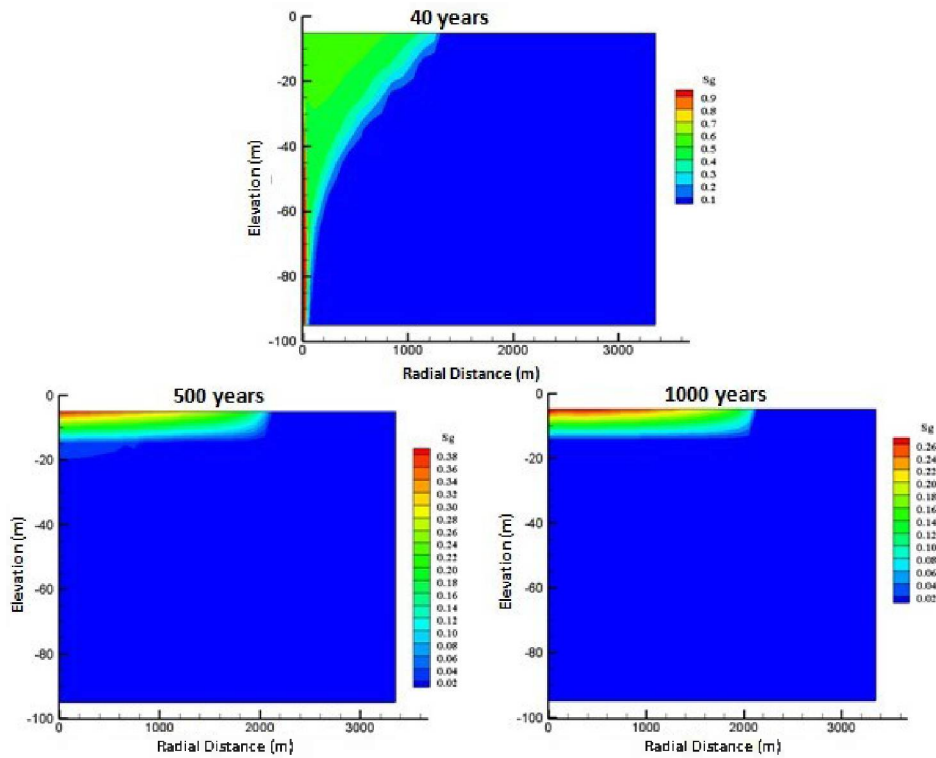

Figure 4.17. Spatial distribution of CO_2 gas saturation after 40, 500 and 1000 years.
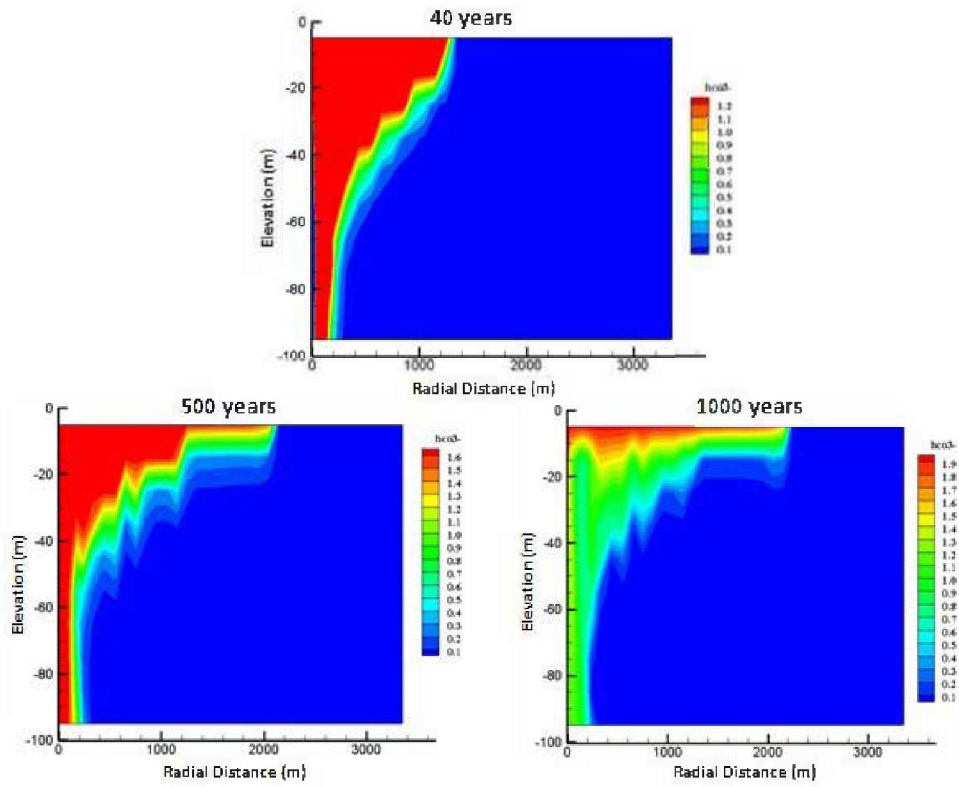
Figure 4.18. Spatial distribution of bicarbonate concentration (mol/kg water) due to the dissolution of CO_2 gas after 40, 500 and 1000 years.
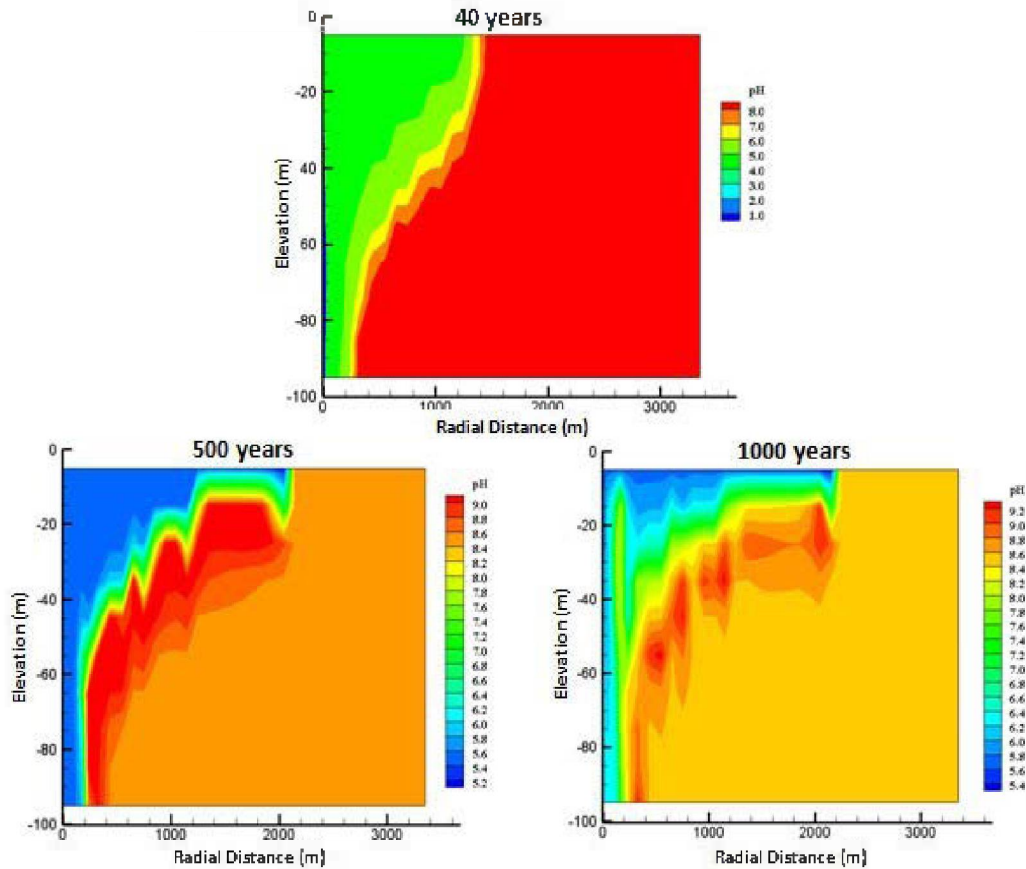
Figure 4.19. Spatial distribution of pH value due to the dissolution of CO_2 gas or mineral composition after 40, 500 and 1000 years.

After the injection period of 40 years, the dissolution/precipitation of minerals present in the aquifer rock occurs due to the chemical reactions between the dissolved CO_2 and minerals. The increased acidity from dissolved CO_2 induces dissolution of the primary host rock minerals. H^+ in the aqueous phase interacts with silicate minerals such as feldspars and clay minerals, releasing cations such as Ca^{2+} and Mg^{2+}. Figure 4.20 shows oligoclase volume fraction changes due to acidity increasing. Oligoclase has the largest volume change of the entire mineral composition system. The mineral dissolution increases concentrations of cations such as Na^+, Ca^{2+} and Mg^{2+}, which in turn causes complexing of dissolved cations with the bicarbonate ion to form $NaHCO_3$, $CaHCO_3^+$ and $MgHCO_3^+$, etc. These tend to increase CO_2 solubility and enhance solubility trapping during the long storage time. Also, there are many precipitation reactions between the aqueous species dissolved in the saline water due to the pH value change that form illite, smectite-na, ankerite, dawsonite, magnesite, and smectite-ca. The combined phenomenon of mineral dissolution and precipitation in the saline aquifer can result in changes of porosity and permeability. Figure 4.21 shows the porosity change after 1000 years of CO_2 storage. The precipitation reaction dominates the geochemical reaction process in the two phase area of the model for the long storage period, porosity tends to decrease in the two phase zone around the flow front of CO_2 gas, the dissolution reaction dominates the geochemical reaction process in the front area of CO_2 gas for the long storage period, and porosity tends to increase in the area adjacent to the CO_2 gas front. Figure 4.22 shows the volume of injected CO_2 gas permanently sequestrated in the mineral phase. The maximum volume of CO_2 gas that can be

99

permanently sequestrated in the mineral phase is 22 kg/m^3. From the result of present modeling work, the main trapping mechanism of CO_2 injection in Gulf Coast Sediments is mineral trapping.

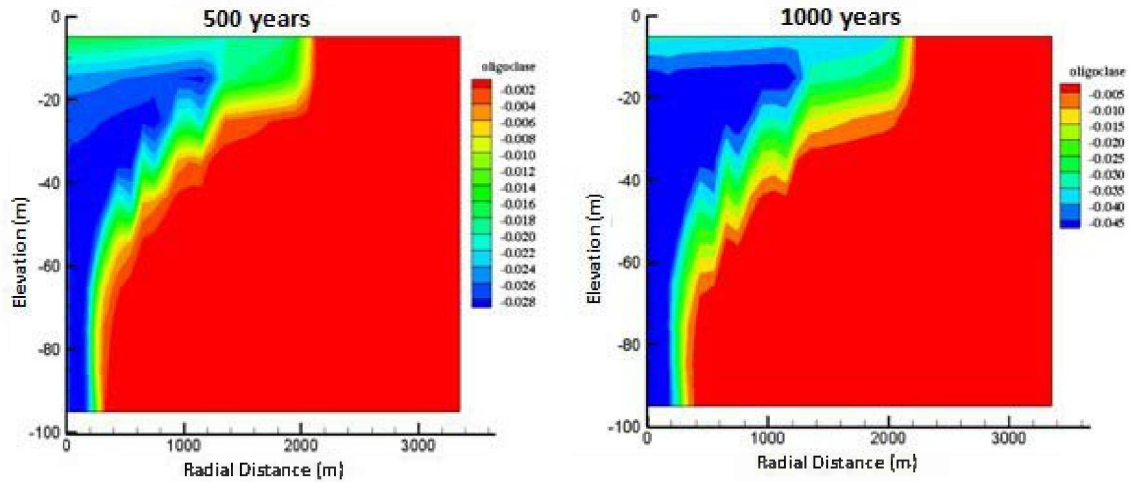Figure 4.20. Spatial distribution of oligoclase volume fraction change due to increasing acidity after 500 and 1000 years (negative means dissolution).
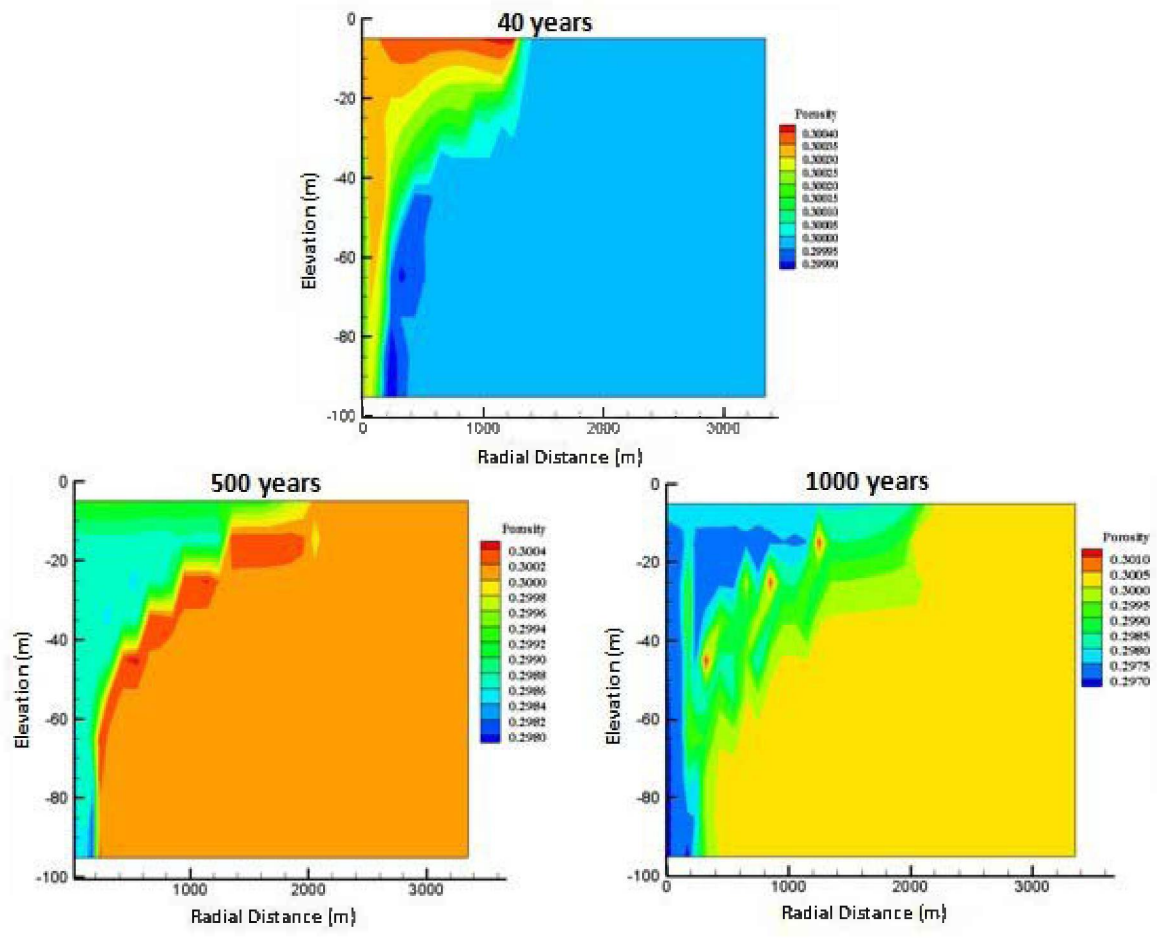
Figure 4.21. Spatial distribution of porosity due to the CO_2 injection after 40, 500 and 1000 years.
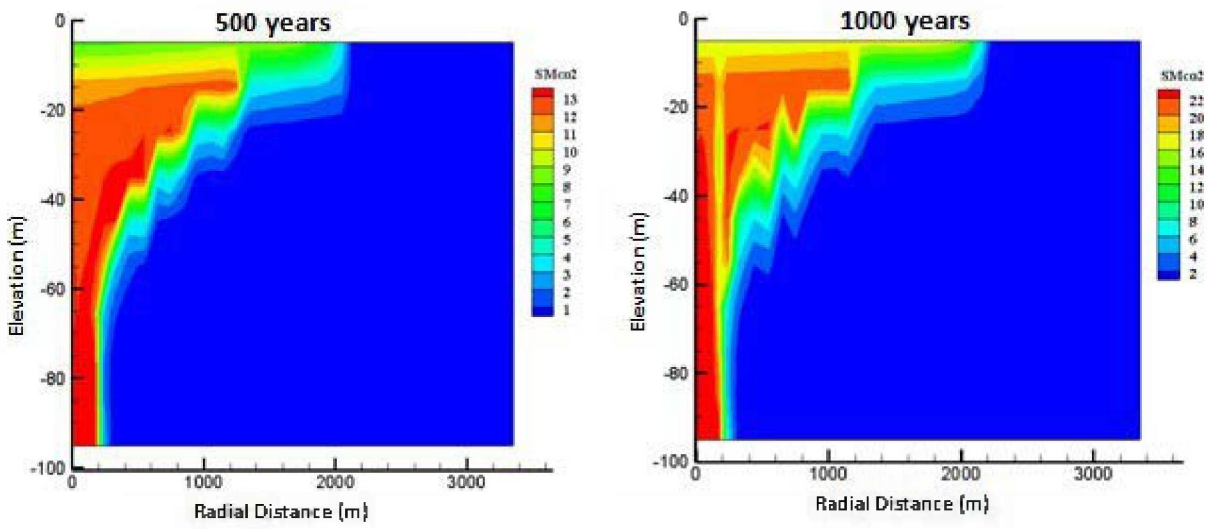

Figure 4.22. Volume distribution of CO_2 sequestrated as mineral in the formation rock (kg/m^3 mineral medium) due to CO_2 injection after 500 and 1000 years.

THMC Mathematical Model

A THMC (Thermal-Hydrological-Mechanical-Chemical) simulator is described in this section. The governing equations for this simulator are conservation of mass, describing fluid flow and mass transport, conservation of momentum, describing the mean stress field, conservation of energy, describing heat flow energy transport, and a geochemical reaction formulation describing the geochemistry occurring during CO_2 geo-sequestration. This simulator is based on TOUGH-ECO2N (Pruess, 2005), TOUGHREACT (Xu *et al.*, 2006b), and TOUGH2-CSM (Winterfeld and Wu, 2014).

The conservation of mass equation is based on the TOUGH2-CSM one (Equation 3.15), generalized to account for rate-dependent and equilibrated chemical reactions:

$$\frac{\partial M^k}{\partial t} = \nabla \cdot \boldsymbol{F}^k + q^k + R_{req}^k + R_r^k \tag{4.9}$$

where k refers to primary components, R_{req} refers to equilibrated chemical reactions, and R_r refers to rate-dependent chemical reactions. The conservation of energy and momentum equations are those for TOUGH2-CSM.

In geochemical reaction systems, the dissolution rate of a certain minerals (i.e., $CaCO_3$) is very fast. Thus, the those minerals are always at equilibrium. The mineral saturation index controls the dissolution of the mineral, and is expressed as:

$$F_m = \log \Omega_m = \log \left\{ X_m^{-1} \lambda_m^{-1} K_m^{-1} \prod_{\kappa=1}^{N_c} C_\kappa^{v_{m\kappa}} \gamma_\kappa^{v_{m\kappa}} \right\} = 0 \tag{4.10}$$

where m is the equilibrium mineral index, X_m is the mole fraction of the m-th mineral phase, λ_m is its thermodynamic activity coefficient (for pure mineral phases, X_m and λ_m are taken equal to one), K_m is the corresponding equilibrium constant of the equilibrium mineral, C_j is the concentration of related primary chemical species or components, v_{mj} is the stoichiometric coefficient of j-th basis species in the m-th mineral equilibrium reaction, and γ_k is the activity coefficient of primary chemical species. Reactions involving aqueous and gaseous phases are also assumed to be at equilibrium, so according to the Mass-Action Law:

$$F_g = \log \Omega_g = \log \left\{ \left(p_g \Gamma_g K_g \right)^{-1} \prod_{\kappa=1}^{N_c} C_\kappa^{v_{g\kappa}} \gamma_\kappa^{v_{g\kappa}} \right\} = 0 \tag{4.11}$$

where subscript g is gas index, p is the partial pressure (in bars), and Γ is the fugacity coefficient. The fugacity coefficient depends on temperature and pressure (Spycher *et al.* 2003).

Aqueous chemical reactions are assumed to be at local equilibrium as well. By making use of the mass action equation for the dissociation of the i-th aqueous complex, the concentrations of aqueous complexes can be expressed as functions of the concentrations of primary chemical species:

$$c_k = \gamma_k^{-1} K_k^{-1} \prod_{j=1}^{N_c} C_j^{v_{m\kappa}} \gamma_j^{v_{m\kappa}} \tag{4.12}$$

where c_k is the molal concentration of k-th secondary aqueous complex, c_j is molal concentration of the jth basis species, and K_k is the equilibrium constant of the k-th secondary complex-forming reaction.

The expression of kinetic rate is given by Lasaga *et al.* (1994):

$$r_n = f\left(c_1, c_2, \ldots, c_{N_c}\right) = \pm k_n A_n \left|1 - \Omega_n^\theta\right|^\eta \quad n = 1 \ldots N_c \tag{4.13}$$

where positive values of r_n indicate dissolution, and negative values precipitation, k_n is the rate constant (moles per unit mineral surface area and unit time) which is temperature dependent, A_n is the specific reactive surface area per kg, Ω_n is the kinetic mineral saturation ratio. The parameters θ and η must be determined from experiments; usually, but not always, they are taken equal to one. The temperature dependence of the reaction rate constant can be expressed reasonably well via an Arrhenius equation (Lasaga 1984; Steefel and Lasaga 1994).

For the internal generation term R^κ by geochemical reaction, the mass loss and gain of each primary species κ can be expressed as follows:

$$R^\kappa = \sum_{k=1}^{N_x} v_{kj} C_k + \sum_{i=1}^{N_g} v_{ij} C_g + \sum_{m=1}^{N_p} v_{mj} C_m - \sum_{n=1}^{Nq} v_{nj} r_n \Delta t \tag{4.14}$$

where C are concentrations (chemical reactions are always solved per kg of water, and concentration units used here are mol/kg which is close to mol/l when density is close to 1 kg/l); subscripts j, k, i, m and n are the indices of basis species, aqueous complexes, gas, minerals at equilibrium and minerals under kinetic constraints, respectively; N_C, N_x, N_g, N_p and N_q are the number of the base species, aqueous complex, gas, minerals, andminerals under kinetic constraint; v_{kj}, v_{ij}, v_{mj}, and v_{nj} are stoichiometric coefficients of the basis species in the aqueous complexes, gas, equilibrium and kinetic minerals, respectively.

Fully Coupled Solution Method for THMC Simulator

For the fully coupled approach, the mathematical equations for fluid flow, solute transport and geochemical reactions are solved simultaneously. These equations are discretized using the Integral Finite Difference method (Narasimhan and Witherspoon, 1985) over a grid cell. The equation system for the multi-component reactive solute transport can then be expressed as follows:

$$R_{\beta,n}^{\kappa,k+1} = M_{\beta,n}^{\kappa,k+1} - M_{\beta,n}^{\kappa,k} - \frac{\Delta t}{V_n}\left\{ \sum_m A_{nm}\left[u_{\beta,nm}^{k+1} X_{\beta,nm}^{\kappa,k+1} \rho_{\beta,nm}^{k+1} + \underline{D}_{\beta,nm}\rho_{\beta,nm}^{k+1} \frac{X_{\beta,m}^{\kappa,k+1} - X_{\beta,n}^{\kappa,k+1}}{d_{nm}} \right] + \right.$$
$$\left. V_n q_{\beta,n}^{\kappa,k+1} + V_n R_{\beta,n}^{\kappa,k+1} \right\}$$

(4.15)

$$F^{k+1} = F\left(X_\beta^{\kappa,k+1} \right) = 0$$

(4.16)

For each volume element V_n, there are NEQ ($N_c+N_p+2N_g$) equations, so a fully coupled reactive solute transport system with NEL grid blocks represents a total of NEL×NEQ coupled non-linear equations. The unknowns are the NEL×NEQ independent primary variables {x_i; $i = 1, \dots$, NEL×NEQ}, which completely define the state of the reactive solute transport system at time level t_{k+1}. These equations are solved using the Newton-Raphson iteration, which is implemented as follows. We introduce an iteration index p and expand the residuals R and F at iteration step $p+1$ in a Taylor series in terms of those at index p. The Taylor series expansions of the residual equations for x_i (p is NR-iteration index) are:

$$R_{\beta,n}^{\kappa,k+1}\left(x_{i,p+1} \right) = R_{\beta,n}^{\kappa,k+1}\left(x_{i,p} \right) + \sum_i \left. \frac{\partial R_{\beta,n}^{\kappa,k+1}}{\partial x_i} \right|_p \left(x_{i,p+1} - x_{i,p} \right) = 0$$

(4.17)

$$F^{k+1}\left(x_{i,p+1} \right) = F^{k+1}\left(x_{i,p} \right) + \sum_i \left. \frac{\partial F^{k+1}\left(x_i \right)}{\partial x_i} \right|_p \left(x_{i,p+1} - x_{i,p} \right) = 0$$

(4.18)

Retaining only first order terms, we obtain a set of NEL×NEQ linear equations for the increments ($x_{i,p+1}-x_{i,p}$):

$$-\sum_i \left. \frac{\partial R_{\beta,n}^{\kappa,k+1}}{\partial x_i} \right|_p \left(x_{i,p+1} - x_{i,p} \right) = R_n^{k+1}\left(x_{i,p} \right)$$

(4.19)

$$-\sum_i \left. \frac{\partial F^{k+1}}{\partial x_i} \right|_p \left(x_{i,p+1} - x_{i,p} \right) = F^{k+1}\left(x_{i,p} \right)$$

(4.20)

The fluid flow and reactive solute transport equations are solved iteratively until prescribed convergence criteria are satisfied.

Sequentially Coupled Solution Method for THMC Simulator

In the sequentially coupled solution procedure, fluid flow, heat flow and geomechanics are solved for first, followed by solute transport, and then chemical reactions. For the first part of

this solution, only the mass balances for the three components H_2O, NaCl, and CO_2, and only the mass loss or gain for H_2O and CO_2 in chemical reactions, are considered, along with the energy and momentum conservation equations.

After the above solution, the Darcy velocity for each phase is used to solve for solute transport of the other gaseous and aqueous species. The aqueous species are subject to transport in the liquid phase as well as to local chemical reactions between solid and gas phases. Transport equations are written in terms of primary chemical components. Advection and diffusion processes are considered for chemical transport, and the diffusion coefficients are assumed to be the same for all species.

Finally, chemical reactions are solved for on a grid block by grid block basis. The main equations for chemical reactions are mole balance equations for each primary chemical species and saturation index for mineral and gas species. The chemical reactions for primary species are fed back to the first two steps of this solution for the next iteration.

Verification and Validation of THMC Simulator

The fully coupled THMC model was verified against different analytical solutions for the mechanisms involved in the THMC processes, including equilibrium chemical reactions, kinetic chemical reactions, heat conduction, and consolidation. For the equilibrium chemical reactions and kinetic chemical reactions, the analytical solutions derived by Xu and Pruess (1998, 1999) were used to verify the numerical scheme for chemical reactions in the model. For thermal effects, the analytical solution of a 1D heat conduction problem was derived to verify the heat conduction calculation in the model. For geomechanics, the analytical solution of a 1D consolidation problem was used to verify the model. The verification of the equilibrium chemical reactions is shown below.

1D Reactive Transport with Equilibrium Chemical Reaction

Consider a one-phase, saturated semi-infinite porous medium under steady-state uniform flow. In the porous medium, a mineral *AB(s)* is dissolving into the fluid and releasing chemical species *A* and *B*. This chemical reaction is under equilibrium condition. An analytical solution to this problem was derived by Xu and Pruess (1998, 1999). The saturation index of mineral *AB(s)* controls the local equilibrium of the dissolution/-precipitation of mineral *AB(s)*, and it can be expressed as follows:

$$F_{AB} = \log \Omega_{AB} = \log \left\{ \frac{c_A c_B}{K_g} \right\} = 0 \tag{4.21}$$

where F_{AB} is the saturation index of mineral *AB(s)*, and K_{AB} is the equilibrium constant for mineral AB(s).

Values for simulation parameters are shown in Table 4.31. Figure 4.23 shows the numerical and analytical solutions for this problem. The numerical results agree well with the analytical solution.

Table 4.31: Initial parameters for 1D Reactive Transport with Equilibrium Chemical Reaction.

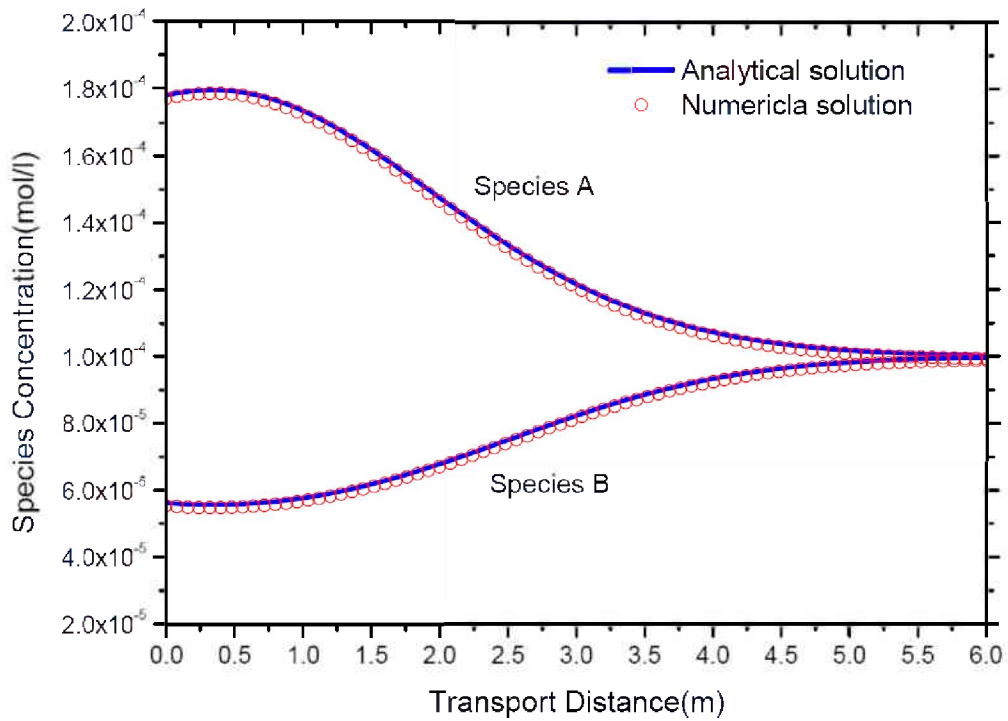| Parameter	Value
Formation length	6.0 m
Grid size	0.04 m
Porosity	0.30
Equilibrium constant	10^{-8}
Dispersion coefficient	$1 \ m^2/s$
Simulation time	1.5 days
Pore velocity	0.1 m/day
Initial concentrations	
Chemical species A	10^{-4} mole/l
Chemical species B	10^{-4} mole/l
Inlet concentration difference	2×10^{-3} mole/l

Figure 4.23. Concentration profiles for two species A and B in a problem involving dissolution of a mineral AB(s) under conditions of local equilibrium

Applications in CO₂ Geo-sequestration

The sequentially and fully coupled THMC models are applied to simulate fluid transport, geomechanics, and geochemistry in saline aquifers during CO2 injection and sequestration periods. The geomechanical processes affect mean stress, volumetric strain, rock permeability and porosity. In addition, the geochemical processes, namely the geochemical reactions of rock minerals, gaseous CO2 and formation fluid, affect the solubility of gaseous CO2, rock permeability, and porosity. Nine simulation examples were presented to simulate the THMC processes during CO2 injection and geo-sequestration processes. The first three cases are THC models to test the validity of the chemical reaction calculation by the fully coupled THMC simulator: two batch reaction models and one 1D reactive transport model. The next three cases are THMC models to simulate THMC processes during CO2 injection and sequestration periods by the sequentially coupled simulator: one 1D THMC model with complex chemical reactions and geomechanics, one 2D THMC model with complex chemical reactions and geomechanics, and one 2D layered model with complex chemical reactions and geomechanics. The last three cases are THMC models to evaluate the effects of CO2 dissolution, chemical equilibrium reactions, and chemical kinetic reactions on THMC processes by fully coupled simulator. Two of these are illustrated below, a THC batch reaction model to test the validity of the chemical reaction calculations and a THMC model to evaluate the effects of CO2 dissolution, chemical equilibrium reactions, and chemical kinetic reactions.

Batch Reaction with Equilibrium Chemical Reactions

The objective of this example is to validate the equilibrium chemical reaction calculation with the TOUGHREACT simulator. The batch reactor has a single grid cell. There are three phases: aqueous, gaseous, and solid. The chemical reactions for this system are equilibrium ones and consist of various reactions centered around H_2O, CO_2, $CaCO_3$ and $NaCl$ components. The aqueous phase consists of H_2O, dissolved CO_2, various ions, and other reaction products; the solid phase consists of $CaCO_3$ and the gaseous phase consists of CO_2 and vaporized H_2O. The six primary species are: H_2O, H^+, Ca^{2+}, Na^+, HCO^{-3}, and Cl^-. There are twelve aqueous chemical reactions, one gas dissolution and one calcite dissolution, shown below:

$$CO_2 \,(aq) \leftrightarrow H^+ + (HCO_3)^- - H_2O \tag{4.22}$$

$$(CO_3)^{2-} \leftrightarrow (HCO_3)^- - H^+ \tag{4.23}$$

$$OH^- \leftrightarrow H_2O - H^+ \tag{4.24}$$

$$CaCl^+ \leftrightarrow Ca^{2+} + Cl^- \tag{4.25}$$

$$CaCl_2 \,(aq) \leftrightarrow Ca^{2+} + 2Cl^- \tag{4.26}$$

$$CaCO_3 \,(aq) \leftrightarrow Ca^{2+} + (HCO_3)^- - H^+ \tag{4.27}$$

$$(CaHCO_3)^+ \leftrightarrow Ca^{2+} + (HCO_3)^- \tag{4.28}$$

$$Ca(OH)^+ \leftrightarrow Ca^{2+} + H_2O - H^+ \tag{4.29}$$

$$NaCl\,(aq) \leftrightarrow Na^+ + Cl^- \tag{4.30}$$

$$Na(CO_3)^- \leftrightarrow Na^+ + (HCO_3)^- - H^+ \tag{4.31}$$

$$NaHCO_3\,(aq) \leftrightarrow Na^+ + (HCO_3)^- \tag{4.32}$$

$$Na(OH) \leftrightarrow Na^+ + H_2O - H^+ \tag{4.33}$$

The calcite dissolution, occurring between solid and aqueous phases, is:

$$CaCO_3\,(S) \leftrightarrow Ca^{2+} + (HCO_3)^- - H^+ \tag{4.34}$$

The gas dissolution, occurring between gaseous and aqueous phases, is:

$$CO_2\,(g) \leftrightarrow H^+ + (HCO_3)^- - H_2O \tag{4.35}$$

These equilibrium constants for these chemical reactions are calculated from the EQ3/6 database (Wolery, 1992), and are shown in Table 4.32.

Table 4.32. Equilibrium constants for chemical reactions in the batch system.

Chemical Reactions	log Keq at 75 °C
$CO_2\left(aq\right) \rightleftharpoons H^+ + HCO_3^- - H_2O$	-6.296079058
$CO_3^{2-} \rightleftharpoons HCO_3^- - H^+$	10.09857011
$OH^- \rightleftharpoons H_2O - H^+$	12.70652234
$CaCl^+ \rightleftharpoons Ca^{2+} + Cl^-$	0.508190954
$CaCl_2\left(aq\right) \rightleftharpoons Ca^{2+} + 2Cl^-$	0.549797292
$CaCO_3\left(aq\right) \rightleftharpoons Ca^{2+} + HCO_3^- - H^+$	6.248545668
$CaHCO_3^+ \rightleftharpoons Ca^{2+} + HCO_3^-$	-1.247810694
$Ca\left(OH\right)^+ \rightleftharpoons Ca^{2+} + H_2O - H^+$	11.21829089
$NaCl\left(aq\right) \rightleftharpoons Na^+ + Cl^-$	0.582622874
$NaCO_3^- \rightleftharpoons Na^+ + HCO_3^- - H^+$	10.26267908
$NaHCO_3\left(aq\right) \rightleftharpoons Na^+ + HCO_3^-$	0.23805711
$Na\left(OH\right)\left(aq\right) \rightleftharpoons Na + H_2O - H^+$	12.88172362
$CaCO_3\left(s\right) \rightleftharpoons Ca^{2+} + HCO_3^- - H^+$	1.114784395
$CO_2\left(g\right) \rightleftharpoons H^+ + HCO_3^- - H_2O$	-8.168289161

The initial pressure is 2.0×10^7 Pa, the temperature is 75 °C, the initial gas saturation is 0.5, the initial porosity is 0.3, and the rock is 50 volume percent $CaCO_3(s)$ and the rest non-reactive. The initial concentrations of aqueous species are given in the second column of Table 4.33. The geochemical reaction system is in equilibrium, so the system reaches equilibrium once CO_2 contacts the aqueous phase. The simulation results from this model are shown in column three, those from TOUGHREACT are shown in column four, and the error between the two in column five of Table 4.33. The maximum error is 5.25% of the dissolved concentration for CO_2 gas. This error may result from different calculations for the gas properties. A real gas law in used in the fully coupled simulator, but TOUGHREACT uses an ideal gas law. The two dissolution reactions for CO_2 gas and calcite dominate the batch reaction system. The concentrations of CO_2 (aq) and Ca^{2+} have a dramatic increase due to dissolution of CO_2 and calcite.

Table 4.33. Comparison between the fully coupled simulator and TOUGHREACT.

Species	Initial data	Fully-coupled Model	TOUGHREACT	Errors (%)
H_2O	1.000777701	1.031017331	1.031033599	0.001577854
H^+	3.086551864E-05	2.4055743895E-05	2.320015337E-05	3.687865815
Ca^{2+}	4.480199727E-03	3.7897236091E-02	3.724830775E-02	1.742168652
Na^+	0.900002495	0.89104278323	0.891138857	0.010781010
HCO_3^-	1.997463783E-03	6.4692789596E-02	6.338577944E-02	2.061992718
Cl^-	0.91063342	0.912581963	0.912466106	0.012697125
OH-	1.434349562E-08	1.892240965E-08	1.9503686368E-08	2.980342807
$CaCl^+$	1.724770935E-04	1.393001567E-03	1.3709958965E-03	1.605086527
$CaCl_2(aq)$	5.920365310E-05	4.642689752E-04	4.5762974529E-04	1.450786367
NaCl(aq)	8.929786726E-02	8.604992977E-02	8.6185575073E-02	0.15738748
$NaHCO_3(aq)$	4.299625245E-04	1.336103042E-02	1.3114010731E-02	1.88363186
$CaHCO_3^+$	2.141691073E-05	5.577979596E-03	5.3798849686E-03	3.682135008
$CO_2(aq)$	4.313682112E-02	1.032978014	0.98246004305	5.141987347
CO_3^{2-}	3.706358704E-08	1.625055163E-06	1.6483202384E-06	1.411441489
$CaCO_3(aq)$	2.193772781E-08	7.349152087E-06	7.3491650522E-06	0.000176421
$CaOH^+$	2.770726632E-10	2.960947889E-09	3.0037454186E-09	1.424805505
NaOH(aq)	3.695749549E-09	4.712255947E-09	4.8647524129E-09	3.134722045
$NaCO_3^-$	3.145720198E-09	1.297723419E-07	1.3184608858E-07	1.572854132
$CaCO_3(s)$	0.0	-4.1862475439E-02	-4.096034049E-02	2.202459596
$CO_2(g)$	0.0	1.0623616063	1.009385089	5.248395074
P_{co2}(bar)	197.7152456	177.226201	168.4964335	5.180980581

Note: The unit of the concentration of aqueous species is mol/l; Minus sign of $CaCO_3$ concentration means dissolution concentration of solid $CaCO_3$ into aqueous phase; CO_2 concentration means dissolution concentration of gaseous CO_2 into aqueous phase; P_{CO2} is the partial pressure of gaseous CO_2.

THMC Model with CO_2 Dissolution

The objective of this THMC model is to exam the effects of CO_2 gas dissolution on the THMC processes of CO_2 sequestration. The chemical reaction system is defined as pure CO_2 dissolution.

This chemical reaction system does not consider any chemical equilibrium and kinetic reaction between mineral and aquifer water.

The 1D model is radial and contains a CO_2 injection well at the center. The top and bottom are sealed by upper caprock and lower bedrock. This sandstone aquifer is initially homogenous and isotropic. The hydro-geological properties of the model are given in Table 4.34.

Table 4.34. Initial parameters for the THMC Model.

Hydrological parameter	
Permeability	10^{-13} m^2
Formation thickness	100 m
Formation length	10000 m
Porosity	0.30
Temperature	75 °C
Initial pressure	2×10^7 Pa
CO2 injection rate	90 kg/s
CO2 enthalpy	5.632×10^5 J/kg
Relative permeability	
Liquid	van Genuchten function (1980)
Gas	Corey function (1954)
Capillary pressure	van Genuchten function (1980)
Stress	
Biot coeffcient	1.0
Poisson's ratio	0.25
Young's modulus	5.0×10^9 Pa
Initial mean stress	4.71×10^7 Pa
Linear thermal expansion	1×10^{-5} 1/°C

The temperature of injected CO_2 is 32 °C, in order to keep it under supercritical conditions. The model is discretized logarithmically into 100 grid blocks in the radial direction. Only small amounts of primary chemical species are in the original aquifer water. The initial concentrations of $H+$ and HCO^{-3} are 0.4320×10^{-8} mol/l and 0.1960×10^{-7} mol/l, respectively. The boundary conditions of constant pressure and mean stress are assigned to the outer radius of the simulation model. All of the aqueous chemical reactions are in equilibrium. These reactions are:

$$OH^- \leftrightarrow H_2O - H^+ \tag{4.36}$$

$$(CO_3)^{2-} \leftrightarrow (HCO_3)^- - H^+ \tag{4.37}$$

$$CO_2 (aq) \leftrightarrow H^+ + (HCO_3)^- - H_2O \tag{4.38}$$

In addition, gas dissolution, occurring between gaseous and aqueous phases, is:

$$CO_2 (g) \leftrightarrow H^+ + (HCO_3)^- - H_2O \tag{4.39}$$

There are three primary aqueous species (H_2O, H+, and HCO^{-3}) and one primary gaseous species (CO_2) that are associated with the mass balances, one saturation index equation to solve for CO_2 dissolution, one energy balance equation is to for solve temperature, and one momentum balance equation to solve for mean stress. This fully coupled system thus contains seven equations and the same number of unknowns. Some results for the non-isothermal case are shown in Figures 4.24-4.29.
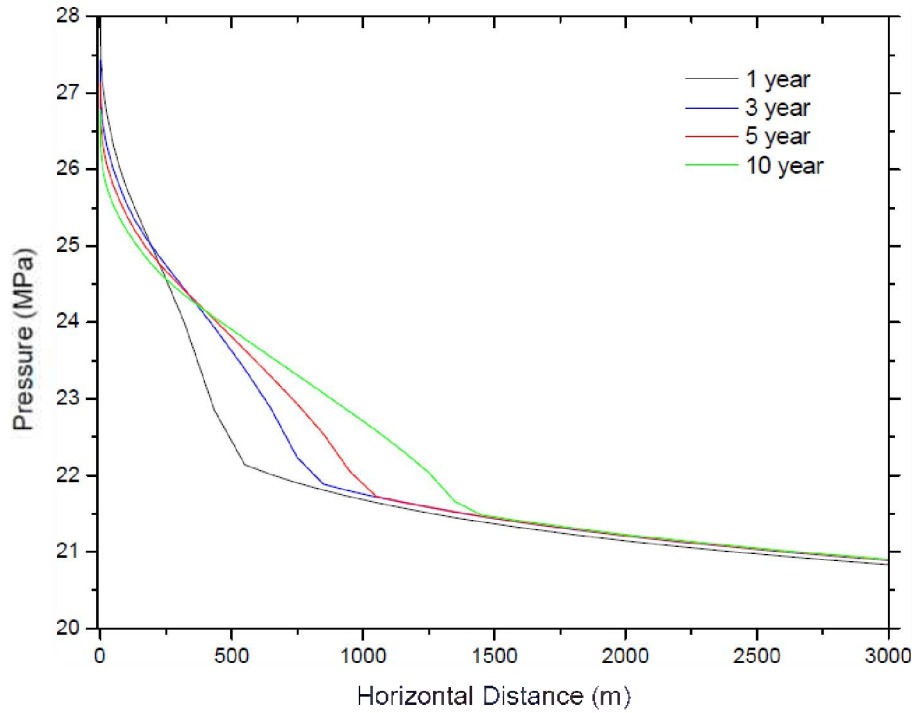

Figure 4.24. Pressure evolution subjected to supercritical CO_2 injection
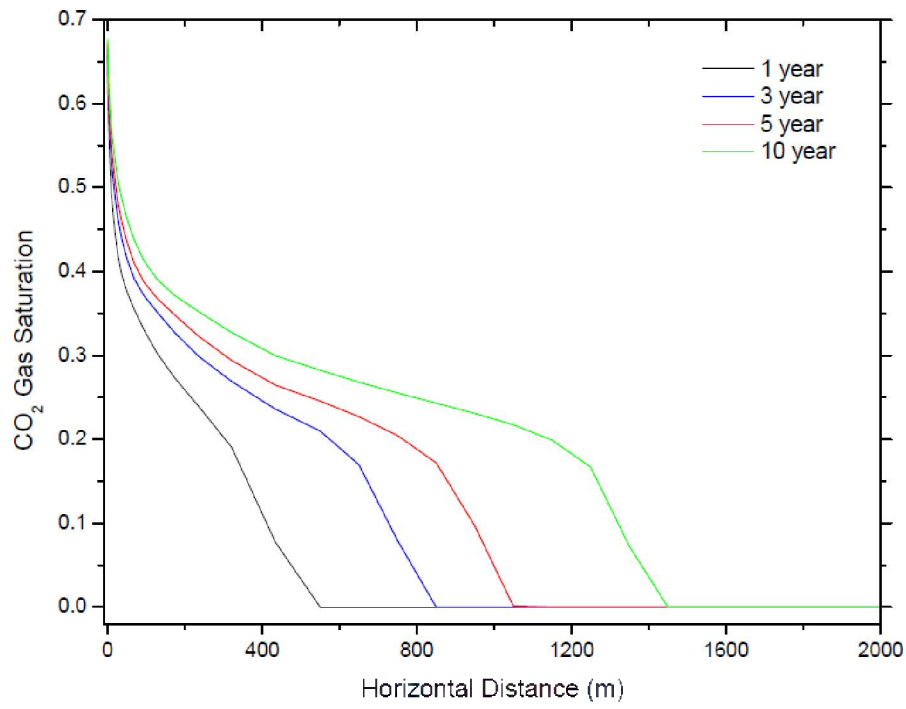
Figure 4.25. CO_2 gas saturation evolution subjected to supercritical CO_2 injection.
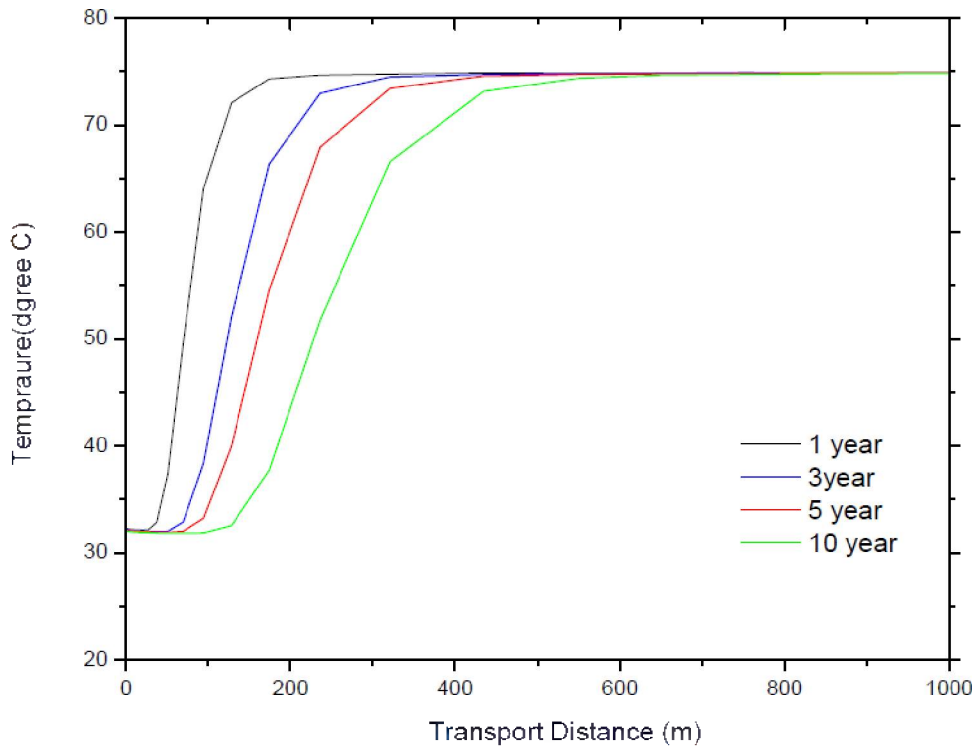
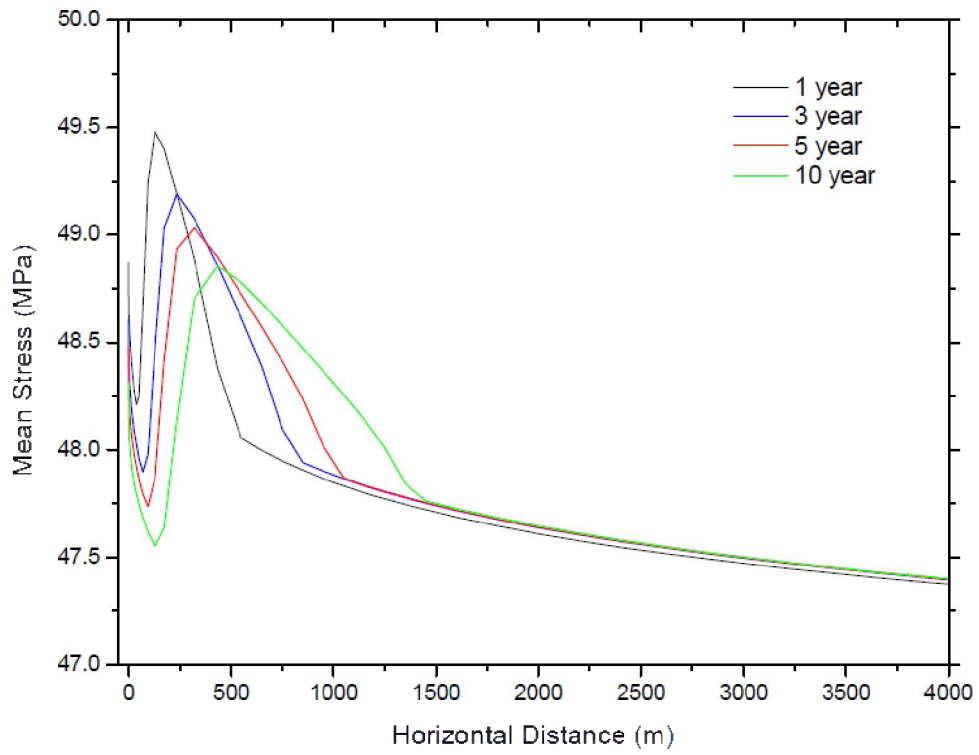Figure 4.26. Temperature evolution subjected to low temperature supercritical CO_2 injection.

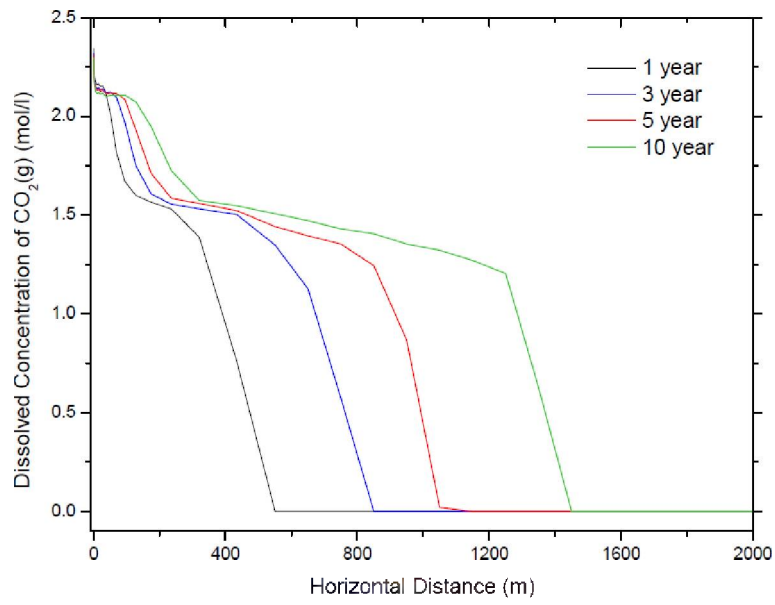Figure 4.27. Mean stress evolution subjected to low temperature supercritical CO_2 injection.

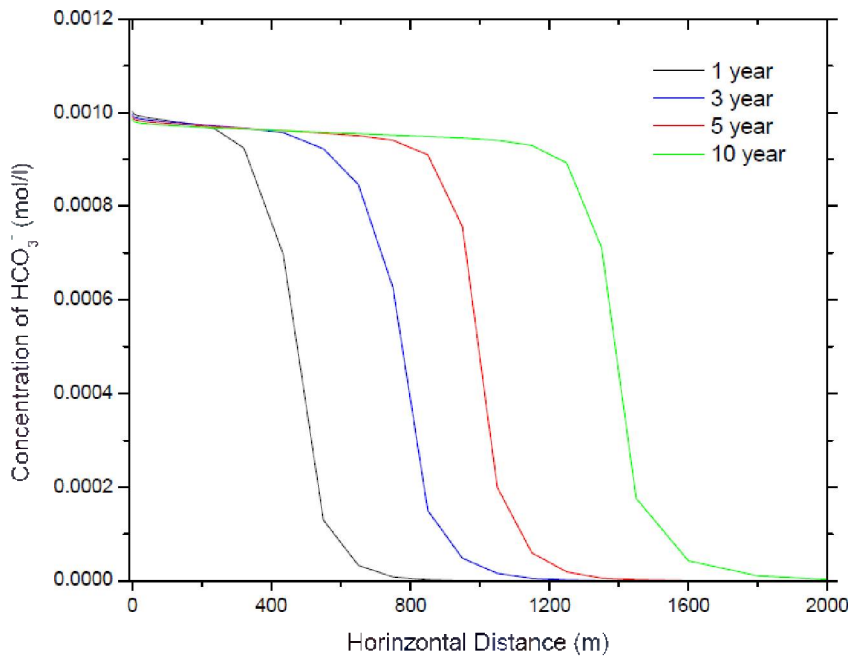Figure 4.28. Dissolved concentration of $CO_2(g)$ in aqueous phase for nonisothermal case.

Figure 4.29. Concentration of bicarbonate ion subjected to supercritical CO_2 injection.

In Figure 4.24, the pressure continues to build up in the two phase areas (shown later in Figure 4.25), and then moves laterally past that area. The pressure near the injection point continues to increase after the first year, and then tends to decrease later along with increasing pressure in the far end of the aquifer. The pressure profiles in the two phase area have a high slope compared with the single phase gas and water areas.

Figure 4.25 shows the CO_2 saturation profile during 10 years of CO_2 injection. The CO_2 gas front is located at 550 m after 1 year, 850 m after 3 years, 1,150 m after 5 years, and 1,450 m after 10 years. The two phase gas-liquid zone exists within these intervals, and the pressure buildup is significant in this zone.

Figure 4.26 shows the spatial distribution of temperature. Gaseous CO_2 with a temperature of 32 °C is injected into the formation. The temperature front moves with the CO_2 gas that moves laterally. The thermal effect has a significant impact on the temperature of the model. The temperature of formation becomes 32 °C within 38 m of the wellbore after 1 year, 70 m after 3 years, 95 m after 5 years and 130 m after 10 years.

Figure 4.27 shows the mean stress profile. The thermal effect has a significant impact on the mean stress profile. An interval subjected to low temperature supercritical CO_2 shows a decrease in mean stress. Mean stress decreases significantly with a maximum value of 2×10^6 Pa in the low temperature area in Figure 4.26.

Figure 4.28 shows the concentration of dissolved $CO_2(g)$. The CO_2 dissolution only occurs within the two phase $CO_2(g)$-H_2O area. The maximum dissolved concentration of $CO_2(g)$ occurs near the wellbore with a value of 2.32 mol/l. The thermal effect has a significant impact on chemical reactions. Low temperature can help more supercritical CO_2 to dissolve into the aqueous phase, and assist in solubility trapping of supercritical CO_2.

Figure 4.29 shows the spatial distribution of the concentration of HCO^{-3}. This chemical species as a byproduct of CO_2 dissolution.

Summary and Conclusions

We developed a novel mathematical model of THMC processes in porous and fractured saline aquifers. The novel framework models were designed to keep a generalized computational structure, which can be easily applied for the numerical simulation of other THMC processes. In this case, we are simulating geo-chemical reactions associated with CO_2 sequestration in saline aquifers. Two computational frameworks, sequentially coupled and fully coupled, were used to simulate the reactions and transport.

We verified capabilities of the THMC model to treat complex THMC processes during CO_2 sequestration by analytical solutions and we constructed reactive transport models to analyze the THMC process quantitatively. We presented here one of these analytical solutions, 1D reactive transport under chemical equilibrium. We also presented here two of the reactive transport models, a batch reaction model with equilibrium chemical reactions and a THMC model with CO_2 dissolution. The analytical solutions were matched well by simulation. Some findings from

the reactive transport models include the following. The long term fate of supercritical CO_2 under the subsurface is to be sequestrated permanently as rock mineral in the form of carbonates. Structural trapping is the dominant sequestration mechanism during the supercritical CO_2 injection period, and mineral trapping is the dominant one during the long term storage period. In a typical sandstone formation, with 60 percent quartz, 30 percent plagioclase feldspar minerals, 5 percent chlorite minerals, and 5 percent clay minerals, the efficacy of solubility trapping is 20 percent at the early injection period, which decreases to 12 percent after 10,000 years; the efficacy of mineral trapping is zero percent at early the injection period, and increases to 65 percent after 10,000 years. For coupled THMC processes during CO_2 sequestration, the geochemical reactions do not have a significant impact on pore pressure, mean stress and temperature, but the thermal energy transport affects those and the geochemical reactions in the saline aquifer, especially for cold CO_2 injection into a deep saline aquifer. Low temperatures also accelerates equilibrium dissolution of gas and minerals, but slows down kinetic dissolution/precipitation of minerals, such as anorthite and kaolinite.

Task 5.0: Study of Instability of CO_2 Dissolution-Diffusion-Convection Processes

Literature Survey

Density-driven flows in porous media play important roles in a wide variety of applications, such as reservoir engineering, geothermal reservoirs, agricultural product storage system, packed-bed catalytic reactors, and pollutant transport underground and in the atmosphere. Studies on density-driven flows that are directly related to geological CO_2 sequestration are relatively few. The majority of these studies are theoretical and numerical in nature; only few papers present experimental results on CO_2 diffusion-convection processes. A review of these studies is presented below.

Density-driven flow caused by a concentration gradient has a significant effect on fluids mixing in a porous medium under certain conditions. For CO_2 sequestration in saline aquifers, three mechanisms contribute to the mixing of CO_2 with formation brine and dissolution (Ennis-King and Paterson, 2003). These mechanisms are: diffusion of CO_2 into the aqueous phase, reactions in the aqueous phase between dissolved CO_2 and minerals that depletes dissolved CO_2 and draws more dissolution, and convective mixing triggered by the 1% density difference between brine saturated with CO_2 and unsaturated brine. The convective mixing process, in particular, takes place when the brine underlying the gas phase carbon dioxide beneath the seal becomes saturated with dissolved gas. With the creation of a density inversion, when the layer of saturated brine becomes thick enough, an instability occurs and plumes of brine saturated with CO_2 migrate downwards, slowly being diluted as they go. The importance of the convection is that it increases the mixing and dissolution rates by orders of magnitude above pure diffusion. For storage in a formation with no structural closure, the competition between updipping migration and dissolution determines the ultimate distance that the injected carbon dioxide would migrate from the injection site and this has significant bearing on the choice of suitable storage sites.

A lot of theoretical work has been done on the modeling of density-driven flows. Since the governing differential equations are highly non-linear and strongly coupled through dependency of density and viscosity to pressure, temperature, and concentration, there is no analytical solution and numerical methods are necessary to predict flow and transport behavior.

Lindeberg and Wessel-Berg (1996) first proposed that injection of CO_2 into a saline formation and its subsequent diffusion in long times might result in vertical convection. In the same year, they analyzed the basic equations for heat and CO_2 transport which was subject to both temperature variations and molecular diffusion. Real data from North Sea sequestration reservoirs were used to calculate the corresponding Rayleigh numbers, and the conditions under which vertical convective flow might occur were evaluated in media subjected to both thermal gradients and the presence of a CO_2 dissolution-induced dense layer.

Ennis-King and Paterson (2002) used the TOUGH2 simulator to evaluate the CO_2 dissolution rate due to convective mixing. In the same year, they presented that diffusion of CO_2 into the brine layer beneath the CO_2-cap makes CO_2-saturated brine denser than the surrounding unsaturated brine in the lower layers. The existence of denser fluid on top of a lighter fluid

makes the system unstable, and convective mixing is then generated. They found that convective mixing can considerably improve the rate of CO_2 dissolution in the brine. The important issue in their model was that they decoupled the multi-phase flow and convection-diffusion processes by simply imposing a boundary condition on top of the brine layer.

Ennis-King and Paterson (2003) performed a linear stability analysis to investigate the role of anisotropy with respect to the onset of convection and compared that with results from numerical flow simulations. Then, Ennis-King *et al.* (2005) developed new results of the onset of convection for a porous medium with anisotropic permeability subject to a rapid change in boundary conditions. Linear stability analysis and the energy method were used to define the critical time at which the instability occurred and the dimensionless Rayleigh-Darcy number for both thermal and solute-driven convection in an infinite horizontal slab. This was then applied to determine the critical time for the geological storage of carbon dioxide. The time scale for the onset of convection in geological storage could range from less than a year (high-permeability formations) to decades or centuries (low-permeability ones).

Hassanzadeh *et al.* (2005) presented numerical modeling of convective mixing for geological storage of CO_2 in saline aquifers. They pointed out that the time to the onset of instability depends on the Rayleigh number and the heterogeneity of the formation. Two field scale problems were studied. The first case was based on the Nisku aquifer; more than 60% of the ultimate dissolution was achieved after 800 years. The second case was for the Glauconitic sandstone aquifer where there was no convective instability.

Riaz *et al.* (2006) used linear stability analysis based on the dominant mode of the self-similar diffusion operator to find a scaling relationship for onset of natural convection. The nonlinear simulations at short times showed good agreement with the linear stability predictions. The dimensional analysis for typical aquifers shows that for a permeability variation of 1-3000 mD, the critical time can vary from 2000 years to about 10 days while the critical wavelength can be between 200 m and 0.3 m.

Xu *et al.* (2006a) also used linear stability analysis and global stability analysis to develop a scaling relationship for onset of convection. The results obtained from these two approaches indicated that an anisotropic system for CO_2 sequestration becomes more unstable when either the vertical or horizontal permeability increases.

Hassanzadeh *et al.* (2006 and 2007) studied the effect of various boundary and initial conditions on the onset of convection in a homogenous and isotropic porous medium using linear stability analysis. They applied the theoretical result to 24 cases in the Alberta basin aquifers and found that more than 50% of the aquifers in the Alberta basin are likely to develop convection over a long period of time and only ten sites had pure diffusive mixing corresponding to cases with low Rayleigh numbers. The onset time of convection was in the range between 1 year and 310 years, and the wavelength was between 1.6 m and 39 m.

Farajzadeh *et al.* (2007) studied the transient density-driven natural convection problem when the top of the porous medium initially saturated with a liquid is exposed to a CO_2 rich gaseous phase, and quantified it numerically. The simulation results showed that the nonlinear behavior

of the flow was strongly dependent on the Rayleigh number. With increasing Rayleigh number, natural convection effects become more significant.

Ennis-King and Paterson (2007) investigated the effect of coupling of geochemical reactions with convective mixing of dissolved carbon dioxide during geological storage by both analytical and numerical techniques. By means of scaling arguments and stability analysis, they found that the time for the onset of convection could be increased by up to an order of magnitude due to consumption of dissolved carbon dioxide via mineralization.

Hong and Kim (2008) extended the instability study considered by Ennis-King *et al.* (2005), Xu *et al.* (2006a), and Hassanzadeh *et al.* (2006) by employing the energy method and linear amplification theory to the larger time domains and anisotropic cases. The resulting stability criteria compared reasonably well with previous theoretical predictions. The anisotropy effect made the system more stable and decelerated the dissolution process.

Rapaka *et al.* (2008) described and used the non-modal stability theory to compute maximum amplifications possible, optimized over all possible initial perturbations. They also presented the details of three-dimensional spectral calculations of the governing equations. The results of the amplifications predicted by non-modal theory compared well to those obtained from the spectral calculations. Then, Rapaka *et al.* (2009) extended the analysis conducted by Rapaka *et al.* (2008) to the important cases of anisotropic and layered porous media with a permeability variation in the vertical direction. Green and Ennis-King (2009, 2010) also extended the study with anisotropic permeability to a vertical heterogeneity model consisting of a random and uncorrelated distribution of horizontal impermeable barriers with a given overall volume fraction and a given distribution of lengths. Numerical simulations were carried out on 2D vertical sections for deep CO_2 injection in heterogeneous formations and convection of dissolved CO_2, using multiple realizations for the permeability distribution.

Javaheri *et al.* (2009a, b) applied the linear stability analysis of density-driven miscible flow for CO_2 sequestration to deep inclined and homogeneous saline aquifers. The effect of inclination and its influence on the pattern of convection cells was investigated and the results were compared with the horizontal layer. In the same year, they investigated the onset of double-diffusive buoyancy-driven flow resulting from vertical temperature and concentration gradients in a horizontal layer of a saturated and homogenous porous medium using amplification factor theory. The effect of geothermal gradient was considered in this work as a second incentive for convection and the double-diffusion convection. It was indicated that the geothermal effects on the onset of natural convection are negligible compared to the solute effects induced by dissolution and diffusion of CO_2 in deep saline aquifers.

In the above literature review, a number of theoretical and numerical studies on density driven flow for CO_2 sequestration in deep saline aquifers were conducted. The literature search showed that only limited experimental data exist on accelerated mass transfer of CO_2 into reservoir brine due to density driven convective mixing under realistic reservoir conditions. Yang and Gu (2006) studied the mass transfer of CO_2 into a reservoir brine sample experimentally at high pressures and elevated temperatures. They determined the mass-transfer rate of CO_2 into the brine by monitoring the pressure decay inside a closed, visual, high-pressure PVT cell. The detailed

experimental results showed that the density-driven natural convection greatly accelerates the dissolution process of CO_2 in brine. Farajzadeh *et al.* (2009) did a series of experiments performed in a cylindrical PVT-cell at a pressure range of 10-50 bars, where a fixed volume of CO_2 gas was brought into contact with a column of distilled water. The results showed that the mass transfer rate across the interface was much faster than predicted by Fickian diffusion, the mass transfer rate increased with increasing initial gas pressure and in the long term it was controlled by diffusion. The diffusion-convection flow observed in experiments was studied by theoretical interpretation, indicating good agreement between the experiments and the theoretical results.

Kneafsey and Pruess (2010) presented the results of a series of CSC laboratory tests performed in transparent Hele-Shaw cells containing water overlain by gas. Laboratory flow visualization tests in transparent Hele-Shaw cells performed to elucidate the processes and rates of the CO_2 solute-driven convection (CSC). Observed CO_2 uptake of the convection system indicated that the CO_2 dissolution rate was approximately constant for each test and was far greater than expected for a diffusion-only scenario. Numerical simulations of the system showed good agreement with the experiments for onset time of convection and advancement of convective fingers.

Theoretical and Numerical Characterization of the Instability

We used our modified TOUGH2-MP to run a simulation, based on Pau *et al.* (2010), that models the density-driven flow instability that would occur during CO_2 sequestration. The simulation was two-dimensional with impermeable top and bottom boundaries and periodic left and right ones. Above the top layer was CO_2-saturated brine that diffused through the impermeable top into the simulation domain. The CO_2 would then dissolve in the aqueous phase at the system top boundary, increasing its density. Eventually, density-driven convective flow would force this fluid to the system bottom. The temperature was 45 °C and the pressure was 100 bar, typical of conditions at 1000 m depth in the earth. The diffusivity of CO_2 was $2 \cdot 10^{-9}$ m^2/sec. Permeability and porosity varied randomly in the simulation domain to facilitate density-driven convection. Average permeability was $9.9 \cdot 10^{-12}$ m^2 (10 Darcy) and average porosity was 0.30; point permeability and porosity values fluctuated randomly plus or minus one percent around the average. The system was a 1 m square and was discretized into a 100 x 100 grid. Figure 5.1 shows CO_2 mass fraction at 8.33 days. Density fingers are starting to form uniformly along the entire top boundary. These fingers start to coalesce, and by 16.67 days in Figure 5.2 and 20.83 days in Figure 5.3, only a few prominent fingers are present.
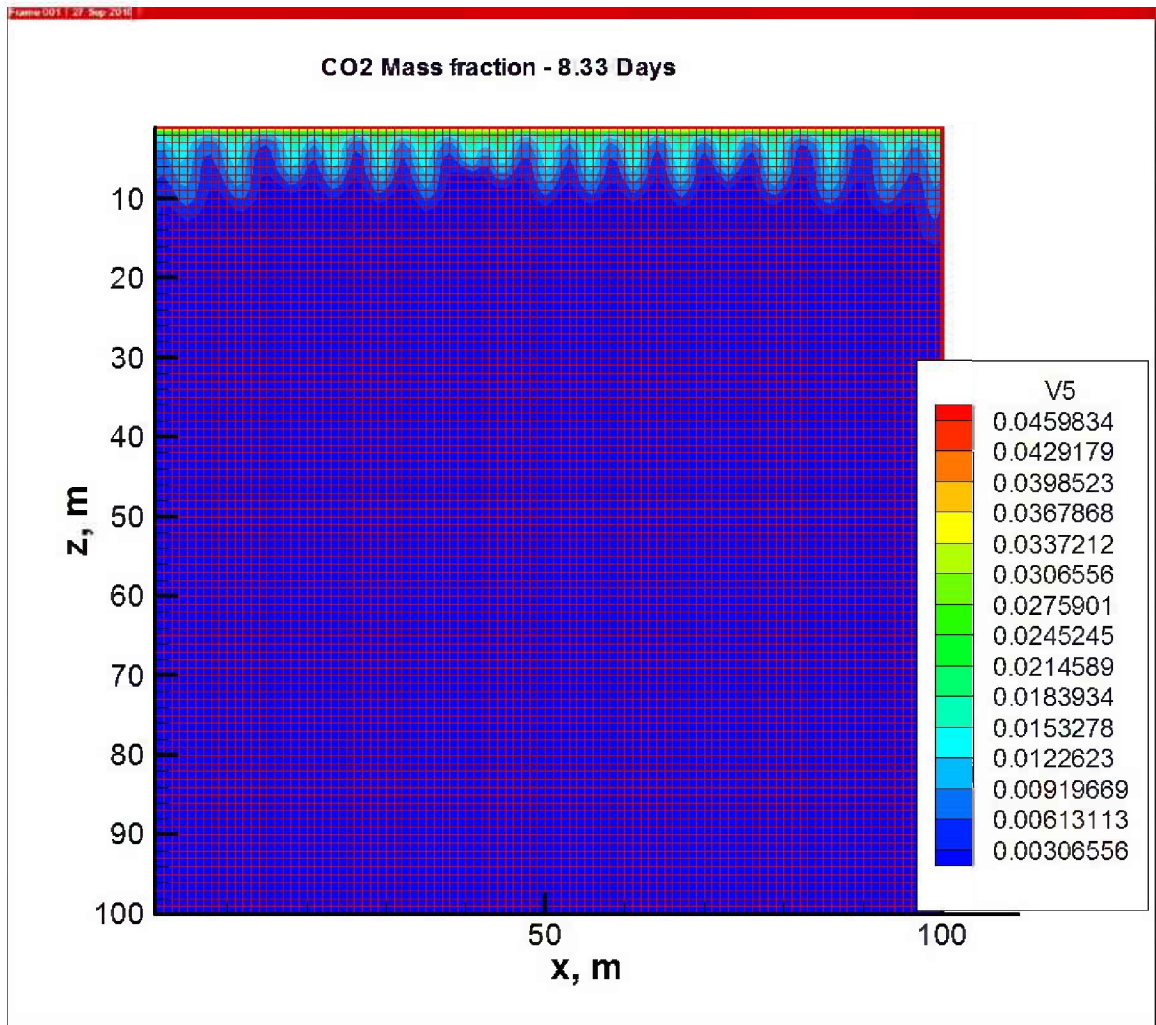
Figure 5.1. CO$_2$ mass fraction at 8.33 days for two-dimensional simulation.
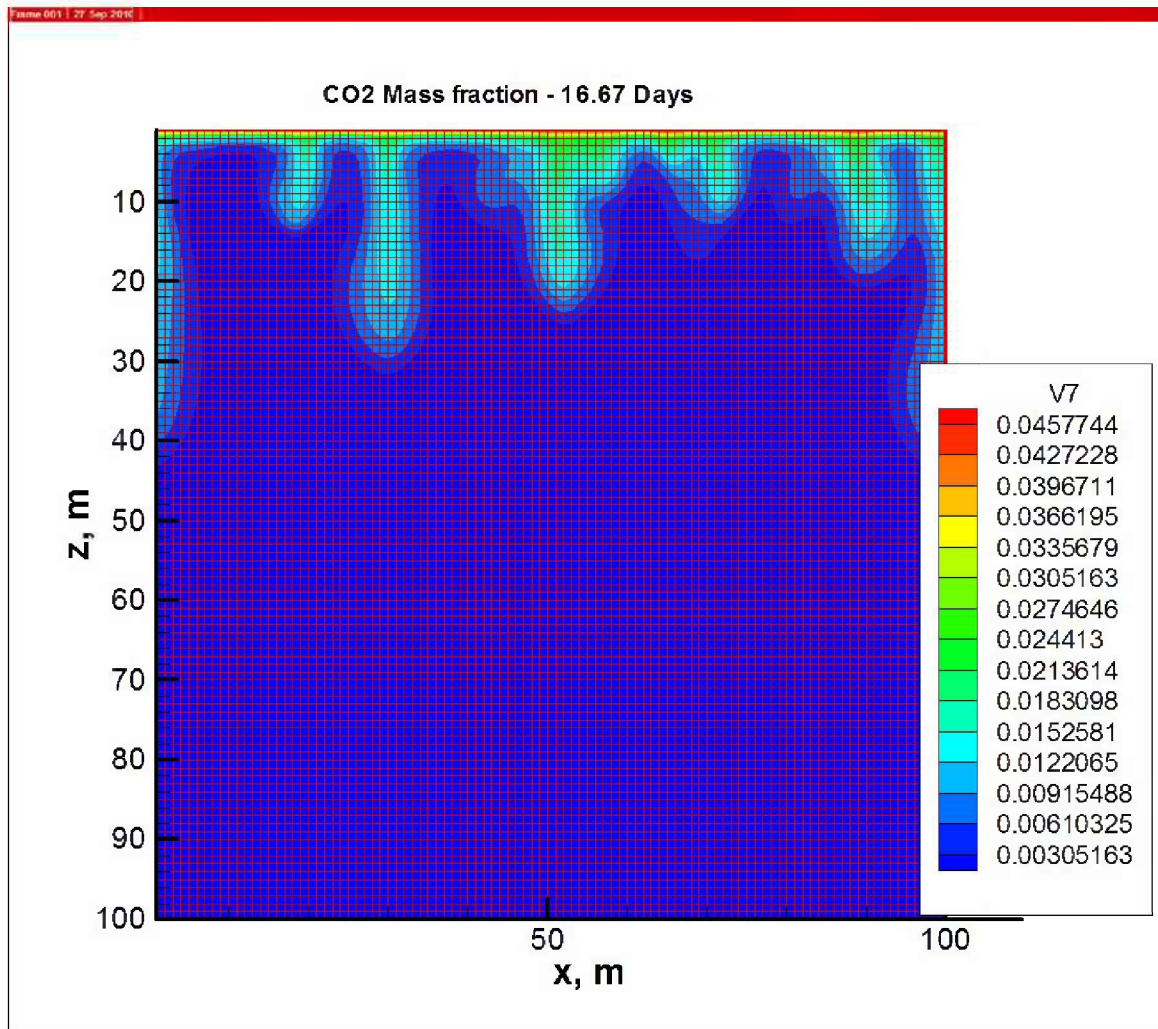
CO2 Mass fraction - 16.67 Days

Figure 5.2. CO$_2$ mass fraction at 16.67 days for two-dimensional simulation.
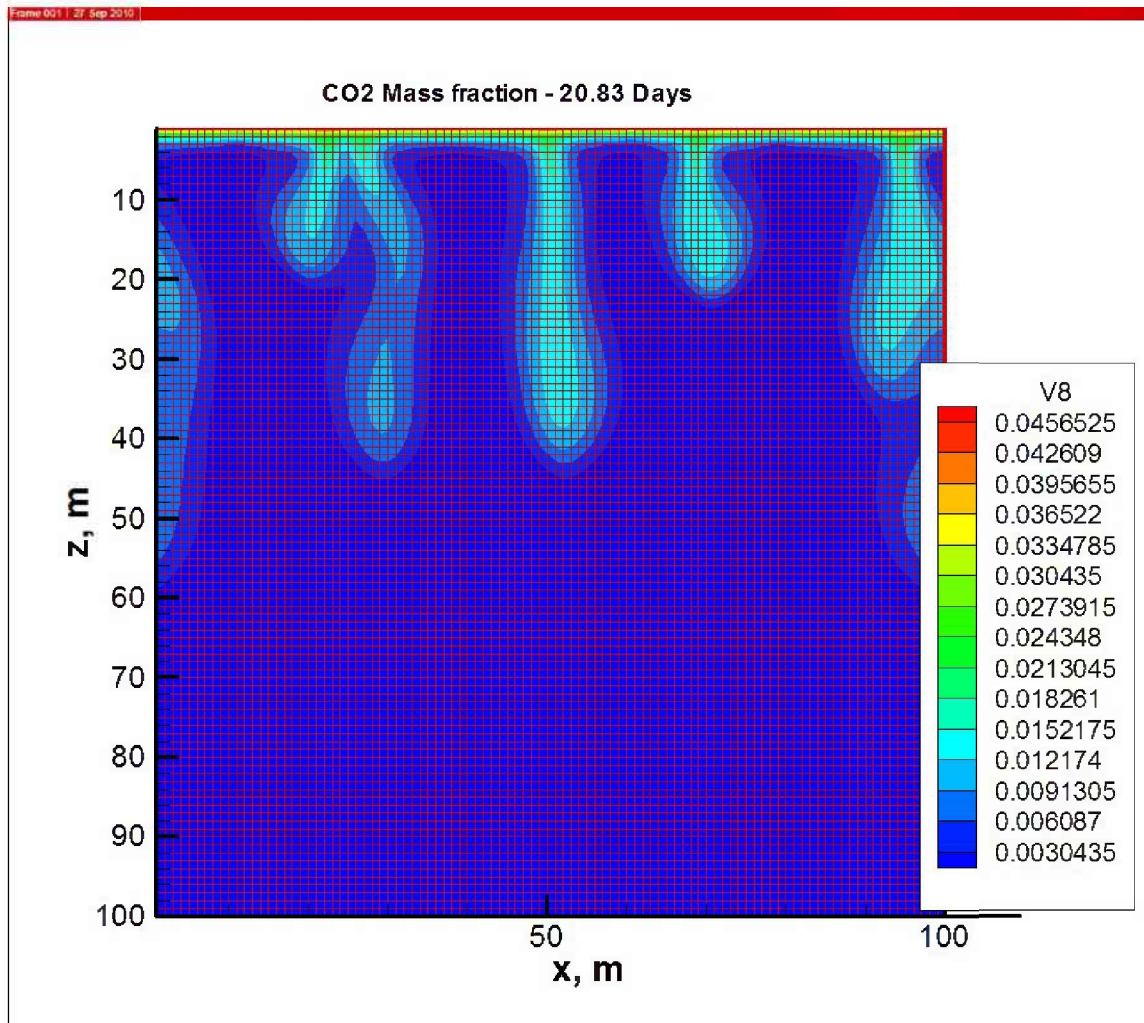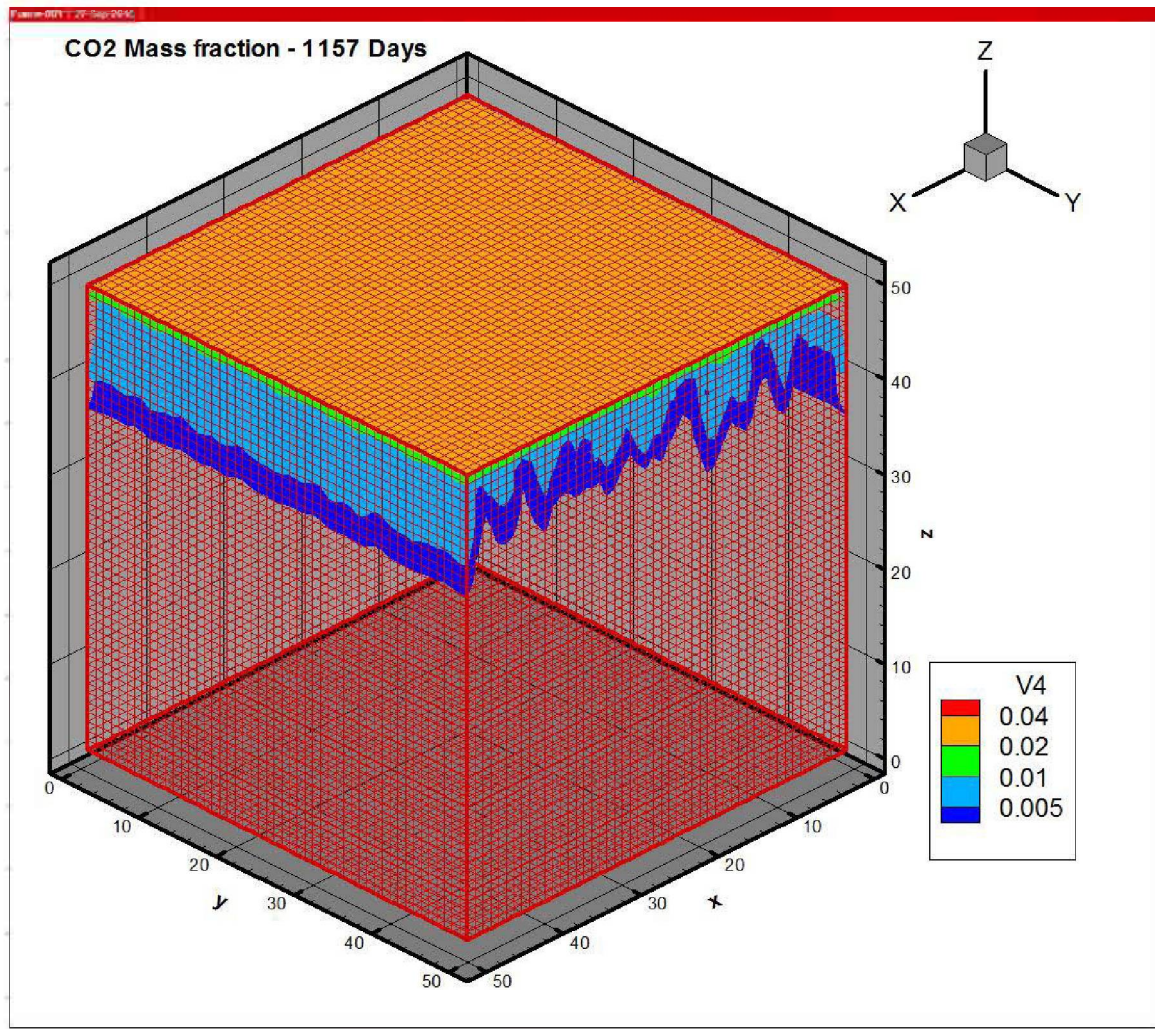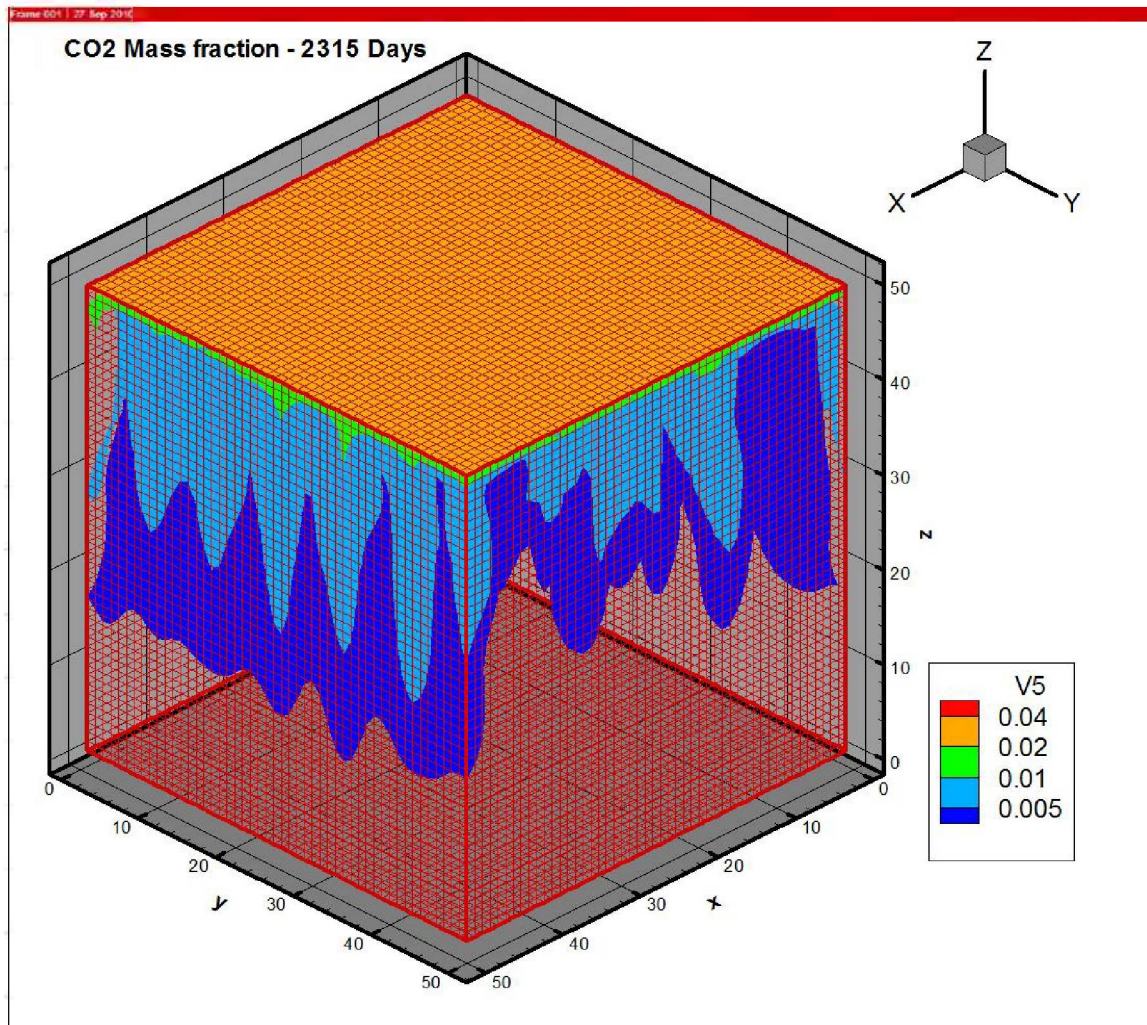
Figure 5.3. CO_2 mass fraction at 20.83 days for two-dimensional simulation.

We ran a three-dimensional version of this problem with average permeability 4.9 10^{-13} m^2 (500 md) and porosity 0.15; point permeability and porosity values fluctuated randomly plus or minus one-half percent around the average. The system was a 10 m cube and was discretized into a 50 x 50 x 50 grid. Figure 5.4 shows CO_2 mass fraction at 1,157 days. Density fingers are starting to form along the top boundary. These fingers grow and coalesce, and by 2,315 days in Figure 5.5 and 3,472 days in Figure 5.6, are fully developed and extend to the bottom of the system.

Figure 5.4. CO$_2$ mass fraction at 1157 days for three-dimensional simulation.

Figure 5.5. CO$_2$ mass fraction at 2315 days for three-dimensional simulation.
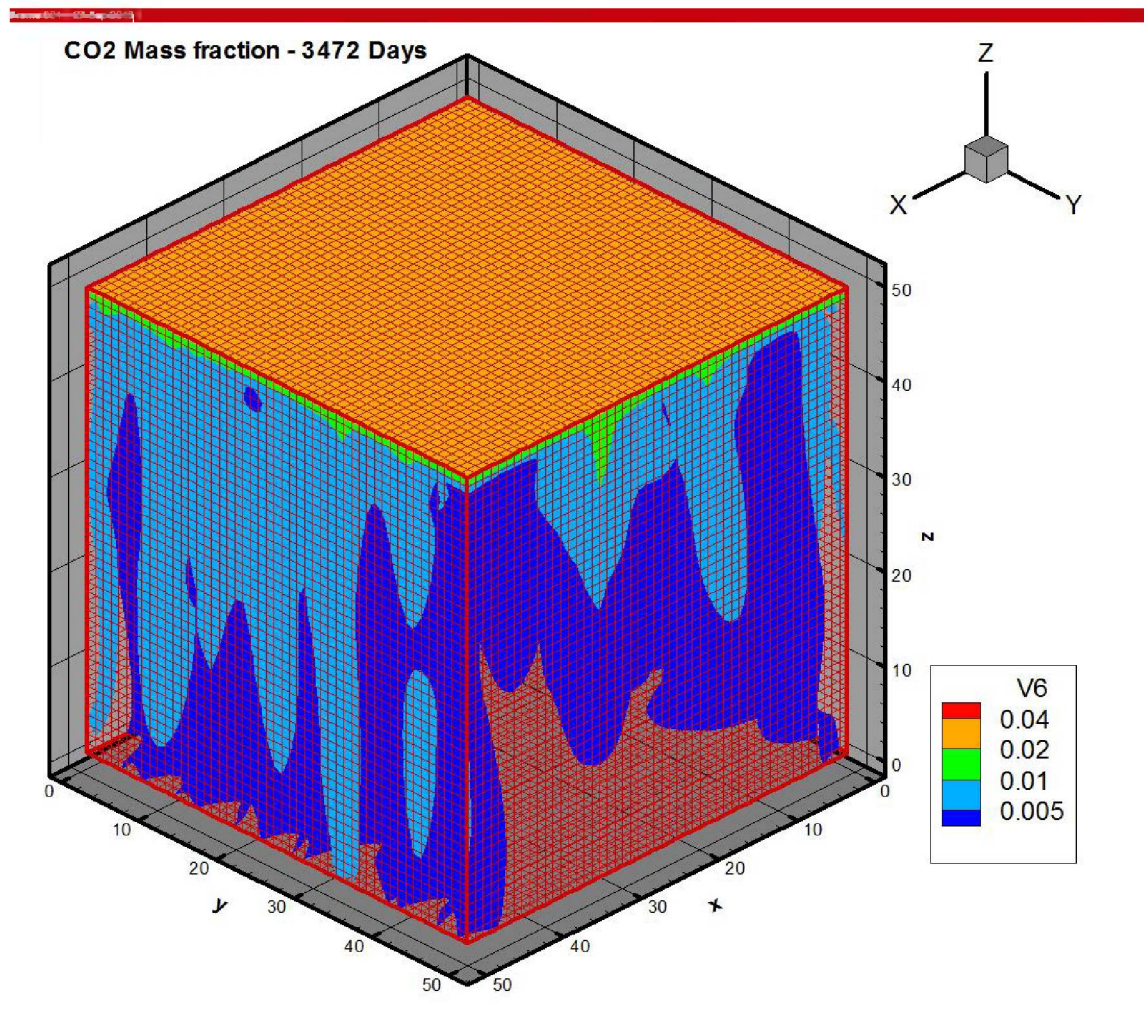
Figure 5.6. CO$_2$ mass fraction at 3472 days for three-dimensional simulation.

We ran another series of density-driven flow instability simulations on TOUGH2-CSM. The simulations were two-dimensional and the top layer was CO_2-saturated brine that diffused through an impermeable barrier into the rest of the simulation domain. The transported CO_2 would then dissolve in the aqueous phase at the system top, increasing the phase's density and eventually causing convective flow that would force this fluid to the system bottom. Permeability and porosity varied randomly in the simulation domain to facilitate density-driven convection, with average permeability $1.9 \cdot 10^{-10}$ m^2 and average porosity 0.30. Point values fluctuated plus or minus one percent around the average. The system was a 1 m square and was discretized into a 100 x 101 grid. Figures 5.7 – 5.10 show the onset of the instability.
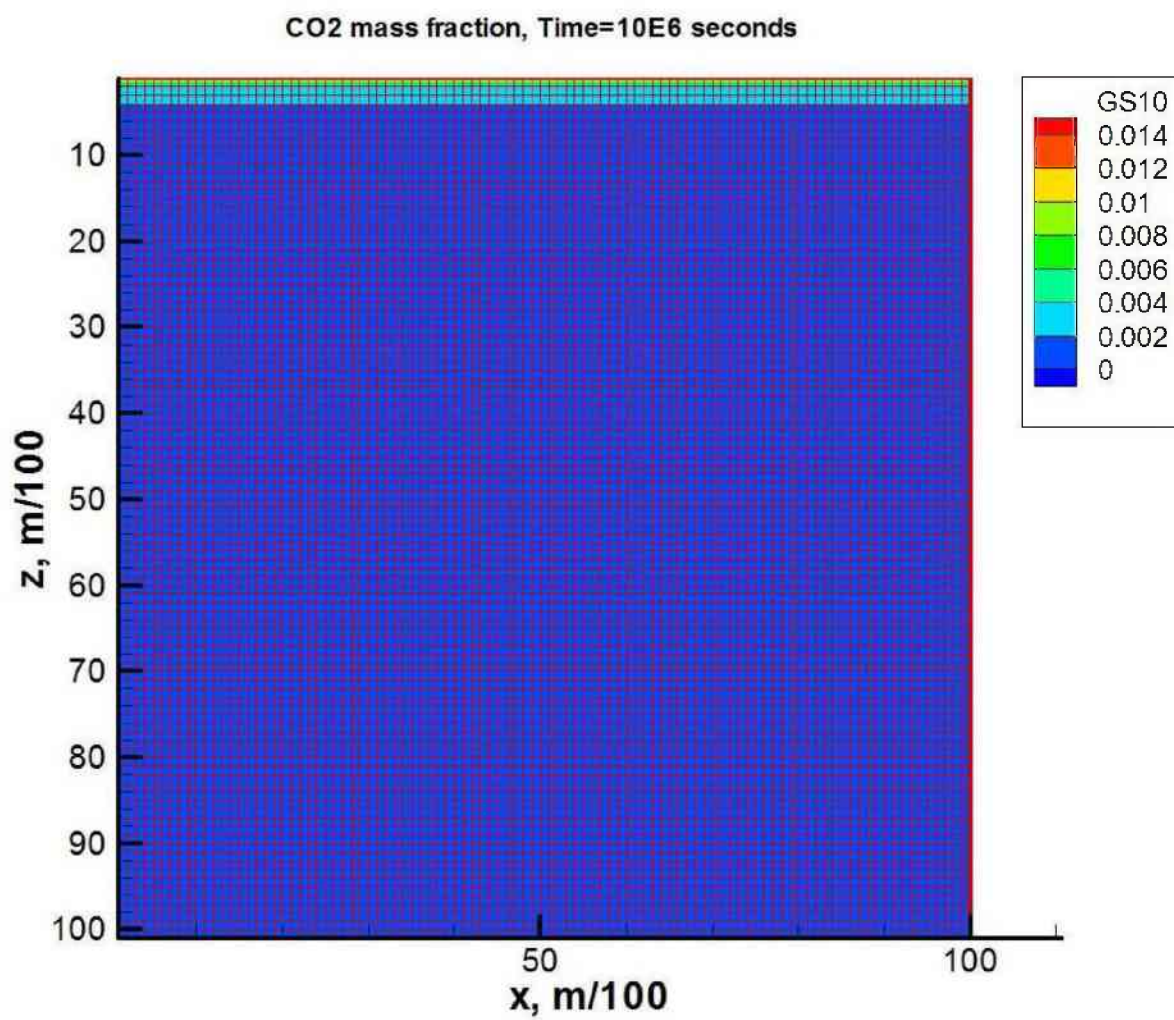
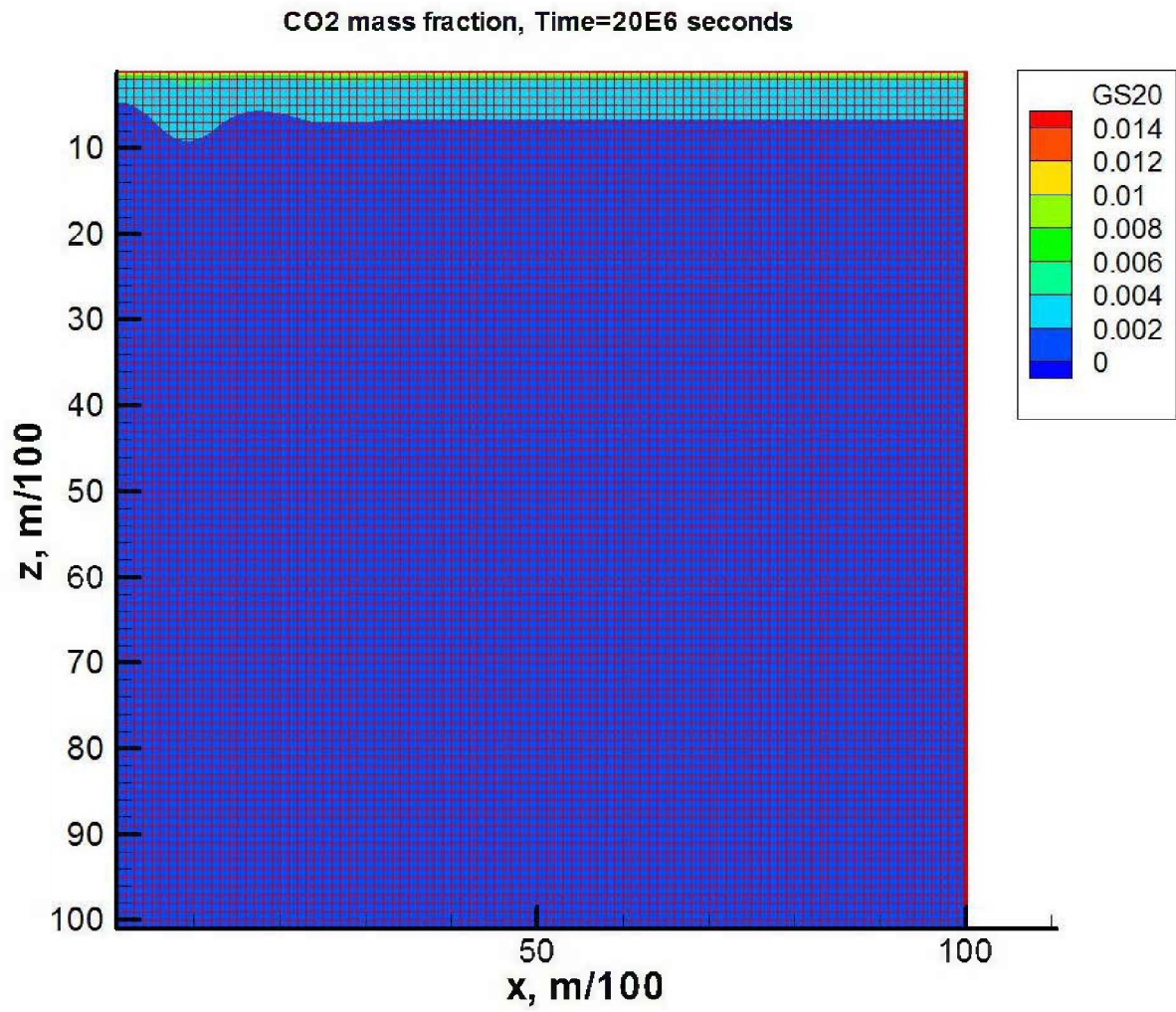Figure 5.7. CO_2 mass fraction at 10E6 seconds for flow instability simulation.

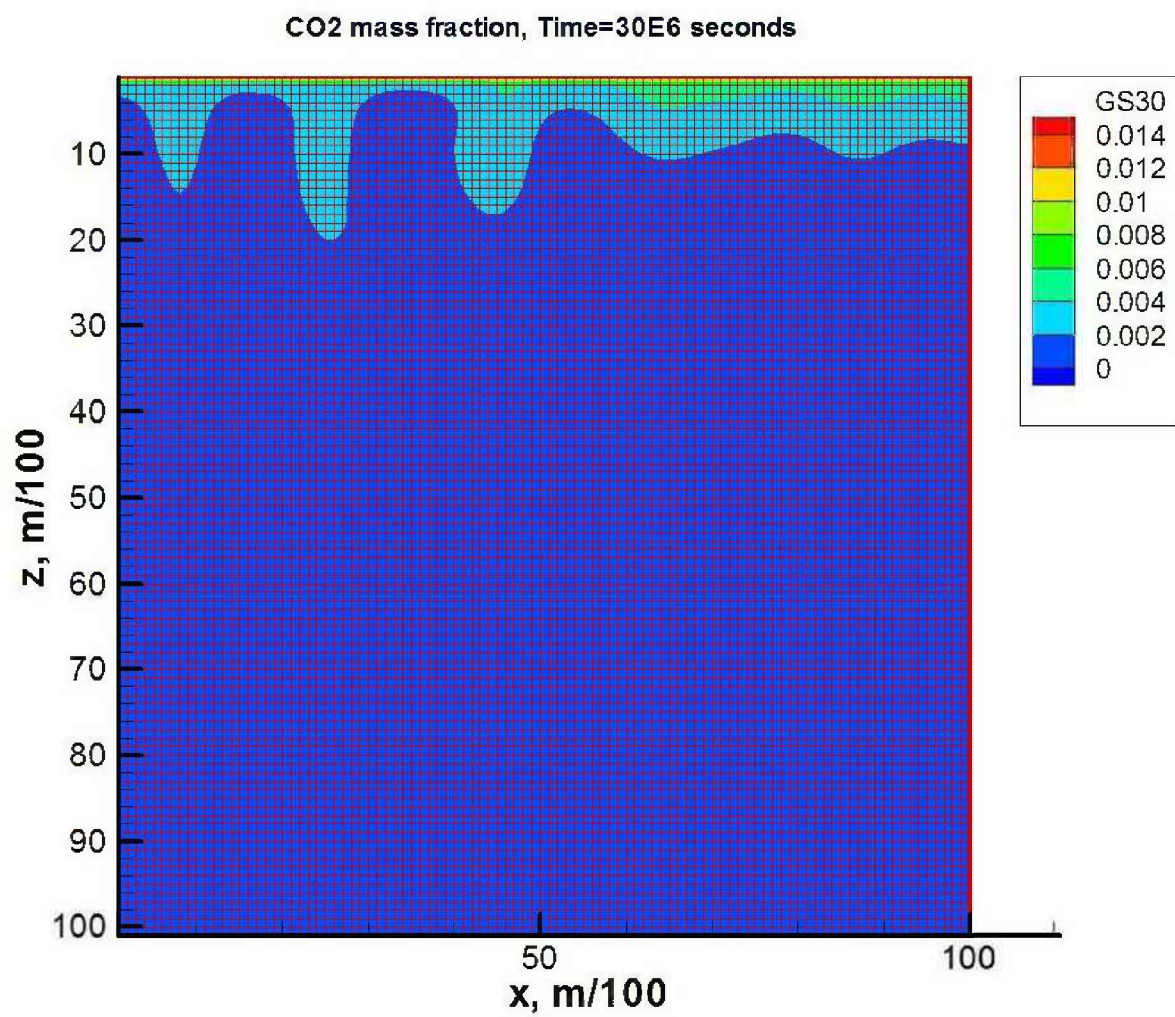Figure 5.8. CO$_2$ mass fraction at 20E6 seconds for flow instability simulation.

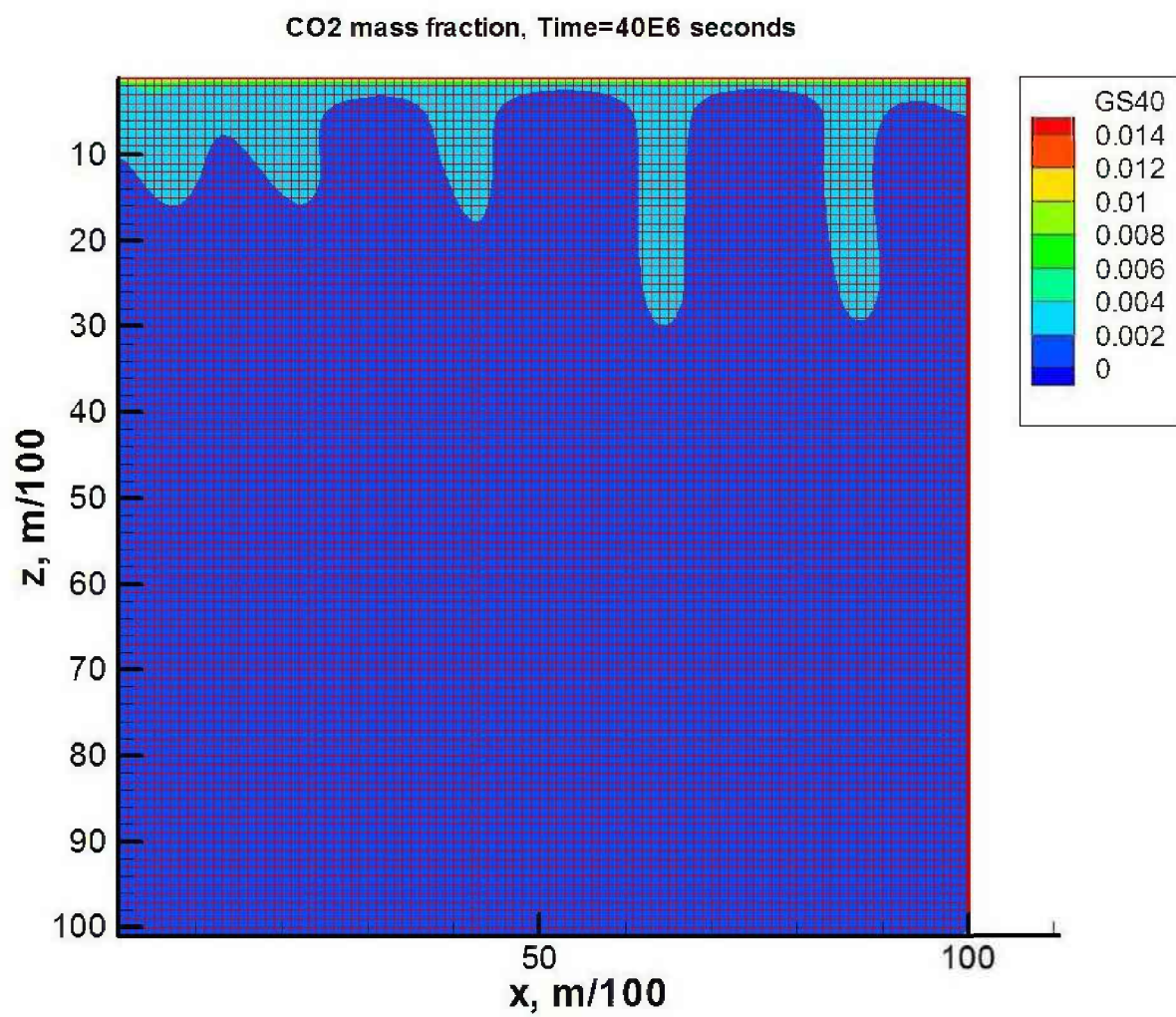Figure 5.9. CO_2 mass fraction at 30E6 seconds for flow instability simulation.

Figure 5.10. CO_2 mass fraction at 30E6 seconds for flow instability simulation.

Figure 5.11 shows horizontally averaged CO_2 mass fraction versus depth for the times shown in Figures 5.7-5.10. The leftmost value (at z=0.01) is the CO_2 mass fraction for the top layer, which contains CO_2-saturated brine. This mass fraction does not change significantly with time. The mass fractions at z=0.02 are just below the impermeable boundary and increase for 10 (times 1E6 seconds) to 20 and decrease for greater times. Figures 5.7-5.10 show that the instability starts after time 20. Prior to that, CO_2 is diffusing through the impermeable boundary and accumulating on the other side. The instability onset causes CO_2 to be transported away from there more rapidly, resulting in a declining mass fraction there. At larger depths (greater than 0.12), the mass fraction curves increase with increasing time.
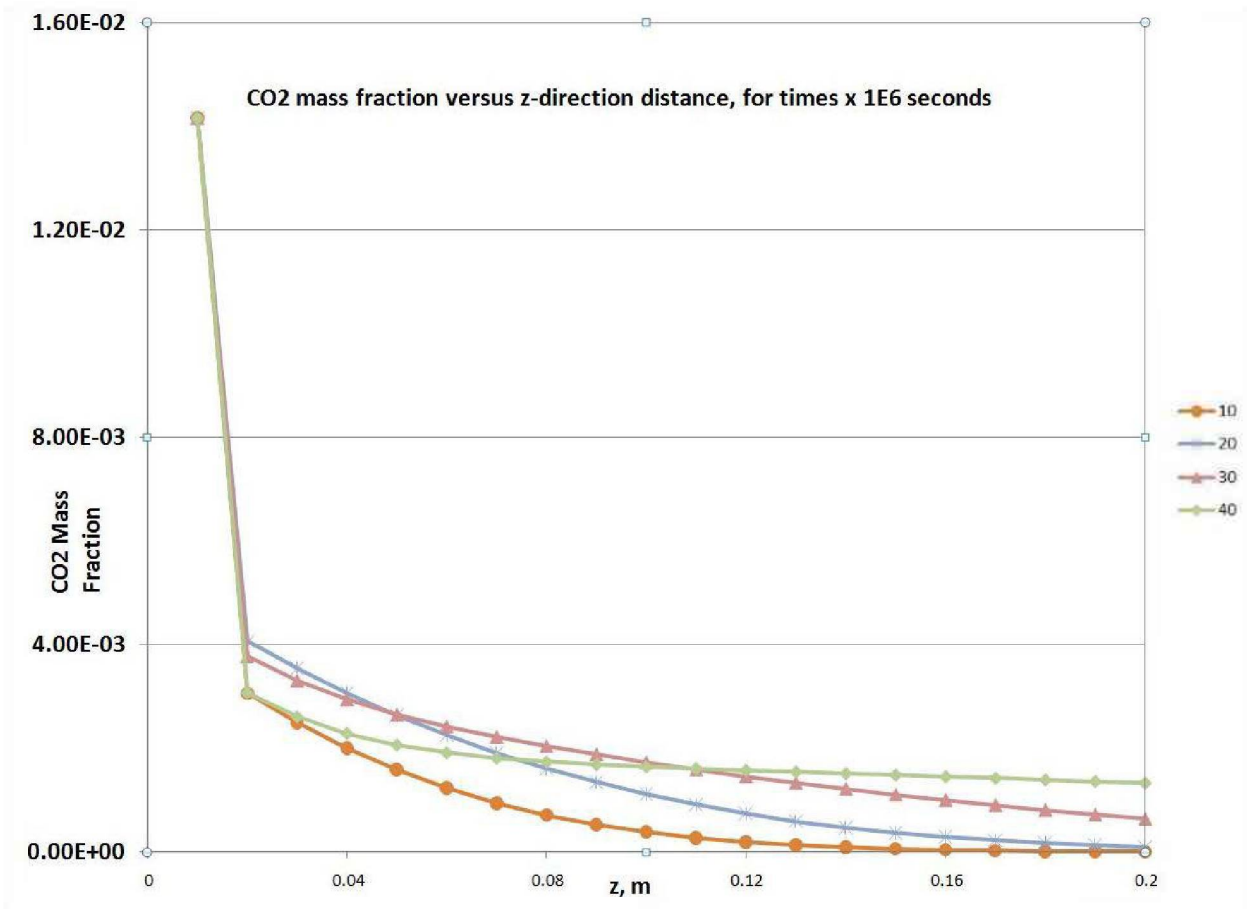
Figure 5.11. Horizontally averaged CO_2 mass fraction versus depth for various times.

We ran another series of simulations of convective mixing with a density contrast caused by variable dissolved CO_2 concentration in saline water. These simulations were modeled after a set of laboratory experiments carried out by Kneafsey (Staff Scientist at LBNL), in which supercritical CO_2 was circulated in the headspace above a brine saturated packed sand in a pressure vessel. As CO_2 is dissolved into the upper part of the saturated sand, liquid phase density increases causing instability and setting off convective mixing. Convection began in the form of small fingers which grew and merged and had the overall effect of increasing the rate of uptake of CO_2 from the headspace into the saturated brine relative to a purely diffusive process. The rate of mixing was determined in the experiments by monitoring the uptake of CO_2 from the headspace. We report below on simulations of this experiment, intended to better understand convective instability and mixing, and to provide a measure of code validation for TOUGH2/ECO2M.

The numerical system modeled had been set up initially as a Hele-Shaw cell (flow in the narrow gap between two plates mimics flow in porous media). We simulated the onset of convection in the form of multiple fingers between two parallel plates set at an aperture of 0.7×10^{-3} m. The gap within the slit is discretized into grid blocks consisting of cubes 0.7×10^{-3} m in edge length, making the numerical simulation two-dimensional. There were 100×100 grid (later 300×300) blocks in each x (vertical) and y (horizontal) directions. The permeability was randomly attributed to grid blocks with a value in the range from 1×10^{-12} to 9×10^{-12} m^2 with no anisotropy in the two spatial directions.

The first row of cells from the top was occupied by gaseous CO_2 with negligible mass fraction (10^{-9}) of liquid water and was at standard atmospheric pressure; the properties of this row remained constant in time. The rest of the model was initialized with hydrostatic pressure and no CO_2 dissolved in the liquid water apart from the second row which was initialized with 0.00142 mass fraction of CO_2 to help initialize instability.

The numerical experiment was run as isothermal. After 50 hours, a set of fingers was already well developed and had an approximate spacing of 2 mm (Figure 5.12a) with a length of 2-3 mm. After 500 hours, the fingers had grown in length and width reaching a spacing of 5 mm (Figure 5.12b) with a length of 2-3 cm. The fingering resembles closely what was observed in the experiments. The numerical experiments following this one will focus on calibrating the model to the actual experiments. In these preliminary simulations, we found that the rate at which fingers developed was too slow by a factor of 100 relative to the laboratory experiments. We adjusted the system properties, processes, and boundary and initial conditions to improve the match between simulated results and experiments.
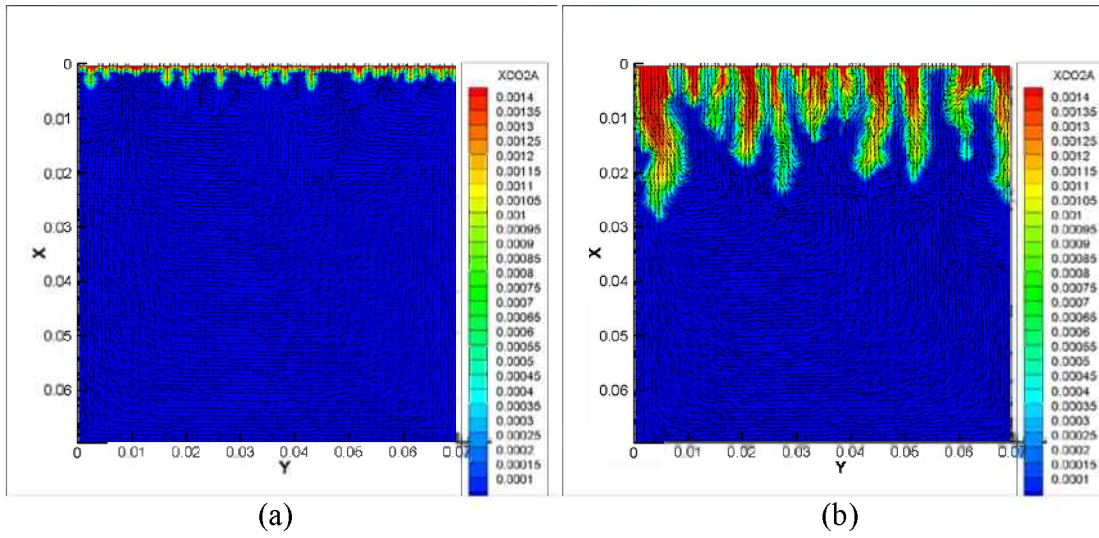
Figure 5.12. Development of fingers in a Hele-Shaw cell with 0.7 mm aperture. CO_2 dissolves in water increasing the its density and initiating convective fingering.

We experimented with a variety of conceptualizations of the top boundary region (headspace and first row of the saturated part of the Hele-Shaw cell). For boundary condition realizations with no liquid or gas flow allowed across the boundary, convective instability appeared to be suppressed, and the system was dominated by diffusion. In contrast, the experiments has shown fingers developing and associated rapid mixing of dissolved CO_2 into the system.

For boundary conditions in which both liquid and gas were allowed to flow across the boundary, convective instability developed fingers that in time merged together and grew to the size of the cell. Convection occurred at two different scales: while convection at the scale of the fingers grew in time, convection at the scale of the cell remained invariant. This type of boundary conditions modeled relatively well the behavior of the fingers away from the boundary, but did not resolve the detailed velocity and geometric structure at the boundary. In particular, the aqueous phase crossed the boundary instead of flowing parallel to it.

We experimented with boundary conditions that allowed only the gaseous phase to pass through, inhibiting the flow of the liquid phase. This condition allowed a better representation of the flow close to the liquid/gas boundary, but still needed to be calibrated to reproduce the time scale at which the experimental fingering occurred.

In the following set of simulations, there are 300×300 grid blocks in each x- (vertical) and y- (horizontal) directions in the high-resolution grid. The permeability is set to equal $b^2/12$ where b is the gap width in meters

The first row of cells at the top was occupied by a two-phase mixture of gaseous CO_2 and water (aqueous phase) held at atmospheric pressure; the properties of this row remained constant in time. The properties of the second row of cells were a function of the type of boundary condition used and was only single phase aqueous (so-called confined boundary condition) or two phase (aqueous+CO_2) (so-called unconfined boundary condition. The rest of the model was initialized with hydrostatic pressure and had initially no CO_2 dissolved in the aqueous phase.

We carried out numerical experiments to test which top boundary condition conceptualization produced better results for validation against the laboratory experiments. For either boundary condition, convective instability developed and the system evolved from diffusion-dominated in the first few minutes of the numerical experiments to convection dominated in the remaining time of the simulation (Figure 5.13). Our results showed good agreement with the laboratory experiments which were characterized by finger development and associated mixing of dissolved CO_2 into the system (Figure 5.14).
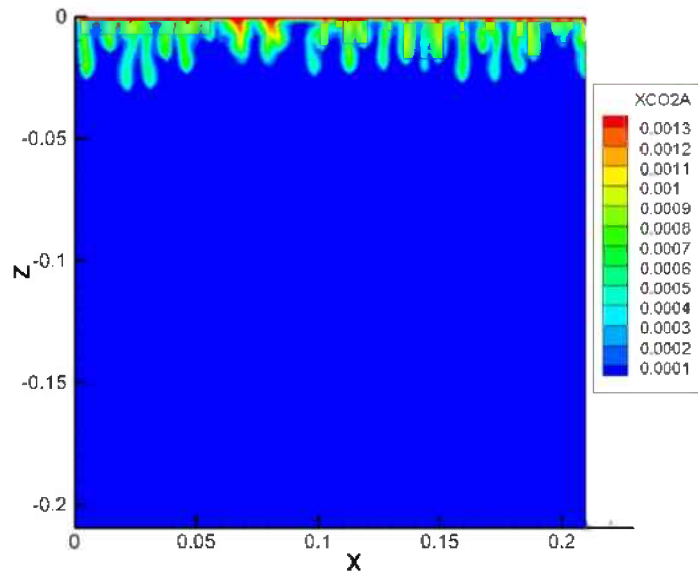
Figure 5.13. Convective instability that developed after the first few minutes of the numerical experiment.
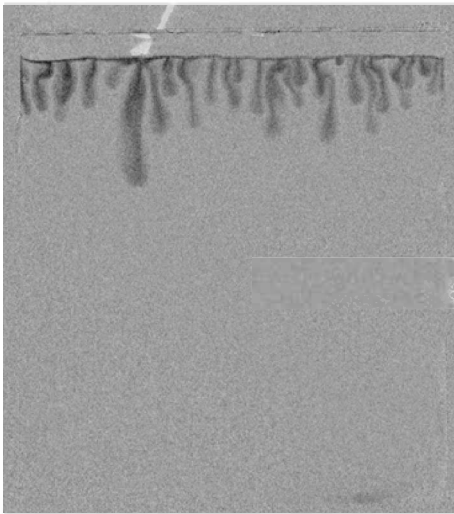
Figure 5.14. Laboratory experiment, characterized by finger development and associated mixing of dissolved CO_2 into the system.

The run times for these simulations were very long. The run time had been on the order of weeks for each 90,000-gridblock numerical experiment that we needed to run to simulate a few hours of laboratory time. To speed up the simulations we compared the results obtained with the equation of state module ECO2M with the results obtained with the module ECO2N, which had a longer history of testing. We compiled TOUGH2/ECO2N for use on a massively parallel cluster we are tested it against standard examples. With the new capabilities of running ECO2N on the cluster, and making key comparisons of ECO2N and ECO2M results, we were able to carry out the following series of validation runs with much greater efficiency than before.

Numerical simulations for CO_2 injection with different size of grid cells in the z-direction were conducted to capture the simulation scale for convective mixing during CO_2 sequestration. This model was conceptualized as a 2D modeling domain with a thickness of 100 m and a radius of 10,000 m, and it was located at depths between 2,000 m (z = 100 m) and 2,100 m (z = 0 m) from the ground surface. It was assumed to be underlain and overlain by two impermeable upper cap-rock and lower bed-rock. A CO_2 injection well was located at the bottom of the modeling domain with 20 m interval. In the x direction, it was subdivided by 120 grid blocks with various spacing. In the z direction, it was subdivided under five cases, the first case was 200 grid blocks with a constant spacing of 0.5 m in the vertical z direction, the second case was 400 grid blocks with a constant spacing of 0.25 m in the vertical z direction, the third one was 500 grid blocks with a constant spacing of 0.2 m in the vertical z direction, the fourth one was 600 grid blocks with a constant spacing of 0.167 m in the vertical z direction, and the fifth one was 800 grid blocks with a constant spacing of 0.125 m in the vertical z direction. The total injection rate was 20 kg/s in the 20m's interval for 10 years' injection period. After CO_2 injection, the simulation ran for another 10 year for CO_2 sequestration. An aqueous diffusivity of 10^{-9} m^2/s of dissolved CO_2 was used in the simulation. Along the top and bottom boundaries, no-flow and constant stress boundary conditions were designed to consider the impermeable seal layers. Along the left boundary, no-flow and constant stress boundary conditions were assigned to consider the radial symmetry of the modeling domain related to the CO_2 injection well. Along the right boundary, the constant pressure and stress boundary conditions were assigned to consider the infinite radial extent of the modeling domain.

From the simulation results of this model, we plotted the mass fraction of aqueous CO_2 in every grid cell, and the vertical mass fraction difference of aqueous CO_2 between two closed grid cells along z direction. The profiles are shown in Figure 5.15 for the five cases with different number of grid cells in z-direction. CO_2 injected into the bottom of a saline aquifer is buoyant, and tends to migrate towards the top of the permeable formation. Then the plume of CO_2 is formed. It is indicated that the CO_2 plume is formed within the area of 1500 m after 10 years' injection period and another 10 years' storage period. Along the edge of the plume, the concentration of aqueous CO_2 decreases rapidly under the conditions of different grid cells in vertical directions. The maximum mass fraction difference of aqueous CO_2 in z-direction for case one is 0.055/m in Figure 5.15b, for case two is 0.065/m in Figure 5.15d, for case three is 0.088/m in Figure 5.15f, for case four is 0.110/m in Figure 5.15h, and for case five is 0.110/m in Figure 5.15j. The first four cases show that the gradient of mass fraction of aqueous CO_2 in z-direction are increasing

with 200, 400, 500 and 600 grid cells, which means that the mass fraction differences are under resolved within 0.5 m, 0.25 m, 0.2 m and 0.167 m grid cells. When the grid resolution increases to 800 with grid cells of 0.125 m, the vertical gradients of mass fraction of dissolved CO_2 are resolved under a diffusivity of 10^{-9} m^2/s of dissolved CO_2 after 20 years. Therefore, the grid resolution, which is around 0.1 m, is adequate to resolve the gradients of dissolved CO_2 concentrations.
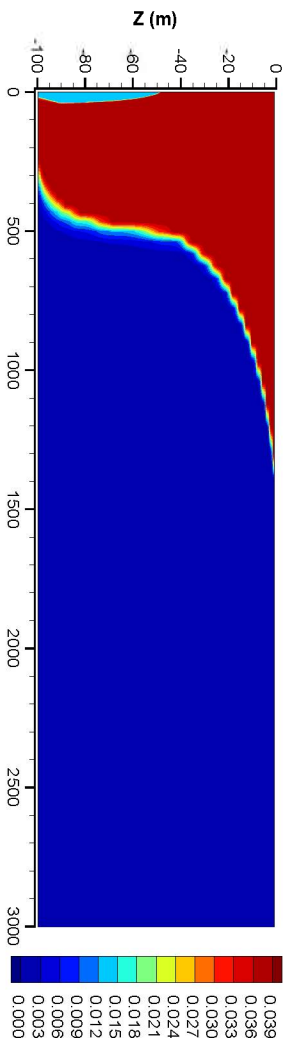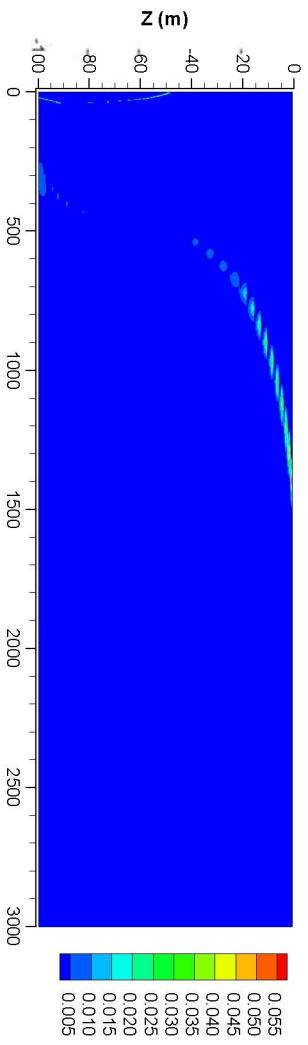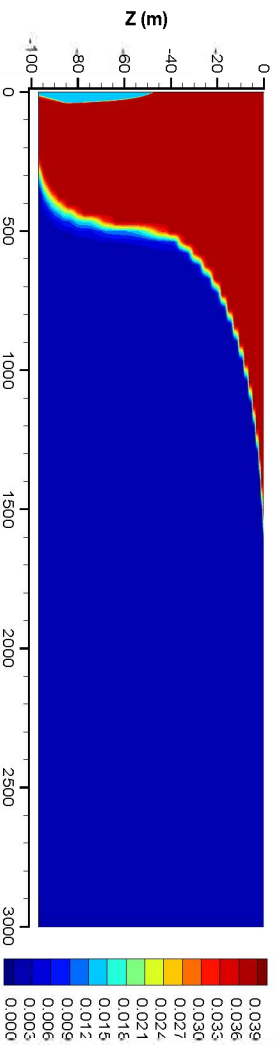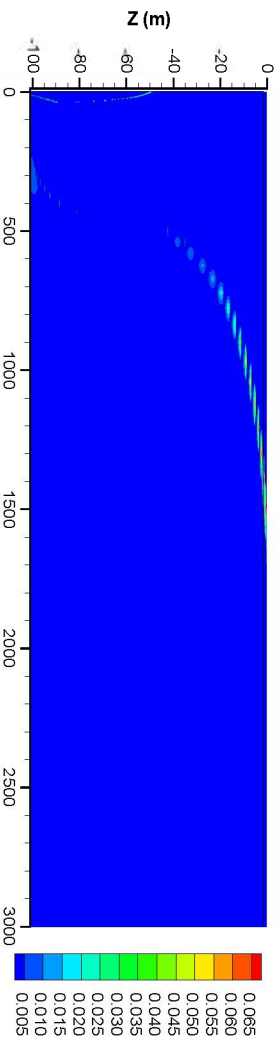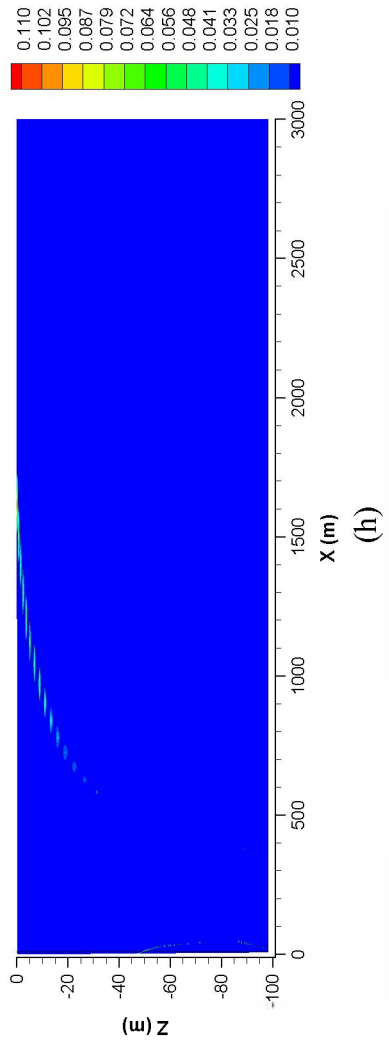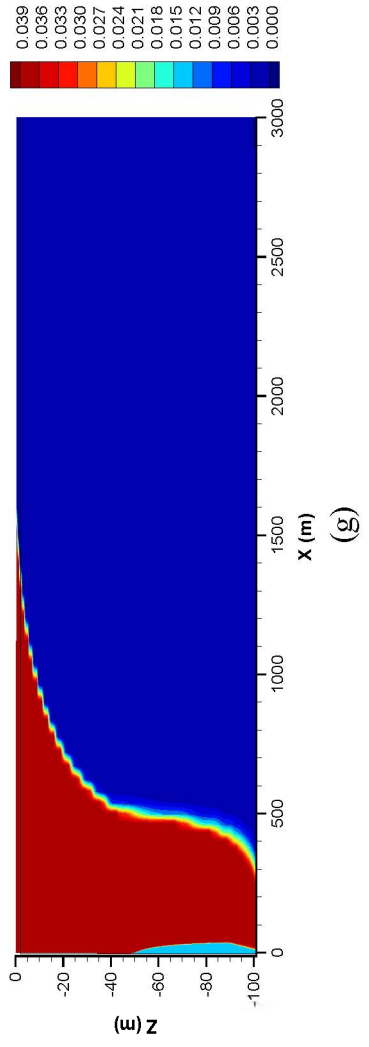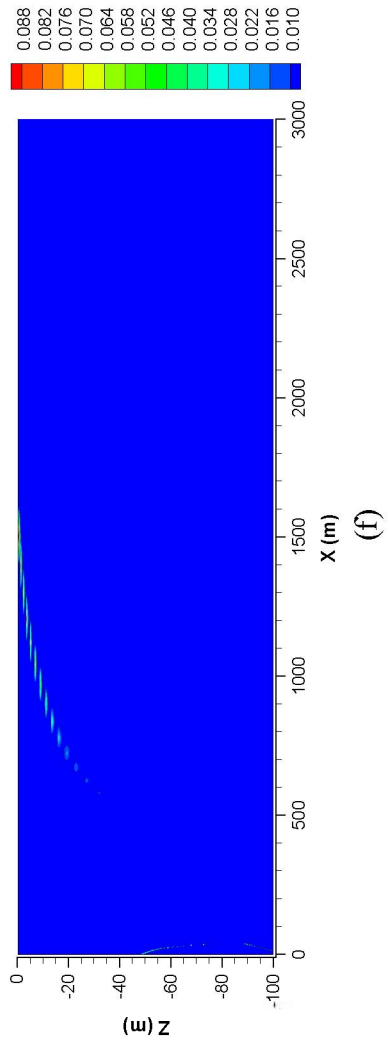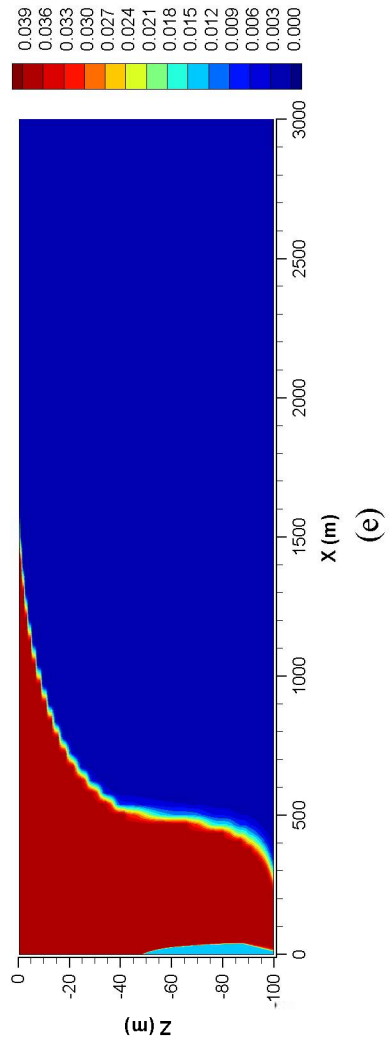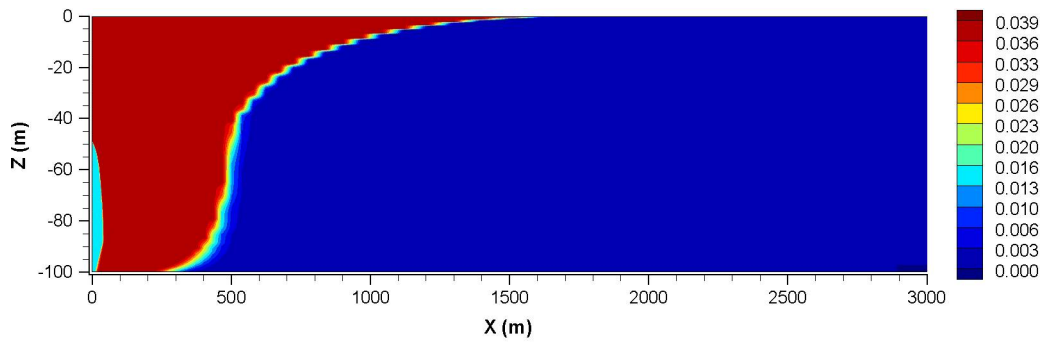
(i)
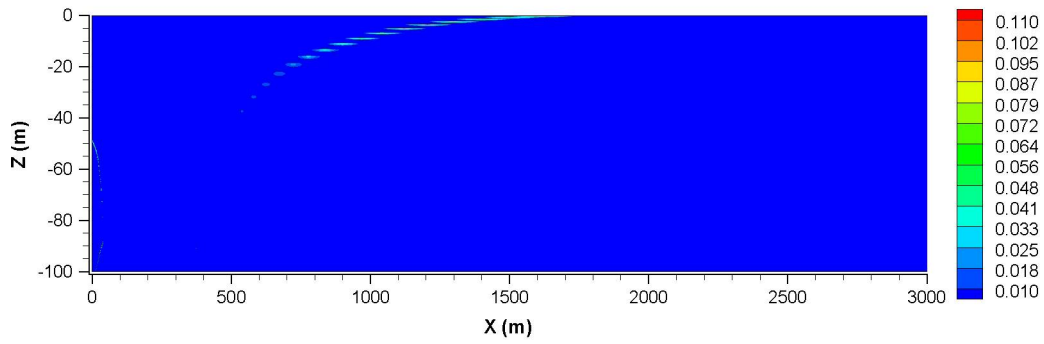
(j)

Figure 5.15. Spatial distribution of mass fraction and vertical mass fraction difference of aqueous CO_2 with different number of grid cells in z direction: a and b with 200 grid cells; c and d with 400 grid cells; e and f with 500 grid cells; g and h with 600 grid cells; i and j with 800 grid cells. a, c, e, g, and i are for mass fraction of aqueous CO_2 after 20 years' sequestration; b, d , f, and j are for vertical mass fraction difference of aqueous CO_2 after 20 years' sequestration.

After we obtained the adequate grid resolution to model the convective mixing, two sets of numerical simulation were conducted to capture the process of dissolution-diffusion-convection. The first set of numerical simulations was a 2D numerical model with four different random seeds (0.6, 0.7, 0.8 and 0.9) to generate the permeability heterogeneity. This 2D numerical model aimed to capture the early time diffusive phenomenon after the CO_2 plume formed due to CO_2 injection. The grid resolution was 10 mm and diffusivity of dissolved CO_2 is 2×10^{-9} m^2/s. The 2D numerical model had 100 grid cells in z-direction and 100 grid cells in x-direction. The model had an isotropic permeability of 10 Darcy (10^{-11} m^2) initially, and an impermeable boundary was assumed at the bottom of the first layer, which allowed CO_2 to diffuse through the impermeable boundary and accumulate on the other side. Figures 5.16-5.19 show the 2D spatial distributions of dissolved CO_2 concentrations for four different random number seeds with different simulation times (4×105 s, 6×105 s, 8×105 s, 1×106 s, 2×106 s, and 3×106 s). The fingers of dissolved CO_2 start to be formed with a length of 0.1 m in vertical direction after 4×10^5 seconds in Figure 5.16a. The fingers continue to increase with a length of 0.2 m in the vertical direction after 6×10^5 seconds in Figure 5.16b. Due to the permeability heterogeneity, the increase of the finger tends to be heterogeneous. After 8×10^5 seconds, 1×10^6 seconds, and 2×10^6 seconds, the fingers of dissolved CO_2 in aqueous phase increase to 0.3 m, 0.4 m and 0.6 m in Figures 5.16c, 5.16d and 5.61e, respectively. Finally, the dissolved CO_2 reaches the lower boundary of the model after 3×10^6 seconds in Figure 5.16f. The fingers of dissolved CO_2 in the aqueous phase in Figures 5.16-5.19 show similar lengths, but have different patterns. The patterns of CO_2 fingers show great differences with time progresses. This phenomenon results from different random seeds used to generate the permeability heterogeneity in the four cases. Figures 5.16-5.19 show that the patterns of CO_2 fingers vary greatly after 1×10^6 seconds. We concluded that before dissolved CO_2 reaches the lower boundary of the model, it is evident that convection patterns are quite different in detail, but have similar length overall. The early time diffusive phenomenon can be captured by fine grid resolution, and the permeability heterogeneity affects the pattern of the CO_2 fingers.
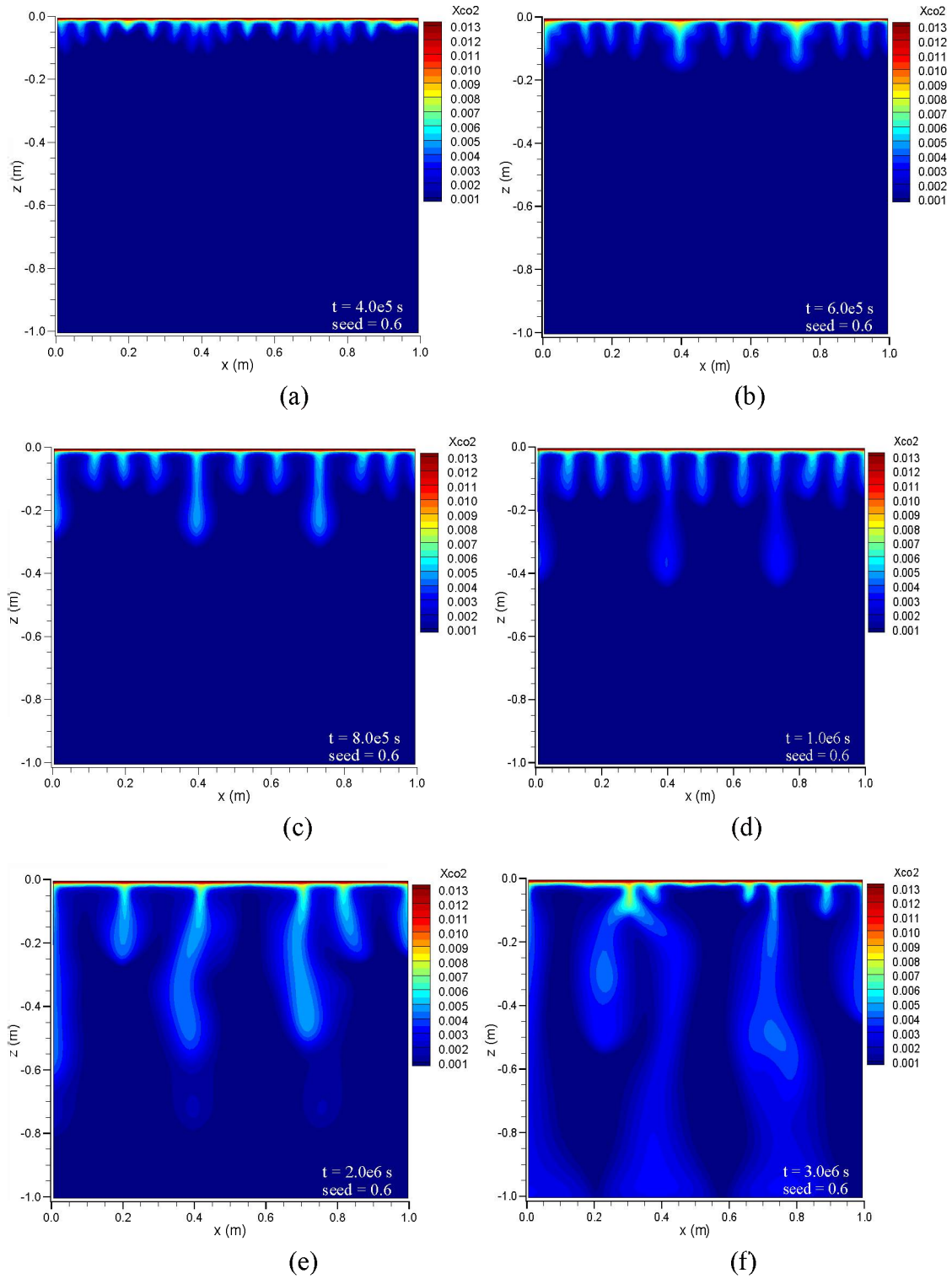
Figure 5.16. Spatial distribution of dissolved CO_2 after six different simulation times for random number seed of 0.6 to generate permeability heterogeneity.

The second set of numerical simulations was a 3D numerical model with two different random seeds (0.8 and 0.9) to generate permeability heterogeneity. This 3D numerical model aimed to capture the diffusive phenomenon after the CO_2 plume due to CO_2 injection with a longer time scale. The grid resolution was 20 cm and diffusivity of dissolved CO_2 was still 2×10^{-9} m^2/s. The 3D numerical model had 100 grid cells in the x-direction, 100 grid cells in the y-direction, and 100 grid cells in the z-direction. The model had an isotropic permeability of 0.5 Darcy (5×10^{-13} m^2) initially, and an impermeable boundary was assumed at the bottom of the first layer, which allowed CO_2 to diffuse through the impermeable boundary and accumulate on the other side. Figures 5.20 and 5.21 show the 3D spatial distributions of dissolved CO_2 concentrations for two different random seeds (0.8 and 0.9) with four simulation times (1×10^8 s corresponds to 3.16 years, 2×10^8 s corresponds to 6.32 years, 3×10^8 s corresponds to 9.48 years, 4×10^8 s corresponds to 12.67 years). Figures 5.20a, 5.20c, 5.20e, 5.20g, 5.21a, 5.21c, 5.21e, and 5.21g provide the 3D non-transparent view for the spatial distribution of dissolved CO_2 in aqueous phase, and Figures 5.20b, 5.20d, 5.20f, 5.20h, 5.21b, 5.21d, 5.21f, and 5.21h provide the 3D transparent view for the spatial distribution of dissolved CO_2 in aqueous phase. The fingers of dissolved CO_2 start to be formed with a length of 3 m in vertical direction after 1×10^8 seconds (3.16 years) in Figure 5.20a and 5.20b. The fingers continue to increase with a length of 8 m in vertical direction after 2×10^8 seconds (6.32 years) in Figures 5.20c and 5.20d. Due to the permeability heterogeneity generated by a random seed, the increase of the finger still tends to be heterogeneous. After 3×10^8 seconds (9.48 years), the fingers of dissolved CO_2 in aqueous phase increase to 12 m in Figures 5.20e and 5.20f. Finally, the dissolved CO_2 reaches the lower boundary of the model after 4×10^8 seconds (12.67 years). Due to the permeability heterogeneity by different random seeds in Figures 5.20 and 5.21, the fingers of dissolved CO_2 have different patterns both at the outer edge of the model and inside the model. From the transparent 3D view in Figures 5.20 and 5.21, it is obvious that the CO_2 fingers have different shapes due to the permeability, especially after 1×10^8 seconds (3.16 years). Furthermore, Figures 5.22 and 5.23 provide the 3D view from below for the iso-surface contour for dissolved CO_2. It corresponds to a density of dissolved CO_2 (14.6 kg/m3) and a mass fraction of dissolved CO_2 (0.015). These 3D iso-surface figures indicate the structure of the 3D fingers clearly. The fingers at early time at 1×10^8 seconds (3.16 years) are approximately cylindrical in shape and in perpendicular direction. With time progresses, the CO_2 fingers become larger and flatter, which is totally different from the 2D fingers as we can see in Figures 5.16-5.19. From Figures 5.22b, 5.22c, and 5.22d, it is obvious that the number of CO_2 fingers is reduced rapidly and the size of an individual finger gets larger and flatter at 2×10^8 seconds (6.32 years), 3×10^8 seconds (9.48 years), and 4×10^8 seconds (12.67 years). Figures 5.24 and 5.25 shows the y-z plane at x=10m. The cross-section along x = 10 m shows a cross-section of the flat 3D CO_2 fingers observed in Figures 5.20 and 5.21. Comparing Figure 5.22 with Figure 5.23, and Figure 5.24 with Figure 5.25, it is indicated that the permeability heterogeneity affects the patterns of CO_2 fingers in the 3D model. With time progressing, the CO_2 fingers tend to become larger and flatter with less rounded edge, which cannot be observed from the 2D contour as shown in Figures 5.16-5.21.
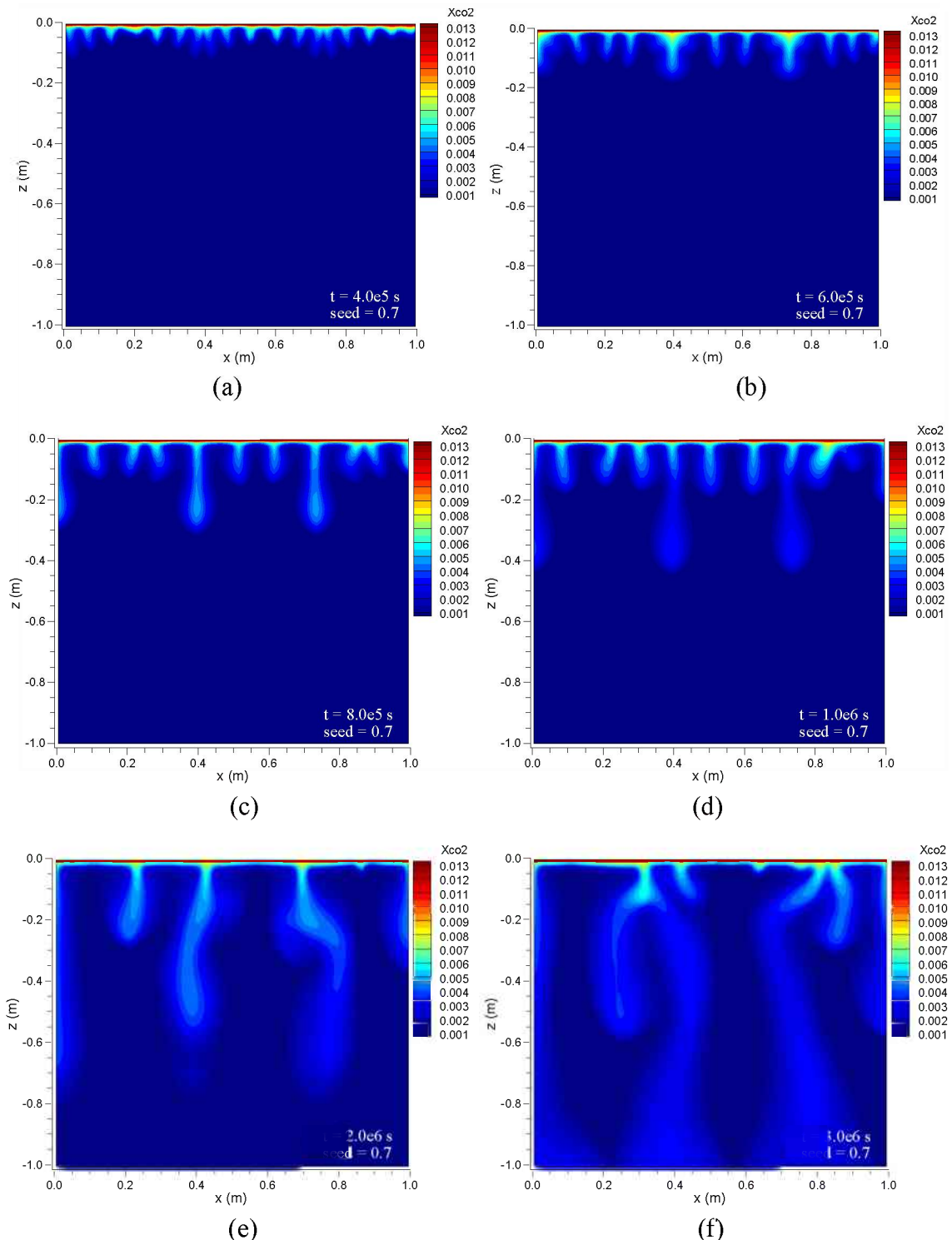
Figure 5.17. Spatial distribution of dissolved CO_2 after six different simulation times for random number seed of 0.7 to generate permeability heterogeneity.
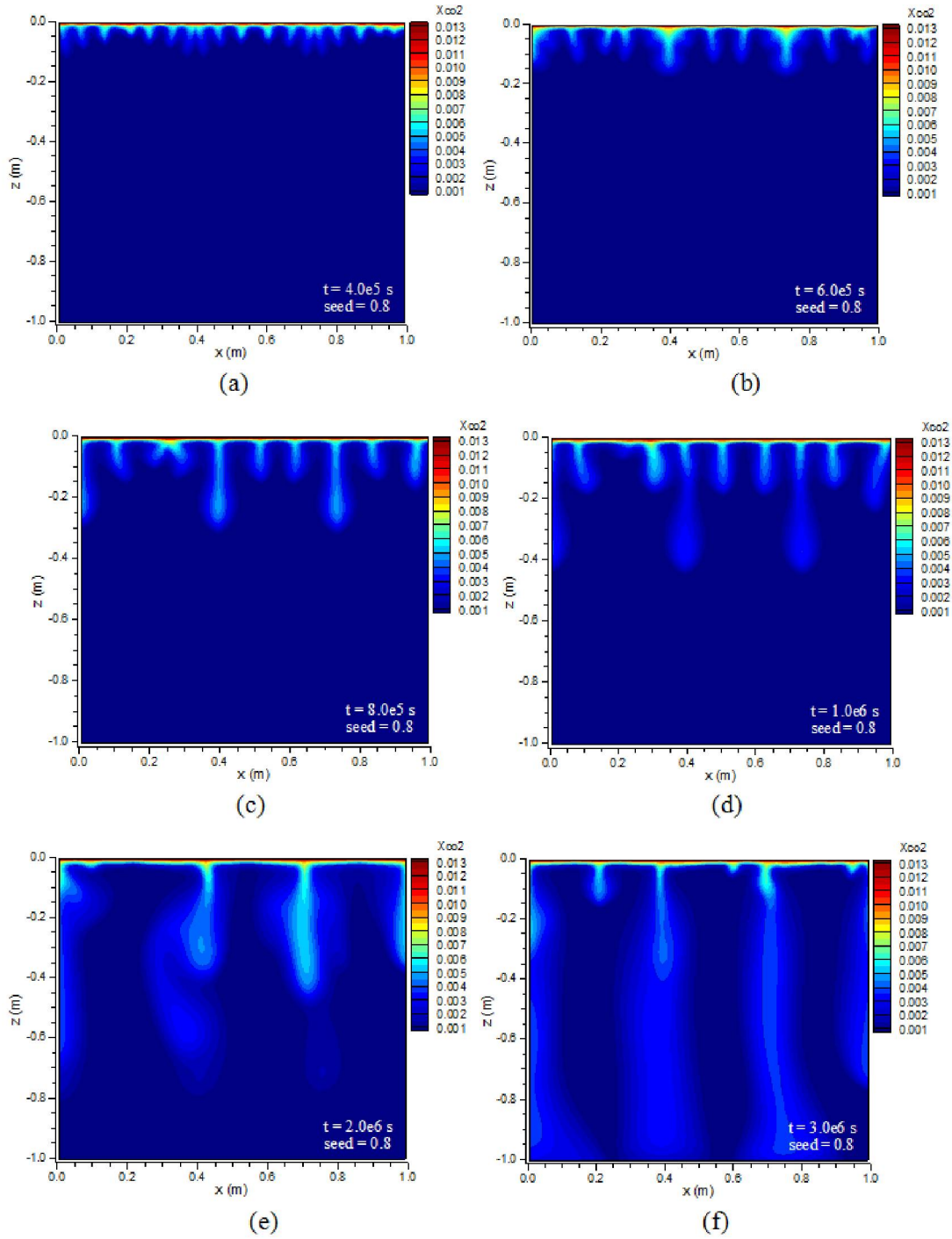
Figure 5.18. Spatial distribution of dissolved CO_2 after six different simulation times for random number seed of 0.8 to generate permeability heterogeneity.
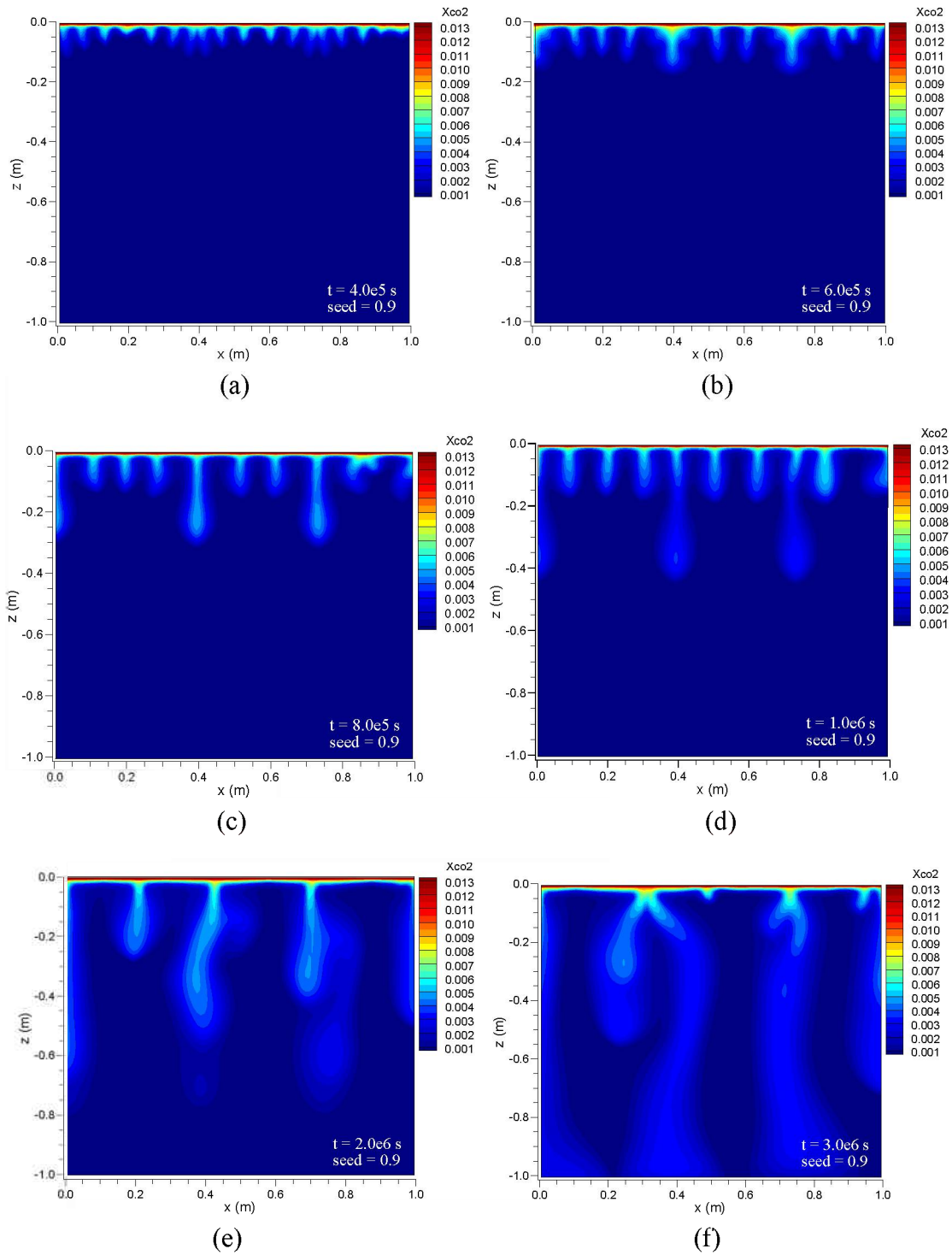
Figure 5.19. Spatial distribution of dissolved CO_2 after six different simulation times for random number seed of 0.9 to generate permeability heterogeneity.

(a)

(b)

(c)

(d)

(e)

(f)

(g)

(h)
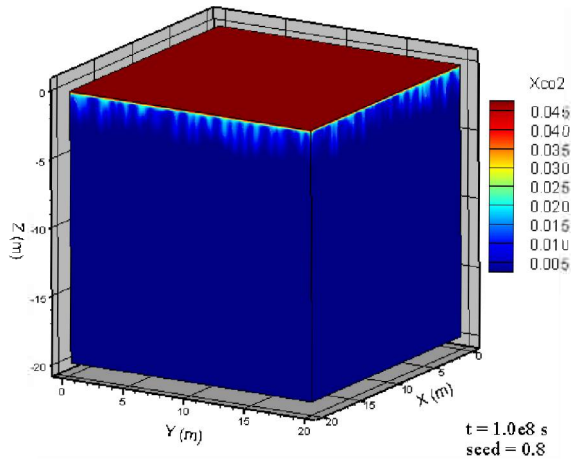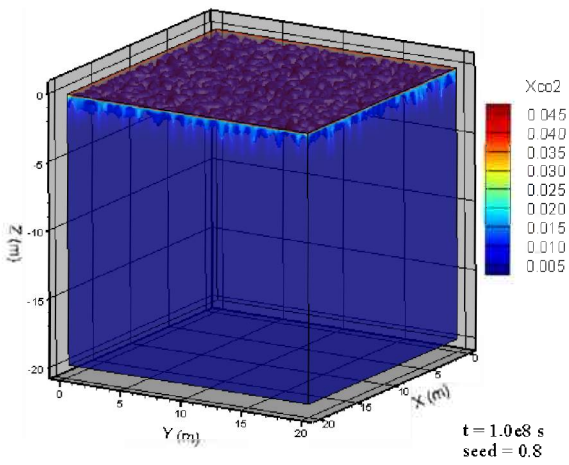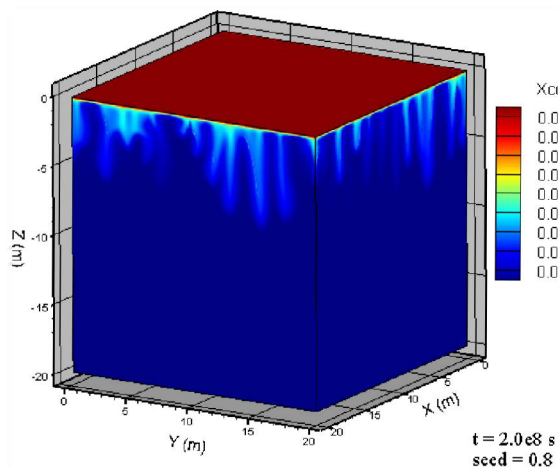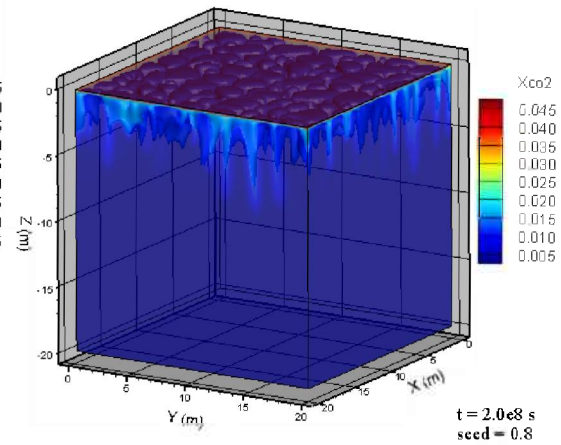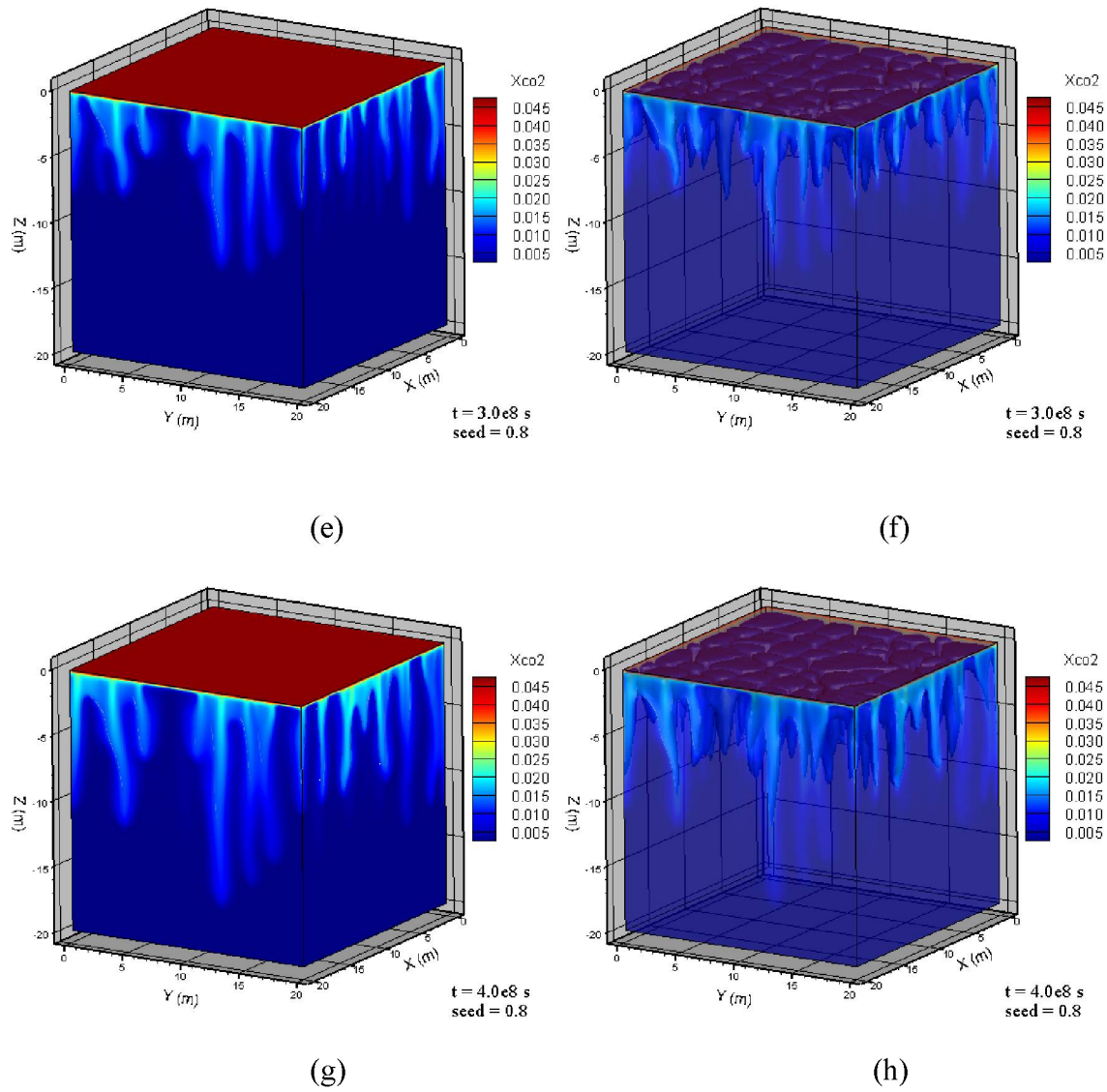
Figure 5.20. 3D views of dissolved CO_2 after four different simulation times, in which a, c, e, and g are non-transparent to show the fingers of aqueous CO_2 in the outside walls of the model, b, d, f and h are transparent to show iso-fraction surface inside the model (seed=0.8).

(a)

(b)

(c)

(d)

156

(e)

(f)

(g)

(h)
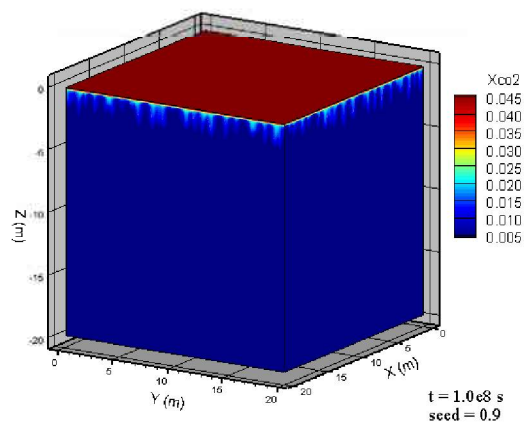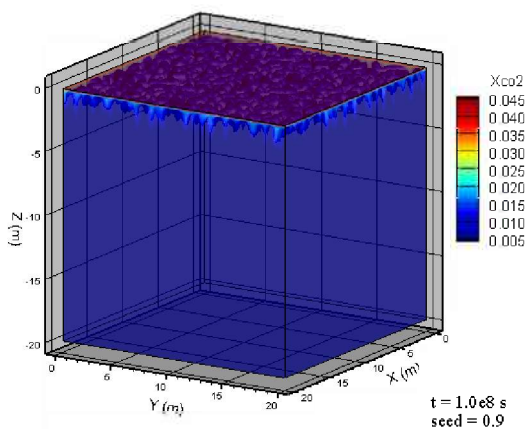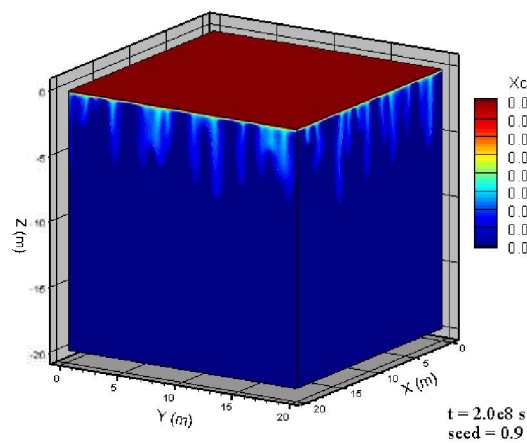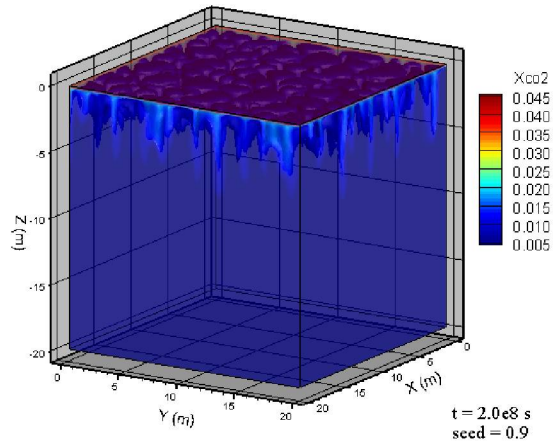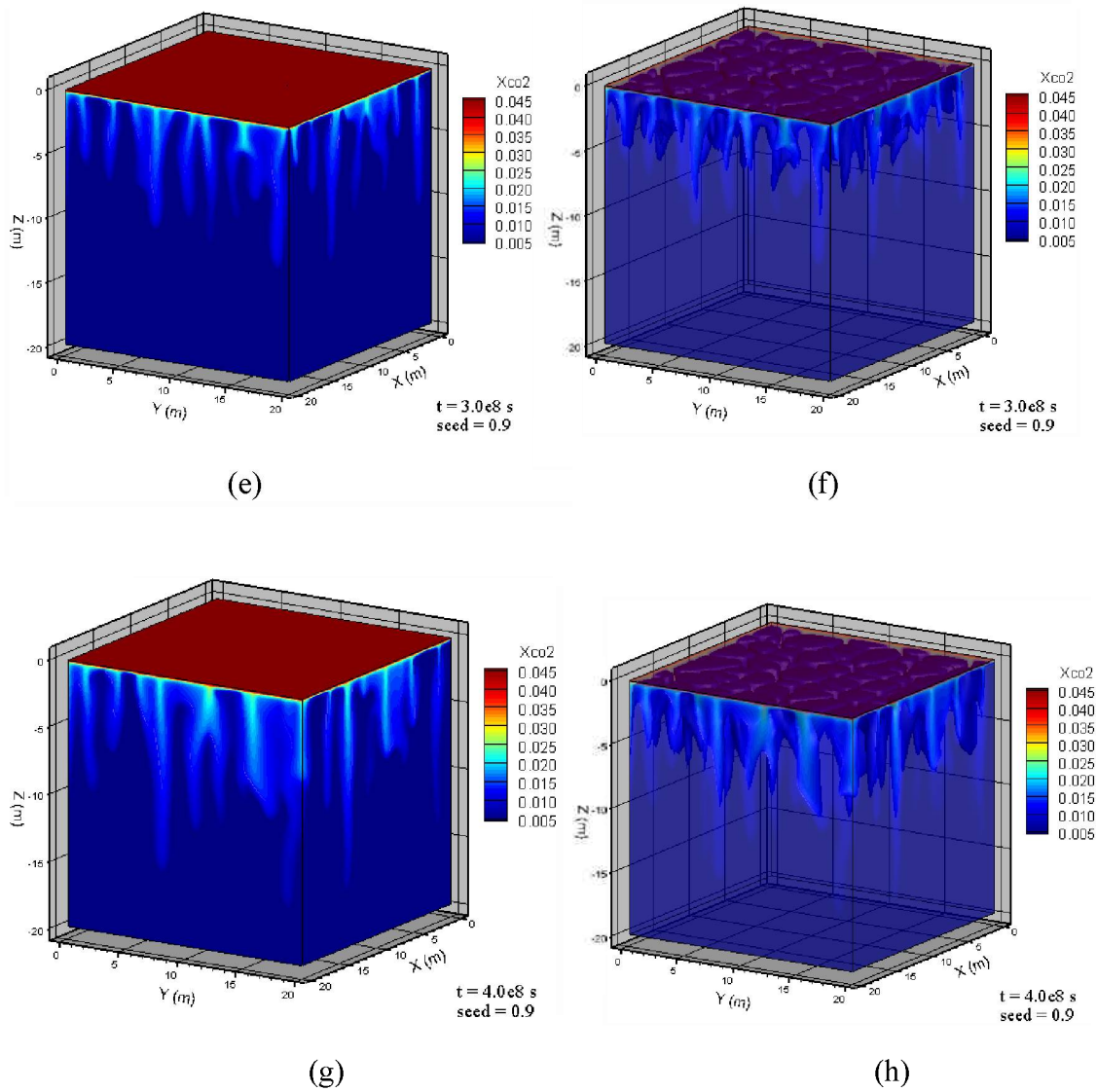
Figure 5.21. 3D views of dissolved CO_2 after four different simulation times, in which a, c, e, and g are non-transparent to show the fingers of aqueous CO_2 in the outside walls of the model, b, d, f and h are transparent to show iso-fraction surface inside the model (seed=0.9).

(a)

(b)

(c)

(d)
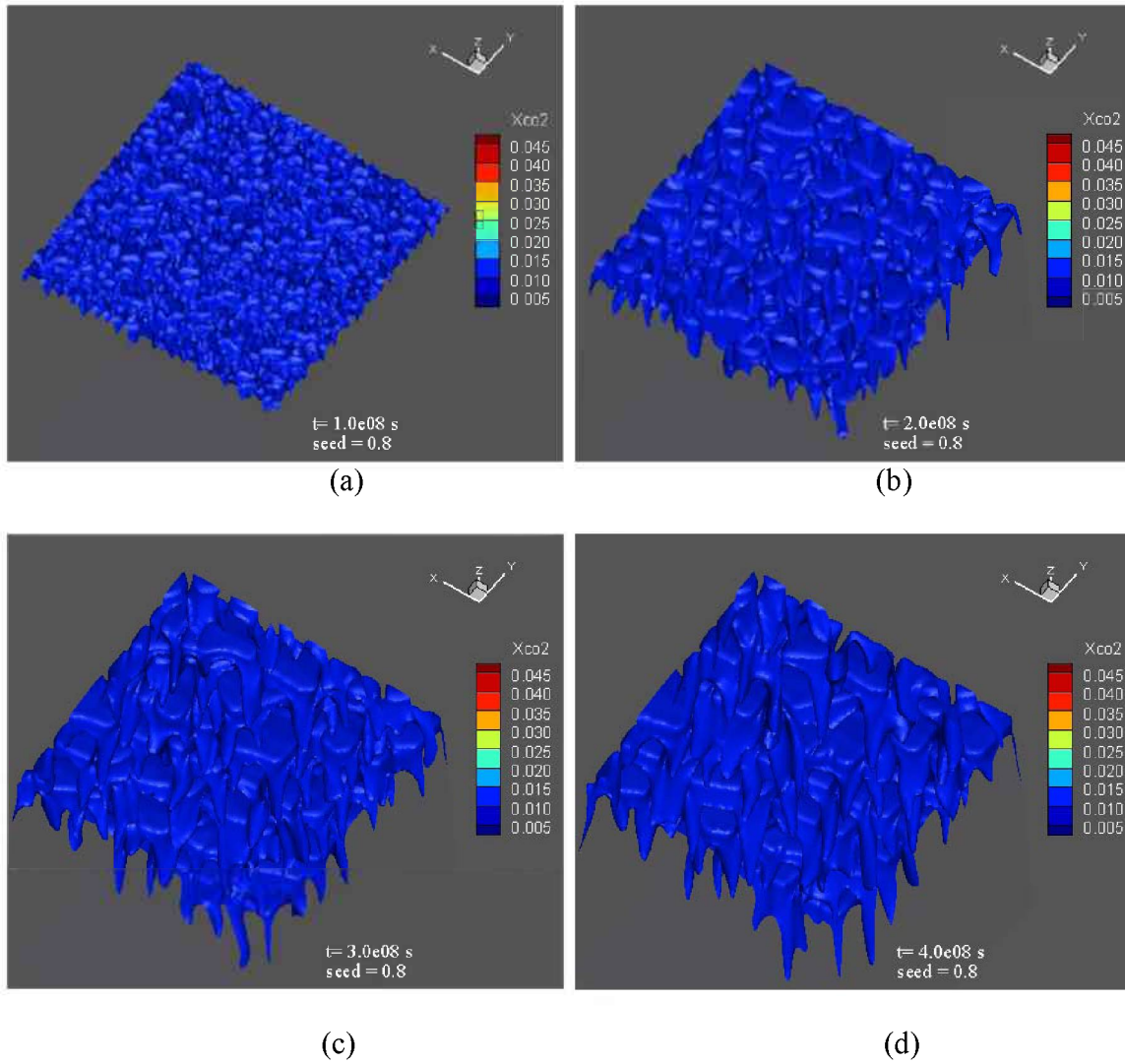
Figure 5.22. Views from below show flat characteristic of the fingers (seed =0.8).
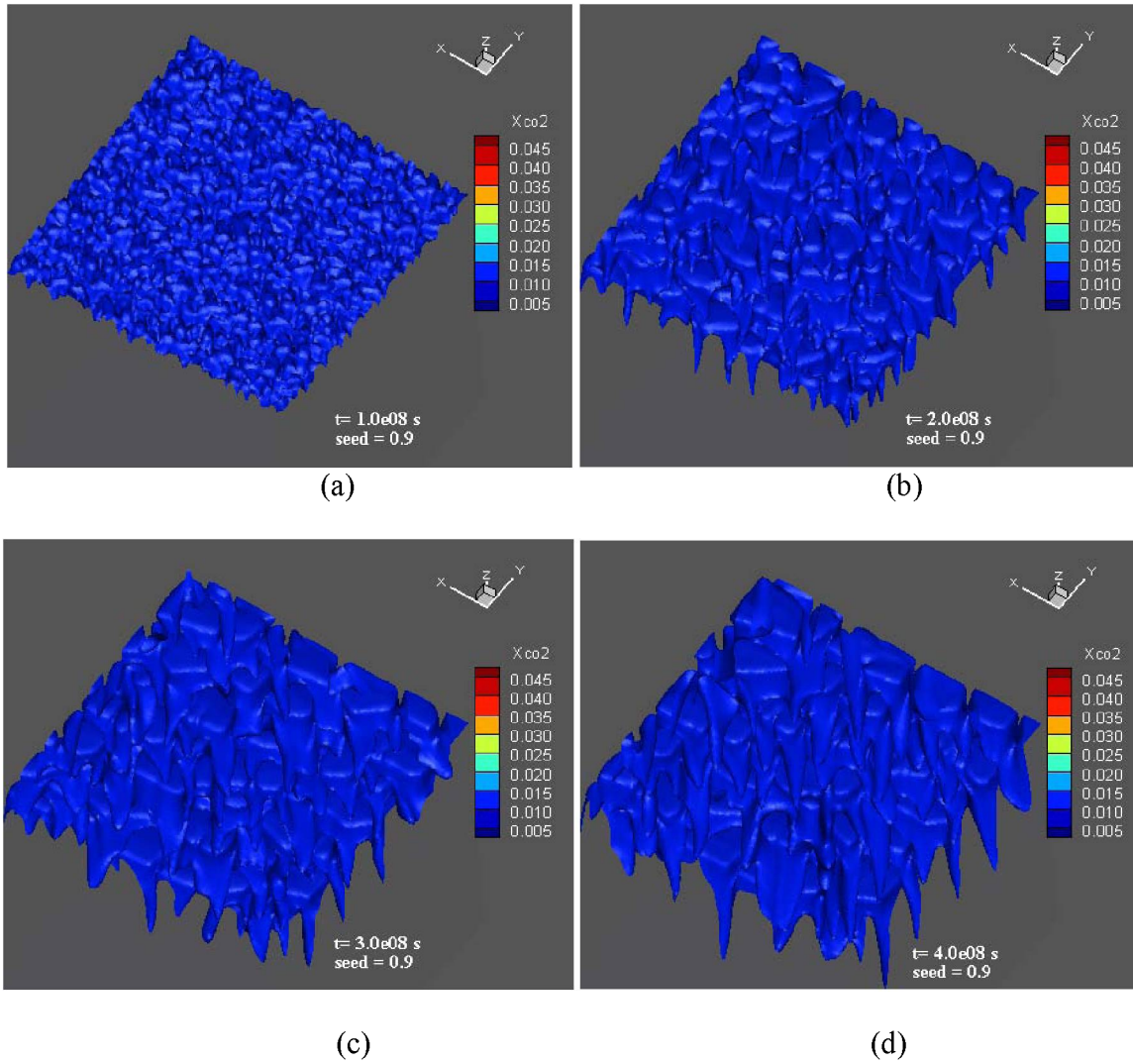
Figure 5.23. Views from below show flat characteristic of the fingers (seed =0.9).
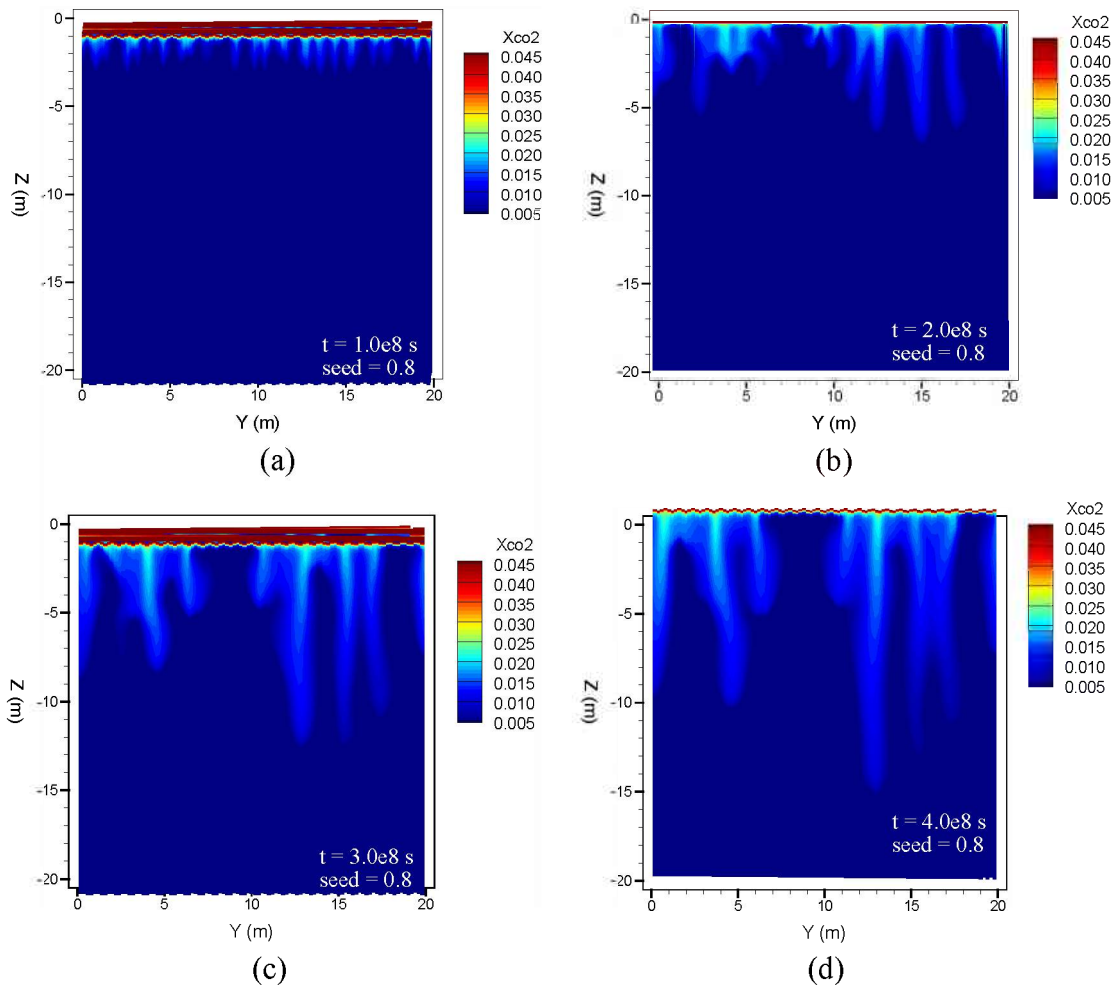
Figure 5.24. 2D spatial distribution of dissolved CO_2 after four different simulation times at a slice inside the 3D model, the slice is located at 10m in the x direction as a yz-plane (seed=0.8).
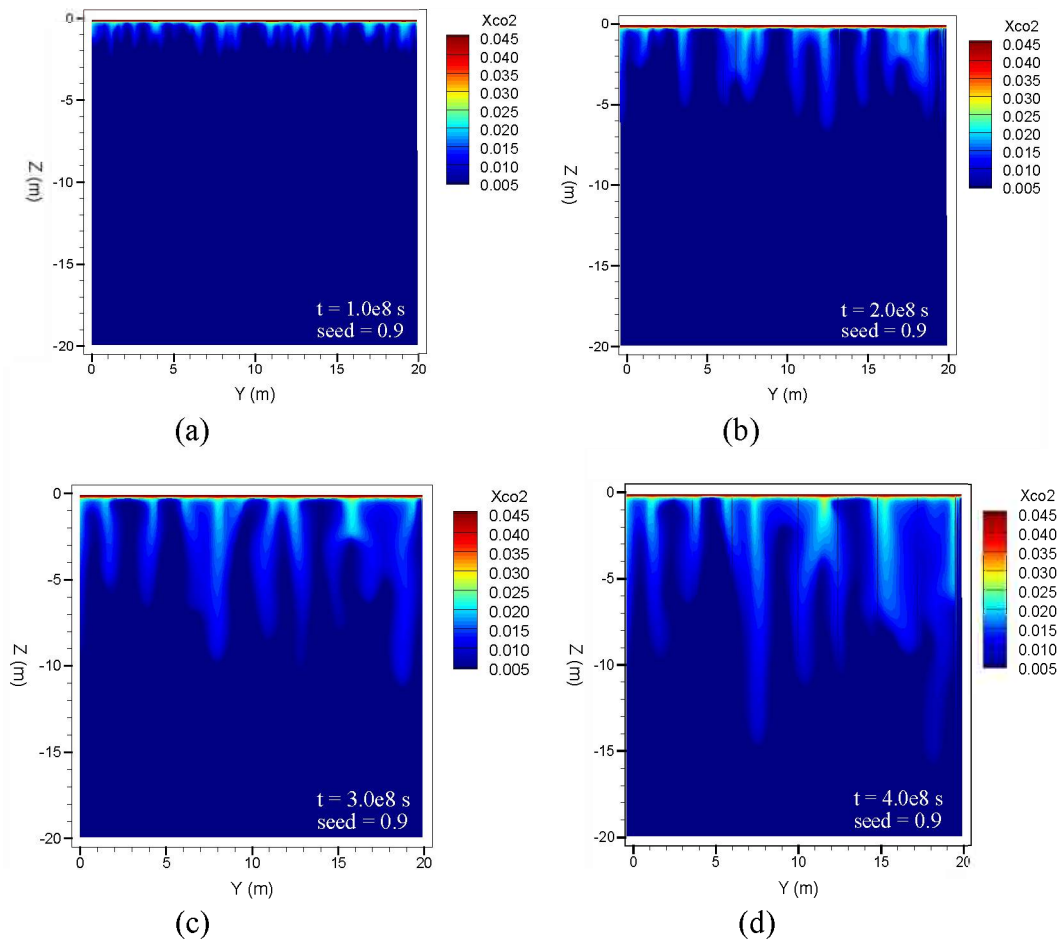
Figure 5.25. 2D spatial distribution of dissolved CO_2 after four different simulation times at a slice inside the 3D model, the slice is located at 10m in the x direction as a yz-plane (seed=0.9).

Summary and Conclusions

We reviewed the literature related to the study of density driven convective flows and on the instability of CO_2 dissolution-diffusion-convection processes. We used our TOUGH2-CSM to run simulations that model the density-driven flow instability that would occur during CO_2 sequestration. CO_2 diffused through the top of the system and dissolved in the aqueous phase there, increasing its density. Density fingers formed along the top boundary, and coalesced into a few prominent ones, causing convective flow that forced the fluid to the system bottom. These simulations were in two and three dimensions.

We ran additional simulations of convective mixing with density contrast caused by variable dissolved CO_2 concentration in saline water, modeled after laboratory experiments in which supercritical CO_2 was circulated in the headspace above a brine saturated packed sand in a pressure vessel. As CO_2 is dissolved into the upper part of the saturated sand, liquid phase density increases causing instability and setting off convective mixing. We obtained good agreement with the laboratory experiments, which were characterized by finger development and associated mixing of dissolved CO_2 into the system. We then varied a wide range of parameters and conceptual models in order to analyze the possibility of convective mixing under different conditions, such as various boundary conditions, and chemical reaction conditions. The CO_2 fingers from different simulations showed great differences as time progressed, caused by permeability heterogeneity. The early time diffusive phenomenon was captured by fine grid resolution, and the permeability heterogeneity affected the pattern of the CO_2 fingers. In addition, the fingers from three-dimensional simulations tended to be larger and flatter than the two-dimensional ones.

Task 6.0: Implementation of Efficient Parallel Computing Technologies

The TOUGH2-CSM code

TOUGH2-MP (Zhang *et al.*, 2008) is a massively parallel version of TOUGH2 (Pruess, 1991) and was developed to significantly improve computational time for large, complex models. It includes many of the TOUGH2 fluid property modules and other capability of the standard TOUGH2. We used the TOUGH2-MP code as the basis for TOUGH2-CSM.

TOUGH2-MP depends on several other thirty party software packages including Metis (http://www-users.cs.umn.edu/~karypis/metis/metis/download.html), Aztec (http://www.cs.sandia.gov/CRF/aztec1.html), and MPICH2 (http://www.mpich.org/). The Metis package contains software for grid domain partitioning, the Aztec package contains software for iterative linear equation solution, and MPICH2, an implementation of MPI (Message Passing Interface), is a message passing library for distributed memory applications used in parallel computing. We compiled the TOUGH2-MP code by compiling the ten FORTRAN files comprising the TOUGH2-MP source code (which includes the ECO2N fluid property package (Pruess and Spycher, 2007)), and linking the two library files generated from the Metis and Aztec software packages.

TOUGH2-CSM Grid Generation

The TOUGH2-CSM grid generation module (MESHMAKER) can generate Cartesian, radial, and MINC (Multiple Interactive Continua) grids (Pruess and Narasimhan, 1985). Arrays dimensioned to preset values and the TOUGH2-MP grid block naming convention introduced limitations on the largest grid the module can generate. We modified the grid generation module extensively. We dimensioned arrays dynamically, based on user input grid size, and introduced a new grid block naming convention. This convention is based on a 62-character alphabet (digits 0-9, followed by upper and case letters, and then lower case letters) with 5-character grid block names, resulting in just under one billion grid block names. The first such grid block name is "00001" and the last is "zzzzz." We also increased the efficiency of the code greatly, allowing much larger grids to be generated than before, and in much less time.

TOUGH2-CSM Grid block Partitioning

TOUGH2-CSM generates sets of algebraic equations that are solved in parallel. The structure of these algebraic equations is determined from the grid blocks and their connections to neighboring ones from input data.

Parallel solution of these algebraic equations requires that the grid blocks be partitioned into many sets and mapped into the distributed memory of the parallel computer. During the partitioning process, special care needs to be taken so that the parallel computational load is balanced, i.e., each processor does approximately the same amount of computation, and the communication between processors required by the parallel solution is minimized.

The actual partitioning of the grid blocks into almost equal-sized parts is performed using three different partitioning algorithms that are implemented in the Metis software (Karypsis and Kumar, 1998). These three algorithms are called K-way, VK-way, and Recursive. K-way is multilevel version of a traditional graph partitioning algorithm that minimizes the number of edges that straddle the partitions. VK-way is a modification of K-way that instead minimizes the actual total communication volume. Recursive is a recursive bisection algorithm which objective is to minimize the number of edges cut. Figure 6.1 illustrates the partitioning of a grid containing fourteen grid blocks between three processors (numbered 0, 1, and 2). The vertices of the graph represent grid blocks and the edges represent connections, i.e., interface areas between pairs of blocks.
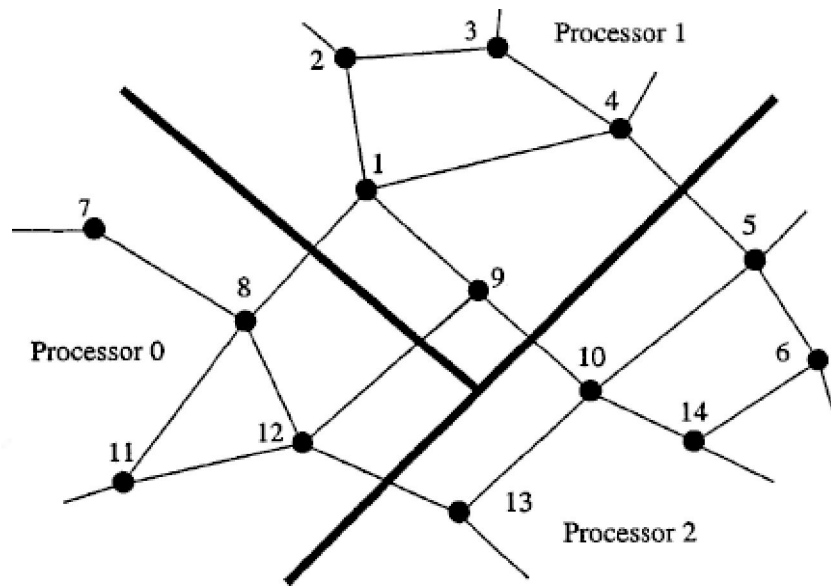
Figure 6.1. Example grid partitioning of fourteen grid blocks (vertices) between three processors (numbered 0, 1, and 2). Partition boundaries are shown by the thicker lines and grid block connections are shown by the thinner lines.

The Metis software partitions the user-input grid during execution of TOUGH2-CSM. This partition is not done in parallel because the Metis software is serial; consequently only a fraction of the memory and computing power of the platform TOUGH2-CSM would be run on can be utilized during a partition with this software. In order to avoid this limitation, we obtained the parallel version of Metis, called ParMetis (Karypsis and Kumar, 1999), and wrote a stand-alone program that uses it and TOUGH2-CSM input data to generate a stand-alone grid partition that is read as input data by TOUGH2-CSM. This capability increased the maximum grid sized we could partition by an order of magnitude.

TOUGH2-CSM Code Platforms

We initially installed TOUGH2-CSM on a Dell PC with eight Intel® Xeon® E5405 2.0 GHz processors with total memory of 15.7 GB, and a Linux operating system.

In August, 2011, we completed the purchase of a cluster computer for our research group (called Energy Modeling Group) from Ace Computers of Arlington Heights, IL. The cluster consisted of a head node and sixteen compute nodes. Each node had 24 GB of memory and two Intel® 5620 2.4GHZ 4-core processors, for a total of 128 cores and 256 processors due to hyperthreading (excluding the head node). There was 10TB of disc storage. The latest Intel® Fortran and C/C++ compilers were included with the cluster, as well as MPICH2.

In November, 2013, we upgraded our cluster computer. We added an additional sixteen compute nodes, also from Ace Computers. Each additional node had 32 GB of memory and two Intel® E5-2620 2.0 GHZ 6-core processors, an addition of 192 cores and 384 processors due to hyperthreading. The entire cluster now as 32 compute nodes, 320 cores, 640 processors, and 896 GB memory.

TOUGH2-CSM Parallel Code Verification

1) In Salah Gas Project

The In Salah Gas Project, located in central Algeria, is a CO_2 storage project. Natural gas produced nearby is high in CO_2 and this CO_2 is injected back into the water leg of a depleting gas field for geological storage. Surface uplift from CO_2 injection has been measured by satellite-based inferrometry and Rutqvist et al. (2010) did a reservoir-geomechanical analysis of In Salah CO_2 injection and surface uplift using the TOUGH2-FLAC numerical simulator in order to determine if the uplift can be explained by pressure changes and deformation in the injection zone only. The TOUGH2-FLAC numerical simulator is a linkage between two existing well established codes, TOUGH2 (Pruess, 1991) that solves nonisothermal, multiphase, multicomponent, fluid flow problems in complex geological systems and FLAC3D (Itasca, 1997), developed for rock and soil mechanics that can handle coupled thermomechanical and hydromechanical processes for single-phase fluid flow.

We reran their analysis on our code, and we used our cluster computer to demonstrate the parallel code's ability to simulate larger problems. The simulation used the sixteen original nodes and all sixteen processors per node, a total of 256 processors.

The simulated domain was 10x10x4 km with one 1.5 km horizontal injection well at 1810 m depth and in the domain center. The domain consisted of four geological layers, shallow overburden, caprock, injection zone, and base, whose properties are shown in Table 6.1.

Table 6.1. Geological layer properties for In Salah CO_2 injection.

Property	Shallow overburden (0–900 m)	Caprock (900–1800 m)	Injection zone (1800–1820 m)	Base (> 1800 m)
Young's modulus, GPa	1.5	20.0	6.0	20.0
Poisson's ratio	0.2	0.15	0.2	0.15
Biot's Coefficient	1.0	1.0	1.0	1.0
Porosity	0.1	0.01	0.17	0.01
Permeability, m^2	10^{-17}	10^{-19}	10^{-14}	10^{-21}
Residual CO_2 saturation	0.05	0.05	0.05	0.05
Residual liquid saturation	0.3	0.3	0.3	0.3
van Genuchten (1980) m	0.457	0.457	0.457	0.457
van Genuchten, P_0, kPa	19.9	621.0	19.9	621.0

The reservoir initially contained water and the initial temperature and pressure at the injection well were 90 °C and 17.9 MPa, respectively. The lateral reservoir boundaries were maintained at constant pressure and CO_2 was injected at 9.734 kg sec^{-1} for three years.

CO_2 injection causes surface uplift, a change in reservoir height. Reservoir height is the sum of grid block height over a z-direction column of grid blocks. Using the definition of linear strain from Equation 3.27, we express grid block l height, Δz_l, as:

$$\Delta z_l = \Delta z_{l,0}\left(1 - \varepsilon_z\right)$$ (6.1)

where ε_z is z-direction linear strain and $\Delta z_{l,0}$ is grid block height at zero strain. Given initial grid block height $\Delta z_{l,i}$ and linear strain $\varepsilon_{z,i}$, we can write Equation 6.1 as:

$$\Delta z_l = \Delta z_{l,i}\frac{\left(1 - \varepsilon_z\right)}{\left(1 - \varepsilon_{z,i}\right)}$$ (6.2)

and surface uplift, Δz_{uplift}, then becomes:

$$\Delta z_{uplift} = \sum_l \left(\Delta z_l - \Delta z_{l,i} \right) = \sum_l \Delta z_{l,i} \frac{\left(\varepsilon_{z,i} - \varepsilon_z \right)}{\left(1 - \varepsilon_{z,i} \right)}$$

(6.3)

where the sum over index l refers to a z-direction column of grid blocks. Finally, we express linear strain in terms of volumetric strain by assuming isotropic strain:

$$\varepsilon_z = \frac{\varepsilon_v}{3}$$

(6.4)

and calculate surface uplift using Equations 6.3 and 6.4.

We simulated a 5 x 5 x 4 km quarter symmetry element of their system with a 1000 x 1000 x 60 grid (60 million grid blocks). The areal grid was uniform. Layers 1-5 were shallow overburden, 6-30 were caprock, 31-40 were injection zone, and 41-60 were base. The injection zone layers were 2 m thick and layer thickness gradually increased away from there, as shown in Table 6.2.

Table 6.2. Layer thicknesses for In Salah simulation.

Layer	Thickness, m	Layer	Thickness, m	Layer	Thickness, m
1-5	180.00	17	15.21	48	6.46
6	181.64	18	12.14	49	9.55
7	144.97	19	9.69	50	14.12
8	115.71	20	7.74	51	20.88
9	92.36	21	6.17	52	30.86
10	73.72	22	4.93	53	45.63
11	58.84	23	3.93	54	67.45
12	46.96	24	3.14	55	99.72
13	37.48	25	2.51	56	147.42
14	29.92	26-45	2.00	57	217.94
15	23.88	46	2.96	58	322.19
16	19.06	47	4.37	59	476.30
				60	704.14

The simulation took 21.9 days to run with 97.6% of the time used for linear equation solution. The Jacobian matrix had four variables per grid block (three from the ECO2N property module and mean stress) resulting in a total of 240 million equations.

Figure 6.2 shows surface uplift after three years of CO_2 injection. The maximum uplift occurs in the vicinity of the injection well, centered at the origin, and is about 0.02 m. This is in agreement with the value shown in Rutqvist et al. (2010) for caprock permeability of 10^{-19} m^2.
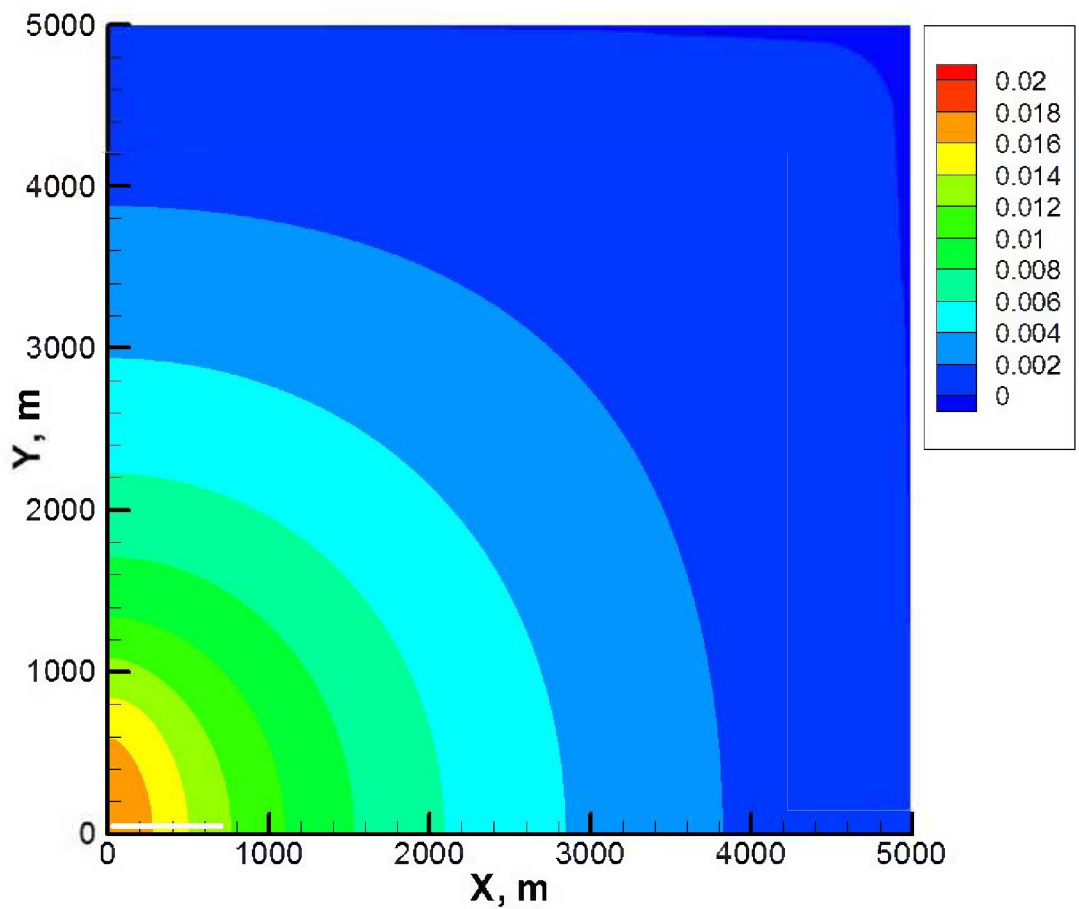
Figure 6.2. Surface uplift, m, for TOUGH2-CSM In Salah CO_2 injection simulation; injection well shown by thick horizontal line at origin.

Summary and Conclusions

We developed a massively parallel reservoir simulator, called TOUGH2-CSM, for modeling THM processes in fractured and porous media brine aquifers. The starting point for our simulator is the massively parallel TOUGH2-MP code. We made enhancements and modifications to the original code in order to substantially increase the grid size that could be run. We installed and ran TOUGH2-CSM on various platforms, including a multi-core PC and a cluster.

We verified the numerical implementation and parallel code using an example problem from the literature. This problem, with a grid size of sixty million, utilized the cluster's entire memory and all of its processors. We obtained a good match of surface uplift after three years of CO_2 injection into the water leg of a depleting gas field.

Task 7.0: Implementation of General Fracture Conceptual Models

Introduction

The technique used in developing and implementing general fracture conceptual models to simulating flow and transport processes of CO_2 in fractured reservoirs follows a generalized dual-continuum methodology (Kazemi, 1969; Pruess and Narasimhan, 1985; Wu and Pruess, 1988; Wu and Qin, 2009). This method treats fracture and matrix flow and interactions using a multi-continuum numerical approach, including the double- or multi-porosity method, the dual-permeability method, and the more general MINC method (Pruess and Narasimhan, 1985). It has been shown (e.g., Wu et al. 2004a and b) that the same continuum concept is also applicable to multiphase flow though single or multiple discrete fractures or fracture network.

The MINC approach is a generalization of the double-porosity concept, originally developed by Barenblatt *et al.* (1960) and Warren and Root (1963) among others, to multiple porous continua. The double-porosity approach is used to describe fluid flow in fractured reservoirs, an idealization of which is shown in Figure 7.1. In these reservoirs, the fractures have larger permeability and smaller porosity relative to those of the porous rock matrix. As a result, a pressure change in the reservoir would travel through the fractures much faster than through the rock matrix. The double-porosity approach assumes that global fluid and heat flow occur mostly through the fractures with a quasi-steady exchange between the fractures and matrix that is dependent on pressure and temperature differences between them.

For many systems, such as those with complex, multiphase flow or large matrix volumes, the assumption of quasi-steady exchange between the fractures and matrix is not a good one because the time scale associated with flow through the matrix is too large. We use the MINC approach to describe flow in these systems. In the MINC approach, flow within the matrix is described more accurately by subdividing the matrix into nested volumes, as shown in Figure 7.2, with flow occurring between adjacent nested matrix volumes as well as between the fractures and the outer matrix volume. Flow within the matrix is one-dimensional and transient and the MINC approach reduces to the double-porosity one if there is only one matrix subdivision.
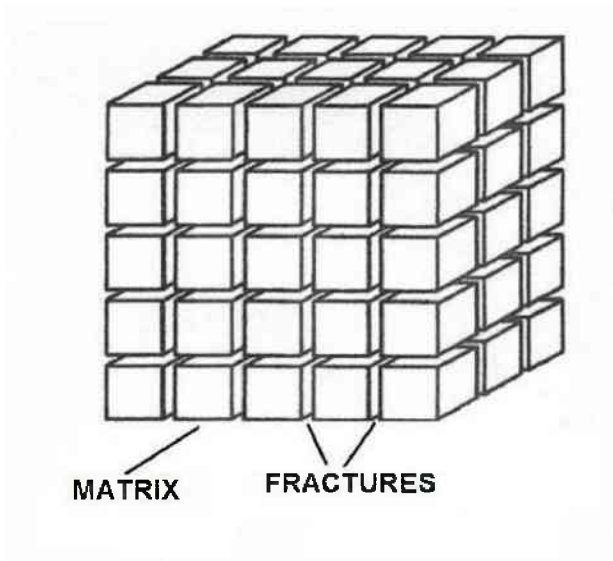
171

Figure 7.1. Idealized double porosity model of a fractured reservoir showing fractures and matrix blocks, adapted from Pruess *et al.* (1999).
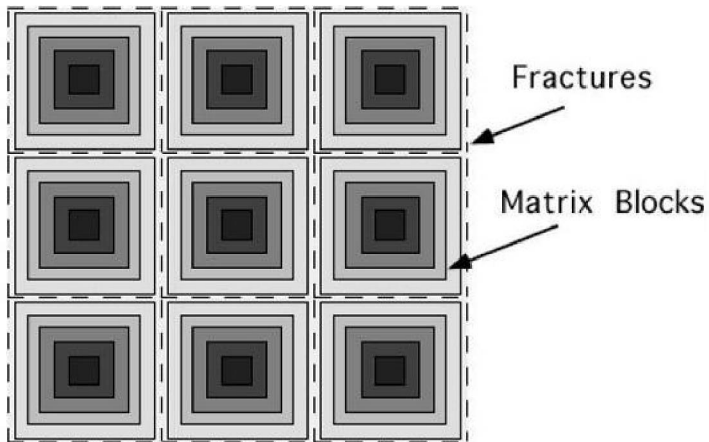
Figure 7.2. Idealized MINC grid showing fractures and nested matrix volumes, adapted from Pruess *et al.* (1999).

172

TOUGH2-CSM Multiple-Porosity Geomechanical Equations

Bai *et al.* (1993) present a generalization of Hooke's law for a single-porosity medium (Equation 3.2) to a multi-porosity one, a common example of which is the double-porosity medium consisting of a network of fractures and rock matrix:

$$\boldsymbol{\tau} - \sum_j \alpha_j P_j \boldsymbol{I} = 2G\boldsymbol{\varepsilon} + \lambda (tr\varepsilon) \boldsymbol{I} \tag{7.1}$$

where subscript j refers to a multi-porosity continuum such as fracture or matrix. Expressions for the generalized Biot's coefficients, α_j, for a double-porosity medium have been presented by Wilson and Aifantis (1982):

$$\alpha_1 = 1 - \frac{K}{K_*} \tag{7.2}$$

and

$$\alpha_2 = \frac{K}{K_*} \left(1 - \frac{K_*}{K_s} \right) \tag{7.3}$$

where K_s is the solid modulus, K_* is the modulus of the porous medium without the fractures, subscript 1 refers to the fractures, and subscript 2 refers to the matrix. We obtain Hooke's law for a thermo-multi-poroelastic medium by including the temperature term from Equation 3.4 in Equation 7.1 for each multi-porosity continuum, since temperature varies between multi-porosity continua:

$$\boldsymbol{\tau} - \left[\sum_j \left(\alpha_j P_j + 3\beta K \omega_j \left(T_j - T_{ref} \right) \right) \right] \boldsymbol{I} = 2G\boldsymbol{\varepsilon} + \lambda (tr\varepsilon) \boldsymbol{I} \tag{7.4}$$

where ω_j is the multi-porosity continuum volume fraction.

We combine Equations 7.4, 3.5, and 3.6 to obtain the thermo-multi-poroelastic Navier equation:

$$\nabla \left[\sum_j \left(\alpha_j P_j + 3\beta K \omega_j T_j \right) \right] + (\lambda + G) \nabla (\nabla \cdot \boldsymbol{u}) + G\nabla^2 \boldsymbol{u} + \boldsymbol{F}_b = 0 \tag{7.5}$$

Taking the divergence of Equation 7.5 and following the same steps as for the single-porosity derivation results in an equation analogous to Equation 3.12 relating volumetric strain, mean stress, pore pressures, and temperatures:

$$K\varepsilon_v = \tau_m - \sum_j \left(\alpha_j P_j + 3\beta K \omega_j \left(T_j - T_{ref} \right) \right) \tag{7.6}$$

and an equation analogous to Equation 3.14 relating mean stress, pore pressures, temperatures, and body force:

$$\nabla \cdot \left[\frac{3(1-\upsilon)}{1+\upsilon} \nabla \tau_m + \mathbf{F}_b - \frac{2(1-2\upsilon)}{1+\upsilon} \nabla \left[\sum_j \left(\alpha_j P_j + 3\beta K \omega_j T_j \right) \right] \right] = 0 \tag{7.7}$$

Discretization of Multiple-Porosity TOUGH2-CSM Conservation Equations

The multiple-porosity TOUGH2-CSM mass, energy, and momentum balance equations are discretized in space using the integral finite difference method (Narasimhan and Witherspoon, 1976). For a multiple-porosity system, the simulation domain is subdivided into primary grid blocks with unstrained volume $V_{n,0}$ and each primary grid block is subdivided into porous continua, each with unstrained volume $V_{n,0,j}$. The mass and energy conservation equations are integrated over each porous continuum volume and the resulting set of these equations in residual form is:

$$\left[M_{n,j}^k (1 - \varepsilon_{v,n}) \right]^{l+1} - \left[M_{n,j}^k (1 - \varepsilon_{v,n}) \right]^l - \frac{\Delta t}{V_{n,0,j}} \left[\sum_m A_{nm,0} \left(1 - \varepsilon_{A,nm} \right) F_{nm,j}^k + V_{n,0,j} \left(1 - \varepsilon_{v,n} \right) q_{n,j}^k \right]^{l+1} = 0 \tag{7.8}$$

where the subscripts n and j appearing together refer to porous continuum j in primary grid block n. The multiple-porosity geomechanical equations are integrated over each primary grid block volume. When this is applied to Equation 7.6, we obtain the following:

$$K \varepsilon_{v,n} = \tau_{m,n} - \sum_j \left(\alpha_j P_{n,j} + 3\beta K \omega_{n,j} \left(T_{n,j} - T_{ref} \right) \right) \tag{7.9}$$

When this is applied to Equation 7.7, we obtain the following:

$$\sum_m \left[\begin{array}{l} \left(\frac{3(1-\upsilon)}{(1+\upsilon)} \right)_{nm} \dfrac{\tau_n - \tau_m}{D_{n,0}\left(1-\varepsilon_{D,n}\right) + D_{m,0}\left(1-\varepsilon_{D,m}\right)} + \left(\mathbf{F}_b \cdot \mathbf{n} \right)_{nm} - \\ \left(\frac{2(1-2\upsilon)}{(1+\upsilon)} \right)_{nm} \sum_j \left(\begin{array}{l} \alpha_j \dfrac{P_{n,j} - P_{m,j}}{D_{n,0}\left(1-\varepsilon_{D,n}\right) + D_{m,0}\left(1-\varepsilon_{D,m}\right)} + \\ \left(3\beta K \omega_j \right)_{nm} \dfrac{T_{n,j} - T_{m,j}}{D_{n,0}\left(1-\varepsilon_{D,n}\right) + D_{m,0}\left(1-\varepsilon_{D,m}\right)} \end{array} \right) \end{array} \right] A_{nm,0} \left(1 - \varepsilon_{A,nm} \right) = 0 \tag{7.10}$$

Consider a simulation domain discretized into N_v grid blocks with N_k mass components. When using the single-porosity approach, N_k mass conservation equations, one momentum conservation equation, and one energy conservation equation are associated with each grid block for a total of $N_v(2+N_k)$ equations for the entire simulation domain. When using the MINC approach with N_ϕ multi-porous continua in each primary grid block, N_k mass conservation equations and one energy conservation equation are associated with each porous continua, and one momentum equation is associated with each primary grid block for a total of N_v

$(1+N_\phi(1+N_k))$ equations for the entire simulation domain. The number of conservation equations for single-porosity and multi-porosity simulations are summarized in Table 7.1.

Table 7.1. Number of conservation equations for single-porosity and multi-porosity cases.

Porosity	Number Grid Blocks	Porous Continua/ Grid Block	Mass, Energy Conservation Equations/GB	Momentum Conservation Equations/GB	Total Equations/ GB	Total Equations
Single	N_v	1	$1+N_k$	1	$2+N_k$	$(2+N_k)N_v$
Multi	N_v	N_ϕ	$(1+N_k)N_\phi$	1	$(1+N_k)N_\phi+1$	$((1+N_k)N_\phi+1)N_v$

Verification and Application Examples for Multiple-Porosity TOUGH2-CSM

We describe two simulations to provide model verification and application examples. The first, one-dimensional consolidation of a double-porosity medium, is compared to the analytical solution. The second is a match of published results from the literature, a simulation of CO_2 injection into hypothetical aquifer-caprock systems. In this problem, the authors modeled geomechanical processes by coupling two simulators, TOUGH2, which simulates fluid flow and heat transport, and FLAC, which simulates rock mechanics with thermomechanical and hydromechanical interactions.

1) One-Dimensional Consolidation of Double-Porosity Medium

In this one-dimensional consolidation problem, a z-direction stress is applied to the top of a fluid-filled double-porosity (fracture and matrix) porous rock column, instantaneously inducing a deformation and a pore pressure increase. Fluid then is allowed to drain out of the column top and the pore pressure increase dissipates. An analytical solution to this problem was presented by Wilson and Aifantis (1982). In their analysis, strain is uniaxial and z-direction stress is constant throughout the process.

We simulate this problem in two steps. The first step is the load application to produce the pore pressure increase. We start from an unstrained state where pore pressures (fracture and matrix) and mean stress are both equal ($\tau_{m,0} = P_{1,0} = P_{2,0}$) and impose a greater mean stress at the column top ($\tau_{m,1}$) that induces a pore pressure increase ($P_{j,1}$) in the column after the system equilibrates. For uniaxial deformation in an isothermal, double-porosity system, mean stress, z-direction stress, and pore pressures are related by:

$$\tau_m = \frac{1}{3}\frac{(1+v)}{(1-v)}\left(\tau_{zz} - \sum_j \alpha_j P_j\right) + \sum_j \alpha_j P_j \tag{7.11}$$

and using this equation, we calculate the constant z-direction stress ($\tau_{zz,0}$) from the imposed mean stress ($\tau_{m,1}$) and the equilibrated pore pressures ($P_{j,1}$).

The second step is simulation of fluid drainage. The column is initially at the above equilibrated state. We set the pore pressures at the column top to the initial pore pressures ($P_{j,0}$). Because z-direction stress is constant, the mean stress at the column top must set as well, calculated from

Equation 7.11 using $\tau_{zz,0}$ and $P_{j,0}$. Fluid then drains out of the column top as the pore pressures return to the initial values, $P_{j,0}$.

Our simulated column was 400 m long with rock properties shown in Table 7.2. The column was subdivided into 400 grid blocks each of which contained two porous continua, fracture and matrix.

Table 7.2. Rock properties for one-dimensional consolidation of double-porosity column

	Fracture	Matrix
Young's modulus, GPa	8.0	8.0
Poisson's ratio	0.2	0.2
Porosity	0.004	0.032
Permeability, m2	$8.9 \cdot 10\text{-}13$	$8.9 \cdot 10\text{-}17$
Biot's coefficient	0.1	0.9
Volume fraction	0.5	0.5

Initial pore pressures and mean stress were 5.0 MPa and the imposed mean stress was 8.0 MPa. The resulting equilibrium pore pressures were 6.2 MPa and the calculated z-direction stress was 9.8 MPa. We ran the drainage portion of the simulation for 4000 seconds with one second time steps. Comparison of simulated fracture pressure with the analytical solution is shown in Figure 7.3, with excellent agreement.
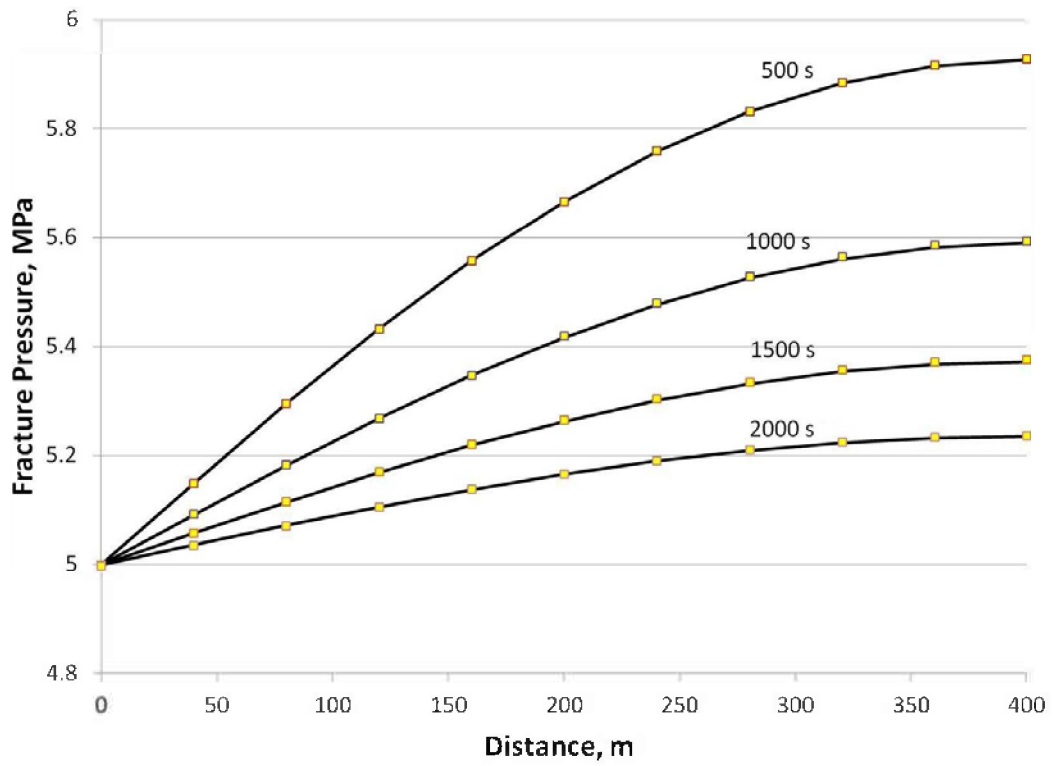
Figure 7.3. Comparison of fracture pressure analytical solution (solid lines) to simulation (points) for one-dimensional consolidation of double-porosity column.

2) CO$_2$ Sequestration in an Aquifer-Caprock System

Rutqvist and Tsang (2002) simulated CO$_2$ injection into a hypothetical aquifer-caprock system to study CO$_2$ plume spread, ground surface uplift, the possibility of mechanical failure, and other changes induced by the injection. Their system consisted of a 200 m thick aquifer bounded below by a 1500 m thick base rock and above by 100 m caprock and a 1200 m zone that extends to the surface. In addition, a fault zone, extending through the caprock, was modeled as a high permeability zone. Rock properties for these zones are shown in Table 7.3.

Table 7.3. Rock properties for aquifer-caprock system.

Property\Layer	Upper	Cap	Aquifer	Base	Fault
Young's modulus, GPa	5.0	5.0	5.0	5.0	2.5
Poisson's ratio	0.25	0.25	0.25	0.25	0.25
Biot's coefficient	1.0	1.0	1.0	1.0	1.0
Zero stress porosity	0.1	0.01	0.1	0.01	0.1
Residual porosity	0.09	0.009	0.09	0.009	0.05
Zero stress permeability, m^2	10^{-15}	10^{-17}	10^{-13}	10^{-17}	10^{-12}

CO$_2$ was injected at a constant rate, 0.05 kg/sec-m, at the aquifer bottom for ten years. They simulated this system using the coupled TOUGH2-FLAC simulator (Rutqvist *et al.*, 2002), with TOUGH2 handling multiphase flow and heat transport and FLAC handling rock deformation.

We reran their case of homogeneous caprock without fractures, using effective stress dependent porosity and permeability (Equations 3.48 and 3.49). Figures 7.4 and 7.5 compare CO$_2$ saturation profiles after ten years injection, with quantitative similarity.
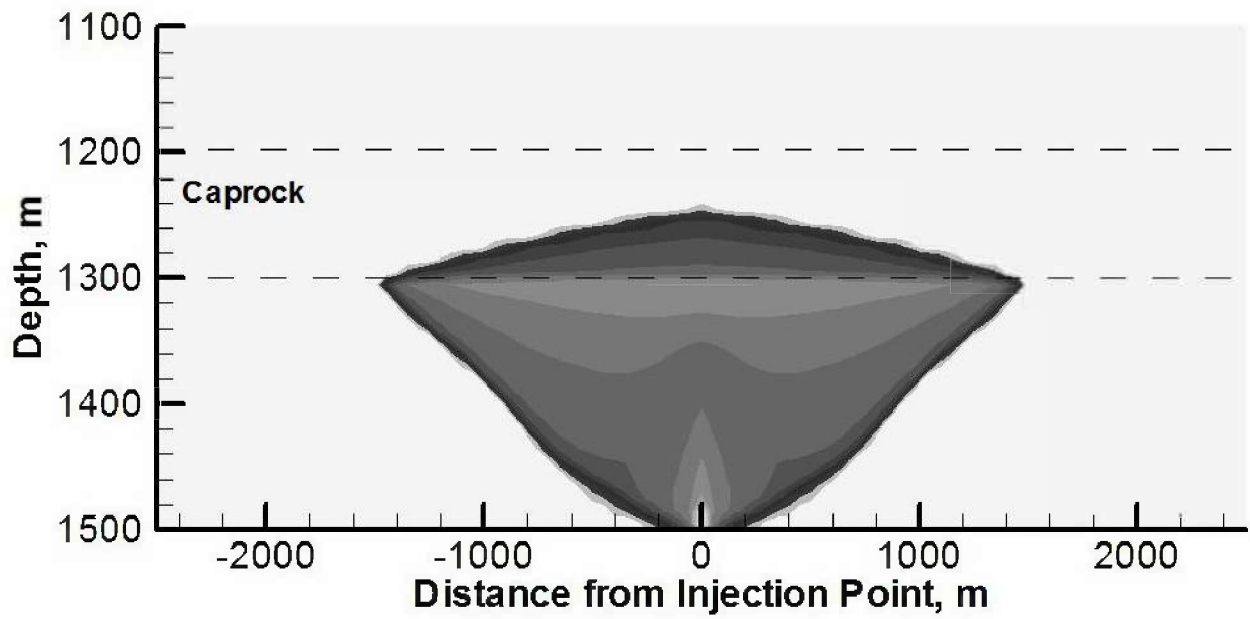
Figure 7.4. CO_2 saturation profile at ten years for TOUGH2-CSM simulation.
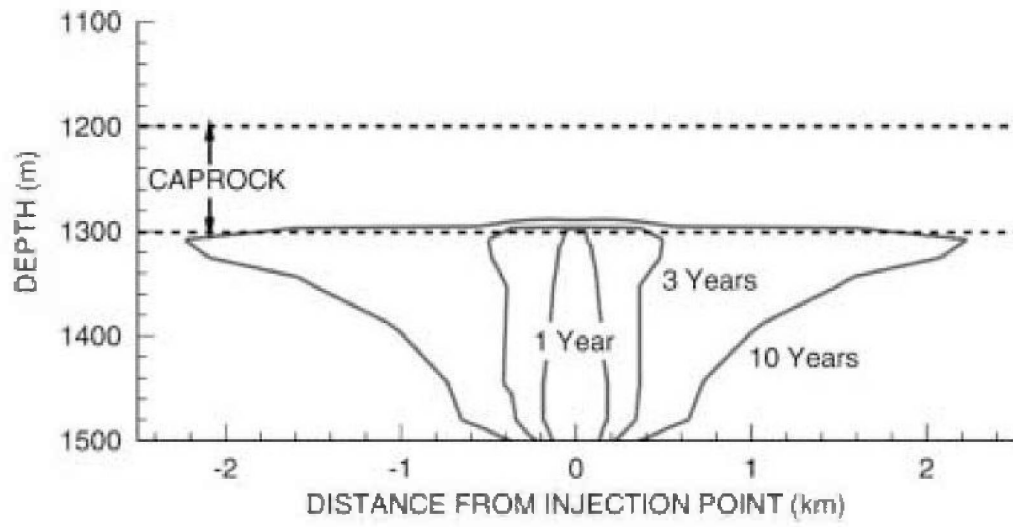
Figure 7.5. Rutqvist and Tsang (2002) CO_2 saturation.

CO_2 injection increases the pore pressure, resulting in changes to mean stress and volumetric strain. Ground surface uplift is calculated from volumetric strain changes by summation over z-direction grid block columns and the assumption of strain isotropy. Figures 7.6 and 7.7 compare surface uplift at various times. These simulations show similar surface uplift profiles.
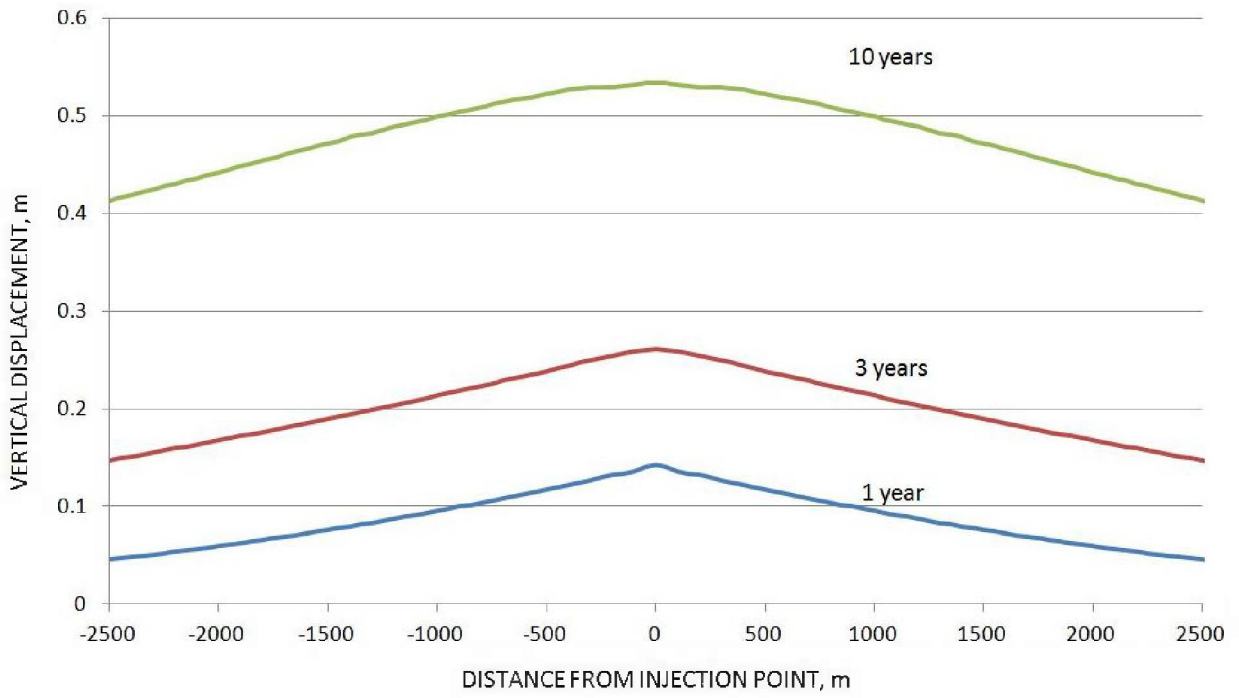
Figure 7.6. TOUGH2-CSM surface uplift at 1, 3, and 10 years.
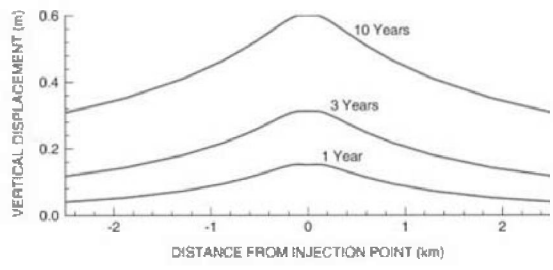
Figure 7.7. Rutqvist and Tsang (2002) surface uplift.

Rutqvist and Tsang (2002) also studied the effects of a vertical fracture zone in the caprock above the aquifer. We simulated this fracture zone by treating a column of grid blocks spanning the caprock zone as double porosity (fracture and matrix) with the rest of the grid being single porosity. Figures 7.8 and 7.9 compare CO_2 saturation profiles after ten years injection, again with quantitative similarity.
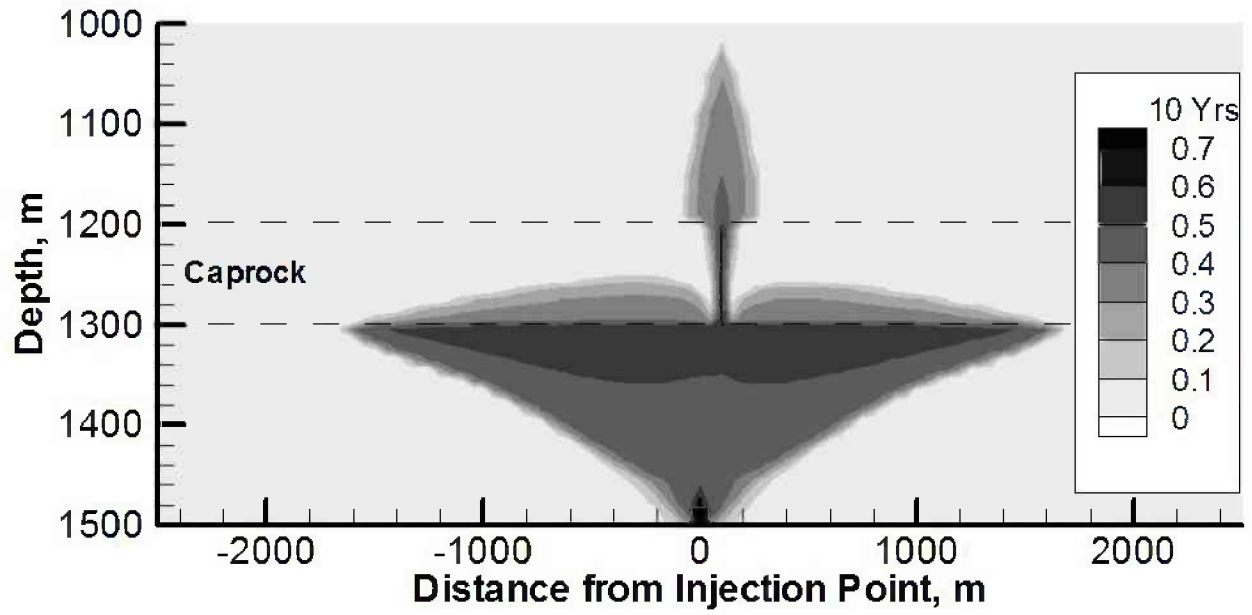
Figure 7.8 TOUGH2-CSM CO_2 saturation profile at 10 years with fracture in caprock.
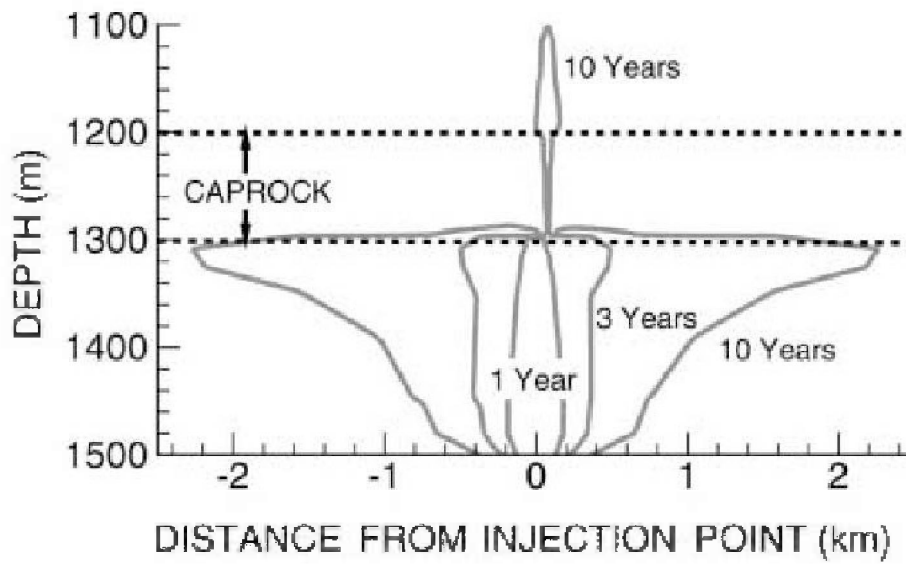
Figure 7.9 Rutqvist and Tsang (2002) CO_2 saturation profile with fracture in caprock.

Summary and Conclusions

We extended the single-porosity TOUGH2-CSM formulation to multi-porosity media, an example of which is fractured brine aquifers. We developed an extended version of Hooke's law for thermo-multi-poroelastic media. We then derived, using that version of Hooke's law and the other fundamental equations describing deformation of elastic media, a momentum conservation equation for multi-porosity media that relates mean stress and porous continua pressures and temperatures. We incorporated that momentum conservation equation alongside the mass and energy conservation equations from the TOUGH2 formulation. We simulate multi-porosity media using the MINC model.

We verified the simulator formulation and numerical implementation using an analytical solution and an example problem from the literature. For the former, we simulated one-dimensional consolidation problem of a double-porosity medium. For the latter, we simulated CO_2 injection into a hypothetical aquifer-caprock system and obtained a good match of CO_2 saturation profiles for a vertical fractured zone present in the caprock, as well as a good match of surface uplift and CO_2 saturation profiles for the system with unfractured caprock.

References

Abousleiman Y., Cheng, A. H.-D., Cui L., Detournay, E., and Roegiers, J.-C.: Mandel's problem revisited. Géotechnique. 46:2 (1996) pp. 187-195.

Allis, R., White, S., Chidsey, T., Gwynn, W., Morgan, C., Adams, M., *et al.*: 2001. Natural CO_2 reservoirs on the Colorado plateau and southern rocky mountains: candidates for CO_2 sequestration. Proceedings of the First National Conference on Carbon Sequestration, Washington, DC, May 2001.

André, L., Audigane, P., Azaroual, M., and Menjoz, A.: Numerical modeling of fluid-rock chemical interactions at the supercritical CO_2-liquid interface during CO_2 injection into a carbonate reservoir, the Dogger aquifer (Paris Basin, France). Energy Conversion and Management: 48, 1782-1797, 2007.

Audigane, P., Gaus, I., Pruess, K., Xu, T.: A long term 2D vertical modeling study of CO_2 Storage Sleipner (North Sea) using Toughreact. PROCEEDINGS, TOUGH Symposium 2006, Lawrence Berkeley National Laboratory, Berkeley, California, May 15-17, 2006.

Audigane, P., Gaus, I., Czernichowski-Lauriol, I., Pruess, K., and Xu, T.: Two-dimensional reactive transport modeling of CO_2 injection in a saline aquifer at the Sleipner site, North Sea. American Journal of Science, 307, 974-1008, 2007.

Bachu, S.: Sequestration of CO_2 in geological media in responseto climate change: capacity of deep saline aquifersto sequester CO_2 in solution. Ener. Convers. Mgmt (2003), 44, 3151–3175.

Bachu, S., Gunter, W. D., and Perkins, E. H.: Aquifer disposal of CO_2: Hydrodynamic and mineral trapping. Energy Conrers. Mgmt (1994), 35(4), 269-279.

Bacona, D. H., Sassb, B. M., Bhargavab, M., Sminchakb, J., asd Guptab, N.: Reactive transport modeling of CO_2 and SO_2 injection into deep saline formations and their effect on the hydraulic properties of host rocks. Energy Procedia: 1, 3283-3290, 2009.

Bai, M., Elsworth, D., and Roegiers, J.-C.: Modeling of naturally fractured reservoirs using deformation dependent flow mechanism. Int. J. Rock Mech. Min. Sci. and Geomech. Abstr. 30:7 (1993), pp.1185-1191.

Barenblatt, G.E., Zheltov, I.P. and Kochina, I.N.: Basic concepts in the theory of seepage of homogenous liquids in fractured rocks. J. Appl. Math. (USSR) 24:5 (1960), pp.1286-1303.

Bear, J.: *Dynamics of fluids in porous materials*. Elsevier, New York, USA, 1972.

Berger, P. M., Roy, W. R., and Mehnert, E.: Geochemical modeling of carbon sequestration, MMV, and EOR in the Illinois Basin. Energy Procedia: 1, 3437-3444, 2009.

Bethke, C. M.: 2002. The Geochemists Workbench Release 4.0: A Users Guide to Rxn, Act2, Tact, React, and Gtplot.

Biot, M.A.: General theory of three-dimensional consolidation. J. Appl. Phys. 12 (1941), pp. 155-164.

Biot, M.A. and Willis, D.G.: The elastic coefficients of the theory of consolidation. *J. Appl. Mech.* 24 (1957), pp. 594–601.

Cantucci, B., Montegrossi, G., Vaselli, O., Tassi, F., Quattrocchi, F., and Perkins, E. H.: Geochemical modeling of CO_2 storage in deep reservoirs: The Weyburn Project (Canada) case study. Chemical Geology: 265, 181-197, 2009.

Carroll, M.M. and Katsube, N.: The role of the Terzaghi stress in linearly elastic deformation. ASME J. Energy Res. Technol. 105 (1983), pp. 509-511.

Cipoli F., Gambardella B., Marini L., Ottonello G., and Zuccolini M. V.: Geochemistry of high-PH waters from serpentinites of the Gruppo di Voltri (Genova, Italy) and reaction path modeling of CO_2 sequestration in serpentinite aquifers. Applied Geochemistry: 19, 787-802, 2004.

Corey, A. T.: 1954. The Interrelation between Gas and Oil Relative Permeabilities. Producers monthly, 19(1), 38-41.

Credoz, A., Bildstein, O., Jullien, M., Raynal, J., Petronin, J., Lillo, M., Pozo, C., and Geniaut, G.: 2009. Experimental and Modeling Study of Geochemical Reactivity between Clayey Caprocks and CO_2 in Geological Storage Conditions. Energy Procedia, 1(1), 3445-3452.

Davies, J. P. and Davies, D. K.: Stress-dependent permeability: characterization and modelling. SPE Journal 6:2 (2001), pp. 224-235.

Davison, R., Mayder, A., Hladiuk, D., and Jarrell, J. L: Zama acid gas disposal/miscible flood implementation and results, 47th Annual Technical Meeting of the Petroleum Society in Calgary, Alberta, Canada, June 10 -12, 1996.

Delshad, M., Thomas, S. G., and Wheeler, M. F.: Parallel numerical reservoir simulations of non-isothermal compositional flow and chemistry. 2009 SPE Reservoir Simulation Symposium held in The Woodlands, Texas, USA, 2-4 February 2009.

Doughty, C.: Flow modeling for CO_2 sequestration: the Frio Brine Pilot: presented at the American Geophysical Union Fall Meeting, San Francisco, California, December 5–9, 2005, paper GC13A-1220. GCCC Digital Publication Series #05-03d, pp. 1-2.

Duan, Z. H., and Sun, R.: (2003) An improved model calculating CO_2 solubility in pure water and aqueous NaCl solutions from 257 to 533 K and from 0 to 2000 bar. Chem. Geol. 193, 257–271.

Emberley, S., Hutcheon, I., Shevalier, M., Durocher, K., Mayer, B., Gunter, W. D., and Perkins, E. H.: 2005. Monitoring of Fluid-rock Interaction and CO_2 Storage through Produced Fluid Sampling at the Weyburn CO2-injection Enhanced Oil Recovery Site, Saskatchewan, Canada. Applied Geochemistry, 20(6), 1131-1157.

Ennis-King, J. and Paterson, L.: Rate of dissolution due to convective mixing in the underground storage of carbon dioxide, presented at 6th International Conference on Greenhouse Gas Control Technologies, Kyoto, Japan, 2002.

Ennis-King, J., Paterson, L.: Role of convective mixing in the long-term storage of carbon dioxide in deep saline formations. SPE Annual Technical Conference and Exhibition held in Denver, Colorado, U.S.A., 5-8 October 2003.

Ennis-King, J., Paterson, L.: Coupling of geochemical reactions and convective mixing in the long-term geological storage of carbon dioxide. International Journal of Greenhouse Gas Control I, 86-93, 2007.

Ennis-King, J., Preston, I., and Paterson, L.: Onset of convection in anisotropic porous media subject to a rapid change in boundary conditions, Phys. Fluids , 17 084107, 2005.

Farajzadeh, R., Salimi, H., Zitha, P. L. J., and Bruining, H.: Numerical simulation of density-driven natural convection in porous media with application for CO_2 injection projects. International Journal of Heat and Mass Transfer 50, 5054-5064, 2007.

Farajzadeh, R., Zitha, P. L. J., and Bruining, H.: Enhanced mass transfer of CO_2 into water: experiment and modeling. 2009 SPE EUROPEC/EAGE Annual Conference and Exhibition held in Amsterdam, The Netherlands, 8-11, June 2009.

Feely, R. A., Sabine, C. L., Lee, K., Berelson, W., Kleypas, J., Fabry, V. J., and Millero, F. J.: 2004. Impact of anthropogenic CO2 on the CaCO3 system in the oceans. Science, 305 (5682), 362-366.

Förster, R. Giese, C. Juhlin, B. Norden, N. Springer, and CO2SINK Group: The Geology of the CO2SINK Site: From Regional Scale to Laboratory Scale, Energy Procedia, Vol. 1, Issue 1, February 2009, Pages 2911-2918.

Frangeul, J., Nghiem, L., Emmanuel, C., and Thibeau, S.: Sleipner/Utsira CO_2 geological storage: full field flow and geochemical coupling to assess the long term fate of the CO_2: Dallas, Texas, 18-21 April, 2004, Proceedings AAPG Annual Conference, AAPG 86278, 2004.

Gaus, I., Azaroual, M., and Czernichowski-Lauriol, I.: Reactive transport modeling of dissolved CO_2 in the cap rock base during CO_2 sequestration (Sleipner Site, North Sea). Second Annual Conference on Carbon Sequestration, May 5-8th, 2003.

Gaus, I., Azaroual, M., and Czernichowski-Lauriol, I.: Reactive transport modelling of the impact of CO_2 injection on the clayey cap rock at Sleipner (North Sea), Chemical Geology 217 (2005) 319– 337.

Geertsma, J.: The effect of fluid pressure decline on volumetric changes of porous rock. Trans. AIME 210 (1957), pp. 331-339.

Gobran, B.D., Brigham, W.E. and Ramey, H.J. Jr.: Absolute permeability as a function of confining pressure, pore pressure, and temperature. SPE Formation Evaluation, March 1987, pp. 77-84.

Gherardi, F., Xu, T., and Pruess, K. 2007.: Numerical modeling of self-limiting and self enhancing caprock alteration induced by CO_2 storage in a depleted gas reservoir. Chemical Geology, 244(1-2), 103-129.

Green C., P., Ennis-King, J., and Pruess, K.: Effect of vertical heterogeneity on long-term migration of CO_2 in saline formations. Energy Procedia 1: 1823-1830, 2009.

Green, C. P. and Ennis-King, J.: Effect of vertical heterogeneity on long-term migration of CO_2 in saline formations. Transp. Porous Med., 82, 31-47, 2010.

Gunter, W.D., Perkins, E.H., and Hutcheon, I.: Aquifer disposal of acid gases: modeling of water-rock reactions for trapping of acid wastes. Applied Geochemistry: 15, 1085-1095, 2000.

Gunter, W.D., Mavor, M.J., and Robinson, J.R.: CO_2 storage and enhanced methane production: field testing at Fenn-Big Valley, Alberta, Canada, with Application, Proceedings of the 7th International Conference on Greenhouse Gas Control Technologies: Volume I. Rubin, E.S., Keith, D.W., and Gilboy, C.F. (eds), Elsevier Ltd., 413-421 (2005).

Gutierrez, M. and Lewis, R.W.: Petroleum reservoir simulation coupling fluid flow and geomechanics. SPE Reservoir Evaluation and Engineering, June 2001, pp. 164-172.

Hassanzadeh, H., Pooladi-Darvish, M., and Keith, D.: Modeling of convective mixing in CO_2 storage. Journal of Canadian Petroleum Technology. 44 (10) 43-51, 2005.

Hassanzadeh, H. Pooladi-Darvish, M. and Keith, D.: Stability of a fluid in a horizontal saturated porous layer: Effect of non-linear concentration profile initial and boundary conditions, Transport Porous Med (2006) 65: 193-211, 2006.

Hassanzadeh, H., Pooladi-Darvish, M., and Keith, D.: Scaling behavior of convective mixing, with application to geological storage of CO_2. AIChE Journal, Vol. 53, No. 5: 1121-1131, May 2007.

Holt, T., I., et al.: Underground storage of CO_2 in aquifers and oil reservoirs. Ener. Convers. Mgmt. (1995), 36, 535–538.

Hong, J. S. and Kim, M. C.: Effect of anisotropy of porous media on the onset of buoyancy-driven convection. Transport Porous Med 72, 241-253, 2008.

IPCC: 2005. IPCC Special Report on Carbon Dioxide Capture and Storage. New York, NY, USA: Cambridge University Press.

IPCC: 2007. Climate Change 2007: The Physical Science Basis. Contribution of Working Group I to the Fourth Assessment Report of the Intergovernmental Panel on Climate Change. Cambridge, United Kingdom and New York, NY, USA: Cambridge University Press.

Itasca Consulting Group, Inc.: FLAC3D manual: fast Lagrangian analysis of continua in three dimensions-version 2.0. Itasca Consulting Group, Inc, Minnesota, 1997.

Jaeger, J. C., Cook, N. G. W. and Zimmerman, R. W.: *Fundamentals of rock mechanics*, Wiley-Blackwell Publishing, MA, 2007.

James, C., *et al.*, 2005: Anthropogenic ocean acidification over the twenty-first century and its impact on calcifying organisms, Nature 437, 681-686 (29 September 2005).

Javaheri, M., Abedi, J., and Hassanzadeh, H.: Onset of convection in CO_2 sequestration in deep inclined saline aquifers. Journal of Canadian Petroleum Technology, v48, n8, p22-27, August 2009a.

Javaheri, M., Abedi, J., and Hassanzadeh, H.: Linear stability analysis of double-diffusive convection in porous media, with application to geological storage of CO_2. Transp. Porous Med. December 2009b.

Johnson, J. W., Nitao, J. J., and Knauss, K. G.: 2001, Reactive transport modeling of CO_2 storage in saline aquifers to elucidate fundamental processes, trapping mechanisms and sequestration partitioning. The First National Conference on Carbon Sequestration, May 14-17, 2001, Washington, DC.

Karypis, G. and Kumar, V.: A parallel algorithm for multilevel graph partitioning and sparse matrix ordering. Journal of Parallel and Distributed Computing 48 (1998), pp. 71-85.

Karypis, G. and Kumar, V.: A fast and high quality multilevel scheme for partitioning irregular graphs. Siam J. Sci. Comput. 20:1 (1999), pp. 359-392.

Katz, D.L. and R.L. Lee.: *Natural gas engineering*, McGraw-Hill Publ. Comp., New York, NY 1990.

Kazemi, H.: Pressure transient analysis of naturally fractured reservoirs with uniform fracture distribution. Soc. Pet. Eng., (1969). 451-62. Trans., AIME, 246.

Ketzer, J. M., Iglesias, R., Einloft, S., Dullius, J., Ligabue, R., and de Lima, V.: Water-rock- CO_2 interactions in saline aquifers aimed for carbon dioxide storage: Experimental and numerical

modeling studies of the Rio Bonito Formation (Permian), southern Brazil. Applied Geoche-mistry: 24, 760-767, 2009.

Kharaka, Y. K., Cole, D. R., Thordsen, J. J., Kakouros, E., and Nance, H. S.: Gas-water-rock interactions in sedimentary basins: CO_2 sequestration in the Frio Formation, Texas, USA. Journal of Geochemical Exploration: 89, 183-186, 2006.

Kneafsey, T. J., Pruess, K.: Laboratory flow experiments for visualizing carbon dioxide-induced, density-driven brine convection. Transp. Porous Med 82, 123-139, 2010.

Kumar, A., Ozah, R., Noh, M., Pope, G.A., Sepehrnoori, K., Bryant, S., and Lake, L.W.: Reservoir simulation of CO_2 storage in deep saline aquifers, SPE 89343, SPE Journal, 2005.

Lasaga, A. C.: 1984. Chemical kinetics of water-rock interactions. Journal of Geophysical Research, 89(B6), 4009-4025.

Lagneau V., Pipart A. and Catalette H.: (2005) Reactive transport modelling and long term behaviour of CO_2 sequestration in saline aquifers. Oil and Gas Science and Technology 60: 231-247.

Leverett, M.C.: Capillary behavior in porous media. Trans. AIME 142 (1941), pp. 341-358.

Law, H. S. and Bachu, S.: Hydrological and numerical analysis of CO_2 disposal in deep aquifer systems in the Alberta sedimentary basin. Ener. Convers. Mgmt (1996), 37(6-8), 1167-1174.

Lindeburg, E.: Escape of CO_2 from large horizontal aquifers confined only by a cap seal. Conference: Greenhouse Gases: Mitigation Options (1995).

Lindeberg, E. and Wessel-Berg, D.: Vertical convection in an aquifer column under a gas cap of CO_2, Energy Conversion and Management, 38 S 229-234, 1996.

Mandel, J.: Consolidation des sols (etude mathematique). Geotechnique (1953) pp. 3287–3299.

Mavor, M.J. and Gunter, W.D.: Secondary porosity and permeability of coal vs. gas composition and pressure, SPE Reservoir Evaluation and Engineering, 114-125 (2006).

McKee, C.R., Bumb, A.C. and Koenig, R.A.: Stress-dependent permeability and porosity of coal and other geologic formations. SPE Formation Evaluation 3:1 (1988), pp. 81-91.

McTigue, D.F.: Thermoelastic response of fluid-saturated porous rock. Journal of Geophysical Research 91:9 (1986), pp. 9533-9542.

Michael, K. and Buschkuehle, B.E.M.: Acid-gas injection at West Stoddart, British Columbia: An analogue for the detailed hydrogeological characterization of a CO_2 sequestration site, Journal of Geochemical Exploration, 89:280-283 (2006).

Millero, F. J. 1995. Thermodynamics of the carbon dioxide system in the oceans. Geochimica et Cosmochimica Acta, 59(4), 661-677.

Mito, S., Xue, Z., and Ohsumi, T.. Case study of geochemical reactions at the Nagaoka CO_2 injection site, Japan. International Journal of Greenhouse Gas Control: 2, 308-319, 2008.

Narashimhan, T. N. and Witherspoon, P. A.: An integrated finite difference method for analysis of fluid flow in porous media. Water Resources Res. 12 (1976), pp. 57–64.

Nghiem, L., Sammon, P., Grabenstetter, J., and Ohkuma, H.: Modeling CO_2 storage in aquifers with a fully-coupled geochemical EOS compositional simulator, SPE/DOE 14th Symposium on Improved Oil recovery, Tulsa, Oklahoma, 17-21 April, 2004.

Norris, A.: On the correspondence between poroelasticity and thermoelasticity. J. Appl. Phys. 71 (1992), pp.1138-1141.

Nur, A. and Byerlee, J.D.: An exact effective stress law for elastic deformation of rock with fluids. J. Geophys. Res. 76 (1971), pp. 6414-6419.

Ostensen, R.W.: The effect of stress-dependent permeability on gas production and well testing. SPE Form. Eval. 1:3 (1986), pp. 227–235.

Ozah, R.C., Lakshminarasimhan, S., Sephrenoori, K., and Bryant, S.L.: Numerical simulation of the storage of pure CO_2 and CO_2-H_2S gas Mixture in Deep Saline Aquifers. 2005 SPE Annual Technical Conference and Exhibition held in Dallas, Texas, U.S.A., 9-12 October 2005.

Palmer, I., Mavor, M., and Gunter, B.: Permeability changes in coal seams during production and injection, Proceedings of the 2007 International Coalbed Methane Symposium in Tuscaloosa, Alabama, Paper 0713.

Parkhurst, D. L., Appelo, C. A. J., et al.: 1999. User's guide to PHREEQC (Version 2): A computer program for speciation, batch-reaction, one-dimensional transport, and inverse geochemical calculations.

Pau, G. S. H., Bell, J. E., Pruess, K., Almgren, A. S., Lijewski, M. J., and Zhang, K.: High resolution simulation and characterization of density-driven flow in CO_2 , Adv. Water Res. 2010; 33: 443–445.

Pruess, K.: TOUGH2—a general purpose numerical simulator for multiphase fluid and heat flow. Lawrence Berkeley National Laboratory Report LBL-29400, Berkeley, CA, 1991.

Pruess, K.: Numerical simulation of CO_2 leakage from a geologic disposal reservoir, including transitions from super- to sub-critical conditions, and boiling of liquid CO_2, Soc. Pet. Eng. J., pp. 237 - 248, June 2004.

Pruess, K.: 2005. ECO2N: A TOUGH2 fluid property module for mixtures of water, NaCl, and CO_2. Lawrence Berkeley National Laboratory, Berkeley, California.

Pruess, K.: Leakage of CO_2 from geologic storage: Role of secondary accumulation at shallow depth, Int. J. Greenhouse Gas Control, Vol. 2, Issue 1, pp. 37–46, doi:10.1016/S1750-5836(07)00095-3, 2008.

Pruess, K. and Narasimhan, T.N.: A practical method for modeling fluid and heat flow in fractured porous media. Soc. Pet. Eng. J. 25:1 (1985), pp. 14-26.

Pruess, K., Oldenburg, C. and Moridis G.: TOUGH2 user's guide, version 2.0. Report LBNL-43134, Lawrence Berkeley National Laboratory, Berkeley, California, 1999.

Pruess, K. and Spycher, N.: ECO2N – a fluid property module for the TOUGH2 code for studies of CO_2 storage in saline aquifers, Energy Conversion and Management, Volume 48, Issue 6, June 2007, Pages 1761-1767.

Pruess, K., Xu T., Apps, J., and Garcia, J.: Numerical modeling of aquifer disposal of CO_2. SPE/EPA/DOE Exploration and Production Environmental Conference held in San Antonio, Texas, 26-28 February 2001.

Raistrick, M., Hutcheon, I., Shevalier, M., Nightingale, M., Johnson, G., Taylor, S., Mayerb, B., Durocher, K., Perkins, E., and Gunter, B.: Carbon dioxide-water-silicate mineral reactions enhance CO_2 storage; evidence from produced fluid measurements and geochemical modeling at modeling at the IEA Weyburn-Midale Project. Energy Procedia: 1, 3149-3155, 2009.

Rapaka, S., Chen, S., Pawar, R. J., Stauffer P. H. and Zhang, D.: Non-modal growth of perturbations in density-driven convection in porous media. Journal of Fluid Mechnanics, 609, 285-303, 2008.

Rapaka, S., Pawar, R. J., Stauffer, P. H., Zhang, D., and Chen, S.: Onset of convection over a transient basestate in anisotropic and layered porous media. Journal of Fluid Mechanics, 641: 227-244, 2009.

Riaz, A. Hesse, M., Tchelepi, A., and Orr, F. M. Jr.: Onset of convection in a gravitationally unstable, diffusive boundary layer in porous media, Journal of Fluid Mechanics, 548, 87-111, 2006.

Ringrose, P. and Iding, M.: Assessing the long-term performance of the In Salah CO_2 storage site, 33rd International Geological Congress-Oslo, Aug. 6-14, 2008.

Rumpf B., Nicolaisen H., Ocal C., and Maurer G.: (1994) Solubility of carbon dioxide in aqueous solutions of sodium chloride: experimental results and correlation. J. Sol. Chem. 23, 431–448.

Rutqvist, J. and Tsang, C.F.: A study of caprock hydromechanical changes associated with CO_2-injection into a brine formation. Environ. Geol. 42 (2002), pp. 296–305.

Rutqvist, J., Vasco, D.W. and Myer L.: Coupled reservoir-geomechanical analysis of CO_2 injection and ground deformations at In Salah Algeria. Int. J. of Greenhouse Gas Control 4 (2010), pp. 225–230.

Rutqvist, J., Wu Y.-S., Tsang, C.F. and Bodvarsson, G.A.: Modeling approach for analysis of coupled multiphase fluid flow heat transfer and deformation in fractured porous rock. Int. J. Rock Mech.and Min. Sci. 39 (2002), pp. 429–442.

Sorensen, J. A., Holubnyak, Y. I., Hawthorne, S. B., Miller, D. J., Eylands, K., Steadman, E. N., and Harju, J. A.: Laboratory and numerical modeling of geochemical reactions in a reservoir used for CO_2 storage. Energy Procedia: 1 3391-3398, 2009.

Spencer, L., Xu, Q., LaPedalina, F., and Weir, G., Site characterization of the Otway basin storage pilot in Australia. Proceeding of the 8th International Conference on Greenhouse Gas Control technologies, 19-22 June 2006, Trondheim, Norway.

Spycher, N., Pruess, K., and Ennis-King, J.: CO_2-H_2O mixtures in the geological sequestration of CO_2. I. Assessment and calculation of mutual solubilities from 12 to 100°C and up to 600 bar. Geochimica et Cosmochimica Acta (2003), 67(16), 3015–3031.

.
Spycher, N. and Pruess., K.: CO_2-H_2O mixtures in the geological sequestration of CO_2. II. Partitioning in chloride brines at 12-100°C and up to 600 bar. Geochimica et Cosmochimica Acta (2005), 69(13), 3309–3320.

Stalker, L., Boreham, C., Underschultz, J., Freifeld, B., Perkins, E., Schacht, U. and Sharma, S.: Geochemical monitoring at the CO2CRC Otway Project: tracer injection and reservoir fluid acquisition, Energy Procedia 1:2119-2125 (2009).

Steefel, C. I. and Lasaga, A. C. 1994.: A coupled model for transport of multiple chemical species and kinetic precipitation/dissolution reactions with application to reactive flow in single phase hydrothermal systems. American Journal of Science, 294(5), 529-592.

Terzaghi, K.: The shearing resistance of saturated soils and the angle between the planes of shear. Proceedings of international conference on soil mechanics and foundation engineering, Harvard University Press, Cambridge, MA, USA, 1936, pp. 54-56.

Thibeau, S., Chiquet, P., Mouronval, G., and Lescanne, M.: Geochemical assessment of the injection of CO_2 into Rousse depleted gas reservoir. Energy Procedia: 1, 3383-3390, 2009.

Todesco, M., Rutqvist, J., Pruess, K. and Oldenburg, C.: SGP-TR-173, multiphase fluid circulation and ground deformation: a new perspective on bradyseismic activity at the Phlegrean fields (Italy). Proceedings Twenty Eighth Workshop on Geothermal Reservoir Engineering, January 27-29, 2003, Stanford University, Stanford, CA, USA, 2003.

van der Meer, L. G. H.: The conditions limiting CO_2 storage in aquifers. Ener. Convers. Mgmt., (1993) 34 (9-11), 959–966.

van der Meer, L. G. H.: The CO_2 storage efficiency of aquifers. Ener. Convers. Mgmt. (1995), 36 (6-9), 513-518.

van Genuchten, M.Th.: A closed-form equation for predicting the hydraulic conductivity of unsaturated soils. Soil Sci. Soc. 44(1980), pp. 892-898.

Verma, A., and Pruess, K.: Thermohydrological conditions and silica redistribution near high-level nuclear wastes emplaced in saturated geological formations. J. Geophys. Res. 93 (1988), pp. 1159-1173.

Vinsome, P.K.W. and Westerveld, J. : A simple method for predicting cap and base rock heat losses in thermal reservoir simulators, J. Canadian Pet. Tech., 19 (3), 87–90, July-September 1980.

Warren, J.E. and Root, P.J.: The behavior of naturally fractured reservoirs. Society of Petroleum Engineers Journal, Transactions AIME 228, September 1963, pp. 245-255.

Weir, G. J., *et al.*: Reservoir storage and contaminant of greenhouse gases, Transport in porous media (1996), 23, 37-60.

Wellman, T. P., Grigg, R. B., McPherson, B. J., Svec, R. K., and Lichtner, P. C.: 2003. Evaluation of CO_2-brine-reservoir rock interaction with laboratory flow tests and reactive transport modeling. SPE 80228 International Symposium on Oilfeld Chemistry, 5-7 February 2003, Houston, Texas.

White, S., Weir, G., and Kissling, W.: 2002. Numerical simulation of CO2 sequestration in natural CO_2 reservoirs on the Colorado Plateau. Proceedings of the First National Conference on Carbon Sequestration, Washington, DC, May 2001.

White, S., Allis, R., Moore, J., Chidsey, T., Morgan, C., Gwynn, W., and Adams, M.: 1995. Natural CO_2 reservoirs on the Colorado plateau and southern Rocky Mountains, USA, a numerical model. Proc. Greenhouse Gas Control Technologies 6th Conference, Kyoto, Japan, Oct. 2002.

White, S. P., Allis, R., Moore, J., Chidsey, T., Morgan, C., Gwynn, W., Adams, M.: Simulation of reactive transport of injected CO_2 on the Colorado Plateau, Utah, USA. Chemical Geology 217, 387-405, 2005.

Whittaker, S.G.: (2005): Geological characterization of the Weyburn field for geological storage of CO_2: Summary of phase I results of the IEA GHG Weyburn CO_2 monitoring and storage project; in Summary of Investigations 2005, Volume 1, Saskatchewan Geological Survey, Sask. Industry Resources, Misc. Rep. 2005-4.1, CD-ROM, Paper A-1, 6p.

Wilson, R.K. and Aifantis, E.C.: On the theory of consolidation with double porosity. Int. J. Eng. Sci. 20:9 (1982), pp. 1009-1035.

Wigand, M., Carey, J.W., Chutt, H., Spangenberg, E., and Erzinger, J.: Geochemical effects of CO_2 sequestration in sandstone under simulated simulated in situ conditions of deep saline aquifers. Applied Geochemistry: 23, 2735-2745, 2008.

Winterfeld, P.H. and Wu, Y.-S.: Simulation of CO_2 sequestration in brine aquifers with geomechanical coupling, in *Computational models for CO_2 sequestration and compressed air energy storage*," chapter 8, edited by J. Bundschuh and R. Al-Khoury, CRC Press, 2014.

Wolery, T. J.: 1992. EQ3/6: A software package for geochemical modeling of aqueous systems: Package overview and installation guide (version 7.0). Lawrence Livermore National Laboratory Livermore, CA.

Wong, S., Gunter, W.D. and Gale, J.: Site ranking for CO_2-enhanced coalbed methane demonstration pilots, Proceedings of the 5th International Conference on GHG Control Technologies, Cairns, Australia, (Editors: Williams, D., Durie, B., McMullan, P., Paulson, C., Smith, A.) CSIRO Publishing, 531-536 (2001).

Wu, Y.-S. and Pruess, K.: A multiple-porosity method for simulation of naturally fractured petroleum reservoirs, SPE Reservoir Engineering, 3 (1988), 327-336.

Wu, Y. S., Liu, H. H. and Bodvarsson, G. S.: A triple-continuum approach for modeling flow and transport processes in fractured rock, Journal of Contaminant Hydrology, 73 (2004a), 145-179.

Wu, Y. S., Pan L., and Pruess, K.: A physically based approach for modeling multiphase fracture-matrix interaction in fractured porous media, Advances in Water Resources, Vol. 27 (2004b), 875-887.

Wu, Y.-S. and Qin, G.: A general numerical approach for modeling multiphase flow and transport in fractured porous media, Communications in Computational Physics, Vol. 6, No. 1, pp.85-108, 2009.

Xu, T. and Pruess, K. 1998.: Coupled modeling of non-isothermal multiphase flow, solute transport and reactive chemistry in porous and fractured media: 1. Model development and validation. Lawrence Berkeley National Laboratory, Berkeley, California.

Xu, T. and Pruess, K. 1999.: An improved equilibrium-kinetics speciation algorithm for redox reactions in variably saturated subsurface flow systems. Computers and Geosciences, 25(6), 655-666.

Xu, T., Apps, J. A., and Pruess, K.: Analysis of mineral trapping for CO_2 disposal in deep aquifers. Lawrence Berkeley National Laboratory Report LBNL-46992, Berkeley, California, 2001.

Xu, T., Apps, J. A., and Pruess, K.: Reactive geochemical transport simulation to study mineral trapping for CO_2 disposal in deep arenaceous formations. Journal of Geophysical Research: 108, B2, 2003.

Xu, T., Apps, J. A., and Pruess, K.: Numerical simulation of CO_2 disposal by mineral trapping in deep aquifers. Applied Geochemistry: 19, 917-936, 2004a.

Xu, T., Apps, J. A., Pruess, K., and Yamamoto, H.: Injection of CO_2 with H_2S and SO_2 and subsequent mineral trapping in sandstone-shale formation. Lawrence Berkeley National Laboratory Report LBNL-57426, Berkeley, California, 2004b.

Xu, X., Chen, S., and Zhang, D.: Convective stability analysis of the long-term storage of carbon dioxide in deep saline aquifers. Advances in Water Resources, 29, 397-407, 2006a.

Xu, T., Sonnenthal, E., Spycher, N., and Pruess, K.: 2006b. TOUGHREACT-a simulation program for non-isothermal multiphase reactive geochemical transport in variably saturated geologic media: Applications to geothermal injectivity and CO_2 Geological Sequestration. Computers Geosciences, 32(2), 145-165.

Xu, T., Apps, J. A., Pruess, K., and Yamamoto, H.: Numerical modeling of injection and mineral trapping of CO_2 with H_2S and SO_2 in a sandstone formation. Chemical Geology: 242, 319-346, 2007.

Xu, T., Kharaka, Y. K., Doughty, C., Freifel, B. M., and Daley, T. M. Reactive transport modeling to study changes in water chemistry induced by CO_2 injection at the Frio-I Brine Pilot, Chemical Geology: 271, 153-164, 2010.

Yang, C. and Gu, Y.: Accelerated mass transfer of CO_2 in reservoir brine due to density-driven natural convection at high pressures and elevated temperatures. Ind. Eng. Chem. Res., 45, 2430-2436, 2006.

Zerai, B., Saylor, B. Z., and Matisoff, G. Computer simulation of CO_2 trapped through mineral precipitation in the Rose Run Sandstone, Ohio. Applied Geochemistry: 21, 223-240, 2006.

Zhang, K., Doughty, C., Wu, Y.-S., and Pruess K.: Efficient parallel simulation of CO_2 geologic sequestration in saline aquifers. 2007 SPE Reservoir Simulation Symposium held in Houston, Texas, U.S.A., 26-28 February 2007.

Zhang, K., Wu, Y.-S. and Pruess, K.: User's guide for TOUGH2-MP - a massively parallel version of the TOUGH2 code. Report LBNL-315E, Lawrence Berkeley National Laboratory, Berkeley, CA, USA, 2008.

Zimmerman, R.W.: *Compressibility of sandstones*. Elsevier, Amsterdam, The Netherlands, 1991.

Zwingmann, N., Mito, S., Sorai, M., Ohsumi, T.: 2005 - Pre-injection characterization and evaluation of CO_2 sequestration potential in the Haizume Formation, Niigata Basin, Japan.

Appendix A: Publications/Presentations Generated from this Research

Huang, Z., Winterfeld, P. H., Wu, Y.-S.: Parallel fully-coupled hydromechanical modeling of CO_2 leakage through fluid-driven fracture zones during injection, submitted to International Journal of Green House Gas Control.

Pruess, K.: Modeling CO_2 leakage scenarios, including transitions between super- and sub-critical conditions, and phase change between liquid and gaseous CO_2, Energy Procedia, Volume 4, 2011, Pages 3754–3761.

Winterfeld, P. H., Wu, Y.-S.: Numerical simulation of CO_2 sequestration in saline aquifers with geomechanical effects, 10th Annual Conference on Carbon Capture and Sequestration, May 2-5, 2011, in Pittsburgh, PA.

Winterfeld, P. H., Wu, Y.-S.: SPE 141514 - Parallel simulation of CO_2 sequestration with rock deformation in zaline aquifers, 2011 SPE Reservoir Simulation Symposium held 21-23 February, 2011, in The Woodlands, TX.

Winterfeld, P. H., Wu, Y.-S.: A novel fully coupled geomechanical model for CO_2 sequestration in fractured and porous brine aquifers, XIX International Conference on Computational Methods in Water Resources (CMWR 2012), held at the University of Illinois at Urbana-Champagne, June 17-22, 2012.

Winterfeld, P. H., Wu, Y.-S., Pruess, K., and Oldenburg, C.: Development of advanced thermal-hydrological-mechanical model for CO_2 storage in porous and fractured saline aquifers, TOUGH Symposium 2012, held at Lawrence Berkeley National Laboratory, Berkeley, California, September 17-19, 2012.

Winterfeld, P.H. and Y.S. Wu: Simulation of CO_2 sequestration in brine aquifers with geomechanical coupling, in *Computational models for CO_2 sequestration and compressed air energy storage,*" chapter 8, edited by J. Bundschuh and R. Al-Khoury, CRC Press, 2014.

Winterfeld, P. H. and Wu, Y.-S.: Simulation of THM processes in fractured reservoirs, in *Dynamics of fluids and transport in fractured-porous media*, AGU Books, to be published.

Wu, Y.-S., Xiong, Y., Zhang, R., and Winterfeld, P. H.: Simulation of coupled thermal-hydrological–mechanical–chemical (THMC) processes in porous media," presented at the XX International Conference on Computational Methods in Water Resources (CMWR 2014), June 10-13, 2014, at the University of Stuttgart, Germany.

Zhang, R., Yin, X., Winterfeld, P. H. and Wu, Y.-S.: A fully coupled model of nonisothermal multiphase flow, geomechanics, and chemistry during CO_2 sequestration in brine aquifers, TOUGH Symposium 2012, held at Lawrence Berkeley National Laboratory, Berkeley, California, September 17-19, 2012.

Zhang, R., Yin, X., Wu, Y.-S., and Winterfeld, P. H.: A fully coupled model of nonisothermal multiphase flow, solute transport and reactive chemistry in porous media, SPE Annual Technical Conference and Exhibition held in San Antonio, Texas, USA, 8-10 October 2012.

Appendix B: Participating Researchers/Students

Colorado School of Mines:

- Yu-Shu Wu, Professor, Petroleum Engineering
- Xiaolong Yin, Assistant Professor, Petroleum Engineering
- Philip H. Winterfeld, Research Associate Professor, Petroleum Engineering
- Ronglei Zhang, Ph. D. Student, Petroleum Engineering

Colorado School of Mines/University of California, Riverside:

- Zizhong Chen

Lawrence Berkeley National Laboratory:

- Karsten Pruess
- Curt Oldenburg